

DISSERTATION

submitted to the

Combined Faculties of Natural Sciences and Mathematics
of Heidelberg University, Germany
for the degree of

DOCTOR OF NATURAL SCIENCES

put forward by

Ingo Hermann, M.Sc.
born in Backnang

Oral examination: May 5, 2021

DEVELOPMENT OF NOVEL METHODS IN QUANTITATIVE MAGNETIC RESONANCE IMAGING

Referees:

Prof. Dr. rer. nat. Lothar R. Schad
Prof. Dr. rer. nat. Peter Bachert

Development of novel methods in quantitative magnetic resonance imaging:

Quantitative magnetic resonance imaging (MRI) is a non-invasive and versatile tool for the assessment of anatomical structures. In recent years, MRI has evolved rapidly and is of high clinical interest because of its potential to distinguish diseased from healthy tissue. A variety of methods have been proposed for quantitative cardiac MRI, but insufficient precision and practicality limit its clinical use. One objective of this work was to analyze the effects of blood flow in relation to T_1 relaxation times of blood for conventional inversion recovery (IR) and saturation recovery (SR) methods. Simulations, phantom, and in vivo experiments were performed to validate the effects of flow. The in-flow of non-prepared spins resulted in decreased T_1 times, and thus SR methods were found to be more resistant to flow effects. Based on this, a sequence was developed for simultaneous quantification of T_1 , T_2 , and T_2^* . Phantom measurements were performed with high accuracy in agreement with simulations and good visual image quality was observed in the myocardium compared to reference methods and in patients. In the second part of the work, a novel renal magnetic resonance fingerprinting (MRF) approach was developed for the simultaneous quantification of T_1 and T_2^* within four slices. Simulations showed good agreement with phantom measurements and a convergence of the reconstructed relaxation times. In vivo measurements benefited from a 10-fold speedup compared to conventional methods and good reproducibility for repeated measurements. Additionally, this technique has been used in brain scans at two centers to study white matter lesions in patients with multiple sclerosis. Complex and computationally costly data processing was replaced by a neural network combining noise reduction, T_1 and T_2^* reconstruction, distortion correction, and white matter, gray matter and lesion segmentation. Robust and accurate parameter maps provide reconstructions with a 100-fold speed up, and therefore ideal for clinical applications.

Entwicklung neuartiger Methoden in der quantitativen Magnetresonanztomographie:

Die quantitative Magnetresonanztomographie (MRT) ist ein nicht-invasives und vielseitiges Werkzeug für die Beurteilung anatomischer Strukturen. In den letzten Jahren hat sich die MRT rasant weiterentwickelt und ist aufgrund ihres Potenzials, krankes von gesundem Gewebe zu unterscheiden, von hohem klinischen Interesse. Speziell für die quantitative kardiale MRT wurde eine Vielzahl von Methoden vorgeschlagen, aber unzureichende Präzision und Praktikabilität begrenzen den klinischen Einsatz. Ein Ziel dieser Arbeit war es, die Auswirkungen des Blutflusses in Bezug auf die T_1 -Relaxationszeiten des Blutes für konventionelle Inversions- (IR) und Saturierungs- (SR) Methoden zu analysieren. Es wurden Simulationen, Phantom- und in vivo-Experimente durchgeführt, um die Auswirkungen des Flusses zu validieren. Der Einlauf von nicht preparierten Spins führte zu verringerten T_1 -Zeiten, und somit erwiesen sich die SR-Methoden als resistenter gegenüber Flusseffekten. Darauf basierend wurde eine Sequenz zur simultanen Quantifizierung von T_1 , T_2 und T_2^* entwickelt. Phantommessungen wurden mit hoher Genauigkeit in Übereinstimmung mit Simulationen durchgeführt und es wurde eine gute visuelle Bildqualität im Myokard im Vergleich zu Referenzmethoden und in Patienten beobachtet. Im zweiten Teil der Arbeit wurde ein neuartiger renaler Magnetresonanz-Fingerprinting (MRF)-Ansatz zur simultanen Bestimmung von T_1 und T_2^* innerhalb von vier Schichten entwickelt. Simulationen zeigten eine gute Übereinstimmung mit Phantommessungen und Konvergenz der rekonstruierten Relaxationszeiten. In vivo Messungen profitieren von einer 10-fachen Beschleunigung im Vergleich zu konventionellen Methoden und guter Reproduzierbarkeit bei wiederholten Messungen. Zusätzlich wurde diese Technik in Kopf Messungen benutzt und an zwei Zentren zur Untersuchung von Läsionen der weißen Substanz bei Patienten mit Multipler Sklerose eingesetzt. Die komplexe und rechenintensive Datenverarbeitung wurde durch ein neuronales Netzwerk ersetzt, und dabei die Rauschunterdrückung, die Rekonstruktion von T_1 und T_2^* , die Verzerrungskorrektur und die Segmentierung der weißen Substanz, grauen Substanz und Läsionen kombiniert. Robuste und genaue Parameterkarten liefert die Rekonstruktion mit 100-facher Beschleunigung, und somit ideal für klinische Anwendungen.

ACKNOWLEDGEMENT

*Physics is, hopefully, simple.
Physicists are not.*

- Edward Teller

A big thank you goes out to all the people for their help, support, guidance, and fun that made this dissertation so enjoyable.

First and foremost, I would like to thank Prof. Dr. Lothar Schad for the opportunity to work in his group and the start of a great academic journey. He gave me the opportunity to visit many conferences and meet cooperation partners all over the world. And his trust in my work, which allowed me to explore new frontiers in MRI.

Furthermore, I would like to thank Prof. Dr. Peter Bachert for his willingness to act as the second referee for this thesis and for his lecture in medical physics, where my MRI journey began.

I'd like to thank Sebastian Weingärtner, who supervised me throughout my academic years. He gave me a lot of input in the last years and captivated me for cardiac MRI. He intended me as his first member in the MARS lab where I am part of his amazing group. All the support with writing papers, programming with IDEA, and all his food for thoughts.

Likewise, I would like to thank Frank Zöllner, who was always the first one with me in the office, which led to discussions and chats we had in the early morning. His willingness to include me in so many projects and his enforcement to publish and to do what I have in mind. The valuable ideas he gave me over the years.

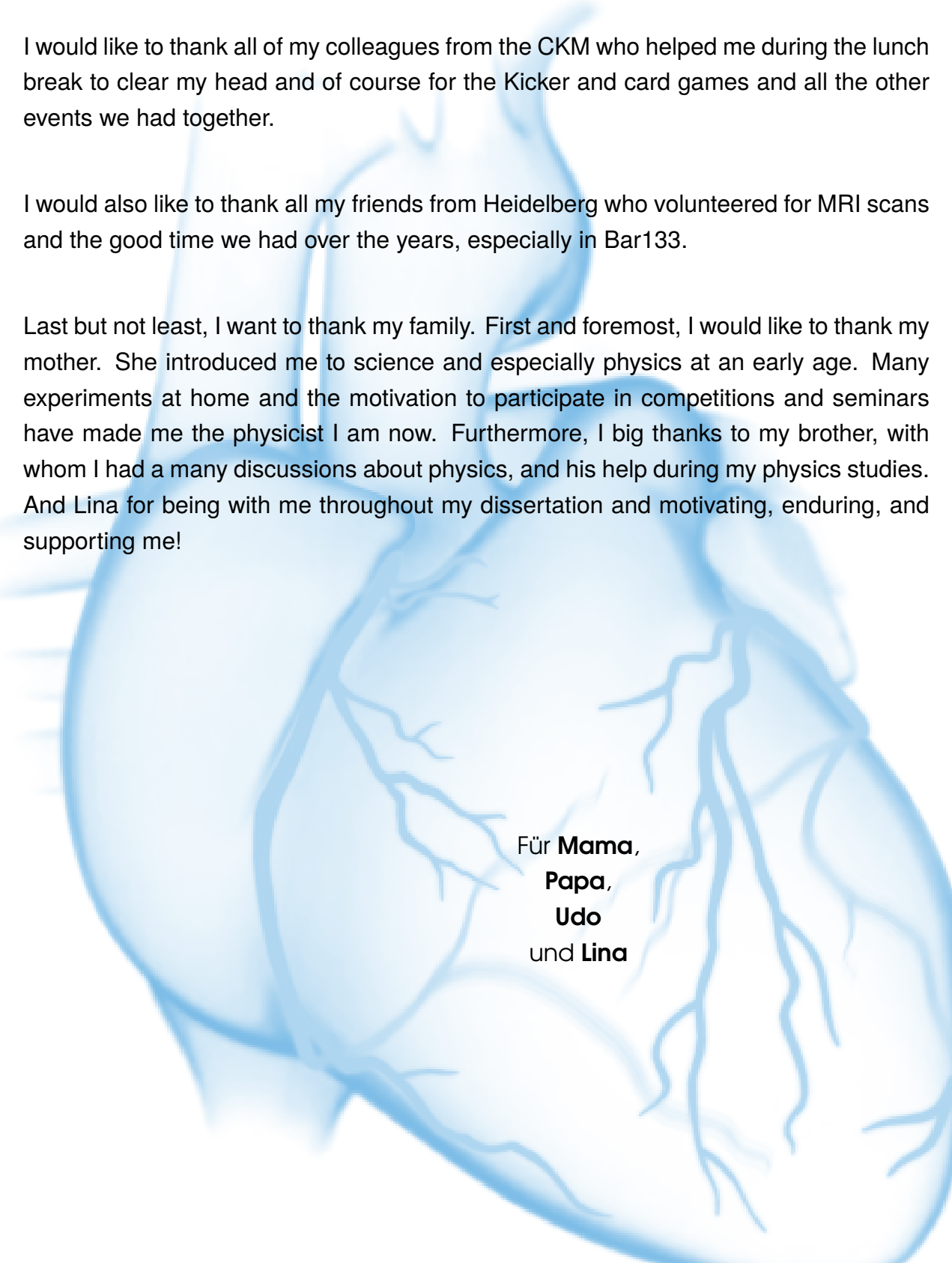
Especially, I would like to thank Jorge Chacón-Caldera as my amazing office mate and for all his input, guidance and support he gave me over the years at CKM. All the parties and events we attended together and all the matches we won in Tisch-Kicker in the lunch break!

I am also grateful to Eloy Martínez-Heras and all my friends from Barcelona for the warm welcome and the good cooperation we had in the last years.

I would like to thank all of my colleagues from the CKM who helped me during the lunch break to clear my head and of course for the Kicker and card games and all the other events we had together.

I would also like to thank all my friends from Heidelberg who volunteered for MRI scans and the good time we had over the years, especially in Bar133.

Last but not least, I want to thank my family. First and foremost, I would like to thank my mother. She introduced me to science and especially physics at an early age. Many experiments at home and the motivation to participate in competitions and seminars have made me the physicist I am now. Furthermore, I big thanks to my brother, with whom I had a many discussions about physics, and his help during my physics studies. And Lina for being with me throughout my dissertation and motivating, enduring, and supporting me!



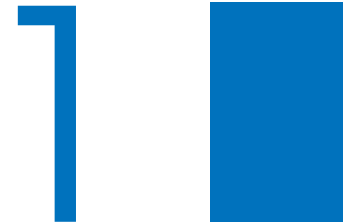
Für **Mama**,
Papa,
Udo
und **Lina**

CONTENTS

1	Introduction	1
1.1	MRI History	2
1.2	Imaging	3
1.3	Quantitative MRI	5
1.4	Quantitative Cardiac Magnetic Resonance	6
1.5	Magnetic Resonance Fingerprinting	9
2	Publications	11
I	Towards measuring the effect of flow in blood T_1 assessed in a flow phantom and in vivo	15
II	Free-breathing simultaneous T_1 , T_2 , and T_2^* quantification in the myocardium	39
III	Magnetic Resonance Fingerprinting for simultaneous renal T_1 and T_2^* mapping in a single breath-hold	67
IV	Accelerated white matter lesion analysis based on simultaneous T_1 and T_2^* quantification using Magnetic Resonance Fingerprinting and Deep Learning	85
V	Lesion probability mapping in MS patients using a regression network on MR Fingerprinting	113
3	Discussion	129
3.1	The effect of flow on cardiac T_1 measurements	129
3.2	Simultaneous quantification of T_1 , T_2 , and T_2^*	131
3.3	Simultaneous quantification using Magnetic Resonance Fingerprinting	133
3.4	Deep Learning accelerated reconstruction	135
3.5	Deep Learning lesion probability mapping	136
4	Conclusion	137
	References	139
	List of Publications	151
	Abbreviations	155

*Measure what can
be measured, and
make measurable
what cannot be
measured.*

- Galileo Galilei



INTRODUCTION

Magnetic resonance imaging (MRI) is a constantly evolving tool for the non-invasive study of the anatomical structures and functions of the human body. MRI offers the ability to provide information for the diagnosis of disease, visualization of abnormalities, and detection of early stages in pathologies. With its excellent soft tissue contrast, MRI has become a powerful tool with a broader and more distinctive range of techniques compared to computed tomography and ultrasound. Besides, MRI is harmless to the human body because it uses low-energy electromagnetic waves for non-ionizing radiation. MRI is particularly important for functional imaging, such as visualization of neurologically activated brain areas, detection of tissue changes through quantification of relaxation times, and functionality through cine imaging and flow measurements.

Especially, quantitative MRI has emerged in recent decades as a promising tool for clearly distinguishing between healthy and diseased tissue. Diseases such as heart failure, chronic kidney disease, and multiple sclerosis can be detected at early stages, allowing early drug treatment and increasing life expectancy. Quantification of tissue relaxation times opened a new field of MR physics with its enormous potential to track changes in anatomy and the ability to compare between different images, patients, and manufacturers, making it a stable and robust modality. The leading cause of death in this century is ischemic heart disease, with more than eight million deaths per year [1]. Therefore, quantitative cardiac MRI is essential to detect edema, fibrosis, iron overdose, and oxygenation, without the need for contrast agents that could be deposited in the body. The three tissue relaxation times T_1 , T_2 , and T_2^* are excellent biomarkers for assessing multiple pathologies due to their sensitivity to microstructural and metabolic changes. However, long measurement times and long breath-hold commands reduce patient comfort and complicate practicality in clinical practice. Despite the well-organized healthcare system in Germany, these long measurement times lead to higher costs, resulting in waiting times of several months for an MRI examination.

This work aimed to develop and improve different imaging techniques for the simultaneous quantification of tissue relaxation times in clinically feasible measurement times. In one part of the work, quantification of tissue relaxation times in the myocardium was performed under free-breathing conditions. This novel method was validated in healthy volunteers and myocardial patients. Additionally, the effects of blood flow were analyzed to understand the underlying processes of flow that influence the measurement of the in vivo relaxation times. In a second part, an MR fingerprinting (MRF) sequence was developed and optimized for simultaneous quantification of T_1 and T_2^* relaxation times in the kidneys across four slices. The same method was additionally applied to patients with multiple sclerosis (MS) in the brain. The entire post-processing pipeline such as denoising, distortion correction and masking was accelerated and combined through a single neural network to improve clinical applicability.

The following section explains the basics and underlying principles of MRI with a histological introduction with all the necessary concepts for the developed techniques.

1.1 MRI History

The foundation for MRI was laid with the discovery of the proton spin in 1922 by the Stern-Gerlach experiment [2]. This quantum mechanical property formed the basis for further experiments and theoretical considerations and was first measured by Isidor Rabi in 1938 [3]. There, a transition between discrete energy states was induced by an oscillating magnetic field in a static magnetic field. In 1948, Felix Bloch [4] and Edward Purcell [5] were the first to independently demonstrate nuclear magnetic resonance (NMR) in condensed matter, for which they were awarded the Nobel Prize in 1952. In these NMR experiments, the longitudinal relaxation time T_1 and the transverse relaxation time T_2 are essential parameters, which are well described by the Bloch equations. These relaxation times form the basis of all MR sequences with their unique contrast for different tissues. But it was not until the year 1973, Peter Mansfield [6] and Paul Lauterbur [7] introduced spatial encoding of the NMR signal, making MR imaging possible. Their work was awarded in 2003 with the Nobel Prize which laid the foundations of magnetic resonance imaging. As a non-invasive technique with no exposure to ionizing radiation and based on the strong dispersion from the T_1 and T_2 relaxation times for different tissues, it has become one of the most important imaging modalities in clinical use. Its rapidly developing field and increasing interest led to years of research to accelerate imaging and improve image quality.

1.2 Imaging

MRI sequences, which are a repetitive series of radio frequency (RF) pulses and gradients, offer a wide flexibility to obtain different contrasts and functionalities. They can be divided into two main classes: Spin-echo (SE) sequence [8], where an echo is formed using RF pulses, and gradient-echo (GRE) sequence [9], where an echo is formed using gradients. GRE sequences have become an important technique for modern MR examinations since the 1990s. GRE sequences are much shorter than SE sequences because only a single RF pulse needs to be applied in conjunction with a gradient reversal without any refocusing pulse. Additionally, small flip angles reduce measurement time and yield the highest contrast, as shown theoretically by Ernst in 1966 [10]. Therefore, the Signal-to-Noise (SNR) ratio is lower compared with SE sequences and it is susceptible to inhomogeneities of the magnetic field and off-resonance effects [11]. Nevertheless, GRE allows acquisition of the entire k-space within a few hundred milliseconds, which is short enough to image the myocardium in diastole [12]. The revolutionary step of GRE sequences was proposed by Mansfield and Maudsley in 1976 [13]. Rapidly successive RF pulses are used to acquire the entire k-space, preventing the longitudinal or the transverse magnetization from fully recovering. Hence, the magnetization settles into a steady-state after multiple excitations. However, the residual transverse magnetization after each excitation must be disrupted with spoiler gradients, which was proposed by Haase and Frahm in 1986 [14]. Especially for T_2^* quantification, GRE sequences are essential. The gradient reversal can be repeated several times to generate multiple echoes from a single RF pulse (illustrated in Figure 1A). In this process, the signal intensity decreases exponentially with time constant T_2^* [15]. Small flip angles are generally used in spoiled GRE and therefore, the signal is very low, especially for echoes with long TEs. Another strategy to deal with the transverse magnetization is the use of gradient refocusing, which was already laid in 1958 by Carr [16]. This sequence is called balanced steady-state free precession (bSSFP) which effectively refocuses every gradient moment after one repetition time (TR) (shown in Figure 1B). This allows the use of higher flip angles because multiple echoes overlap after each TR, which leads to an increased SNR. In the myocardium, for example, bSSFP provides high contrast between the myocardial wall and the blood pool because of its T_1 over T_2 dependence [17]. However, bSSFP is susceptible to B_0 inhomogeneities and off-resonance effects, such that signal modulations and intravoxel dephasing results in band-like artifacts [18]. The fastest technique for acquiring the k-space is echo-planar imaging (EPI) (illustrated in Figure 1C). It was a break-through for functional imaging and was proposed by Stehling in 1991 [19].

An entire k-space can be scanned with only one RF pulse in a fraction of a second. The k-space is commonly sampled in a linear manner such that small phase encoding gradients are applied after one set of frequency encoding gradients to move to the next k-space line. In the middle of the k-space, the sum of the small positive acquired

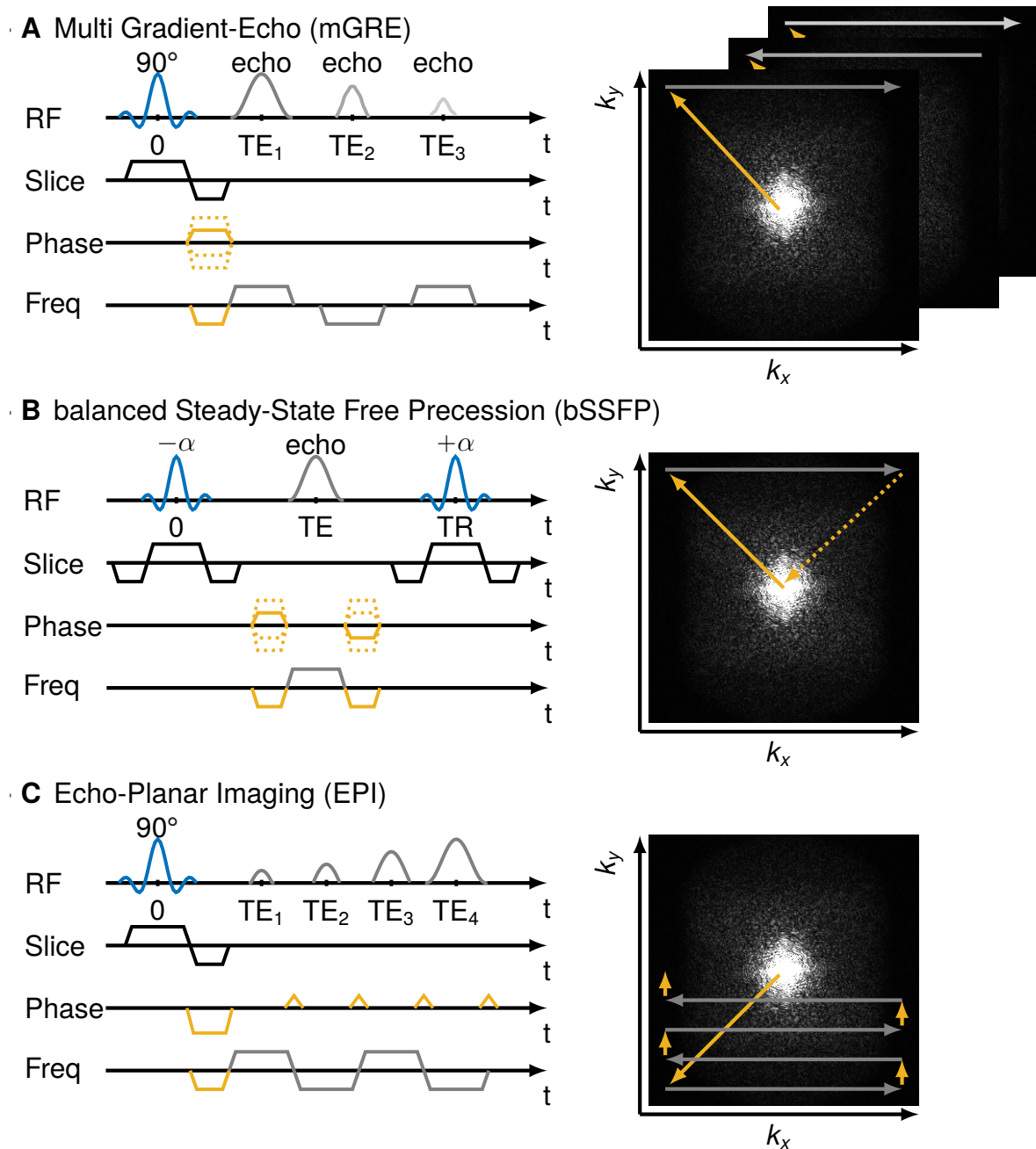


Figure 1: Schematic of three different readouts is shown with the corresponding radio-frequency pulse (RF), the slice selection gradients (Slice), the phase encoding gradients (Phase), and the frequency encoding gradient (Freq) and the corresponding trajectory in the k-space on the right side. **A** depict the multi gradient-echo readout, **B** the balanced steady-state free precession readout, and **C** the echo-planar imaging readout.

gradient compensates for the initially applied negative gradient, thus ensuring maximum re-phasing of the spins in the middle of the k-space [20]. EPI is susceptible to magnetic field inhomogeneities due to the long echo train succeeding the RF pulse caused by time dependent dephasing. Its main use is in neural applications due to the advantage of fast image acquisition [21]. GRE sequences are an essential tool for rapid k-space acquisitions and therefore single-shot imaging, especially when acceleration techniques are used to undersample the k-space. This enables the possibility to acquire multiple weighted images in clinically acceptable measurement time, which is needed for quantification.

1.3 Quantitative MRI

The crucial invention of measuring tissue properties as T_1 and T_2 opened the widely developing field of quantitative MRI in the 1980s. In 1971, Raymond Damadian first demonstrated that these relaxation times differed in healthy and diseased tissue [22]. This established the use of MRI to study disease. As early as 1970, Look and Locker [23] established a sequence for quantifying T_1 relaxation time in vivo and formed the basis for myocardial T_1 mapping, which has been the gold standard method in cardiac imaging in recent decades. In the 1990s, Hawkes et al. [24] demonstrated the application of MRI in the heart and showed a clear separation between the myocardial walls and the cavities of the individual chambers. Quantitative MRI is based on a series of contrast weighted image acquired with different echo times (TE), repetition times (TR), and inversion times (TI). The relaxation times can then be determined for each voxel by an exponential fit over their dependence as provided in the Bloch equations [4] (Equation 1).

$$\begin{aligned}
 \frac{dM_x(t)}{dt} &= \gamma(\mathbf{M}(t) \times \mathbf{B}(t))_x - \frac{M_x(t)}{T_2} \\
 \frac{dM_y(t)}{dt} &= \gamma(\mathbf{M}(t) \times \mathbf{B}(t))_y - \frac{M_y(t)}{T_2} \\
 \frac{dM_z(t)}{dt} &= \gamma(\mathbf{M}(t) \times \mathbf{B}(t))_z - \frac{M_z(t) - M_0}{T_1}
 \end{aligned} \tag{1}$$

It was shown by Larsson et al. [25] in 1989 that T_1 and T_2 times change significantly during disease development. Quantitative MRI provides imaging biomarkers for characterization of tissue pathologies, follow-up, and treatment planning. However, all quantification methods in MRI suffered from the long measurement time due to the need to

repeat scans with different scan parameters and were therefore difficult to use in clinical practice. Especially for body parts moving due to respiratory or cardiac motion.

1.4 Quantitative Cardiac Magnetic Resonance

Heart failure is the leading cause of death in the modern world [1, 27] and therefore, quantitative MRI in the myocardium has gained increasing attention. It strives for early diagnosis and detection of abnormalities, differentiation of pathologies, and guiding treatment after drug or surgery [28]. In particular, the assessment of diffuse myocardial disease has been a breakthrough for T_1 , T_2 , and T_2^* mapping, as it has historically been difficult to quantify non-invasively [29, 30]. Parametric measurements of cardiac magnetic resonance hold promise for improved diagnostic decision making and provide endpoints that reflect disease progression (Table 1). In particular, myocardial T_1 mapping is most commonly used for assessing ischemic and non-ischemic cardiomyopathies. It has been shown to be sensitive to a wide range of cardiomyopathies with high precision and reproducibility [31, 32, 33]. The methods are based on either inversion or saturation recovery (SR) pulses [34, 35]. Multiple images are acquired at different times after inversion/saturation pulses (Figure 2). This leads to a sampling of the T_1 relaxation curve and thus to the quantification of T_1 by an exponential fit. Modified look-locker inversion recovery (MOLLI) [36] is the gold standard technique for quantifying T_1 by acquiring one image per diastolic phase following an inversion recovery pulse. However, the accuracy of the T_1 estimation is affected by repetitively acquired excitation pulses that interfere with the sampling of the relaxation curve. The z-magnetization is reduced by each image acquisition, which results in a reduced T_1 time. A correction has been proposed for this method, however, still underestimates T_1 due to magne-

Table 1: Indication of pathologies for T_1 , T_2 and T_2^* mapping according to the clinical recommendations for cardiovascular magnetic resonance mapping [26].

	T_1	T_2	T_2^*
Decrease	Anderson-Fabry, iron overload, fat, hemorrhage	iron overload, hemorrhage	iron overload, hemorrhage, stress-induced ischemia
Mild increase	diffuse fibrosis, scar, subacute inflammation	diffuse fibrosis	subacute inflammation
Moderate increase	amyloid, acute inflammation, acute ischemia, necrosis	amyloid, necrosis, scar	acute inflammation, acute ischemia, necrosis

tization transfer (occurs by transfer of spin states) and T_2 effects (faster dephasing) [37, 38]. Therefore, saturation-based methods have been proposed to overcome the loss in accuracy. Saturation recovery single-shot acquisition (SASHA) [39] provides accurate T_1 times because the initial magnetization is reset by the saturation pulse before the image readout. However, the saturation pulse results in lower SNR than MOLLI because the magnetization needs to regrow. Therefore, SR methods suffer from lower precision due to a smaller dynamic range of the relaxation curve sampling, especially in patients with high heart rates. Nevertheless, the accuracy of SR methods is independent of heart rate and acquisition scheme and less susceptible to effects such as flow compared to IR-based methods because the magnetization history is reset at each heartbeat [34, 40].

T_2 quantification in the heart has a high clinical value for reliable differentiation between healthy and diseased myocardial tissue [41, 42]. In particular, for the assessment of edema in patients with amyloidosis, it showed higher performance compared to T_1 mapping [43, 44]. Conventionally, T_2 mapping is performed by acquiring T_2 preparation pulses with different durations that precede single-shot acquisitions. The first single-shot image is acquired without any preparation to sample the T_2 relaxation curve at time $t = 0$. The following two images are acquired with an additional T_2 preparation prior to the image acquisition, preceded by a three-second rest period to ensure full recovery of the magnetization before each preparation [45]. T_2 is then quantified by an exponential fit with two or three parameters to additionally cover the background noise [46]. However, it has been shown that magnetic field strength, sequence acquisition parameters, and post-processing algorithms limit the robustness of the quantification [47]. Therefore, it has been shown that a fourth single-shot image following a saturation pulse to mimic very long T_2 yields robust quantification and is less susceptible to technical factors [48, 49].

Myocardial T_2^* -mapping is a promising tool for assessing iron deposits in several iron storage diseases [50] because the T_2^* relaxation time is inversely proportional to the iron concentration [51]. The T_2^* relaxation must be sampled more densely compared with the T_2 relaxation because of its inherently shorter relaxation time course. T_2^* is shorter than T_2 due to magnetic field inhomogeneities which additionally perturb the spins. Therefore, T_2^* is typically measured at field strengths of 1.5 T yielding a slower exponential decay of T_2^* [52]. Typically, the sampling is performed using a multi-gradient echo (multi-GRE) with eight to twelve echoes in the range of 1-18 ms. Conventionally, a two-parameter exponential fit is used to quantify T_2^* , but for short T_2^* times, such as in iron deposit, the signal from echoes with long echo times reaches the noise floor. This can be corrected by either a three-parameter fit model or a truncation

model, where echoes reaching the noise floor are excluded from the analysis [53]. In particular, because of its susceptibility to inhomogeneities and the relatively fast decay, T_2^* measurements are the most challenging in clinical practice in contrast to T_1 and T_2 .

The conventional methods listed so far for quantifying T_1 , T_2 , and T_2^* each require one breath-hold per slice, which is time-consuming if the whole heart and multiple relaxation times are acquired. Nowadays, a variety of methods have been proposed that access either multiple parameters, multiple slices, or both in a single scan [54, 55, 56, 57, 58, 59, 60]. However, until now no method for cardiac imaging was proposed for the simultaneous quantification of T_1 , T_2 , and T_2^* under free breathing.

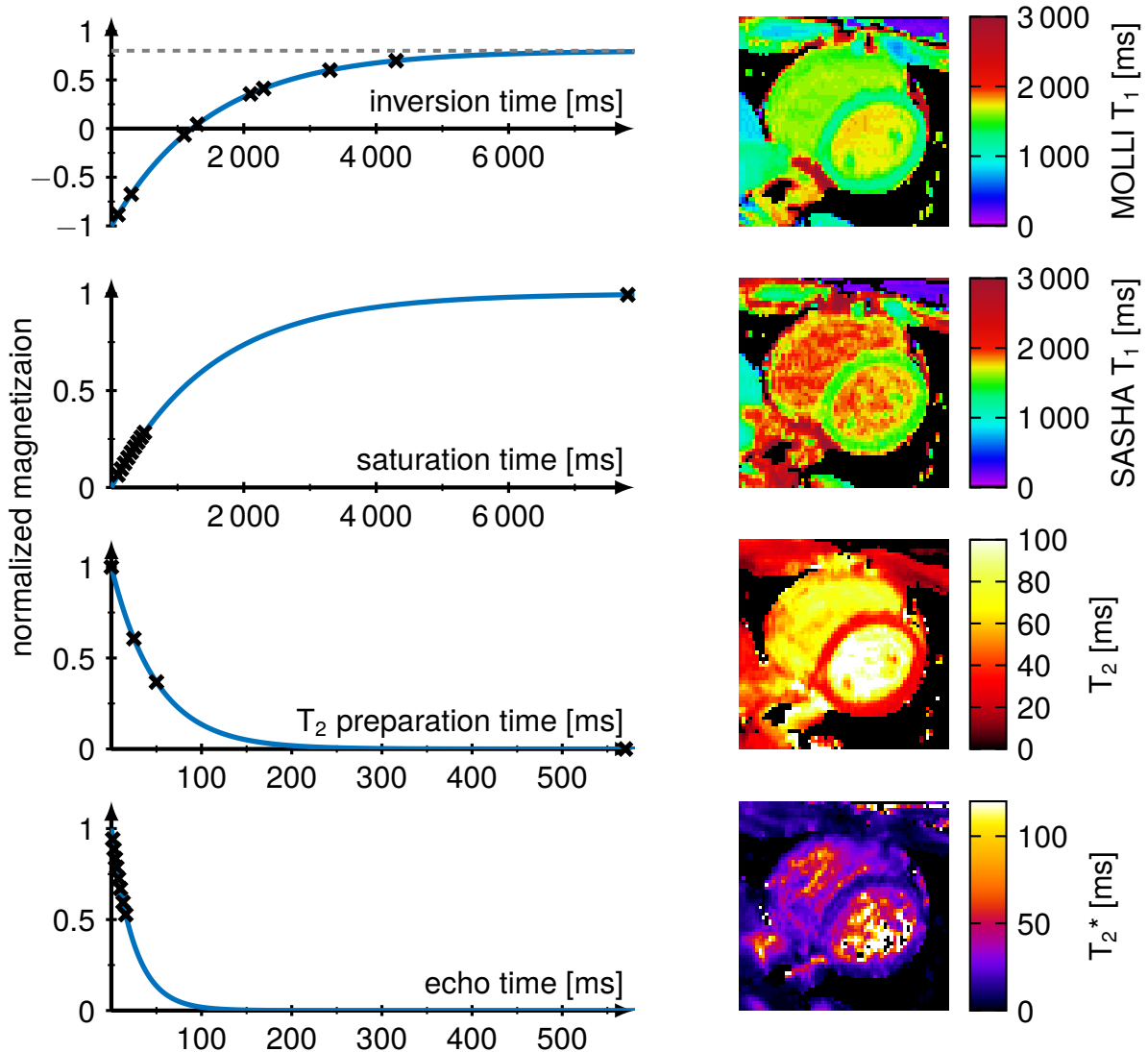


Figure 2: Normalized magnetization is shown for T_1 (MOLLI, SASHA), T_2 (T_2 prepared bSSFP) and T_2^* (multi-GRE) is shown along the recovery time. On the right side, the corresponding maps for one healthy example are shown in the short axis view.

1.5 Magnetic Resonance Fingerprinting

In 2013, Ma et al. [61] initiated a completely new approach for quantitative MRI called magnetic resonance fingerprinting (MRF). This method allows simultaneous quantification of multiple tissue parameters such as T_1 , T_2 , and T_2^* in a fraction of the time normally required to obtain these parameters. Rather than sampling the relaxation curve at a specific position, MRF relies on the pseudo-random acquisition with varying TE, TR, and flip angle to generate a unique signal evolution (fingerprint) for different tissue types (illustrated in Figure 3). Bloch simulations are used to generate a large number of fingerprints for a preselected combination of parameters, which is written into a dictionary. The captured fingerprints are then correlated with all the simulated fingerprints,

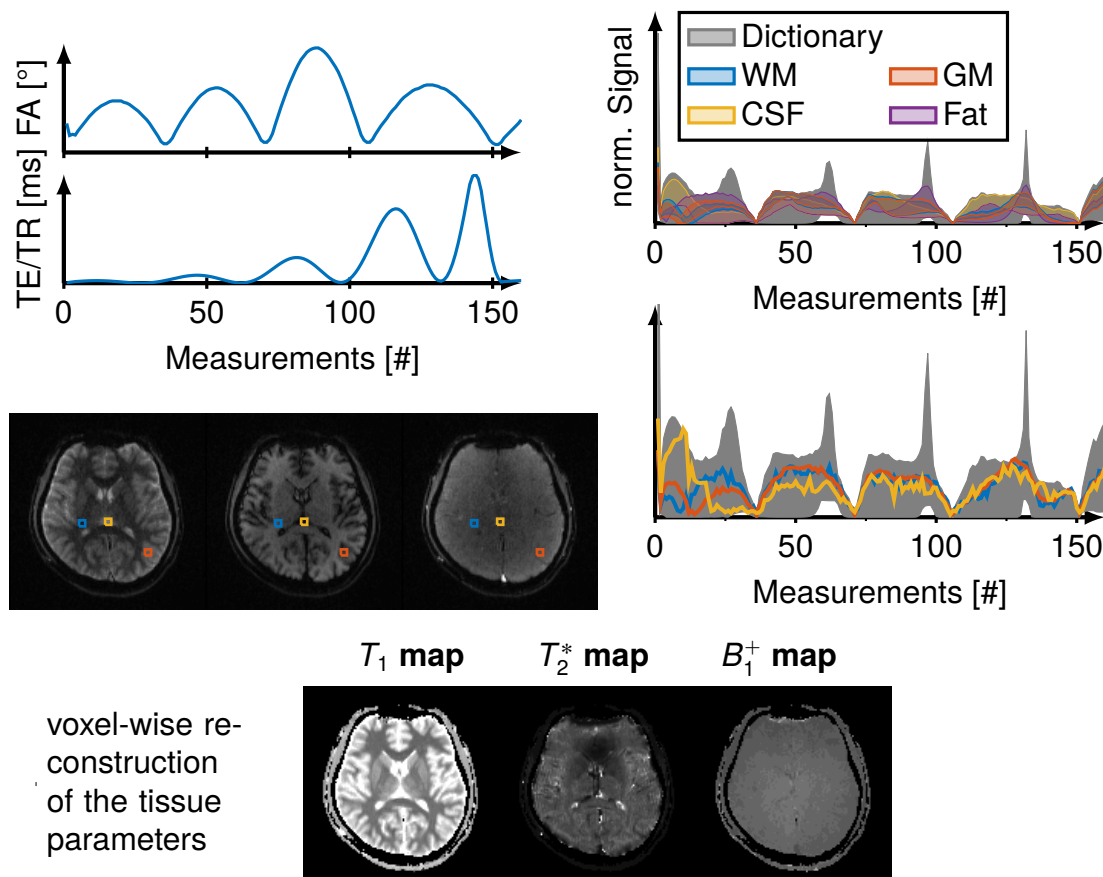


Figure 3: The MRF pipeline is shown. Various FA, TE, and TR generate different contrast shown on the left side. With these known parameters, the Bloch equations are used to calculate a dictionary for a variety of combinations, which results in unique fingerprints for white matter (WM, blue), gray matter (GM, orange), cerebrospinal fluid (CSF, yellow), and fat (violet). In gray, the entire calculated dictionary is shown. In the brain, the corresponding fingerprints for 3 areas corresponding to WM (blue), GM (orange), and CSF (yellow) are depicted. On the bottom the reconstructed T_1 , T_2^* and B_1^+ maps are depicted.

and the best correlation yields the parameter values that best match the tissue parameters. Conventionally, thousands of severely undersampled images are acquired, resulting in severe artifacts such as aliasing in each image. However, the fingerprint obtained from all data is spatio-temporally incoherent and the reconstruction yields highly accurate, precise, and repeatable parameters such as T_1 , T_2 [61], T_2^* [62, 63] as well as the transmission field B_1^+ [64], the static magnetic field B_0 inhomogeneities [61], proton density M_0 [65] and perfusion [66]. Thus, MRF offers the possibility to obtain any tissue property that could be measured conventionally. For this purpose, different signal readouts such as spiral [61, 67], cartesian [62, 64], and radial [68] are used for fast k-space sampling. Most MRF sequences include T_1 quantification and therefore additional inversion recovery pulses are played before the first excitation pulse. Additional contrasts could be implemented similarly as in cardiac imaging and preparation pulses are used for generating additional contrast.

One disadvantage of MRF is the high computational cost of computing the dictionary, which contains a large number of parameter combinations. The dictionary increases exponentially for each additional parameter and thus the voxel-wise signal matching duration also increases exponentially. Therefore, several approaches have been proposed to reduce the computational cost, such as a more effective representation of the dictionary by singular vector deconvolution [69] or compression of information by compressed sensing [70]. However, Deep Learning has been shown to provide promising results for large-scale reconstruction within seconds compared to conventional computations lasting several hours [71, 72, 73, 74]. Moreover, Deep Learning enables more efficient dictionary representation, as the traditional MRF dictionary only contains certain fingerprint parameters [75]. Therefore, Deep Learning was implemented in this work to increase accuracy and reducing reconstruction time.



PUBLICATIONS

This dissertation is structured in a cumulative form according to the regulations for the award of the doctoral degree of the Faculty of Physics and Astronomy of the Ruperto-Carola University Heidelberg. All publications were processed in the context of this dissertation and were not considered for any other dissertation. However, in this thesis, the publications are not listed in chronological order of their publication date. The publications are numbered with roman numbers. Sections, figure and table captions as well as the citations with the bibliography are numbered in each publication starting from 1 and apply only to the respective publication.

I am the first author of all publications in this dissertation, and publication I, II, III, and IV have been published in internationally recognized peer-reviewed journals. Publication V was submitted to MRM on the 21st of January 2021 and was not peer-reviewed yet. All other publications and conference abstracts are listed in the publications index at the end of this thesis.

Thematic overview

In this work, two different topics have been addressed. The first topic deals with quantitative cardiac magnetic resonance imaging, and the second topic deals with quantification using magnetic resonance fingerprinting for neural and renal applications.

The publication I comprises some results from the previous master's thesis. However, the simulations and measurements were completed as part of this dissertation. In this publication, the effects of flow on conventional myocardial saturation and inversion-based T_1 mapping sequences were evaluated because blood flow is known to reduce T_1 relaxation time in blood during measurement. The inaccuracy of these blood T_1 times

was analyzed using a controllable flow phantom. Furthermore, in vivo measurements in the descending aorta (for the assumption of linear flow) were performed for validation. As Bloch simulations showed, the main effect of flow was observed due to the in-flow of non-prepared spins. Therefore inversion recovery-based methods such as MOLLI are more susceptible to flow. The exchange of blood at each heartbeat compromises the effect of faster growth of the relaxation curve due to spins flowing in and out of the acquired slice, and therefore shows little effect on T_1 -time. Thus, for the first time, we were able to prove the theoretical assumption with well-controlled experiments and estimate the resulting deviations in the extracellular volume (ECV).

With this knowledge, a saturation recovery-based method was developed in the publication II to simultaneously quantify all three relaxation times T_1 , T_2 , and T_2^* during free breathing. Quantification of all three parametric maps is costly, and the parametric maps must be subjected to non-rigid registration, making clinical applicability difficult. Using our method, we combined saturation recovery and T_2 preparation pulses with an multi-GRE readout to obtain intrinsically registered T_1 , T_2 , and T_2^* parametric maps under free-breathing conditions. We evaluated the proposed sequence in phantom measurements and confirmed it with Bloch simulations. In addition, the sequence was tested in ten healthy volunteers with good agreement to the reference method, with the advantage of short acquisition time. The relative short echo times for the T_2^* quantification was compromised by the use of a five parameter truncation fit model. Voxel-wise standard deviation maps were additionally calculated from this fit model. The proposed sequence is now used clinically and two representative patients have been analyzed in this publication.

In the publication III, a different approach was used for quantification compared to the method developed in publication II. A magnetic resonance fingerprinting sequence was developed for simultaneous quantification of T_1 and T_2^* in the kidney, covering four slices in a single breath-hold. The aim of this publication was to use MRF renal applications, outperforming conventional methods in terms of measurement time. The proposed sequence was analyzed in phantom and in vivo measurements in eight healthy volunteers. In addition, reconstruction was performed inline on the scanner to obtain parametric maps during scanning. Furthermore, the use of denoising was evaluated with respect to the image quality of the parametric maps.

In a clinical study at the University Hospital Mannheim and a collaboration with the University Hospital in Barcelona, 50 patients with multiple sclerosis were measured in the whole brain using the MRF sequence from publication III. Several post-processing steps were combined in the reconstruction with a single neural network and compromised in the publication IV. Compared with the relatively short reconstruction for four slices in the kidneys, the reconstruction in the brain covering 60 slices takes hours. In addition, as shown in the publication III, denoising improves the quality of parametric maps but further increases the reconstruction time. Distortion correction has to be performed on the MRF data to align with conventional clinical sequences. Masking of WM and GM are important steps for the analysis of WM lesions in patients with MS. The goal was to combine all these different post-processing steps into a single convolutional neural network (CNN) that requires only a fraction of the time and yielding high accuracy and precision compared to conventional methods.

Further work incorporated the lesion segmentation progress additionally into the reconstruction using deep learning. The aim was to show that the manual segmentation process, which is very time-consuming and suffers from inter and intra-observer variations, can be replaced by an automatic deep learning reconstruction with the advantage of generating lesion probability maps instead of simple binary masks. This is of clinical interest because the neural network could learn to separate different underlying tissues such as myelin. This is compromised in publication V which has been submitted as a technical note to the Journal of Magnetic Resonance in Medicine.

Towards measuring the effect of flow in blood T_1 assessed in a flow phantom and in vivo

Ingo Hermann, Tanja Uhrig, Jorge Chacón-Caldera, Mehmet Akçakaya, Lothar Schad and Sebastian Weingärtner

PHYS. MED. BIOL. 2020, 65 095001

Abstract

Measurement of the blood T_1 time using conventional myocardial T_1 mapping methods has gained clinical significance in the context of extracellular volume (ECV) mapping and synthetic hematocrit (Hct). However, its accuracy is potentially compromised by in-flow of non-inverted/non-saturated spins and in-flow of spins which are not partially saturated from previous imaging pulses.

Bloch simulations were used to analyze various flow effects separately. T_1 measurements of gadolinium doped water were performed using a flow phantom with adjustable flow velocities at 3T. Additionally, in vivo blood T_1 measurements were performed in 6 healthy subjects (26 ± 5 years, 2 female). To study the T_1 time as a function of the instantaneous flow velocity, T_1 times were evaluated in an axial imaging slice of the descending aorta. Velocity encoded cine measurements were performed to quantify the flow velocity throughout the cardiac cycle.

Simulation results show more than 30% loss in accuracy for 10% non-prepared in-flowing spins. However, in- and out-flow to the imaging plane only demonstrated minor impact on the T_1 time. Phantom T_1 times were decreased by up to 200 ms in the flow phantom, due to in-flow of non-prepared spins. High flow velocities cause in-flow of spins that lack partial saturation from the imaging pulses but only lead to negligible T_1 time deviation (less than 30 ms). In vivo measurements confirm a substantial variation of the T_1 time depending on the flow velocity. The highest aortic T_1 times are observed at the time point of minimal flow with increased flow velocity leading to reduction of the measured T_1 time by up to 130 ± 49 ms at peak velocity.

In this work we attempt to dissect the effects of flow on T_1 times, by using simulations, well-controlled, simplified phantom setup and the linear flow pattern in the descending aorta in vivo.

1 Introduction

Quantitative myocardial tissue characterization has increasingly gained attention in cardiac magnetic resonance imaging (MRI) over the past several years for its ability to non-invasively study the myocardial tissue state [1, 2, 3, 4]. Myocardial T_1 mapping is sensitive to changes in the macro-molecular environment and has demonstrated clinical value in various ischemic and non-ischemic cardiomyopathies [5, 6, 7]. Additionally, extracellular volume (ECV) mapping is widely used as a marker for fibrotic remodeling of the myocardium in various pathologies [3, 8, 9, 10, 11]. ECV maps are calculated based on native and post-contrast T_1 times in the myocardium and the blood-pool, and are normalized with the hematocrit (Hct). When hematocrit was not measured, or to achieve a more stream-lined process that does not require blood sampling and testing, it has been proposed to calculate a Hct estimate using blood T_1 times in a technique called synthetic Hct [12]. Therefore, ECV and synthetic Hct values are highly dependent on the quality of blood T_1 measurements.

Several cardiac T_1 mapping sequences have been proposed and can be clinically used for native T_1 and ECV mapping [4, 13, 14, 15, 16]. Modified Look-Locker inversion recovery (MOLLI) [4] is the most widely used method for myocardial T_1 mapping and yields precise T_1 maps but lacks accuracy compared to other T_1 mapping methods [17]. In MOLLI multiple images with different T_1 -weightings are acquired following a non-selective inversion pulse. This repeated image acquisition perturbs the magnetization which is corrected for in the reconstruction (Deichmann correction) [18, 19]. Saturation recovery single-shot acquisition (SASHA) [13] was proposed as an alternative for T_1 mapping with increased accuracy. In SASHA images are acquired every heartbeat following a non-selective saturation pulse with varying saturation time. Due to a reduced dynamic range and suboptimal sampling of the recovery curve for long T_1 times, SASHA T_1 maps suffer from reduced precision compared with MOLLI [20].

Accuracy and precision of myocardial T_1 mapping are integral to its clinical value and have been thoroughly investigated in several recent studies [8, 9, 17, 20, 21, 22]. It was shown that the dominant variability in blood T_1 comes from the biological constituents such as hematocrit, iron, and HDL cholesterol [23]. However, blood T_1 times often fall out of the range for which myocardial T_1 mapping techniques are validated and multiple confounding mechanisms have been proposed [24, 25]. In particular it has been suggested that various flow effects compromise T_1 measurement of the blood-pool [21]. Given the implicit clinical use of blood T_1 times, thorough investigation of the effect of flow is warranted. However, complex flow patterns in the ventricle as well as a

multitude of parameters determining the relevant flow hamper the holistic evaluation of this confounder in vivo.

In this study, we aim to analyze the impact of certain aspects of flow on T_1 measurements with two commonly used myocardial T_1 mapping techniques in well controlled experimental settings in order to further our understanding of flow as a confounding factor. Bloch simulations are performed to shed light on the relative contribution of different flow effects. These effects are then validated in a controlled flow phantom comprising a peristaltic pump with linear flow. Finally, the combined flow dependency of T_1 measurements is studied in vivo by imaging the descending aorta as a proxy, where flow patterns are largely linear and consistently varying across the cardiac cycle.

2 Methods

2.1 Flow effects on blood T_1 measurements

Blood T_1 measurements can be subject to three main flow effects [13, 21, 22] depending on the myocardial T_1 mapping technique (Fig. 1).

- [1] **Non-prepared spins:** In T_1 mapping multiple images are acquired with variable delay following a preparation pulse. During this delay spins that were not subject to the preparation (e.g. far outside the isocenter) can flow into the heart. This increases the signal intensity and therefore decreases the measured T_1 relaxation time.
- [2] **Beat-to-beat exchange:** For sequences such as MOLLI the same magnetization preparation is read out over multiple heartbeats. Spins flowing into the imaging plane from beat-to-beat are not subject to partial saturation by repeated imaging readouts, but are influenced by one slice selective readout only.
- [3] **In- and out-flowing spins:** Fast flowing spins that flow into the imaging plane during the readout lead to faster signal regrowth due to partial saturation by one train of imaging pulses.

The Deichmann correction has been introduced to compensate for signal attenuation by continuous FLASH imaging pulses during inversion recovery of static tissue [19] and is used in MOLLI to reduce the impact of the imaging readout on the T_1 time. However, in the presence of flow, the correction factor will also be subject to various flow-effects, including reduced effect of the repeated imaging readout and imperfect inversion due to in-flow of non-prepared spins.

In this study, we try to disentangle the relative contributions of the in-flow of non-prepared spins, beat-to-beat exchange and the flow effect during the imaging readout. We study the effect on the T_1 time, as well as the uncorrected T_1^* for MOLLI and T_1 times calculated with 2- [26] and 3-parameter models in SASHA.

2.2 Sequence parameters

T_1 maps were generated using a 5(3s)3 MOLLI [27] scheme with and without Deichmann correction (MOLLI T_1 /MOLLI T_1^*) for balanced steady-state free precession (bSSFP) readout and for gradient-echo (GRE) readout (MOLLIGRE T_1 /MOLLIGRE T_1^*). MOLLI maps are reconstructed by a 3-parameter fit with and without the Deichmann correction. SASHA is reconstructed with 3 and 2 parameter fits (SASHA/SASHA 2P) [13, 26]. Reference T_1 times in the phantom were measured with an inversion recovery (IR) in the absence of flow. T_1 maps were reconstructed with a voxel-wise Levenberg-Marquardt non-linear least-square curve fit implemented in-line on the scanner [28, 29, 30]. All measurements were performed in a 3T MRI scanner (Magnetom Skyra; Siemens Healthineers, Erlangen, Germany) with a 28-channel receiver coil array and shared the following common imaging parameters: FOV = 240×240 mm², matrix size (base resolution) = 192×192 (1.3×1.3 mm), slice thickness = 8 mm, bandwidth = 1085 Hz/px, GRAPPA-factor 2 and partial Fourier 6/8. SSFP imaging was performed with TR/TE = 3.6 ms/1.8 ms and high flip angle of 60°, as recommended in flow and SASHA [21], and GRE imaging with TR/TE/ α = 2.9 ms/1.7 ms/8°.

Flow velocity measurements were performed with velocity-encoded retrograded cine using TR/TE/ α = 53.28 ms/4.37 ms/20°, FOV = 166×240 mm², matrix size = 166×240 , slice thickness = 8 mm and interpolated phases = 30 and velocity encoding gradient strength $V_{max} = 20$ cm/s in phantom and $V_{max} = 500$ cm/s in vivo.

2.3 Simulations

We used flow-sensitive Bloch-simulations to determine the relative contribution of the various flow effects for MOLLI and SASHA imaging sequences with bSSFP and GRE readout. All pulse sequences were simulated with the above listed sequence parameters.

For the no flow case, time periods of free relaxation/precession were simulated as

$$\begin{pmatrix} M_x(t+1) \\ M_y(t+1) \\ M_z(t+1) \end{pmatrix} = \begin{pmatrix} E_2 & 0 & 0 \\ 0 & E_2 & 0 \\ 0 & 0 & E_1 \end{pmatrix} \cdot \begin{pmatrix} M_x(t) \\ M_y(t) \\ M_z(t) \end{pmatrix} + \begin{pmatrix} 0 \\ 0 \\ 1 - E_1 \end{pmatrix},$$

with $E_1 = \exp(t/T_1)$, $E_2 = \exp(t/T_2)$ and the time step t . Center of k-space was chosen to calculate the magnitude with $\sqrt{M_x^2 + M_y^2}$. Imaging and preparation pulses were simulated with corresponding rotation matrices. This magnitude is used for fitting MOLLI and SASHA relaxation curves. Along with the undisturbed relaxation curve without saturation by the readout pulses (no excitation pulses simulated), used as a reference relaxation curve, three different scenarios were simulated: 1) Stationary spins which are repeatedly saturated by the imaging pulses at every heartbeat. 2) Non-prepared spins flowing from the scan periphery into the imaging plane. 3) In-flow of unsaturated spins into the imaging plane during the readout at different flow velocities. For flow simulations, the magnetization vector was split in 1000 magnetization packages $(M_x, M_y, M_z)^T = 1/n \cdot \sum_i^n (M_{x_i}, M_{y_i}, M_{z_i})^T$. In-flow of unsaturated spins is simulated by exchanging magnetization packages with fully relaxed magnetization vectors $(1, 0, 0)^T$. All simulated spins are influenced by only one slice selective imaging readout, as fresh spins are flowing into the imaging plane from beat to beat. Therefore, between heartbeats the magnetization vectors are set to the magnetization of the undisturbed spins. The cardiac cycle was simulated with R-R intervals = 1000 ms and blood relaxation times were simulated as $T_1 = 2000$ ms [31, 32, 33, 34] and $T_2 = 200$ ms [34, 35]. For a given velocity the proportion of unsaturated spins flowing into the imaging plane per time step was calculated as follows:

$$\text{percentage of in-flowing spins per time step} = \frac{\text{flow velocity} \cdot \text{time step}}{\text{slice thickness} \cdot \text{readout duration}}.$$

This percentage is used to calculate the amount of magnetization vectors per time step, which are exchanged by the corresponding magnetization vector (all vectors in the magnetization package are the same) from the reference relaxation curve at that time step.

2.4 Phantom experiments

A 30 cm long peristaltic pump (Watson-Marlow-Bredel, 300 Series Laboratory Tube Pumps) was used to circulate gadolinium-doped water from a reservoir outside the scanner bore through a pipe into a dialysis filter (filter with increased diameter, consisting of small fibers). From there the water circulated back outside the bore to the reservoir (Fig. 2). A dialysis filter with a diameter of 6 cm was used. The dialysis filter and a reference probe (3 cm in diameter) with non-flowing solution were placed in a posterior imaging slice (Fig. 2). Additionally, imaging was performed in an anterior slice comprising only the dialysis filter. Imaging was performed at five different flow velocities in both flow directions. T_1 measurements were performed using IR, MOLLI

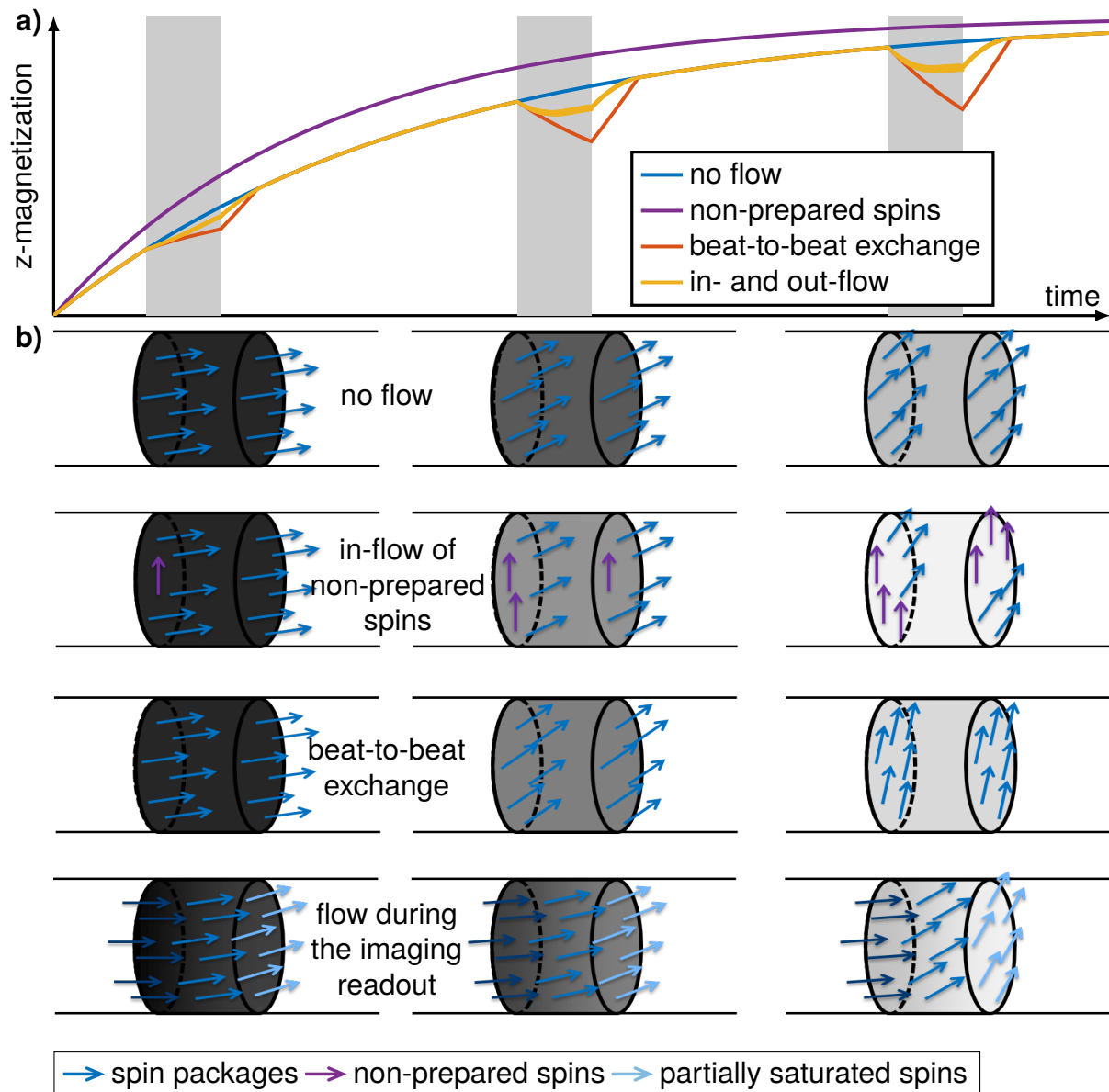


Figure 1: Illustration of the three different flow effects corrupting the measurement of blood T_1 times with myocardial T_1 mapping methods. The top panel a) shows the effect of a T_1 recovery curve over multiple heartbeats, e.g. as seen in MOLLI. In the bottom panel b) sample magnetization packages (arrows) are depicted during magnetization recovery in various flow scenarios. The signal intensity is encoded by the background shading. The first row shows the recovery in the absence of flow. Rows two to four illustrate the following three flow effects. In-flow of non-prepared spins: An increasing amount of non-prepared spins enter the imaging volume and contribute to faster signal recovery. Beat-to-Beat exchange: Flow between the imaging periods in successive heartbeats eliminates the signal attenuation that is seen with repeated imaging pulses in static tissue. Flow during the imaging readout: Spins that are not affected by previous imaging pulses flow into the imaging volume between two imaging pulses are played and thus mitigate the signal attenuation during an individual readout.

T_1/T_1^* , MOLLIGRE T_1/T_1^* , SASHA and SASHA 2P. Additionally, MOLLI and SASHA were performed with a reduced slice thickness of 4 mm to evaluate the flow effect of in-plane saturation. Reference flow velocities were determined by velocity encoded (VENC) cine measurements in the dialysis filter.

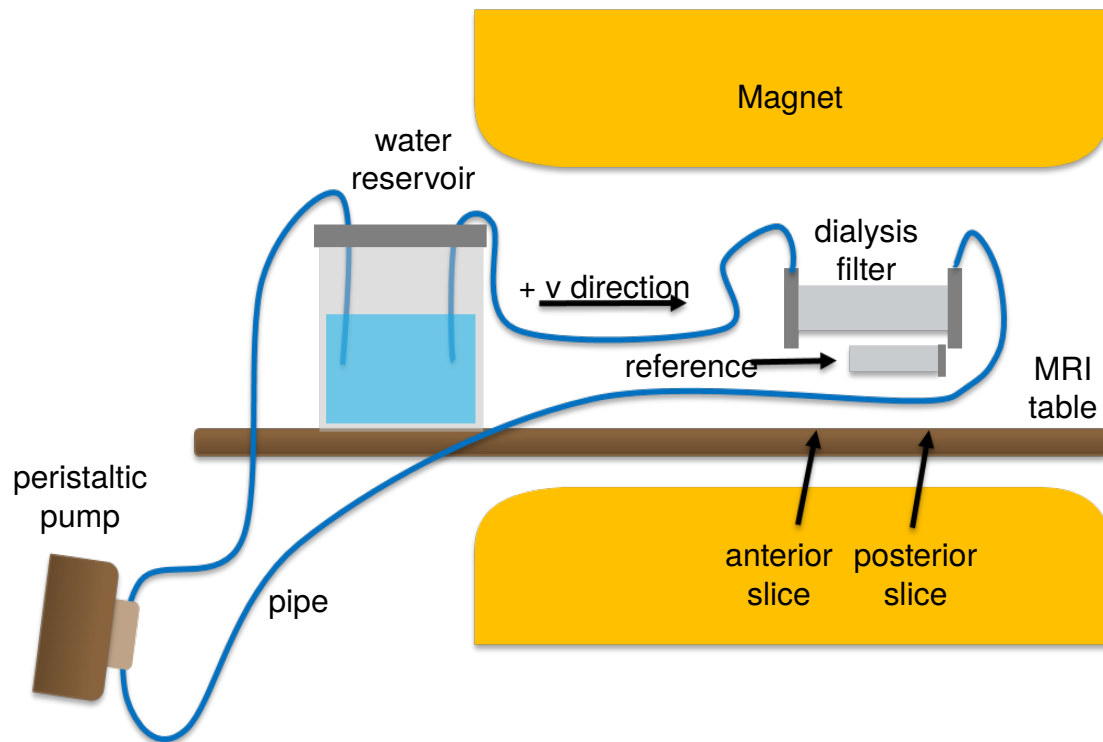


Figure 2: Setup of the flow phantom. A peristaltic pump (Watson-Marlow-Bredel, 300 Series Laboratory Tube Pumps) outside the magnetic safety region was used to pump a mixture of water and gadolinium from a reservoir through a pipe into a 30 cm long dialysis filter (at isocenter) back to the reservoir. The dialysis filter and a reference probe was put into the imaging slice.

2.5 In vivo experiments

In vivo measurements were performed in six healthy subjects (26 ± 5 years, 2 female) in a single axial slice positioned approximately five centimeter below the aortic arch, after they gave written informed consent. T_1 and T_1^* times were calculated and manually drawn region of interests were used to determine mean values and standard deviations in the descending aorta. MOLLI T_1 and T_1^* maps and MOLLIGRE T_1 and T_1^* maps were acquired at various time points in systole and diastole within the cardiac cycle ranging from 250-800 ms after the R-wave. No SASHA measurements were performed in the aorta as no imaging could be performed during systole. For reference, VENC cine measurements were performed to calculate the blood flow velocity in the aorta throughout the cardiac cycle. Reference measurements of the left ventricular blood pool in a mid-ventricular short axis view (SHAX) were performed with all sequences.

3 Results

3.1 Simulations

Figure 3 demonstrates the effects of the previously described flow-induced phenomena studied in isolation with noise-free Bloch simulations for MOLLI and SASHA.

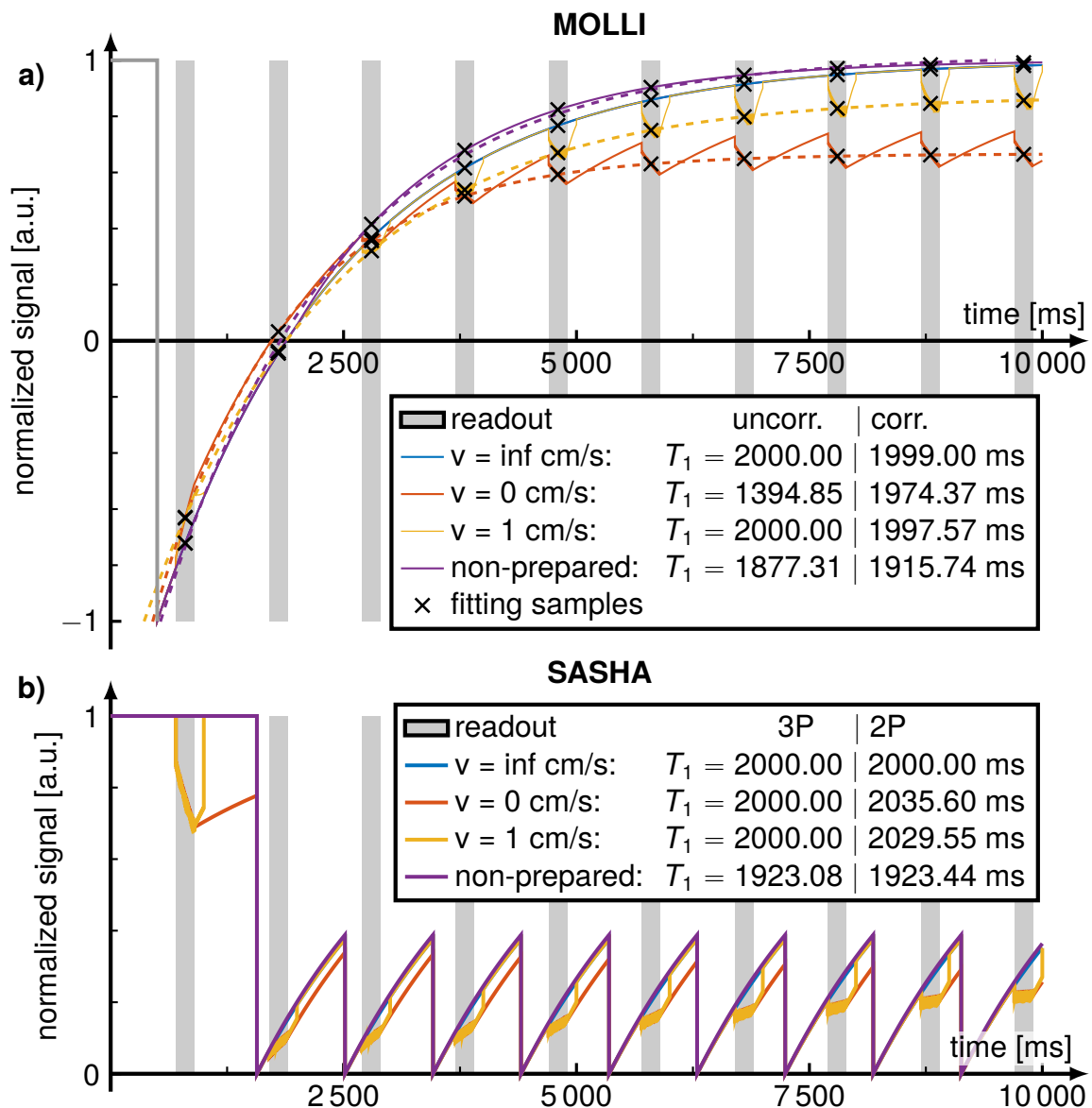


Figure 3: Simulations of three different flow effects compared to no-flow reference for MOLLI a) and SASHA b) sequences: (blue) the baseline relaxation curve after a non-selective preparation recovery pulse; (orange) stationary matter influenced by the imaging pulses; (yellow) flowing matter for a constant velocity of 1 cm/s; and (violet) relaxation curve in the presence of 2% non-prepared in-flowing spins per heartbeat. Dashed lines represent the corresponding 3-parameter model fit. Gray shading depicts the time of imaging readout and crosses indicate the central position of the imaging readout.

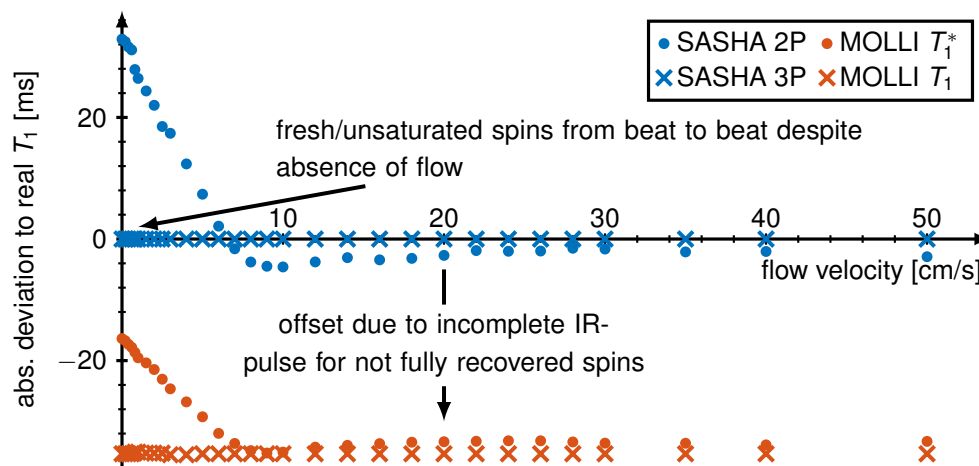


Figure 4: T_1 time for in-flowing and out-flowing spins during a single readout for SASHA (blue) and MOLLI T_1^* , T_1 (orange). Simulations were performed under the assumption that irrespective of the flow velocity, spins are fully exchanged from beat-to-beat.

1) In-flow of non-prepared spins

The simulation results in Figure 3 show that in-flow of 2 % non-prepared spins per heart-beat (purple lines in Fig. 3) leads to faster recovery and shortened apparent relaxation times. This effect is studied in greater detail for various degrees of in-flow in Figure 5. Both MOLLI and SASHA show underestimation, which is increasingly pronounced with higher in-flow. Simulations indicate that for in-flow of 10 % non-prepared spins, T_1 time accuracy is compromised by more than 30 % and 15 % for MOLLI and SASHA, respectively.

2) Beat-to-beat exchange

Repeated application of imaging pulses leads to signal attenuation across heartbeats in stationary tissue (orange lines in Fig. 3). However, our results show that even slow flow velocities cause an exchange of the spins between heartbeats ("beat-to-beat exchange"), such that the imaging signal is just affected by a single set of imaging pulses for any given heartbeat (yellow lines in Fig. 3). Accordingly, the reduced signal attenuation from previous heartbeats leads to reduced underestimation of T_1 times compared with MOLLI values as commonly obtained in stationary tissue. Without Deichmann correction this leads to a major difference ($\Delta T_1^* > 200$ ms), but was largely mitigated when using Deichmann correction ($\Delta T_1^* < 60$ ms).

3) In-flow and out-flow during a readout

Flow during the imaging readout leads to further alteration of the magnetization signal as it leads to faster recovery during one imaging readout (i.e. between two imaging pulses, yellow lines in Fig. 3). This effect is studied in detail in Figure 4 at various flow-velocities.

Increased T_1 times are observed for SASHA 2P and increased T_1^* times for MOLLI at slow flow up to 5 cm/s. However, the magnitude of this effect is small compared to the previously listed contributions ($\sim 1\%$). Furthermore, the effect is strongly mitigated by using MOLLI with Deichmann correction or SASHA with a 3-parameter fit model. Of note, the consistent offset in T_1 observed with MOLLI is due to incomplete inversion efficiency caused by in-flowing spins. This is not due to its intrinsic well documented errors because we assume that all spins exchange from beat-to-beat and therefore no spins are affected by multiple readouts.

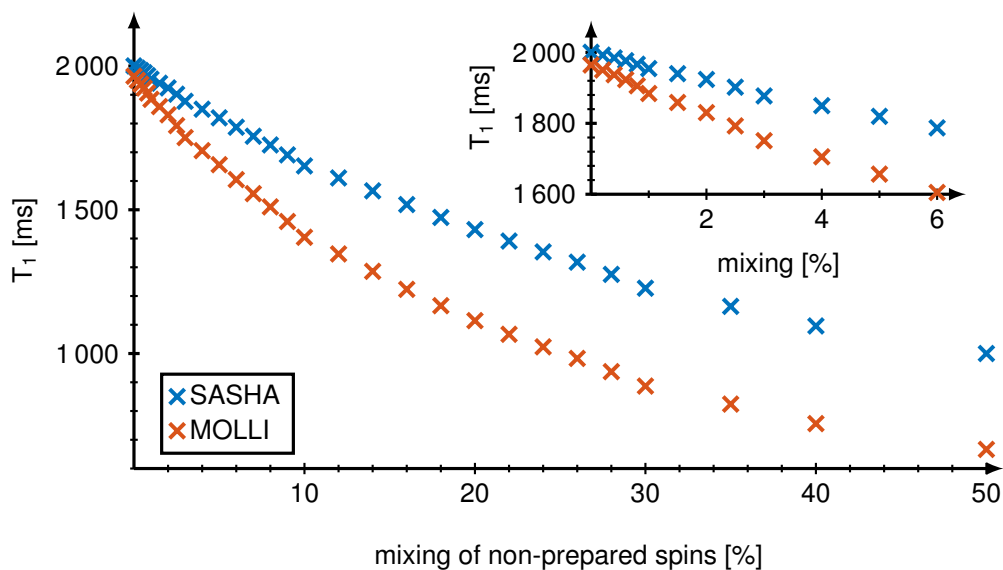


Figure 5: T_1 time as a function of the amount of in-flowing non-prepared spins in percentage per heartbeat for SASHA (blue) and MOLLI T_1^* , T_1 (orange). Of note, the time for in-flow of non-prepared spins is substantially shorter for SASHA due to repeated magnetization saturation in every heartbeat.

3.2 Phantom experiments

Figure 6 shows the T_1 times measured in the flow phantom for various flow velocities. Negative flow direction for T_1 measurements in the posterior slice and positive flow for the anterior slice, lead to in-flow of spins from the reservoir outside the scanner bore, into the imaging plane. For these regimes (blue shaded area, Fig. 6a,b) T_1 times decrease by up to 125 ms with a decrease of 25 ms per 1 cm/s for SASHA/SASHA 2P and up to 250 ms with a decrease of 50 ms per 1 cm/s for MOLLI/MOLLIGRE with and without Deichmann correction. The highest deviation is observed at the largest velocity amplitude ($v \sim 5$ cm/s).

For absolute flow-velocities larger than 1 – 1.5 cm/s all spins from the imaging readout can be assumed to have left the imaging plane during one heartbeat ("beat-to-beat

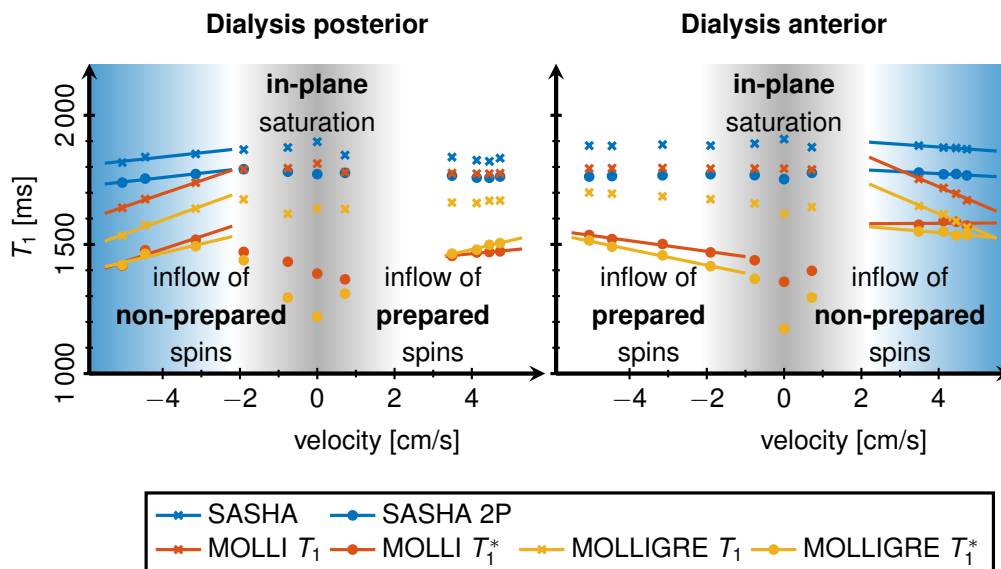


Figure 6: T_1 times measured in the dialysis filter in the anterior and posterior slice for various pump speeds. MOLLI T_1 and T_1^* (orange crosses/ dots), MOLLIGRE T_1 and T_1^* (yellow crosses/dots), SASHA with 3 and 2 parameter fit (blue crosses/dots) and reference measurements (black) are plotted against the flow velocity. The shaded area from blue to gray illustrates the in-flow of non-prepared spins and from gray to white the in-flow of prepared spins

exchange"). However, for slow absolute flow velocities (-1.5 cm/s to 1.5 cm/s) a varying degree of beat-to-beat exchange can affect the T_1 times. In this regime (gray shaded area, Fig. 6a,b) MOLLIs without Deichmann correction show a symmetrical peak for around $v = 0$ cm/s, leading to T_1^* deviation of more than 200 ms. This contribution is largely eliminated when using a Deichmann correction. SASHA shows only minor variation in this flow regime, which is expected as "beat-to-beat exchange" does not affect the SASHA signal due to the repeated saturation.

For large flow-velocities in the opposite flow direction, mostly prepared spins are flowing into the imaging plane. In this regime (white shaded area, Fig 6a,b) varying amount of in-flow/out-flow during the readout is expected to be the dominant effect inducing flow susceptibility. MOLLI without Deichmann correction shows sensitivity to this flow effect, with increasing T_1^* times for increasing flow magnitude. However, the effect is largely mitigated using Deichmann correction. No sensitivity to flow for SASHA or SASHA 2P can be discerned from the noise level in this regime. These findings are corroborated by the results of measurements with different slice thickness (Fig. 7), which also leads to difference in in-flow/out-flow during the readout. All T_1 methods yield excellent agreement for measurements at 4 mm and 8 mm slice thickness (absolute deviation less than 20 ms), except MOLLI without Deichmann correction. Substantial variation up to 80 ms is observed in the presence of flow, but excellent agreement is

shown for the minimal flow case (deviation less than 26 ms).

In the reference probe T_1 maps of SASHA/SASHA 2P achieved good agreement with IR yielding deviations less than 6% whereas MOLLI T_1 /MOLLI T_1^* underestimated the T_1 time of approximately 15%. MOLLIGRE underestimated the T_1 time by almost 20% and MOLLIGRE T_1^* by 28%. All measurements resulted in standard deviations of less than 50 ms for SASHA, SASHA 2P, MOLLI, MOLLIGRE and less than 100 ms for MOLLI T_1^* and MOLLIGRE T_1^* .

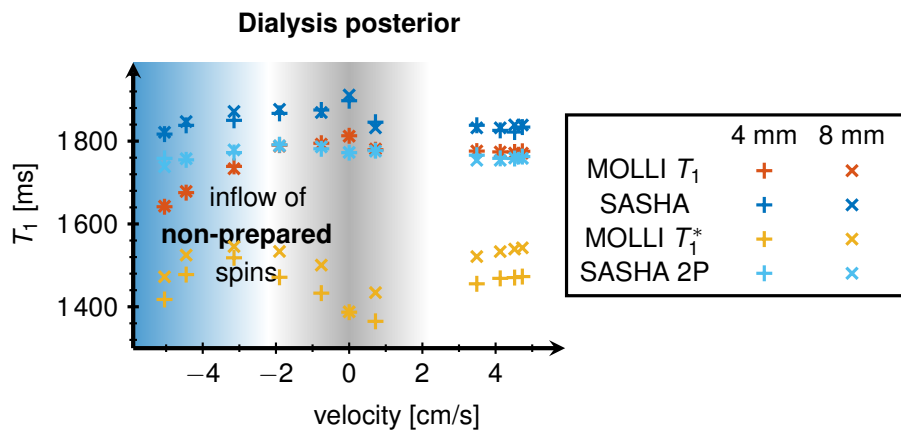


Figure 7: MOLLI (orange), SASHA (blue), MOLLI without Deichmann correction (yellow) and SASHA 2P (bright blue) T_1 times over the flow velocity in the dialysis filter and the reference probe for 4 mm (dots) and 8 mm (crosses) slice thickness.

3.3 In vivo experiments

MOLLI T_1 maps were generated for an axial cross-section of the aorta at various time points throughout the cardiac cycle. Across all subjects, peak velocities up to 120 cm/s were measured with an average peak velocity of 77 ± 24 cm/s. Figure 8 depicts the flow velocity and blood T_1 times as a function of time within the cardiac cycle of one healthy subject. A summary of T_1 times in the absence of flow and during peak velocity are given in Table 1. T_1 times increased with decreasing velocity with differences up to 186 ms. Across all subjects MOLLI and MOLLIGRE measured during the diastole (slow flow) resulted in T_1 times comparable to the left ventricle in the SHAX measurement. Mean differences of T_1 times between peak flow and time point of minimal flow, and their corresponding standard deviations were 163 ± 57 ms for MOLLI, 115 ± 41 ms for MOLLIGRE, 424 ± 192 ms for MOLLI T_1^* and 362 ± 181 ms for MOLLIGRE T_1^* . T_1 maps with Deichmann correction were more precise with standard deviations in the aorta of 107-252 ms over the cardiac cycle. Without Deichmann correction standard deviations vary from 203 ms for MOLLI up to 726 ms for MOLLIGRE respectively.

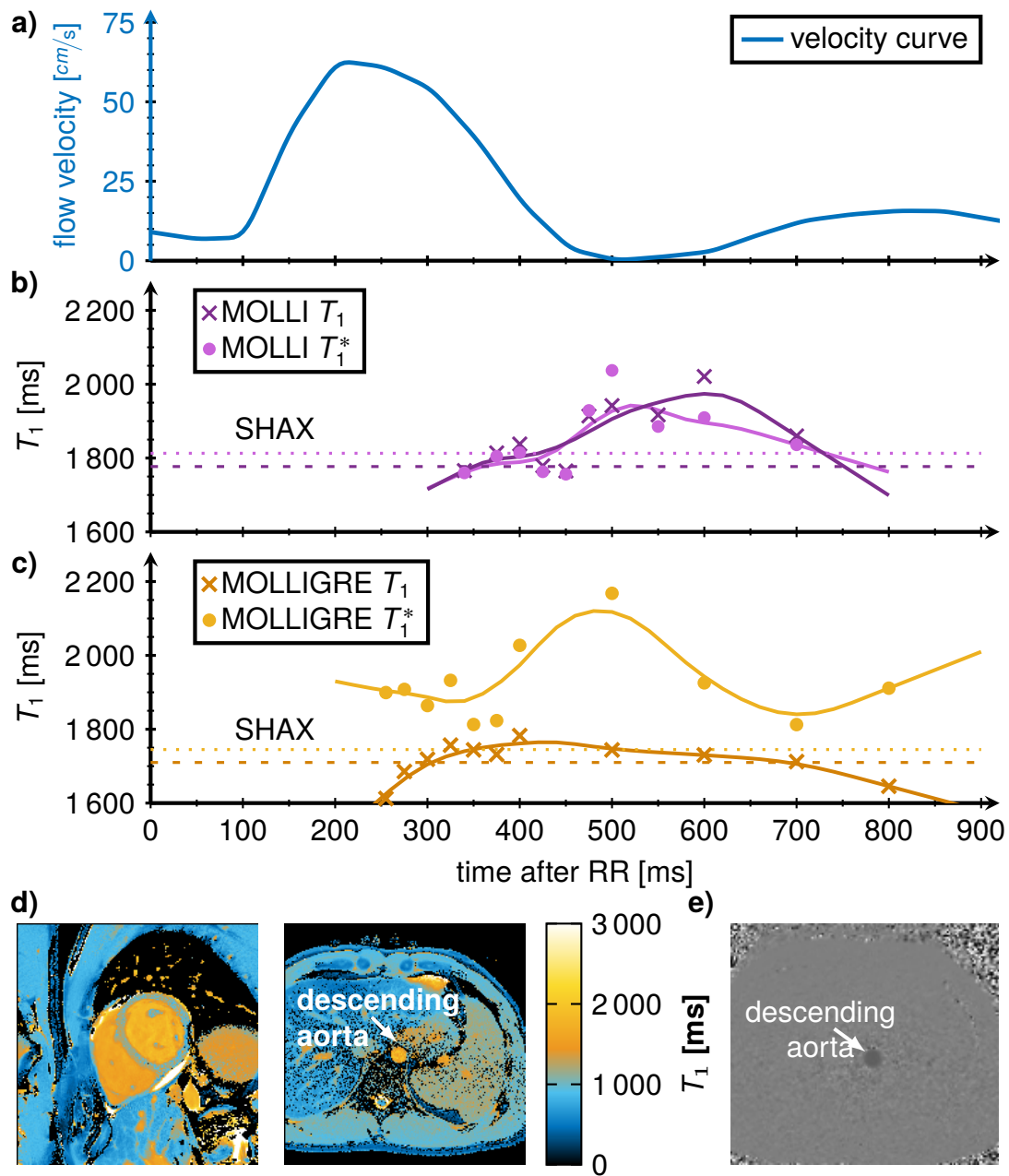


Figure 8: Comparison of blood T_1 times in the aorta measured at various time points of the cardiac cycle in one healthy subject. **a)** Flow velocity measured in a separate VENC scan is depicted in blue. **b)** MOLLIGRE with and without Deichmann correction (purple/pink) and **c)** MOLLIGRE with and without Deichmann correction (orange/yellow) are depicted. SHAX measurements in the left ventricular blood pool are depicted as horizontal lines. **d)** Example T_1 map acquired in short-axis view and in aortic view and **e)** example VENC baseline image of the corresponding slice location.

4 Discussion

In this study we performed flow-dependent T_1 measurements using MOLLI and SASHA to evaluate different contributions of flow effects with simulations, phantom and in vivo measurements. Three flow effects were studied to play a role in blood T_1 measurements:

- In-flow of non-prepared spins from outside the scanner bore increase the signal magnetization and induce a faster T_1 relaxation.
- Sufficiently fast spins flowing outside the imaging plane from heartbeat to heartbeat eliminate the in-plane saturation effect and can result in decreased underestimation of MOLLI T_1 times compared with stationary tissue. However, the effect is small when Deichmann correction is used.
- Spins which flow inside and outside the imaging plane during one readout increase the signal intensity. This leads to higher T_1^* for MOLLI but was mitigated when using Deichmann correction and did not affect SASHA.

Simulations and phantom measurements indicate that in-flow of non-prepared spins is the dominant flow effect. Our results show that this can lead to substantial deviations in the T_1 time, especially for large fractions of in-flowing non-prepared spins. The effect on SASHA T_1 times was substantially smaller compared with MOLLI because a non-selective saturation pulse erases the magnetization every heartbeat. For MOLLI T_1 times in-flow of non-prepared spins exacerbates T_1 underestimation.

The amount of non-prepared spins in blood T_1 measurements depends on a number of system and subject specific patterns. Besides the properties of the individual's circulation, the pulse type, the B_1^+ and B_0 inhomogeneity off the isocenter determine the reach of the preparation pulse. For the commonly used tan/tanh pulse as proposed by Kellman et al. [36] inversion efficiency of less than 0.5 is observed for around 1/3 of the peak B_1 amplitude. Our used body coil with 55 cm length has a 50% B_1 amplitude decrease 15 cm away from the iso-center. Therefore, spins outside the bore are negligibly influenced by the non-selective preparation pulses. Blood takes about 20 seconds for one circulation throughout the entire vascular system. Hence, throughout the inversion span of a typical MOLLI sequence, which reaches up to 5 seconds, non-negligible amounts of un-prepared spins can be expected to flow into the imaging plane.

The impact of the other two flow effects was relatively small compared to in-flow of non-prepared spins. Furthermore, the impact of the beat-to-beat exchange and the

flow during the imaging readout were effectively mitigated using the Deichmann correction for MOLLI or using SASHA. We performed MOLLI experiments with and without Deichmann correction to fully understand the cause of flow susceptibility. Our simulations also showed that for increasing T_1 all flow effects increase. However, simulations and phantom measurements demonstrated higher resilience to flow effects in MOLLI with Deichmann correction, despite the known discrepancy between the assumptions underlying the correction and the MOLLI sequence [25].

Table 1: Tabular of all in vivo blood T_1 values. Aortic blood T_1 times for MOLLI and MOLLIGRE with and without Deichmann correction for six healthy subjects. T_1 times for the time points in the cardiac cycle with no and maximum flow velocities are provided.

subject, gender	Sequence	Deichmann correction	speed [cm/s]	min. flow T_1 [ms]	peak flow T_1 [ms]	diff. T_1 [ms]
1, f	MOLLI	on	76	1917 ± 107	1759 ± 66	158
		off		2126 ± 384	1806 ± 231	319
	MOLLIGRE	on		1838 ± 375	1664 ± 170	174
		off		2456 ± 825	2041 ± 649	415
2, m	MOLLI	on	64	1809 ± 252	1751 ± 121	58
		off		1898 ± 726	1965 ± 386	67
	MOLLIGRE	on		1757 ± 186	1737 ± 133	20
		off		2056 ± 843	1853 ± 656	203
3, m	MOLLI	on	63	1868 ± 123	1681 ± 209	186
		off		1839 ± 366	1159 ± 785	680
	MOLLIGRE	on		1757 ± 186	1737 ± 133	20
		off		2056 ± 843	1853 ± 656	203
4, f	MOLLI	on	54	1973 ± 222	1817 ± 424	156
		off		1921 ± 562	1430 ± 951	490
	MOLLIGRE	on		1930 ± 99	1844 ± 204	86
		off		2150 ± 330	1846 ± 675	304
5, m	MOLLI	on	87	1662 ± 162	1580 ± 410	82
		off		1607 ± 207	1039 ± 725	568
	MOLLIGRE	on		1639 ± 123	1552 ± 185	87
		off		1731 ± 457	1382 ± 627	349
6, m	MOLLI	on	120	1792 ± 174	1650 ± 301	142
		off		1638 ± 203	1297 ± 631	342
	MOLLIGRE	on		1734 ± 213	1650 ± 294	84
		off		1663 ± 452	1445 ± 671	218

PUBLICATION I

The effect of flow on the blood T_1 time plays a role in the calculation of ECV. However, our results indicate that the flow effects are more pronounced for longer T_1 times. The ECV calculation is more susceptible to changes in the post-contrast T_1 times, and thus shows stronger resilience to flow induced variations. Given the simulated effects from Figure 4, errors about 5% can be expected for ECV. However, the synthetic Hct is inversely proportional to the native blood T_1 times. Thus, decreasing blood T_1 times increases the Hct. With flow induced T_1 deviations of up to 20% synthetic Hct may vary by up to 17%. Hence, when using synthetic Hct for ECV calculation this error propagates to the ECV value linearly.

In vivo measurements confirm the flow effect of decreasing T_1 times by increasing flow velocity in the descending aorta. Due to the relatively high standard deviation in vivo, in-flow and out-flow of spins during a readout as observed in phantom can be assumed to be negligible. Flow susceptibility due to varying degrees of "beat-to-beat exchange" can also be assumed to be negligible due to the high ejection fraction in the aorta. Accordingly, our in vivo results in the aorta suggest a strong impact of in-flow of non-prepared spins on the T_1 time, indicating potential in vivo contribution of the dominant effect observed in phantom and simulations.

MOLLI T_1 mapping is well known to be susceptible to variations in prescribed or actual flip-angles [37, 38]. In-flow of spins during the readout, also impacts the amount of signal attenuation in tissue, although with different underlying principles. Therefore, we studied the contribution of flow to MOLLI T_1 times. Simulations suggested that the Deichmann correction is highly effective in mitigating the effects of variable signal saturation in the presence of flow. To further confirm this result, phantom experiments were conducted in a slow flow regime. In these experiments, in-flow during the readout is expected to affect T_1 times independent of the flow direction thus constituting a symmetrical peak. While this effect was observed the relative contribution compared with in-flow of non-prepared spins was almost negligible after Deichmann correction. This was further confirmed in scans with decreased slice thickness, which leads to increased in-flow/out-flow during the readout for a given flow velocity. As shown in our simulations, theoretically there is no need for correcting with Deichmann for sufficient fast flow. Nevertheless, our phantom measurements resulted in decreased T_1 times with higher standard deviations compared with using the Deichmann correction.

SASHA T_1 mapping showed substantially lower susceptibility to flow effects. However, residual changes in T_1 times were induced, primarily due to the in-flow of non-prepared spins. In simulations and phantom experiments, constant flow velocities were simulated throughout the heartbeat. However, in vivo in-flow of non-prepared spins is largely

restricted to the systolic phase, potentially leading to even smaller flow susceptibility in the T_1 measurement. However, no SASHA imaging could be performed to study the flow effect in the aorta directly, as SASHA is incompatible with a variable readout timing with respect to the cardiac cycle.

Overall, our results demonstrate that under controlled conditions the T_1 times of moving fluids can be strongly dependent on flow velocities. These results are obtained in simplified and well controlled conditions. However, a multitude of factors likely determines the effect size on left ventricular blood T_1 as commonly performed. While this limits the feasibility, our results confirm the literature postulation that in-flow of non saturated spins is a potential confounder in blood T_1 measurement. The total in-flow and the flow velocity depends on a number of physiological parameters. The total stroke volume determines how much potentially non-prepared spins can flow in from the periphery. The patient size can affect the amount of blood in the periphery that is potentially not completely prepared. Ejection fraction can also be a confounding factor for blood T_1 measurements as this can variably affect the amount of beat-to-beat exchange. Hence, our results suggest that the use of blood T_1 as an independent parameter warrants careful consideration. Thorough control for flow determining physiology might potentially help to reduce variability [39, 40, 41]. Due to the important role of blood T_1 in ECV mapping and due to its recent use in synthetic Hct numerous clinical studies evaluated cardiomyopathies based on blood T_1 based quantities [3, 9, 10, 11, 22, 27, 42]. As the effects observed in quantitative myocardial tissue characterization are often small it is paramount to understand potential confounders. Our results indicate that measurements in patients with largely varying flow-determining physiology could lead to increased variability in blood T_1 based biomarkers. This can potentially hamper the identification of pathological changes.

This study has several limitations. A number of simplifications had to be made in order to systematically analyze the impact of flow on myocardial T_1 mapping. These simplifications limit the direct feasibility of the results to the measurements of blood T_1 times in the left ventricle. Firstly, the phantom setup was a simplified approach to measure the effects of different flow patterns in isolation. The reservoir was put outside the bore to create an environment where non-prepared spins flow into the imaging plane. However, the fraction of spins that is poorly polarized is likely smaller in vivo than as in this setting. Imaging of the descending aorta was performed as an in vivo model with controllable instantaneous flow velocities. However, different and more variable flow patterns are characteristic for the left ventricle potentially giving rise to different flow response of the T_1 time. A difference in local flow-patterns can potentially have minor impact on the effects of in-/out-flow during the readout. In our simulations we assumed 100% inver-

sion efficiency with a rectangular slice profile without taking the distribution of flip angles into account. However, in-plane saturation only demonstrated minor effects on blood T_1 times. For this reason we suspect that a distribution of flip angles as a result of the slice profile will only play a minor role. However, given our results indicate overall negligible contribution of this flow effect a detailed analysis of turbulent flow in dedicated phantoms or the ventricles might not be required.

5 Conclusion

T_1 times in moving fluids such as blood obtained with commonly used T_1 mapping techniques can be susceptible to flow-effects. In our simplified model analysis, we found the most significant flow effect due to in-flow of non-prepared spins. Other flow-induced effects showed minor impact and were well compensated for using either a Deichmann correction for MOLLI or SASHA. Overall, SASHA proved to be less prone to flow effects as the magnetization is saturated in every heartbeat compared with MOLLI, where a single inversion pulse spans up to five heartbeats. These results are suggestive that in-flow of non saturated spins could potentially be detrimental to blood T_1 measurements with potential implications for analysis of ECV and synthetic Hct, but thorough clinical investigation of the impact is warranted.

References

- [1] Ferreira V. M., Piechnik S. K., Robson M. D., Neubauer S., Karamitsos T. D.. Myocardial tissue characterization by magnetic resonance imaging: novel applications of T1 and T2 mapping *Journal of thoracic imaging* 2014; **29**(3):147-154.
- [2] Hamlin Scott A., Henry Travis S., Little Brent P., Lerakis Stamatios, Stillman Arthur E.. Mapping the Future of Cardiac MR Imaging: Case-based Review of T1 and T2 Mapping Techniques *RadioGraphics* 2014; **34**(6):1594-1611.
- [3] Moon James C., Messroghli Daniel R., Kellman Peter, et al. Myocardial T1 mapping and extracellular volume quantification: a Society for Cardiovascular Magnetic Resonance (SCMR) and CMR Working Group of the European Society of Cardiology consensus statement *Journal of Cardiovascular Magnetic Resonance* 2013; **15**(1):92.
- [4] Messroghli Daniel R., Radjenovic Aleksandra, Kozerke Sebastian, Higgins David M., Sivananthan Mohan U., Ridgway John P.. Modified Look-Locker inversion recovery (MOLLI) for high-resolution T1 mapping of the heart *Magnetic Resonance in Medicine* 2004; **52**(1):141–146.
- [5] Dall'Armellina Erica, Piechnik Stefan K., Ferreira Vanessa M., Si Quang Le. Cardiovascular magnetic resonance by non contrast T1-mapping allows assessment of severity of injury in acute myocardial infarction *Journal of Cardiovascular Magnetic Resonance* 2012; **14**(1):15.
- [6] Radenkovic Dina, Weingärtner Sebastian, Ricketts Lewis, Moon James C., Captur Gabriella. T1 mapping in cardiac MRI *Heart Failure Reviews* 2017; **22**(4):415–430.
- [7] Puntmann Valentina O., Peker Elif, Chandrashekar Y., Nagel Eike. T1 Mapping in Characterizing Myocardial Disease A Comprehensive Review *Circulation Research* 2016; **119**(2):277–299.
- [8] Kim PK, Hong YJ, Im DJ, et al. Myocardial T1 and T2 Mapping: Techniques and Clinical Applications *Korean J Radiol.* 2017; **18**(1):113-131.
- [9] Haaf Philip, Garg Pankaj, Messroghli Daniel R., Broadbent David A., Greenwood John P., Plein Sven. Cardiac T1 Mapping and Extracellular Volume (ECV) in clinical practice: a comprehensive review *Journal of Cardiovascular Magnetic Resonance* 2016; **18**(1):89.

PUBLICATION I

- [10] Messroghli Daniel R., Moon James C., Ferreira Vanessa M., et al. Clinical recommendations for cardiovascular magnetic resonance mapping of T1, T2, T2* and extracellular volume: A consensus statement by the Society for Cardiovascular Magnetic Resonance (SCMR) endorsed by the European Association for Cardiovascular Imaging (EACVI) *Journal of Cardiovascular Magnetic Resonance* 2017; **19**(1):75.
- [11] Ntusi Ntobeko AB, Piechnik Stefan K., Francis Jane M., et al. Subclinical myocardial inflammation and diffuse fibrosis are common in systemic sclerosis – a clinical study using myocardial T1-mapping and extracellular volume quantification *Journal of Cardiovascular Magnetic Resonance* 2014; **16**(1):21.
- [12] Treibel Thomas A., Fontana Marianna, Maestrini Viviana, et al. Automatic Measurement of the Myocardial Interstitium: Synthetic Extracellular Volume Quantification Without Hematocrit Sampling *JACC: Cardiovascular Imaging* 2016; **9**(1):54 - 63.
- [13] Chow Kelvin, Flewitt Jacqueline A., Green Jordin D., Pagano Joseph J., Friedrich Matthias G., Thompson Richard B.. Saturation recovery single-shot acquisition (SASHA) for myocardial T1 mapping *Magnetic Resonance in Medicine* 2014; **71**(6):2082-2095.
- [14] Weingärtner Sebastian, Akçakaya Mehmet, Basha Tamer, et al. Combined saturation/inversion recovery sequences for improved evaluation of scar and diffuse fibrosis in patients with arrhythmia or heart rate variability *Magnetic Resonance in Medicine* 2014; **71**(3):1024-1034.
- [15] Piechnik Stefan K., Ferreira Vanessa M., Dall'Armellina Erica, et al. Shortened Modified Look-Locker Inversion recovery (ShMOLLI) for clinical myocardial T1-mapping at 1.5 and 3 T within a 9 heartbeat breathhold *Journal of Cardiovascular Magnetic Resonance* 2010; **12**(1):69.
- [16] Weingärtner Sebastian, Roujol Sébastien, Akçakaya Mehmet, Basha Tamer A., Nezafat Reza. Free-breathing multislice native myocardial T1 mapping using the slice-interleaved T1 (STONE) sequence *Magnetic Resonance in Medicine* 2015; **74**(1):115-124.
- [17] Roujol Sebastien, Weingärtner Sebastian, Foppa Murilo, et al. Accuracy, Precision, and Reproducibility of Four T1 Mapping Sequences: A Head-to-Head Comparison of MOLLI, ShMOLLI, SASHA, and SAPPHIRE *Radiology* 2014; **272**(3):683-689.

- [18] Look D. C., Locker D. R.. Time Saving in Measurement of NMR and EPR Relaxation Times *Review of Scientific Instruments* 1970; **41**(2):250-251.
- [19] Deichmann R., Haase A.. Quantification of T1 values by SNAPSHOT-FLASH NMR imaging *Journal of Magnetic Resonance* 1992; **96**(3):608 - 612.
- [20] Weingärtner Sebastian, Meßner Nadja M., Budjan Johannes, et al. Myocardial T1-mapping at 3T using saturation-recovery: reference values, precision and comparison with MOLLI *Journal of Cardiovascular Magnetic Resonance* 2016; **18**(1):84.
- [21] Kellman Peter, Hansen Michael S.. T1-mapping in the heart: accuracy and precision *Journal of Cardiovascular Magnetic Resonance* 2014; **16**(1):2.
- [22] Cameron Donnie, Vassiliou Vassilios S., Higgins David M., Gatehouse Peter D.. Towards accurate and precise T1 and extracellular volume mapping in the myocardium: a guide to current pitfalls and their solutions *Magnetic Resonance Materials in Physics, Biology and Medicine* 2018; **31**(1):143–163.
- [23] Rosmini Stefania, Bulluck Heerajnarain, Abdel-Gadir Amna, et al. The Effect of Blood Composition on T1 Mapping *JACC: Cardiovascular Imaging* 2019; **12**(9):1888–1890.
- [24] Choi Eui-Young, Hwang Sung Ho, Yoon Young Won, et al. Correction with blood T1 is essential when measuring post-contrast myocardial T1 value in patients with acute myocardial infarction *Journal of Cardiovascular Magnetic Resonance* 2013; **15**(1):11.
- [25] Shang Yongning, Zhang Xiaochun, Zhou Xiaoyue, et al. Blood T1* correction increases accuracy of extracellular volume measurements using 3T cardiovascular magnetic resonance: Comparison of T1 and T1* maps *Scientific Reports* 2018; **8**:2045-2322.
- [26] Kellman Peter, Xue Hui, Chow Kelvin, Spottiswoode Bruce S., Arai Andrew E., Thompson Richard B.. Optimized saturation recovery protocols for T1-mapping in the heart: influence of sampling strategies on precision *Journal of Cardiovascular Magnetic Resonance* 2014; **16**(1):55.
- [27] Kellman Peter, Wilson Joel R., Xue Hui, Ugander Martin, Arai Andrew E.. Extracellular volume fraction mapping in the myocardium, part 1: evaluation of an automated method *Journal of Cardiovascular Magnetic Resonance* 2012; **14**(1):63.
- [28] Markwardt Craig . MPFIT: A MINPACK-1 Least Squares Fitting Library in C. 1980. [Online; accessed April, 2019].

PUBLICATION I

- [29] Maier Andreas, Syben Christopher, Lasser Tobias, Riess Christian. A gentle introduction to deep learning in medical image processing *Z Med Phys* 2019; **29**(2):96-101.
- [30] Lundervold Alexander Selvikvag, Lundervold Arvid. An overview of deep learning in medical imaging focusing on MRI *Z Med Phys* 2019; **29**(2):102-127.
- [31] Qin Qin, Strouse John J., Zijl Peter C.M.. Fast measurement of blood T1 in the human jugular vein at 3 Tesla *Magnetic Resonance in Medicine* 2010; **65**(5):1297-304.
- [32] Varela Marta, Hajnal Joseph V., Petersen Esben T., Golay Xavier, Merchant Nazakat, Larkman David J.. A method for rapid in vivo measurement of blood T1 *NMR in Biomedicine* 2011; **24**(1):80-88.
- [33] Li Wenbo, Liu Peiying, Lu Hanzhang, Strouse John J., Zijl Peter C.M., Qin Qin. Fast measurement of blood T1 in the human carotid artery at 3T: Accuracy, precision, and reproducibility *Magnetic Resonance in Medicine* 2017; **77**(6):2296-2302.
- [34] Liu Peiying, Chalak Lina F., Krishnamurthy Lisa C., et al. T1 and T2 values of human neonatal blood at 3 Tesla: Dependence on hematocrit, oxygenation, and temperature *Magnetic Resonance in Medicine* 2016; **75**(4):1730-1735.
- [35] Chen Jean J., Pike G. Bruce. Human whole blood T2 relaxometry at 3 Tesla *Magnetic Resonance in Medicine* 2009; **61**(2):249-254.
- [36] Kellman Peter, Herzka Daniel A., Hansen Michael Schacht. Adiabatic inversion pulses for myocardial T1 mapping *Magnetic Resonance in Medicine* 2014; **71**(4):1428-1434.
- [37] Cooper Mitchell A., Nguyen Thanh D., Spincemille Pascal, Prince Martin R., Weinsaft Jonathan W., Wang Yi. How Accurate Is MOLLI T1 Mapping In Vivo? Validation by Spin Echo Methods *PLOS ONE* 2014; **9**(9):1-6.
- [38] Kellman Peter, Herzka Daniel A., Arai Andrew E., Hansen Michael Schacht. Influence of Off-resonance in myocardial T1-mapping using SSFP based MOLLI method *Journal of Cardiovascular Magnetic Resonance* 2013; **15**(1):63.
- [39] Becker Hendrik, Wattenberg Maximilian, Barth Peter, Laser Kai Thorsten, Burchert Wolfgang, Körperich Hermann. Impact of different respiratory monitoring techniques on respiration-dependent stroke-volume measurements assessed by real-time magnetic resonance imaging *Z Med Phys* 2019; **29**(2).

- [40] Collis Tarquin, Devereux Richard B., Roman Mary J., et al. Relations of Stroke Volume and Cardiac Output to Body Composition *Circulation* 2001; **103**(6):820-825.
- [41] Barone-Rochette Gilles, Piérard Sophie, Seldrum Stéphanie, et al. Aortic Valve Area, Stroke Volume, Left Ventricular Hypertrophy, Remodeling, and Fibrosis in Aortic Stenosis Assessed by Cardiac Magnetic Resonance Imaging *Circulation: Cardiovascular Imaging* 2013; **6**(6):1009-1017.
- [42] Ugander Martin, Oki Abiola J., Hsu Li-Yueh, et al. Extracellular volume imaging by magnetic resonance imaging provides insights into overt and sub-clinical myocardial pathology *European Heart Journal* 2012; **33**(10):1268-1278.

Free-breathing simultaneous T_1 , T_2 , and T_2^* quantification in the myocardium

Ingo Hermann, Peter Kellman, Omer B. Demirel, Mehmet Akçakaya, Lothar Schad and Sebastian Weingärtner

MAGN RESON MED. 2021; DOI.ORG/10.1002/MRM.28753

Abstract

Purpose: To implement a free-breathing sequence for simultaneous quantification of T_1 , T_2 , and T_2^* for comprehensive tissue characterization of the myocardium in a single scan using a multi gradient-echo readout with saturation and T_2 preparation pulses.

Methods: In the proposed **Saturation And T_2 prepared Relaxometry with Navigator-gating (SATURN)** technique a series of multi gradient-echo images with different magnetization preparations was acquired during free-breathing. A total of 35 images were acquired in 26.5 ± 14.9 seconds using multiple saturation times and T_2 preparation durations and with imaging at 5 echo times. Bloch simulations and phantom experiments were used to validate a 5 parameter fit model for accurate relaxometry. Free-breathing simultaneous T_1 , T_2 , and T_2^* measurements were performed in 10 healthy volunteers and 2 patients using SATURN at 3T and quantitatively compared to conventional single parameter methods such as SASHA for T_1 , T_2 -prepared bSSFP and multi GRE for T_2^* .

Results: Simulations confirmed accurate fitting with the five parameter model. Phantom measurements showed good agreement with the reference methods in the relevant range for in vivo measurements. Compared to single parameter methods comparable accuracy was achieved. SATURN produced in vivo parameter maps that were visually comparable to single parameter methods. No significant difference between T_1 , T_2 or T_2^* times acquired with SATURN and single parameter methods was shown in quantitative measurements (SATURN $T_1 = 1573 \pm 86$ ms, $T_2 = 33.2 \pm 3.6$ ms, $T_2^* = 25.3 \pm 6.1$ ms; conventional methods: $T_1 = 1544 \pm 107$ ms, $T_2 = 33.2 \pm 3.6$ ms, $T_2^* = 23.8 \pm 5.5$ ms; $p > 0.2$).

Conclusion: SATURN enables simultaneous quantification of T_1 , T_2 , and T_2^* in the myocardium for comprehensive tissue characterization with co-registered maps, in a single scan with good agreement to single parameter methods.

1 Introduction

Quantitative mapping in the myocardium has received major clinical interest, as markers related to myocardial relaxation time yield promising sensitivity to a broad spectrum of cardiomyopathies. T_1 , T_2 , and T_2^* mapping are routinely used in advanced CMR centers and received increasing interest in community recommendations and consensus statements for the assessment of ischemia, fibrosis, edema, and amyloidosis or iron deposition [1, 2, 3, 4].

A wide variety of mapping sequences was proposed in the last decades for non-invasively studying the myocardial tissue state [5, 6, 7, 8, 9]. Myocardial T_1 mapping is most commonly performed based on a series of inversion or saturation recovery images and has shown promise for the assessment of ischemic and non-ischemic cardiomyopathies [1, 4, 10, 11]. While inversion recovery based methods have shown improved precision and map quality, saturation recovery methods yield more accurate T_1 maps insensitive to the heart rate, the magnetization evolution, and other confounders [12, 13, 14].

In addition to T_1 mapping, myocardial T_2 mapping is increasingly used for the reliable assessment of myocardial edema [15]. State of the art cardiac T_2 mapping is performed by acquiring at least three T_2 -prepared balanced steady-state free precession (bSSFP) images to provide robust and reproducible T_2 maps [15, 16, 17, 18].

Myocardial T_2^* quantification has demonstrated high clinical value for the assessment of myocardial iron accumulation [19, 20, 21]. According to relevant guidelines, T_2^* measurements in the myocardium is most commonly performed by acquiring eight echoes with a multi gradient-echo readout and performing an exponential fit [19].

The methods described above each require one breath-hold per slice. Therefore, free-breathing methods and simultaneous quantification of T_1 and T_2 were proposed to improve patient comfort and shorten measurement time [22, 23, 24, 25, 26, 27, 28, 29, 30, 31]. Simultaneous T_1 and T_2 mapping was obtained in a single breath-hold by combining saturation/inversion pulses and T_2 preparation modules to improve the detection of abnormalities by inherently co-registered parametric maps [22, 32, 33]. This method was expanded to a navigator gated free-breathing approach allowing the coverage of T_1 and T_2 in the entire myocardium in a single scan avoiding deviations due to incorrect breath-holds [28, 34]. Magnetic Resonance Fingerprinting was proposed for joint estimation of T_1 and T_2 based on undersampled non-cartesian readouts with varying preparations [25]. Most recently, cardiac multitasking was introduced, as a novel method for multi-parameter mapping, where contrast and physiological variations

are modeled by a low dimensional representation, enabling a continuous acquisition of multi-parametric 3D maps [24].

However, the lack of a combined method for assessment of all three clinically relevant tissue characteristics (T_1 , T_2 , and T_2^*) requires multiple sequences in clinical practice, expanding the scan protocol and prolonging examination duration. Furthermore, many recently developed methods rely on implicit or explicit model-based regularization [35, 36]. This often induces quantification inaccuracies and renders the methods' quantification susceptible to changes in the reconstruction pipeline.

In this study we sought to provide a method for free-breathing assessment of all clinically relevant relaxation times - T_1 , T_2 , and T_2^* . A navigator gated sequence with multi gradient-echo readout and saturation and T_2 preparation pulses is developed. The accuracy of the proposed technique is evaluated in phantom measurements and in vivo image quality is assessed in healthy subjects and a small cohort of patients.

2 Methods

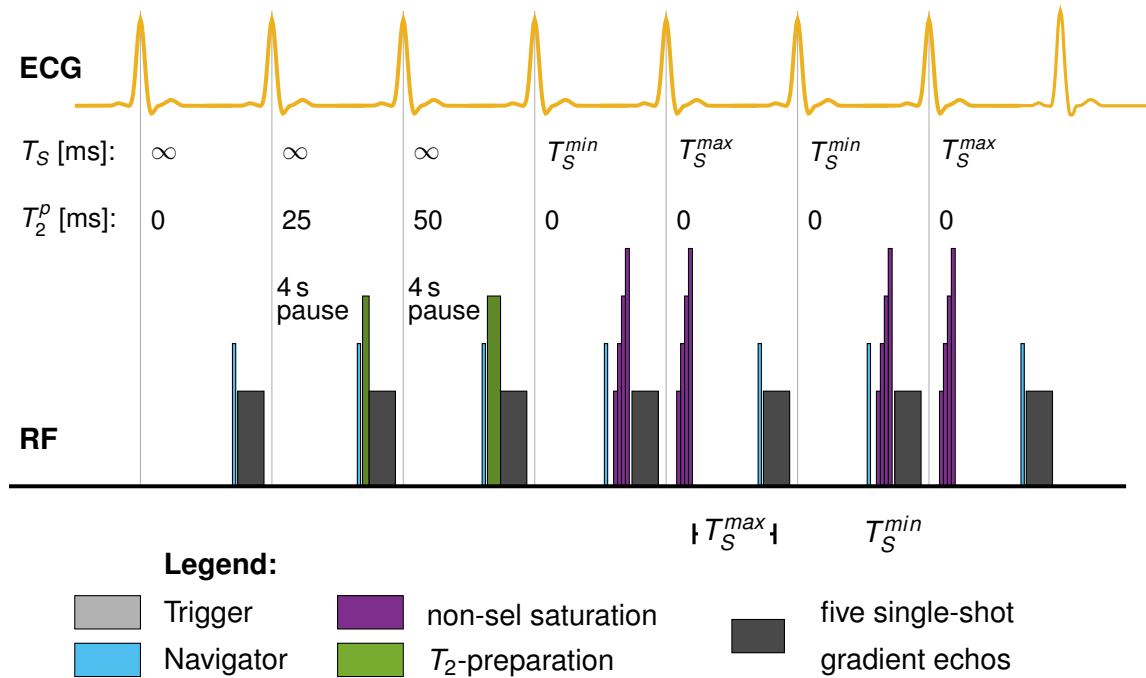
2.1 Sequence design

Figure 1 depicts the sequence diagram of the proposed **Saturation And T_2 prepared Relaxometry with Navigator-gating (SATURN)** sequence. The sequence is based on a single-shot multi gradient-echo readout generating five echoes for each end-diastolic imaging window. We used a prospective navigator on the diaphragm of the liver with a gating window of 4-5 mm depending on the subject's breathing pattern. Navigator gating is performed with the following accept-reject scheme: The first contrast without preparation was repeated if the navigator was rejected. Saturation prepared images were also immediately re-attempted in the next heart beat. No navigator was played during the rest periods before the T_2 preparation. For T_2 -prepared images, T_2 preparation was only performed if the navigator was accepted. In this way, if the navigator was rejected the T_2 -prepared image could be re-attempted immediately, without the need of additional rest-periods. However, in this way, navigator rejections lead to an increase in effective rest periods.

We used saturation and T_2 preparation pulses before the readouts to generate T_1 and T_2 contrasts. Therefore, we combined the SASHA 3-parameter fit model with the T_2 -prepared bSSFP 3-parameter fit model. Since we only use short echo times (TE) for the gradient-echo readout and the noise floor for the T_2^* decay is not corrected, we used a truncation model for T_2^* as previously suggested [39]. The five parameter truncation fit model is given as

$$S(T_S, T_2^p, TE, A, B) = \left(\underbrace{A \left(1 - \exp \left(-\frac{T_S}{T_1} \right) \right)}_{\text{SASHA Fit}} \cdot \underbrace{\exp \left(-\frac{T_2^p}{T_2} \right) + B}_{T_2 \text{ Fit}} \right) \cdot \underbrace{\exp \left(-\frac{TE}{T_2^*} \right)}_{T_2^* \text{ Fit}}. \quad (1)$$

Here, the fitting parameter B is used to account for the T_1 offset. Thus, T_2^* is reconstructed with a truncation model. The first contrast is performed without any preparation



$$S(T_S, T_2^p, TE, A, B) = \left(\underbrace{A \left(1 - \exp \left(-\frac{T_S}{T_1} \right) \right)}_{T_1 \text{ Fit}} \cdot \underbrace{\exp \left(-\frac{T_2^p}{T_2} \right) + B}_{T_2 \text{ Fit}} \right) \cdot \underbrace{\exp \left(-\frac{TE}{T_2^*} \right)}_{T_2^* \text{ Fit}}$$

Figure 1: Sequence diagram for the proposed T_1 , T_2 , and T_2^* mapping technique. Navigator pulses (light blue) are played before the readouts and the preparation pulses. Five different multi gradient-echoes per imaging block are generated. The first contrast is performed without any preparation pulses to image the fully relaxed magnetization signal. Second and third contrasts are prepared with 25 and 50 ms T_2 preparation pulses comprising composite hard pulses [37], respectively. A non-selective saturation recovery (WET) pulse is performed immediately (T_S^{min}) before the readout of contrasts number four and six. The same preparation pulse is played in the systole for contrasts five and seven, facilitating longer T_1 relaxation [38].

representing full magnetization recovery (infinite saturation time, T_S) and T_2 preparation time of $T_2^p = 0$. The second block consists of two different T_2 -weighted contrasts using preparation durations of 25 ms and 50 ms, respectively, as previously recommended [22]. Four seconds of rest-period were inserted before each image without saturation preparation to allow for full magnetization recovery. Due to the rest-periods, full magnetization recovery was assumed prior to the T_2 preparation. The third block acquires images with saturation preparation to sample the T_1 recovery curve. The fourth and sixth image is performed with a saturation pulse before the readout to mimic the effect of a very long T_2 preparation [37] and short saturation times and, thus, T_S and T_2^p was set to T_S^{min} and 0. Image five and seven are acquired with saturation preparation with a maximum T_S for maximum precision [38].

The full acquisition comprises seven different contrast preparations followed by imaging at five echo times, yielding a total of 35 images. Saturation pulses were performed using a composite "Water suppression Enhanced through T_1 -effects" (WET) pulse to reduce the sensitivity to B_1 [40]. The T_2 preparation module consist of a 90° rectangular flip-down pulse, a 270° rectangular flip-up pulse and composite 180° MLEV refocusing pulses in between [41, 42]. Centric k-space reordering was used for increased signal-to-noise ratio and shorter minimum saturation times.

2.2 Sequence parameters

All measurements were performed on a 3T MRI scanner (Magnetom Skyra, Siemens Healthineers, Erlangen, Germany) with a 28-channel receiver coil array. Sequence parameters are listed in Table 1. SATURN was performed using GRAPPA with acceleration factor $R=3$. Additionally, GRAPPA with acceleration $R=4$ was explored for the use in subjects with higher heart rates. SPIRiT [43] with locally-low rank (LLR) reconstruction was used for improved noise-resilience at acceleration $R=4$, as previously proposed [44, 45, 46].

2.3 Simulations

Bloch-simulations were used to calculate the magnetization of the proposed SATURN sequence and validate the accuracy of the quantification. All pulse sequences were simulated with the above listed sequence parameters. The magnetization was simulated with time-steps of 0.1 ms. Imaging and preparation pulses were simulated with corresponding rotation matrices with 100% efficiency. The center of the k-space was chosen to extract the signal magnitude. T_1 (1200-1700 ms), T_2 (20-70 ms) and T_2^* (5-60 ms) were varied and the magnitude was fitted with the proposed five parameter fit model given in Equation 1. Four confounding factors were included in the simulations:

Rest periods before the T_2 preparation pulses was varied between 1 and 10 seconds. For all other simulations, 10 seconds were used to eliminate insufficient recovery as the primary source of inaccuracy. Image noise was added to the simulations. Rician noise was generated with an SNR between 0 and 30 and a Monte Carlo size of 1000. Different heart rates were simulated between 50 and 140 bpm. Finally, imperfect T_2 preparation was simulated by reducing the flip angle of the flip-down and flip-up pulses.

Table 1: Sequence parameters for SATURN and the reference methods (SASHA, T_2 -prepared bSSFP, multi GRE).

Parameters	SATURN	SASHA	T_2 bSSFP	multi GRE
FOV	384x288 mm ²			
In-plane res.	2x2 mm ²			
Slice thickness	8 mm			
Partial Fourier	6/8			
Readout	multi GRE	bSSFP	bSSFP	multi GRE
Flip angle	20°	45°	45°	20°
acq. k-Space lines	36	66	66	11
Bandwidth	1530 Hz/px	1130 Hz/px	1130 Hz/px	965 Hz/px
GRAPPA	R = 3 or 4	R = 2		
Respiration	free-breathing	breath-hold (exhaled)		
Number of echoes	5	1	1	8
TE	1.0-8.5 ms	1.3 ms	1.3 ms	1.6-16.3 ms
TR	10.3 ms	2.7 ms	2.7 ms	18.1 ms
nom. acquisition time	18.5 s	10 s	10 s	8 s

Common parameters are depicted with blue shading. Nominal acquisition time is calculated for a heart rate of 60 bpm and a gating efficiency of 50%.

2.4 Phantom experiments

Phantom measurements were performed to evaluate the accuracy and precision of the proposed SATURN sequence. Reference measurements for T_1 were performed using an inversion-recovery spin echo sequence with $T_1 = 100, 200, 500, 1000, 2000, 5000, 8000$ ms, TE/TR = 12/10000 ms, and imaging geometry as specified above. T_2 reference scans were performed with a spin echo sequence with TE = 17, 30, 50, 100, 150, 250 ms and otherwise identical imaging parameters to the inversion recovery spin-echo (IR-SE). GRE was performed for T_2^* quantification with 12 contrasts ranging from TE = 2-60 ms, TR = 10000 ms and one k-space line per readout with the same imaging

parameters listed above. All measurements were additionally compared with single-parameter methods for myocardial mapping (listed in Table 1): SASHA T_1 [47] with a minimum and maximum saturation time of 103 ms and 600 ms, T_2 -prepared bSSFP using four different T_2 weightings (0 ms, 25 ms, 50 ms and ∞ ms) and a 3 parameter fit model [22, 48], and multi-GRE T_2^* with 8 echoes ranging from 1.6ms-16.3 ms [19] using the 2 parameter truncation model [39]. The cardiac cycle was simulated and set to a heart rate (HR) of 60 beats per minute.

2.5 In vivo experiments

In vivo measurements were performed in 10 healthy volunteers (23-29 years old, 26.1 ± 1.5 y, heart rate: 67.2 ± 7.7 bpm, 3 female), one patient (69 years old, female, heart rate: 72 bpm) with hypertrophic cardiomyopathy (HCM) and one patient (66 years old, male, heart rate: 79 bpm) with suspected hypertensive heart disease (HHD) after written consent was obtained. All images were acquired in the mid-ventricular short-axis view using the parameters described in the previous section.

SATURN was performed with a maximum T_S adjusted to the subject's heart rate. Motion between images from different heart-beats was reduced by retrospective image registration. Rigid registration was performed with mutual information in the region of interest as the similarity metric. Voxel-wise fitting was performed using the five parameter model.

Regions of interest were manually drawn in the entire myocardium, with careful distancing to the epi- and endocardial borders. Bullseye plots were generated for the six mid-ventricular segments of the American Heart Association (AHA) segment model [49].

Standard deviation maps (SD maps) were generated by calculating all partial derivatives of the fit function as previously proposed [50]. The covariance matrix is calculated by the inverse of the Hessian matrix. The square root of the sum of the diagonal entries of the covariance matrix is used as an approximation for the voxel-wise standard deviation of the individual parameters.

2.6 Statistics

The within-segment mean and the within-segment standard deviation of the T_1 , T_2 , and T_2^* times were averaged across all subjects. Additionally, the within-segment mean of the SD T_1 , T_2 , and T_2^* times was calculated respectively. Inter-subject variability was calculated as the standard deviation of the within-segment mean across all subjects.

Pair-wise comparison was performed using Student's t-tests using the Bonferroni correction for multiple comparisons along T_1 , T_2 , and T_2^* . p-values less than 0.05 were considered significant. Significance between segments of the myocardium was tested using the ANOVA test. Relative deviations were compared by dividing the absolute difference between reference and SATURN with the reference.

3 Results

3.1 Simulations

Figure 2A shows the simulated longitudinal magnetization evolution of the proposed SATURN sequence with varying T_1 , T_2 , and T_2^* . Figure 2B plots the fitted relaxation times against the reference relaxation times to depict the measurement accuracy. Accurate multi-parameter quantification for T_1 , T_2 , and T_2^* across the relevant in vivo range ($T_1 = 800 - 2200$ ms, $T_2 = 30 - 70$ ms, $T_2^* = 10 - 60$ ms) was achieved in simulations. One source of deviation for T_2 was incomplete recovery during the rest-periods leading to very slight deviations in T_2 (0.02% for 50ms, <5% deviation for 100 ms) as shown in Supporting Information Figure S1. T_2^* quantification was found to be more susceptible to higher noise levels than T_1 and T_2 . T_1 , T_2 , and T_2^* accuracy were independent of the heart rate. T_2 accuracy was additionally compromised by an imperfect T_2 preparation efficiency resulting in a strong underestimation, especially for longer T_2 times.

3.2 Phantom

Phantom measurements (Figure 3A) showed good agreement with reference methods. Deviations of less than 7.7% for relaxation times across the relevant in vivo range were observed. In Figure 3B the relative difference of the measured relaxation times to the reference is shown as well as exemplary maps are shown for SATURN and the reference are shown below (Figure 3C). SATURN T_1 times compared with the inversion recovery spin-echo, yielding accuracy comparable to SASHA. T_2 times were accurate in the relevant range (5.2% deviation) and decreased when exceeding 100 ms with relative deviations of up to 20%. For T_2^* of less than 100 ms T_2^* accuracy (7.7% deviation) was slightly higher compared with the conventional single parameter method, where a decrease of up to 11 ms was measured compared with the reference GRE. SATURN overestimates long T_2^* times compared with the GRE and multi-GRE [51]. All representative relaxation times per tube are displayed in Supporting Information Table S1.

3.3 In vivo

Average acquisition time for SATURN in the ten healthy subjects was 26.5 ± 14.9 seconds, which corresponds to an average gating efficiency of 54 ± 30 %. The minimal T_S^{min} was

7 ms for every subject and the maximal T_S^{max} was 601 ± 65 ms. Example magnitude data acquired with SATURN in one healthy subject is shown in Figure 4A. Signal intensities from the septum are plotted across 35 measurements along with the fitted signal model (Figure 4B). Visual image quality is high for T_1 and T_2 . Artifacts are observed in T_2^* maps (Figure 5A). Standard deviation maps depict the homogeneous mapping precision throughout the myocardium (Figure 5B).

Example quantitative parameter maps acquired with SATURN compared with the single-parameter reference methods are shown in Figure 5 for one healthy subjects (two more subjects are shown in Supporting Information Figure S2). Visual image quality is comparable with the single parameter scans for T_1 and T_2 . However, some blurring is observed in the SATURN maps. T_1 and T_2 maps depict a homogeneous myocardium clear of artifacts. T_2^* maps acquired with SATURN appear visually smoother than the reference.

Figure 6 shows the in vivo mean T_1 , T_2 , and T_2^* times for SATURN over the conventional methods for all healthy subjects. Below the Bland-Altman plot is depicted. A bias of +29.16 ms was measured for T_1 and a bias of +1.54 ms was measured for T_2^* . T_2

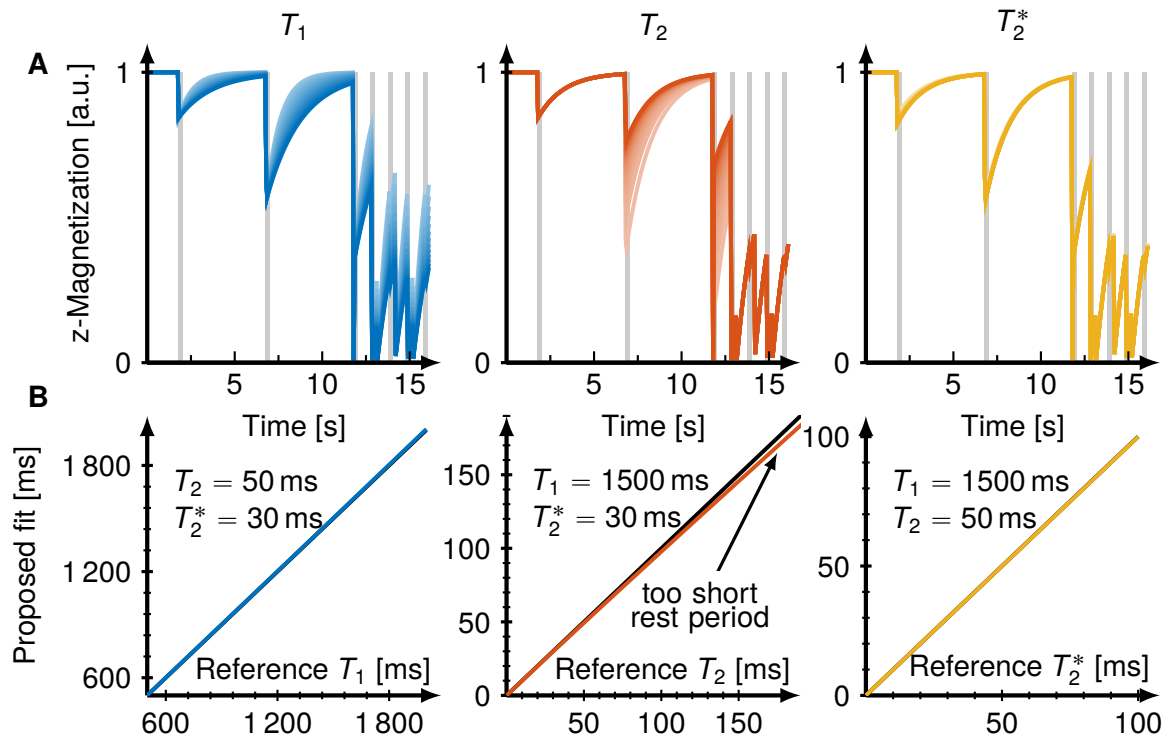


Figure 2: A) Simulated magnetization evaluation of the proposed sequence for varying T_1 (800-2000 ms), T_2 (30-100 ms), and T_2^* (20-100 ms) on the top. Increasing relaxation times are depicted by increasing brightness. **B)** Bottom panel shows the proposed five parameter fit (blue) to the used relaxation time.

times yielded no bias compared with T_1 and T_2^* but limits of agreement of ± 9.4 ms. All representative relaxation times per subject are displayed in Supporting Information Table S2.

Supporting Information Figure S3 shows the difference between SATURN acquired with GRAPPA with acceleration factor R=3, R=4, and R=4 using SPIRiT + LLR regularization. T_2 map quality shows only minor differences between R=3 or R=4 with deviations

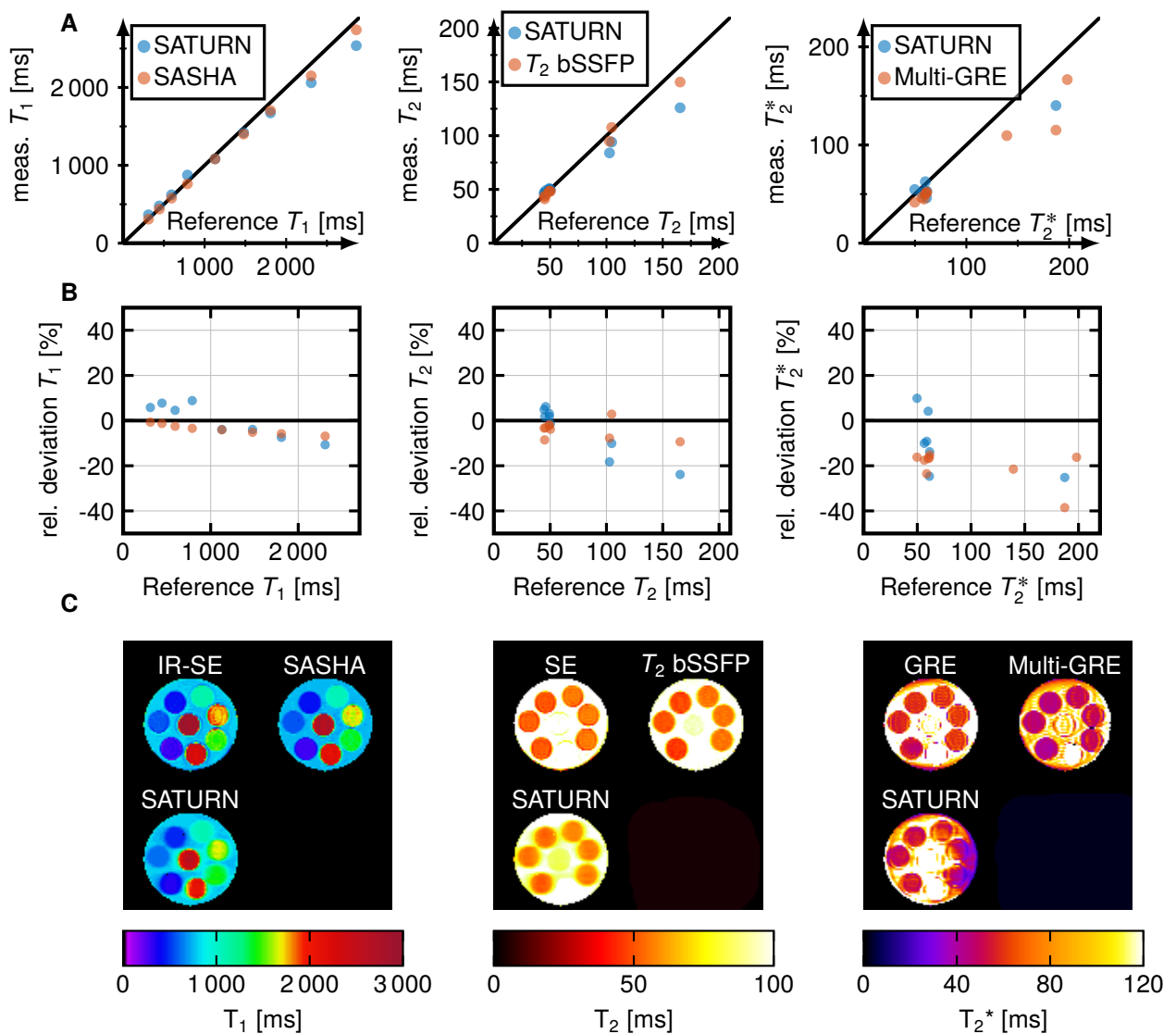


Figure 3: **A)** T_1 , T_2 , and T_2^* acquired with SATURN (blue) and the single parameter methods (red) in a phantom plotted against the reference values. For T_2^* , two tubes with high relaxation times are outside of the depicted range. **B)** Relative difference between the reference method and SATURN and the single parameter models for the different relaxation times. **C)** Representative T_1 , T_2 , and T_2^* maps for SATURN and the reference.

of less than 2%. However, T_1 map quality is improved with 36.2% lower within-segment standard deviations for $R=3$ compared with $R=4$. Precision is regained by using regularization (SPIRiT + LLR) and image quality is visually improved (only 5.4% lower within-segment standard deviations). SATURN T_1 maps appear smoother and more homogeneous when using $R=3$ with smaller variations within the myocardium. Additional artifacts appear in T_2^* maps using $R=4$, which are largely alleviated using regularization.

Figure 7 represents the AHA 6 segment bullseye plots showing the mean quantitative measures across all healthy for the T_1 , T_2 , and T_2^* and the corresponding within-segment standard deviation. The relaxation times in the healthy myocardium measured with SATURN averaged over all six AHA segments were $T_1 = 1573 \pm 86$ ms, $T_2 = 33.2 \pm 3.6$ ms, comparable to the conventional methods ($T_1 = 1544 \pm 107$ ms; $p=0.22$, $T_2 = 33.2 \pm 3.6$ ms; $p=0.98$). T_2^* obtained with SATURN was 25.3 ± 6.1 ms, corresponding to a 5.9% increase compared to the conventional method (23.8 ± 5.3 ms; $p=0.33$) with both methods suffering from artifacts. No significant differences were

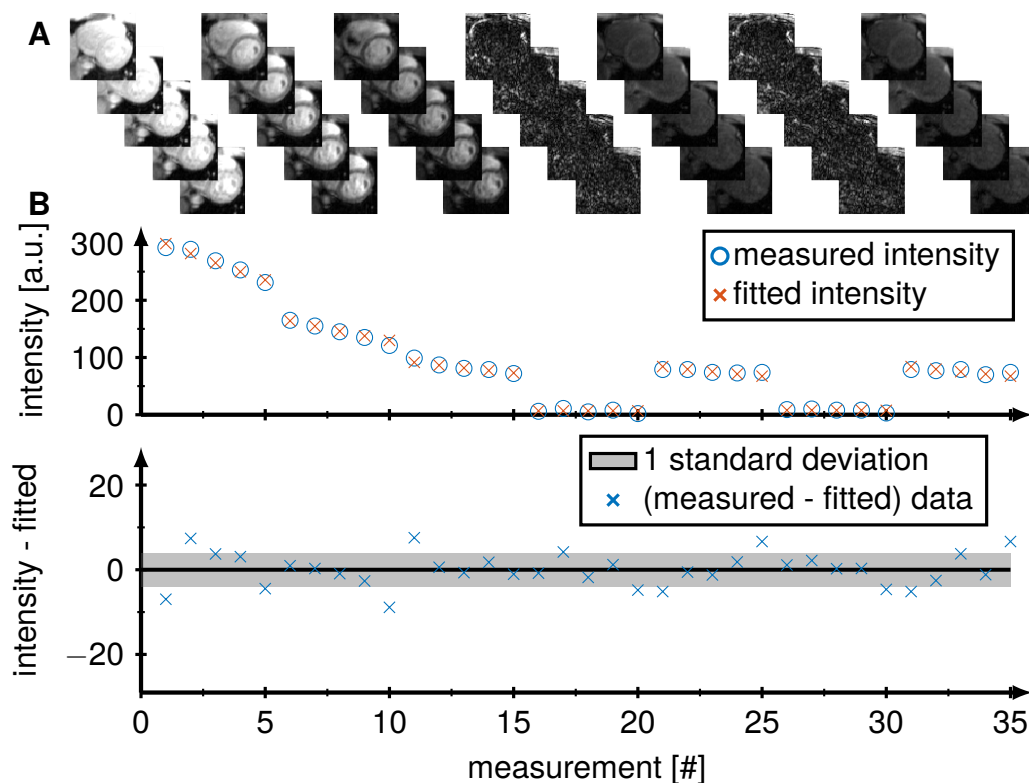


Figure 4: **A)** Magnitude images from the septum are plotted across the 35 measurements. **B)** Image intensities of the acquired (blue) and fitted (orange) signal model and the fit residual of a voxel in the septal myocardium are shown below where the gray area marks deviations of less than 1 standard deviation.

found between the in vivo times measured with SATURN and the conventional methods for neither T_1 , T_2 or T_2^* .

No significant differences among segments were measured for SATURN T_1 ($p=0.36$) but significant differences for T_2 ($p=0.037$) and T_2^* ($p=0.038$), with the lowest T_2 / T_2^* times being observed in the mid-inferior segment. The same trend is observed for the conventional methods. For SASHA T_1 no significant difference among the segments ($p=0.83$) was observed, but significant differences for the single parameter T_2 ($p=0.033$) and T_2^* ($p<0.01$), depicting a similar drop in the mid-inferior segment. Inter-subject variability of 57.9 ms (3.7% compared with the mean value) was observed in T_1 , which is higher than for SASHA (42.3 ms (2.7%)). Inter-subject variability of 3.3 ms (9.9%) for T_2 obtained with SATURN were in the range of the T_2 -prepared bSSFP with 3.2 ms (9.6%), and 3.6 ms (14.2%) for T_2^* compared with the multi GRE 3.2 ms (13.4%) were observed.

SD-maps are calculated for all healthy subjects for SATURN and the conventional methods and resulted in mean values of $\sigma(T_1) = 68$ ms, $\sigma(T_2) = 1.1$ ms and $\sigma(T_2^*) = 3.3$ ms

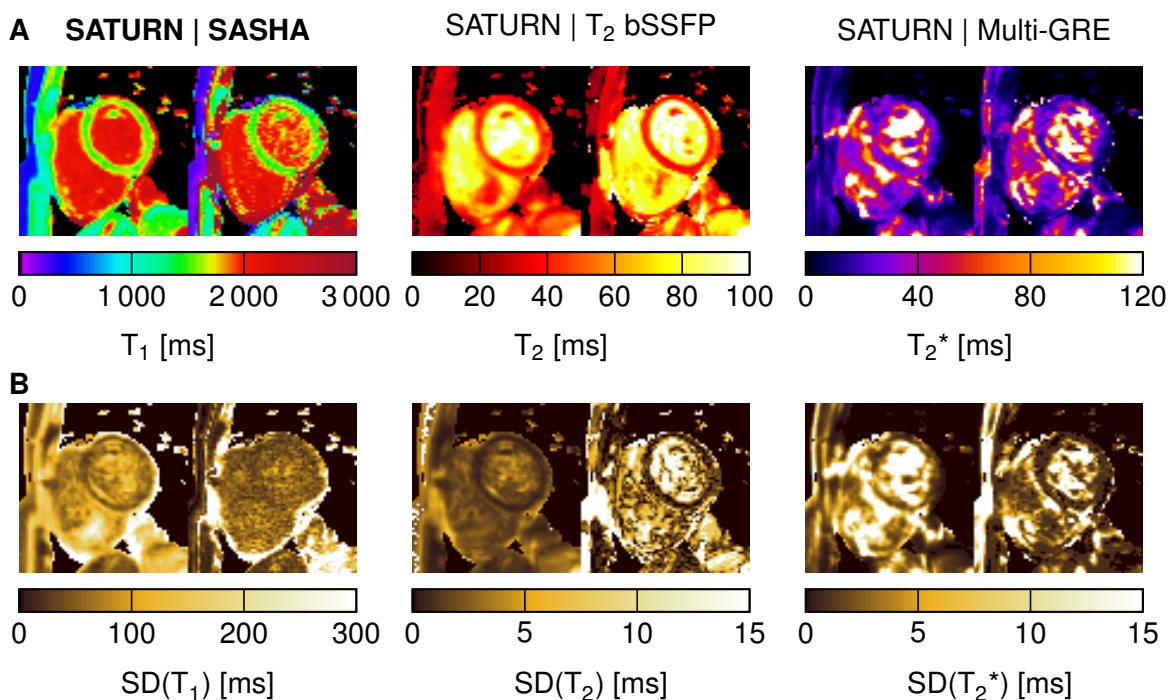


Figure 5: A) In vivo T_1 , T_2 , and T_2^* maps acquired with the proposed SATURN sequence (left) and single parameter reference methods (right) for one healthy subject. Visually homogeneous mapping is achieved throughout the myocardium for T_1 and T_2 , minor artifacts appear in T_2^* maps. Image quality appears visually comparable to the reference methods. **B)** Below the standard deviation (SD) maps are shown for the three relaxation times and the same subject for SATURN and the reference methods.

and for the conventional methods $\sigma(T_1) = 39.3$ ms, $\sigma(T_2) = 1.9$ ms and $\sigma(T_2^*) = 1.5$ ms. Example standard deviation maps are shown in Figure 5B and Supporting Information Figure S2. Figure 8 shows the mean and the standard deviation of the calculated SD maps in each of the 6 segments. For T_1 , SATURN achieved 23.3% lower within-segment standard deviations and improved precision compared with SASHA T_1 map. T_2 shows comparable precision between SATURN and the single parameter method (5.1% deviations). Increased within-segment standard deviations of 8.3% are observed for SATURN T_2^* compared with the reference multi GRE.

Figure 9 shows SATURN T_1 , T_2 , and T_2^* maps for a patient with HCM, and one patient with suspected HHD and the corresponding bullseye plots. Increased T_1 , T_2 , and T_2^* times (1607/47.0/35.5 ms versus 1487/38.5/26.5 ms) are observed in the septal regions compared with the lateral myocardium in the patient with HCM. SATURN shows increased T_1 times and patchy structures in the patient with HHD. T_2^* times are substantially elevated.

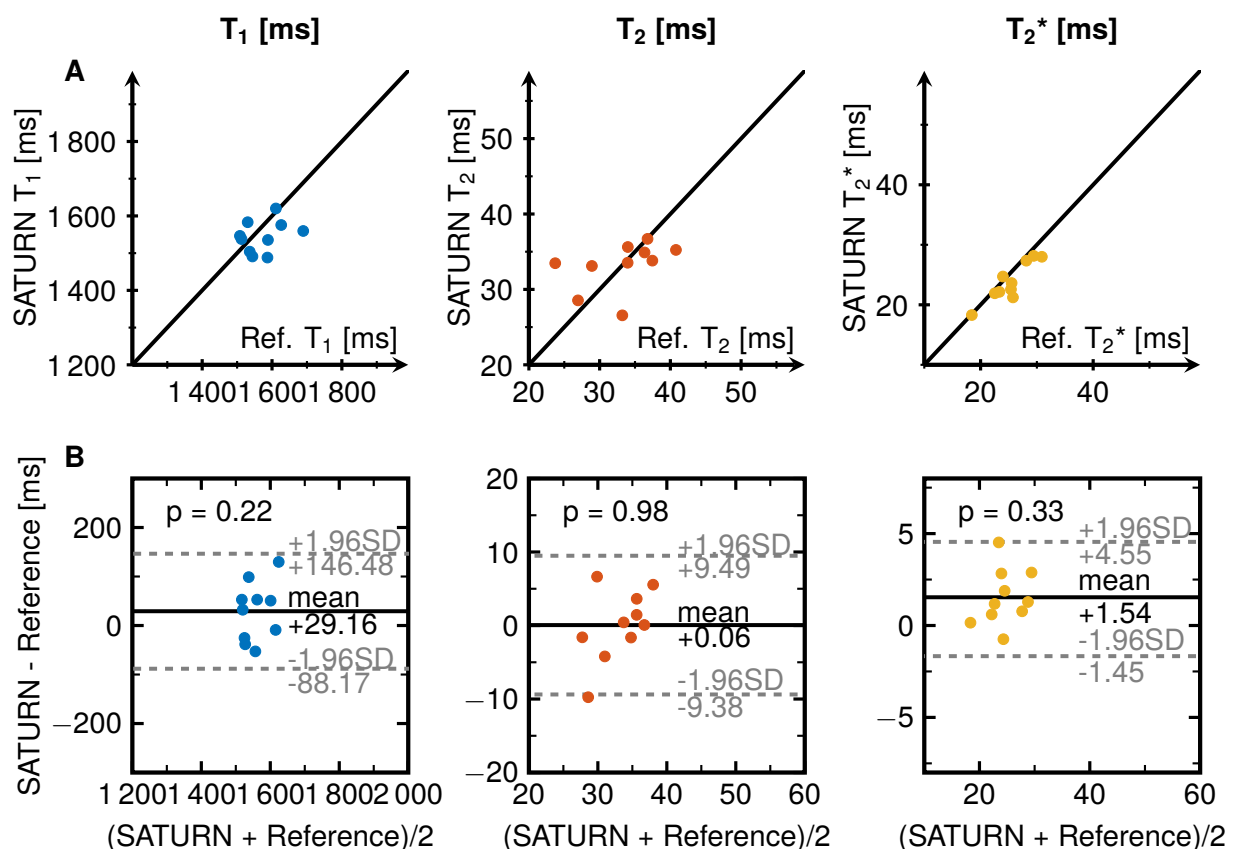


Figure 6: **A)** SATURN over the reference T_1 , T_2 , and T_2^* times for each healthy subject. The black line shows the bisector. **B)** Bland-Altman plot showing the difference between SATURN and the reference over the mean of both. The legend shows the p-value of the Student's t-test.

4 Discussion

In this study, we proposed the SATURN sequence for free-breathing simultaneous quantification of T_1 , T_2 , and T_2^* in the myocardium based on a gradient-echo read-out in combination with saturation pulses and T_2 preparation pulses. We demonstrated good agreement with Bloch simulations and phantom experiments yielding generally accurate T_1 times. However some biases for T_2 and T_2^* are observed. In vivo measurements provided robust image quality comparable to reference methods for all segments in the mid-ventricular short-axis view.

T_1 measurements resulted in good accuracy compared to spin-echo sequences and SASHA in the phantom and in vivo. Mean T_1 times in the six segments are comparable to previously reported values for saturation based T_1 mapping at 3T [12, 51]. T_1 maps yielded similar image quality and smaller within-segment standard deviations compared with SASHA. Similar inter-subject variability was found between SATURN and the reference method.

Our simulations indicate that accuracy in T_2 mapping is compromised for long T_1/T_2

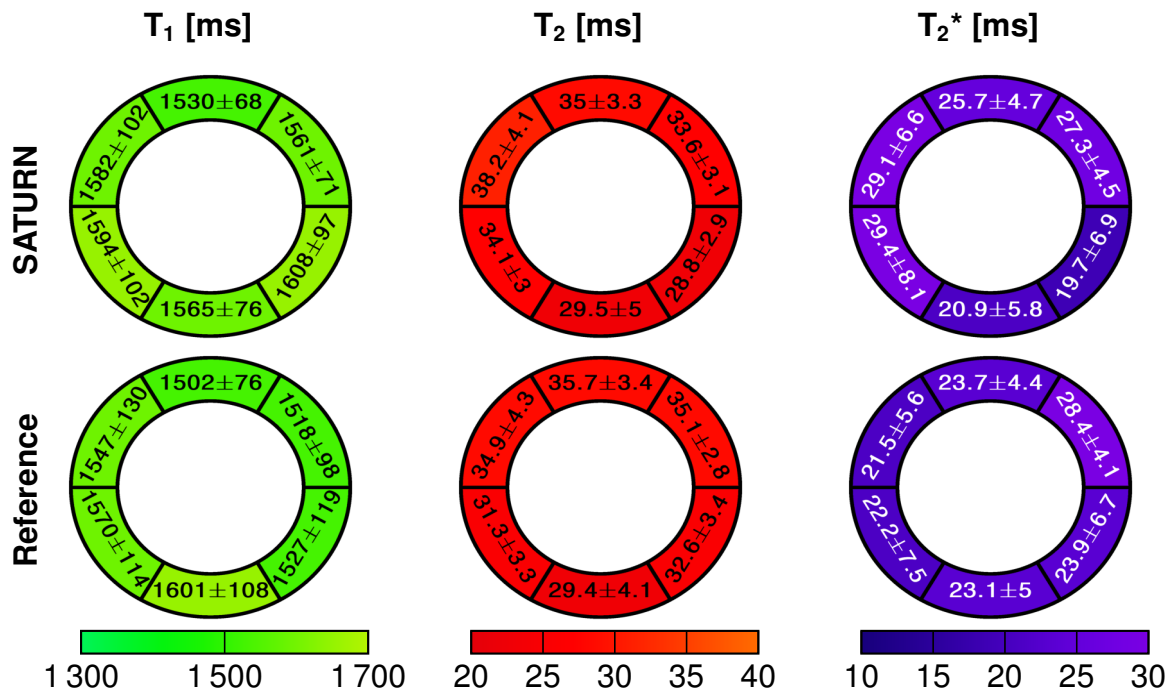


Figure 7: Bullseye plot of T_1 , T_2 , and T_2^* relaxation times acquired with SATURN and the single parameter reference. The bullseye values are reported as the within-segment mean \pm the within-segment standard deviation average across all healthy subjects. Small differences between SATURN and the reference was observed for T_1 and T_2 . T_2^* obtained with SATURN was 5.9% increased compared with the reference.

combinations due to insufficient recovery during the rest-period. However, as this effect is only marked at values outside the relevant in vivo range, a choice of 4 seconds rest periods seemed justified. In vivo T_2 measurements resulted in lower T_2 times than reported in literature [22, 52, 53], but only minor differences were observed between SATURN and the reference T_2 -prepared bSSFP. The lower T_2 times obtained in this study as compared to previous literature [22, 52, 53] are related to the use of a three-parameter fit model, which was previously shown to yield lower T_2 times (Supporting Information Figure S4). Other than that, we observed a drop of T_2 in mid-inferior segments in some healthy subjects due to B_1^+ inhomogeneities, which could be corrected by better shimming routines. We used rest periods before the T_2 preparations instead of saturation pulses directly after the ECG trigger because the SNR of the T_2 -prepared images for the gradient-echo readout was too low for accurate T_2 quantification as numerical simulations showed [54]. T_2 maps in vivo and in phantom appeared visually smoother and more blurred as compared with the conventional single parameter maps due to the centric k-space reordering in SATURN. With centric k-space reordering, the magnetization transfer function acts as a slight low pass filter [55]. We decided in favor of centric k-space reordering due to the improved quantification result and image

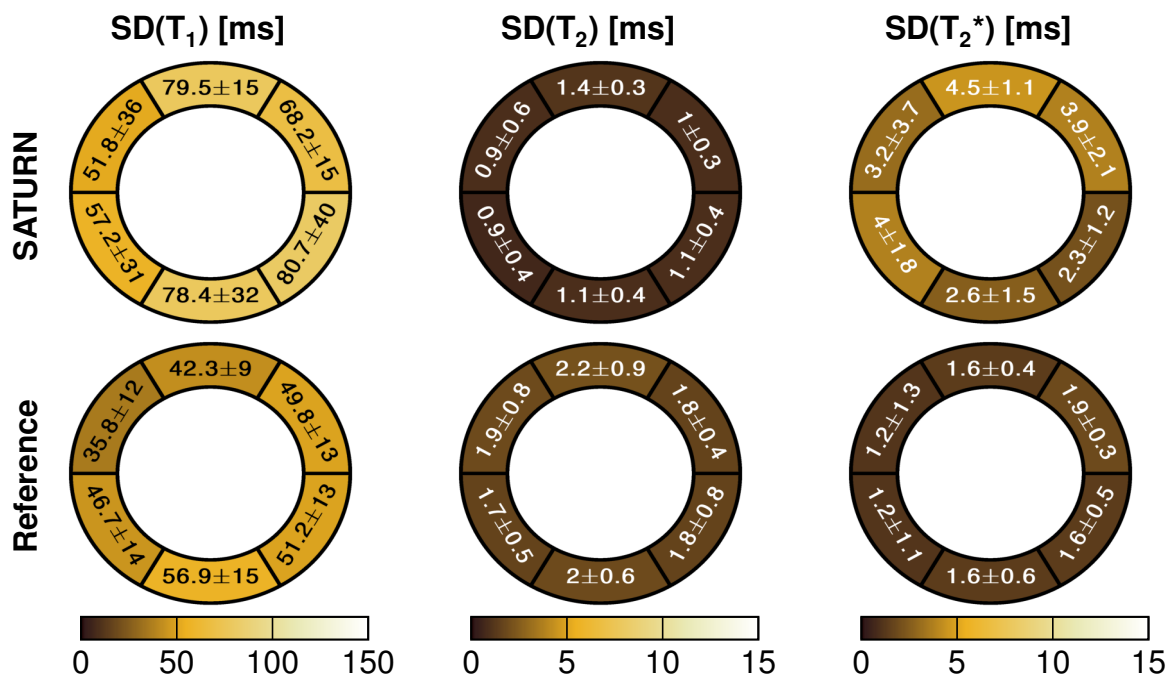


Figure 8: Bullseye plot of T_1 , T_2 , and T_2^* relaxation times acquired with SATURN and the single parameter reference. The bullseye values are reported as the within-segment mean \pm the within-segment standard deviation of the standard deviation map (SD map) for each segment. The voxel-wise standard deviation was higher for T_1 and T_2^* obtained with SATURN and smaller for T_2 compared with the single parameter methods.

quality, especially for T_1 .

Bloch simulations without noise result in accurate T_2^* quantification. However, phantom measurements resulted in deviations of up to 20%, likely due to susceptibility artifacts and increased noise, as this was the dominant factor in the Bloch simulations. Especially for the tubes with very high T_2^* times the quantification in the phantom failed, which might be due to the very short maximum TE of the five echoes from SATURN. However, for T_2^* in the in vivo relevant range SATURN was still observed to be more accurate than the reference GRE method. T_2^* times in vivo are in the range of reported literature [56, 57, 58] and slightly increased compared with the reference GRE (5.9%). The overestimation is likely linked to a shorter maximum TE. However, increased T_2^* times are measured without truncation due to sufficient SNR [39, 59]. A drop in T_2^* was observed in the mid-inferior segment due to B_1^+ inhomogeneities as also observed for T_2 .

Higher accelerations might be necessary for patients with high heart rates to reduce the time per single-shot acquisition. The variability in T_1 maps is increased when using higher acceleration factors (GRAPPA R=4). However, this can be alleviated by using regularization (SPIRiT + LLR) at the cost of inducing complexity in the post-processing. T_2 maps reconstructed using acceleration factors of R=3 and R=4 resulted in visually similar T_2 maps with only slight deviations of 2.1% in the T_2 times and 1.9% in the within-segment standard deviations. Similar to T_1 , for the T_2^* the use of R=4 increases the within-segment standard deviation by 52.4%, which might be due to the low SNR for images with long TEs.

In the patient with HCM we observed an increased T_1 , T_2 , and T_2^* time as reported in literature [60, 61, 62]. Image quality was visually good. For the patient with suspected HHD, increased T_1 and T_2^* was observed in the septal region and patchy structures in the T_1 map as typically observed in HHD [63]. No reference methods were acquired in patients, which will be evaluated in future work.

Simultaneous measurements of T_1 , T_2 , and T_2^* is more time-efficient since all parameters are acquired in one scan (average acquisition time was 26.5 ± 14.9 s). Additionally, they share the same volume and are, therefore, inherently co-registered. This eases the fusion of imaging information as corresponding regions are easy to identify. Furthermore, the assessment of multiple quantitative measures increases the specificity for diagnosis [1, 2, 52].

Free-breathing imaging was achieved by using a prospective navigator on the liver diaphragm. This may minimize the susceptibility to incomplete breath-holds as often

observed in patients suffering from dyspnea. Residual motion is compensated by the use of image registration. We used rigid-registration as previously reported to yield satisfactory results in healthy subjects (Supporting Information Figure S5) [64]. In patients with variable breathing patterns and/or arrhythmia, the motion correction for respiratory as well as the cardiac cycle might be improved by using non-rigid registrations, which is subject of future work. In addition, simultaneous multi slice acquisition [65] can be used to cover multiple slices per acquisition, which enables whole heart imaging in a relatively short time.

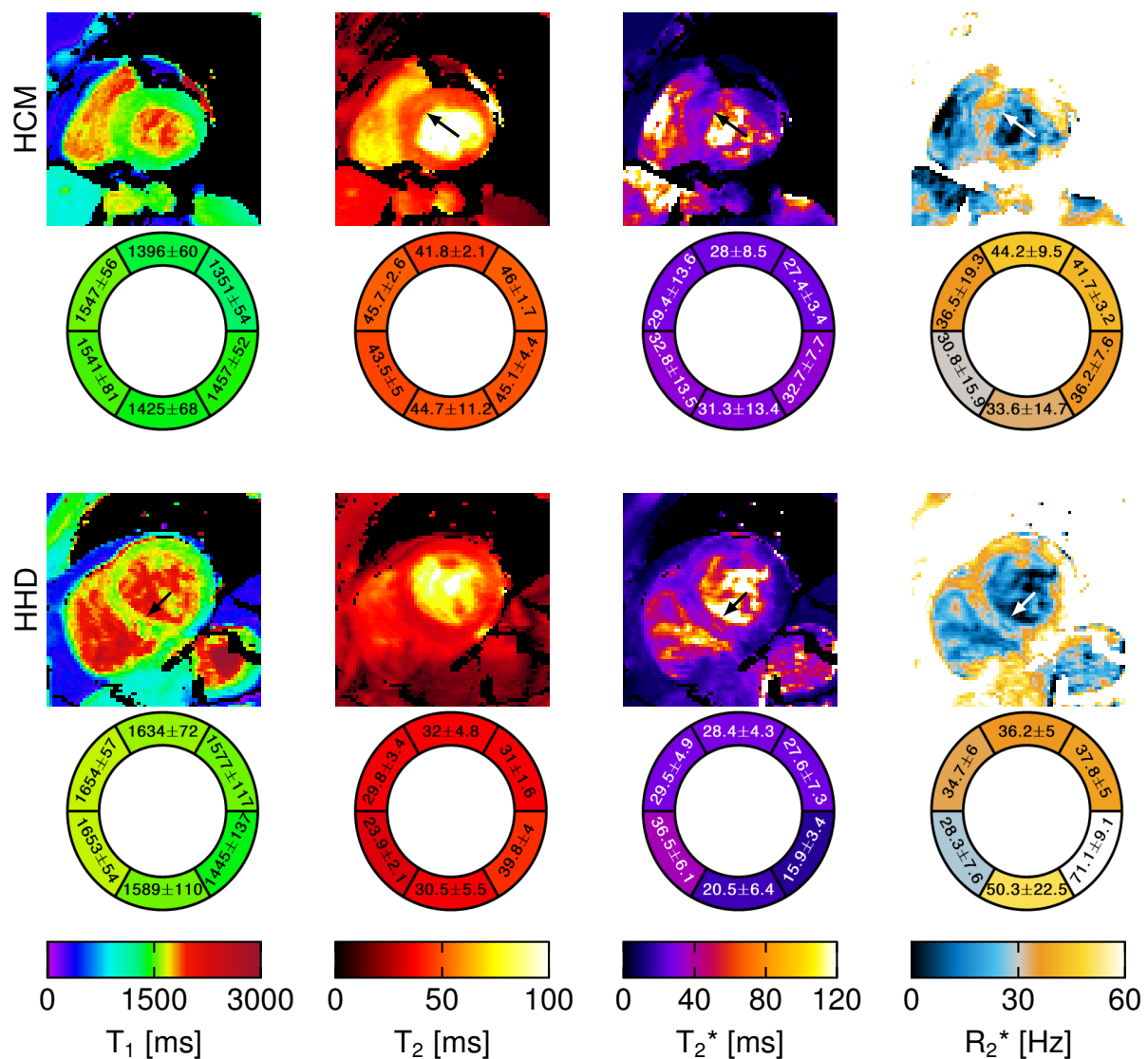


Figure 9: SATURN T_1 , T_2 , and T_2^* maps for a patient with hypertrophic cardiomyopathy (HCM) and one patient with suspected hypertense heart disease (HHD). The corresponding bullseye plots are shown respectively. In the patient with HCM a increased T_1 , T_2 , and T_2^* was observed in the septal region. For the patient with HHD, increased T_1 and T_2^* was observed in the septal region as well as patchy structures in the T_1 map.

Intramyocardial fat is often present in cardiac patients and is known to shorten the T_1 and T_2 times [66]. While variable impact of the fat fraction on bSSFP based cardiac relaxometry has been reported [67], the effects on GRE based mapping, as proposed in this study, are expected to be affected by fewer confounders. Furthermore, in the presence of substantial intramyocardial fat, the T_2^* decay deviates from a monoexponential decay. Dixon-encoding mapping might be used to separate the fat and water signal and overcome the deviations in the quantitative measures [68, 69]. Integration of these techniques in our proposed sequence and dedicated evaluation for fatty storage disease warrant further investigation.

A physics-based five parameter model was used for the quantification. Recent trends emerged using machine learning for improving the reconstruction and fitting with non-explicit modeling and might be applied due to the limited spatial resolution, partial volume effects, and noise [70, 71, 72, 73].

This study has several limitations. Saturation recovery based methods for T_1 quantification suffer from a decreased dynamic range of the T_1 recovery curve, which is known to decrease the precision [38]. However, compared with inversion recovery methods such as MOLLI, the accuracy is not impacted [74] (Supporting Information Figure S1). The dynamical range could be increased by shifting the readout to the succeeding heart-beat, as previously reported [75]. However, in this case, navigator gating may affect the sampling of the saturation recovery. Nonetheless, this modification may lead to valuable improvements in terms of map quality for tachycardiac patients and warrants further investigation. Single-shot imaging suffers from long readout blocks, especially for a multi gradient-echo readout with 5 echoes. Higher heart rates will result in more cardiac motion during the acquisition. Therefore, the maximal TR of the echoes has to be short enough to acquire the whole k-space in one diastolic phase. However, short TR reduces the accuracy of the T_2^* quantification of long T_2^* times as observed under certain circumstances or lower field-strength. Higher acceleration factors enable the sampling of longer echo times in the same acquisition window, albeit at the cost of reduced SNR. We showed that this limitation might be partially compensated for by the use of regularization when using acceleration factors higher than $R=3$. A maximum TE of 8.6 ms is short compared with conventional methods that often use a maximum TE around 16-18 ms [20]. We decided to use a truncation fitting model to increase the quantification accuracy, especially for the low SNR contrasts 4 and 6 [39]. Nevertheless, the use of short echo times might lead to an overestimation of T_2^* . However, an increase of 1.5 ms in T_2^* in vivo compared with the conventional multi GRE was obtained with SATURN. This deviation is explained by the shorter maximum TE relative to the reference method. Increasing the length of the GRE readout train may be con-

sidered in a trade-off against higher acceleration rates if improved accuracy for long T_2^* is desired. Faster acquisition schemes such as radial single-shot images might offer a better compromise between longer TE and short enough acquisition windows, which will be evaluated in further research. Conventionally, T_2^* maps are acquired with lower spatial resolution compared with T_1 and T_2 . Since we are measuring all three parameters from the same scan with the same spatial resolution we acquire with slightly higher resolution for T_2^* as commonly acquired [20]. Furthermore, it is generally recommended to perform T_2^* mapping at 1.5T. Hence, the quality of the T_2^* quantification might show superior results at 1.5T. Blood signal suppression is also often used in T_2^* mapping to alleviate partial volume effects. However, in this study, we refrained from additional blood signal suppression but may benefit from decreased partial voluming due to an increased imaging resolution.

5 Conclusion

SATURN enables joint quantification of the most relevant clinical relaxation times, T_1 , T_2 , and T_2^* , with robust image quality in a single free-breathing scan. Good quantification accuracy was demonstrated in a phantom. In vivo free-breathing imaging yielded high visual image quality.

6 Acknowledgments

The authors acknowledge grant support by the 4TU Federation, ZonMW OffRoad 04510011910073, a NWO Startup STU.019.024 and the NIH R01HL153146, R21EB028369, P41EB027061.

References

- [1] Messroghli Daniel R., Moon James C., Ferreira Vanessa M., et al. Clinical recommendations for cardiovascular magnetic resonance mapping of T1, T2, T2* and extracellular volume: A consensus statement by the Society for Cardiovascular Magnetic Resonance (SCMR) endorsed by the European Association for Cardiovascular Imaging (EACVI) *Journal of Cardiovascular Magnetic Resonance* 2017; **19**(1):75.
- [2] A.S. Lota P.D. Gatehouse, Mohiaddin R.H.. T_2 mapping and T_2^* imaging in heart failure *Heart Fail Rev.* 2017; **22**(4):431–440.
- [3] Dall'Armellina Erica, Piechnik Stefan K., Ferreira Vanessa M., Si Quang Le. Cardiovascular magnetic resonance by non contrast T_1 -mapping allows assessment of severity of injury in acute myocardial infarction *Journal of Cardiovascular Magnetic Resonance* 2012; **14**(1):15.
- [4] Radenkovic Dina, Weingärtner Sebastian, Ricketts Lewis, Moon James C., Captur Gabriella. T1 mapping in cardiac MRI *Heart Failure Reviews* 2017; **22**(4):415–430.
- [5] Ferreira V. M., Piechnik S. K., Robson M. D., Neubauer S., Karamitsos T. D.. Myocardial tissue characterization by magnetic resonance imaging: novel applications of T1 and T2 mapping. *Journal of thoracic imaging* 2014; **29**(3):147-154.
- [6] Hamlin Scott A., Henry Travis S., Little Brent P., Lerakis Stamatios, Stillman Arthur E.. Mapping the Future of Cardiac MR Imaging: Case-based Review of T1 and T2 Mapping Techniques *RadioGraphics* 2014; **34**(6):1594-1611.
- [7] Moon James C., Messroghli Daniel R., Kellman Peter, et al. Myocardial T1 mapping and extracellular volume quantification: a Society for Cardiovascular Magnetic Resonance (SCMR) and CMR Working Group of the European Society of Cardiology consensus statement *Journal of Cardiovascular Magnetic Resonance* 2013; **15**(1):92.
- [8] Messroghli Daniel R., Radjenovic Aleksandra, Kozerke Sebastian, Higgins David M., Sivananthan Mohan U., Ridgway John P.. Modified Look-Locker inversion recovery (MOLLI) for high-resolution T1 mapping of the heart *Magnetic Resonance in Medicine* 2004; **52**(1):141–146.
- [9] Weingärtner Sebastian, Akçakaya Mehmet, Basha Tamer, et al. Combined saturation/inversion recovery sequences for improved evaluation of scar and diffuse

- fibrosis in patients with arrhythmia or heart rate variability *Magnetic Resonance in Medicine* 2014; **71**(3):1024-1034.
- [10] Haaf Philip, Garg Pankaj, Messroghli Daniel R., Broadbent David A., Greenwood John P., Plein Sven. Cardiac T1 Mapping and Extracellular Volume (ECV) in clinical practice: a comprehensive review *Journal of Cardiovascular Magnetic Resonance* 2016; **18**(1):89.
- [11] Puntmann Valentina O., Peker Elif, Chandrashekhar Y., Nagel Eike. T1 Mapping in Characterizing Myocardial Disease A Comprehensive Review *Circulation Research* 2016; **119**(2):277–299.
- [12] Weingärtner Sebastian, Meßner Nadja M., Budjan Johannes, et al. Myocardial T1-mapping at 3T using saturation-recovery: reference values, precision and comparison with MOLLI *Journal of Cardiovascular Magnetic Resonance* 2017; **18**(1):84.
- [13] Kellman Peter, Yue Hui, Chow Kelvin, Spottiswoode Bruce S., Arai Andrew E., Thompson Richard B.. Optimized saturation recovery protocols for T1-mapping in the heart: influence of sampling strategies on precision. *J Cardiovasc Magn Reson* 2014; **16**(1):55.
- [14] Hermann Ingo, Uhrig Tanja, Chacon-Caldera Jorge, Akcakaya Mehmet, Schad Lothar R, Weingärtner Sebastian. Towards measuring the effect of flow in blood T_1 assessed in a flow phantom and in vivo *Physics in Medicine & Biology* 2020; **65**.
- [15] Verhaert David, Thavendiranathan Paaladinesh, Giri Shivraman, et al. Direct T2 Quantification of Myocardial Edema in Acute Ischemic Injury *JACC: Cardiovascular Imaging* 2011; **4**(3):269 - 278.
- [16] Kellman Peter, Aletras Anthony H., Mancini Christine, McVeigh Elliot R., Arai Andrew E.. T2-prepared SSFP improves diagnostic confidence in edema imaging in acute myocardial infarction compared to turbo spin echo *Magnetic Resonance in Medicine* 2007; **57**(5):891-897.
- [17] Giri Shivraman, Chung Yiu-Cho, Mancini Ali, Rajagopalan Sanjay, Raman Subha V., Simonetti Orlando P.. T2 quantification for improved detection of myocardial edema *J Cardiovasc Magn Reson* 2009; **11**(1):56.
- [18] Basha Tamer, Akcakaya Mehmet, Roujol Sébastien, Nezafat Reza. Precision and reproducibility of T2 quantifications in myocardial T2 mapping: Impact of the number of echoes and reconstruction model *Journal of Cardiovascular Magnetic Resonance* 2015; **17**((Suppl 1)).

PUBLICATION II

- [19] Westwood Mark, Anderson Lisa J., Firmin David N., et al. A single breath-hold multiecho T2* cardiovascular magnetic resonance technique for diagnosis of myocardial iron overload *Journal of Magnetic Resonance Imaging* 2003; **18**(1):33-39.
- [20] Kellman Peter, Xue Hui, Spottiswoode Bruce S., et al. Free-breathing T2* mapping using respiratory motion corrected averaging *J Cardiovasc Magn Reson* 2015; **3**(17):1741-1753.
- [21] Triadyaksa Pandji, Oudkerk Matthijs, Sijens Paul E.. Cardiac T2* mapping: Techniques and clinical applications *Journal of Magnetic Resonance Imaging* 2019; **n/a**(n/a).
- [22] Akçakaya Mehmet, Weingärtner Sebastian, Basha Tamer A., Roujol Sébastien, Bellm Steven, Nezafat Reza. Joint myocardial T1 and T2 mapping using a combination of saturation recovery and T2-preparation *Magnetic Resonance in Medicine* 2016; **76**(3):888-896.
- [23] Qi Haikun, Bustin Aurelien, Cruz Gastao, et al. Free-running simultaneous myocardial T1/T2 mapping and cine imaging with 3D whole-heart coverage and isotropic spatial resolution *Magnetic Resonance Imaging* 2019; **63**:159 - 169.
- [24] Christodoulou Anthony G., Shaw Jaime L., Nguyen Christopher, et al. Magnetic resonance multitasking for motion-resolved quantitative cardiovascular imaging *Nature Biomedical Engineering* 2018; **2**(4):215-226.
- [25] Hamilton Jesse I., Jiang Yun, Chen Yong, et al. MR fingerprinting for rapid quantification of myocardial T1, T2, and proton spin density *Magnetic Resonance in Medicine* 2017; **77**(4):1446-1458.
- [26] Cruz G., Jaubert O., Botnar R.M., Prieto C.. Cardiac Magnetic Resonance Fingerprinting: Technical Developments and Initial Clinical Validation *Curr Cardiol Rep* 2019; **21**(9):91.
- [27] Shao Jiaxin, Zhou Ziwu, Nguyen Kim-Lien, Finn J. Paul, Hu Peng. Accurate, precise, simultaneous myocardial T1 and T2 mapping using a radial sequence with inversion recovery and T2 preparation *NMR in Biomedicine* 2019; **32**(11):e4165.
- [28] Qi Haikun, Bustin Aurelien, Cruz Gastao, et al. Free-running simultaneous myocardial T1/T2 mapping and cine imaging with 3D whole-heart coverage and isotropic spatial resolution *Magnetic Resonance Imaging* 2019; **63**:159 - 169.

- [29] Blume Ulrike, Lockie Timothy, Stehning Christian, et al. Interleaved T1 and T2 relaxation time mapping for cardiac applications *Journal of Magnetic Resonance Imaging* 2009; **29**(2):480-487.
- [30] Weingärtner Sebastian, Roujol Sébastien, Akçakaya Mehmet, Basha Tamer A., Nezafat Reza. Free-breathing multislice native myocardial T1 mapping using the slice-interleaved T1 (STONE) sequence *Magnetic Resonance in Medicine* 2015; **74**(1):115-124.
- [31] Ding Haiyan, Manuel Laura, Schär Michael, et al. Three-dimensional whole-heart T2 mapping at 3T *Magnetic Resonance in Medicine* 2015; **74**(3):803-816.
- [32] Santini Francesco, Kawel-Boehm N., Greiser A., Bremerich J., Bieri O.. Simultaneous T1 and T2 quantification of the myocardium using cardiac balanced-SSFP inversion recovery with interleaved sampling acquisition (CABIRIA) *Magnetic Resonance in Medicine* 2015; **74**(2):365-371.
- [33] Kvernby Sofia, Warntjes Marcel Jan Bertus, Haraldsson Henrik, Carlhäll Carl-Johan, Engvall Jan, Ebbers Tino. Simultaneous three-dimensional myocardial T1 and T2 mapping in one breath hold with 3D-QALAS *J Cardiovasc Magn Reson* 2014; **16**:102.
- [34] Guo Rui, Chen Zhensen, Herzka Daniel A., Luo Jianwen, Ding Haiyan. A three-dimensional free-breathing sequence for simultaneous myocardial T1 and T2 mapping *Magnetic Resonance in Medicine* 2019; **81**(2):1031-1043.
- [35] Fessler Jeffrey. Model-Based Image Reconstruction for MRI *IEEE signal processing magazine* 2010; **27**:81-89.
- [36] Mohsin Yasir Q., Lingala Sajan Goud, DiBella Edward, Jacob Mathews. Accelerated dynamic MRI using patch regularization for implicit motion compensation *Magnetic Resonance in Medicine* 2017; **77**(3):1238-1248.
- [37] Akçakaya Mehmet, Basha Tamer A., Weingärtner Sebastian, Roujol Sébastien, Berg Sophie, Nezafat Reza. Improved quantitative myocardial T2 mapping: Impact of the fitting model *Magnetic Resonance in Medicine* 2015; **74**(1):93-105.
- [38] Akçakaya Mehmet, Weingärtner Sebastian, Roujol Sébastien, Nezafat Reza. On the selection of sampling points for myocardial T1 mapping *Magnetic Resonance in Medicine* 2015; **73**(5):1741-1753.

PUBLICATION II

- [39] He Taigang, Gatehouse Peter D., Smith Gillian C., Mohiaddin Raad H., Pennell Dudley J., Firmin David N.. Myocardial T measurements in iron-overloaded thalassemia: An in vivo study to investigate optimal methods of quantification *Magnetic Resonance in Medicine* 2008; **60**(5):1082-1089.
- [40] Ogg R.J., Kingsley R.B., Taylor J.S.. WET, a T1- and B1-Insensitive Water-Suppression Method for in Vivo Localized ¹H NMR Spectroscopy *Journal of Magnetic Resonance, Series B* 1994; **104**(1):1 - 10.
- [41] Brittain Jean H., Hu Bob S., Wright Graham A., Meyer Craig H., Macovski Albert, Nishimura Dwight G.. Coronary Angiography with Magnetization-Prepared T2 Contrast *Magnetic Resonance in Medicine* 1995; **33**(5):689-696.
- [42] Nezafat Reza, Stuber Matthias, Ouwerkerk Ronald, Gharib Ahmed M., Desai Milind Y., Pettigrew Roderic I.. B1-insensitive T2 preparation for improved coronary magnetic resonance angiography at 3 T *Magnetic Resonance in Medicine* 2006; **55**(4):858-864.
- [43] Lustig Michael, Pauly John M.. SPIRiT: Iterative self-consistent parallel imaging reconstruction from arbitrary k-space *Magnetic Resonance in Medicine* 2010; **64**(2):457-471.
- [44] Yaman B., Weingärtner S., Kargas N., Sidiropoulos N. D., Akcakaya M.. Locally Low-Rank tensor regularization for high-resolution quantitative dynamic MRI in *2017 IEEE 7th International Workshop on Computational Advances in Multi-Sensor Adaptive Processing (CAMSAP)*:1-5 2017.
- [45] Moeller S., Weingärtner S., Akçakaya M.. Multi-scale locally low-rank noise reduction for high-resolution dynamic quantitative cardiac MRI in *2017 39th Annual International Conference of the IEEE Engineering in Medicine and Biology Society (EMBC)*:1473-1476 2017.
- [46] Zhang Tao, Pauly John M., Levesque Ives R.. Accelerating parameter mapping with a locally low rank constraint *Magnetic Resonance in Medicine* 2015; **73**(2):655-661.
- [47] Chow Kelvin, Flewitt Jacqueline A., Green Jordin D., Pagano Joseph J., Friedrich Matthias G., Thompson Richard B.. Saturation recovery single-shot acquisition (SASHA) for myocardial T1 mapping *Magnetic Resonance in Medicine* 2014; **71**(6):2082-2095.

- [48] Huang Teng-Yi, Liu Yi-Jui, Stemmer Alto, Poncelet Brigitte P.. T2 measurement of the human myocardium using a T2-prepared transient-state trueFISP sequence *Magnetic Resonance in Medicine* 2007; **57**(5):960-966.
- [49] Cerqueira Manuel D., Weissman Neil J., Dilsizian Vasken, et al. Standardized Myocardial Segmentation and Nomenclature for Tomographic Imaging of the Heart *Circulation* 2002; **105**(4):539-542.
- [50] Kellman P, Arai AE, Xue´ H.. T1 and extracellular volume mapping in the heart: estimation of error maps and the influence of noise on precision *J Cardiovasc Magn Reson* 2013; **15**(1):56.
- [51] Roy Clotilde, Slimani Alisson, Meester Christophe, et al. Age and sex corrected normal reference values of T1, T2 T2* and ECV in healthy subjects at 3T CMR *J Cardiovasc Magn Reson* 2017; **19**(72):1741-1753.
- [52] Kim PK, Hong YJ, Im DJ, et al. Myocardial T1 and T2 Mapping: Techniques and Clinical Applications *Korean J Radiol.* 2017; **18**(1):113-131.
- [53] Pons-Llado Guillem. Reference Normal Values for Myocardial T1 and T2 Maps with the MAGNETOM Vida 3T System and Case Examples form Clinical Practice *MAGNETOM Flash* 2019; **72**(1):29-33.
- [54] Heeswijk Ruud B., Piccini Davide, Feliciano Hélène, Hullin Roger, Schwitter Juerg, Stuber Matthias. Self-navigated isotropic three-dimensional cardiac T2 mapping *Magnetic Resonance in Medicine* 2015; **73**(4):1549-1554.
- [55] Qin Qin. Point spread functions of the T2 decay in k-space trajectories with long echo train *Magnetic Resonance Imaging* 2012; **30**(8):1134 - 1142.
- [56] Kritsaneepaiboon Supika, Ina Natee, Chotsampancharoen Thirachit, Roymanee Supaporn, Cheewatanakornkul Sirichai. The relationship between myocardial and hepatic T2 and T2* at 1.5T and 3T MRI in normal and iron-overloaded patients *Acta Radiologica* 2018; **59**(3):355-362.
- [57] Zaman Arshad, Higgins David M, Kouwenhoven Marc, Kidambi Ananth, Greenwood John P, Plein Sven. Robust myocardial T2 and T2* mapping at 3T *JCMR* 2012; **14**(P306).
- [58] Triadyaksa Pandji, Oudkerk Matthijs, Sijens Paul E.. Cardiac T2* mapping: Techniques and clinical applications *Journal of Magnetic Resonance Imaging* 2020; **n/a**(n/a).

PUBLICATION II

- [59] Sandino Christopher M, Kellman Peter, Arai Andrew E, Hansen Michael S, Xue Hui. Myocardial T2* mapping: influence of noise on accuracy and precision *J Cardiovasc Magn Reson* 2015; **17**:7.
- [60] Xu Jing, Zhuang Baiyan, Sirajuddin Arlene, et al. MRI T1 Mapping in Hypertrophic Cardiomyopathy: Evaluation in Patients Without Late Gadolinium Enhancement and Hemodynamic Obstruction *Radiology* 2020; **294**(2):275-286.
- [61] Ismail MTevfik F, Jabbour Andrew, Gulati Ankur, et al. Role of T1 and T2-mapping in assessing the myocardial interstitium in hypertrophic cardiomyopathy: a cardiovascular magnetic resonance study *J Cardiovasc Magn Reson* 2013; **15**(O32).
- [62] Gastl Mareike, Gotschy Alexander, von Spiczak Jochen, et al. Cardiovascular magnetic resonance T2* mapping for structural alterations in hypertrophic cardiomyopathy *European Journal of Radiology Open* 2019; **6**:78 - 84.
- [63] Reiter Ursula, Reiter Clemens, Kräuter Corina, Fuchsjäger Michael, Reiter Gert. Cardiac magnetic resonance T1 mapping. Part 2: Diagnostic potential and applications *European Journal of Radiology* 2018; **109**:235 - 247.
- [64] Zhou Ruixi, Huang Wei, Yang Yang, et al. Simple motion correction strategy reduces respiratory-induced motion artifacts for k-t accelerated and compressed-sensing cardiovascular magnetic resonance perfusion imaging *Journal of Cardiovascular Magnetic Resonance* 2018; **20**(1):23.
- [65] Weingärtner Sebastian, Moeller Steen, Schmitter Sebastian, et al. Simultaneous multislice imaging for native myocardial T1 mapping: Improved spatial coverage in a single breath-hold *Magnetic Resonance in Medicine* 2017; **78**(2):462-471.
- [66] Kellman Peter, Bandettini W Patricia, Mancini Christine, Hammer-Hansen Sophia, Hansen Michael S, Arai Andrew E. Characterization of myocardial T1-mapping bias caused by intramyocardial fat in inversion recovery and saturation recovery techniques *J Cardiovasc Magn Reson* 2015; **17**(33).
- [67] Rossi Giulia, Hilbert T., Mackowiak Adele LC, Pierzchała K., Kober T., Bastiaansen J.. Fat fraction mapping using bSSFP Signal Profile Asymmetries for Robust multi-Compartment Quantification (SPARCQ) *arXiv: Medical Physics* 2020; .
- [68] Milotta Giorgia, Bustin Aurelien, Jaubert Olivier, Neji Radhouene, Prieto Claudia, Botnar René M.. 3D whole-heart isotropic-resolution motion-compensated joint T1/T2 mapping and water/fat imaging *Magnetic Resonance in Medicine* 2020; **84**(6):3009-3026.

- [69] Jaubert Olivier, Cruz Gastão, Bustin Aurélien, et al. Water–fat Dixon cardiac magnetic resonance fingerprinting *Magnetic Resonance in Medicine* 2020; **83**(6):2107-2123.
- [70] Feng Li, Ma Dan, Liu Fang. Rapid MR relaxometry using deep learning: An overview of current techniques and emerging trends *NMR in Biomedicine* 2020; **n/a**(n/a):e4416.
- [71] Vidyullatha Pellakuri, Rao D.. Machine Learning Techniques on Multidimensional Curve Fitting Data Based on R- Square and Chi-Square Methods *International Journal of Electrical and Computer Engineering (IJECE)* 2016; **6**:974.
- [72] Lundervold Alexander Selvikvåg, Lundervold Arvid. An overview of deep learning in medical imaging focusing on MRI *Zeitschrift für Medizinische Physik* 2019; **29**(2):102 - 127. Special Issue: Deep Learning in Medical Physics.
- [73] Maier Andreas, Syben Christopher, Lasser Tobias, Riess Christian. A gentle introduction to deep learning in medical image processing *Zeitschrift für Medizinische Physik* 2019; **29**(2):86 - 101. Special Issue: Deep Learning in Medical Physics.
- [74] Weingärtner Sebastian, Akçakaya Mehmet, Berg Sophie, Kissinger Kraig V., Manning Warren J., Nezafat Reza. Heart-rate independent myocardial T1-mapping using combined saturation and inversion preparation pulses *J Cardiovasc Magn Reson* 2013; **15**(Suppl 1):P46.
- [75] Meßner N. M., Budjan J., Loßnitzer D., et al. Saturation-Recovery Myocardial T1-Mapping during Systole: Accurate and Robust Quantification in the Presence of Arrhythmia *Scientific reports* 2018; **8**(1):5251.

Magnetic Resonance Fingerprinting for simultaneous renal T_1 and T_2^* mapping in a single breath-hold

Ingo Hermann, Jorge Chacón-Caldera, Irène Brumer, Benedikt Rieger, Sebastian Weingärtner, Lothar Schad and Frank Zöllner

MAGN RESON MED. 2020; 83: 1940-1948

Abstract

Purpose: To evaluate the use of magnetic resonance fingerprinting (MRF) for simultaneous quantification of T_1 and T_2^* in a single breath-hold in the kidneys.

Methods: The proposed kidney MRF sequence was based on MRF echo-planar imaging (EPI). 35 measurements per slice and overall 4 slices were measured in 15.4 seconds. Group matching was performed for in-line quantification of T_1 and T_2^* . Images were acquired in a phantom and eight healthy volunteers in coronal orientation. To evaluate our approach region of interests were drawn in the kidneys to calculate mean values and standard deviations of the T_1 and T_2^* times. Precision was calculated across multiple repeated MRF scans. Gaussian filtering is applied on baseline images to improve SNR and match stability.

Results: T_1 and T_2^* times acquired with MRF in the phantom showed good agreement with reference measurements and conventional mapping methods with deviations of less than 5% for T_1 and less than 10% for T_2^* . Baseline images in vivo were free of artifacts and relaxation times yielded good agreement with conventional methods and literature (deviation T_1 : $7 \pm 4\%$, T_2^* : $6 \pm 3\%$).

Conclusion: In this feasibility study, the proposed renal MRF sequence resulted in accurate T_1 and T_2^* quantification in a single-breath hold.

1 Introduction

Magnetic Resonance Fingerprinting (MRF) is a promising method to quantify multiple tissue properties in a single, time-efficient acquisition. Imaging of the relaxation times T_1 , T_2 , T_2^* has been achieved simultaneously with different acquisition and readout schemes. Its application is increasingly gaining clinical relevance [1, 2, 3, 4, 5, 6, 7]. In MRF unique fingerprints are generated by a pseudo-random pulse design with varying flip angles, echo (TE) and repetition times (TR) to generate different sets of contrast weightings. These are matched with pre-computed dictionaries containing all relevant combinations of physiological tissue parameters.

The original MRF sequence was based on a steady-state free precession (SSFP) readout with highly undersampled spiral k-space readout and remains the most commonly used approach. Recently, an alternative MRF acquisition was proposed based on a Cartesian echo planar imaging readout [8]. Compared to conventional MRF, MRF-EPI affords increased robustness against system imperfections at the trade-off against a reduced number of baseline images. Furthermore, interpretable baseline images in MRF-EPI allow monitoring for patient specific artifacts or motion during the acquisition and facilitates clinical robustness. In-line reconstruction on the scanner with a fast group matching algorithm [9] allows the integration into clinical workflow.

MRF has become a widely available for neuroimaging but application to abdominal imaging is limited [10]. Especially MRF is rarely used for renal imaging.

Chronic kidney disease affects around 10% of the world population and is induced by pathological changes such as inflammation, fibrosis and oedema. These process were shown to increase T_1 [11] and, hence, quantitative renal imaging is clinically relevant for detecting a spectrum of pathologies [12, 13, 14, 15]. Changes in oxygen supply can be visualized in the blood oxygenation level-dependent (BOLD) effect, which correlates with T_2^* , and has been observed to decrease in CKD and kidney transplants [16, 17, 18, 19].

The most commonly used method for renal T_1 mapping is the modified Look-Locker inversion recovery (MOLLI) [20, 21, 11] which is based on an inversion recovery pulse followed by several imaging readouts. However, the repeated imaging acquisitions disturb the longitudinal magnetization recovery and compromise acquisition accuracy [22]. The gold standard technique for T_2^* quantification is multiple gradient echo (multi GRE) [23, 24, 25].

Conventional MRI scans suffer from long acquisition times. Ding et al. have previously demonstrated the clinical value of simultaneous T_1 and T_2^* estimation [26]. Their technique was based on EPI readout with inversion recovery (IR) preparation for T_1 and a

saturation pulse followed by multiple GRE acquisitions for T_2^* quantification. Nevertheless, the low resolution and the long acquisition time for one slice is outperformed by MOLLI and multi GRE. Especially, measuring multiple slices in multiple breath-holds increases the measurement time substantially as 10 to 30 seconds pauses are required between breath-holds. However, MOLLI underestimates the T_1 times as well-known from factors such as magnetization transfer [27] and multi GRE measurements may overestimate T_2^* for long echo times at 3T [28].

In this study, we aim to implement a MRF sequence based on an EPI readout to estimate T_1 and T_2^* times in the entire kidneys in a single breath-hold. Phantom measurements are performed to validate the accuracy and precision of the T_1 and T_2^* quantification for 4 slices and to optimize scan-time efficiency. Whole kidney in vivo MRF maps are acquired and compared to the gold standard methods MOLLI and multi GRE to study the feasibility.

2 Methods

Sequence parameters

All measurements were performed on a 3T MRI scanner (Magnetom Skyra; Siemens Healthineers, Erlangen, Germany) with a 28-channel receiver coil array and shared the following common imaging parameters: FOV = $380 \times 380 \text{ mm}^2$, matrix size (base resolution) = 256×256 ($1.5 \times 1.5 \text{ mm}^2$), slice thickness = 5 mm. The proposed MRF method was based on [8] with the following specific parameters: bandwidth = 1148 Hz/px, GRAPPA-factor 3 with 36 calibration lines, partial Fourier 5/8, fat saturation and varying flip angle α ($17\text{-}43^\circ$), TE (16-76.5 ms), TR (383-625 ms) as shown in Fig. 1. TE and TR are depicted as the same line (gray) because they are proportional to each other, only minimal and maximal values are different. Additionally, T_1 maps were generated using a 5(3s)3 MOLLI [29] scheme with the same common parameters and bandwidth = 1085 Hz/px, GRAPPA-factor 2, partial Fourier 6/8 and flip angle 35° . T_2^* maps were generated using a multi GRE sequence with the same common parameter and bandwidth = 390 Hz/px, GRAPPA-factor 2, partial Fourier 6/8 and flip angle 18° with 12 different TEs varying from 1.7-40 ms.

Dictionary

The dictionaries were generated by Bloch simulations off-line using MATLAB (The MathWorks; Natick, MA). The evolution of the magnetization was simulated with B_1^+ compensation by a scaling factor for the excitation flip angles [2] and pattern matching is performed using the magnitude data. A Group matching algorithm was implemented

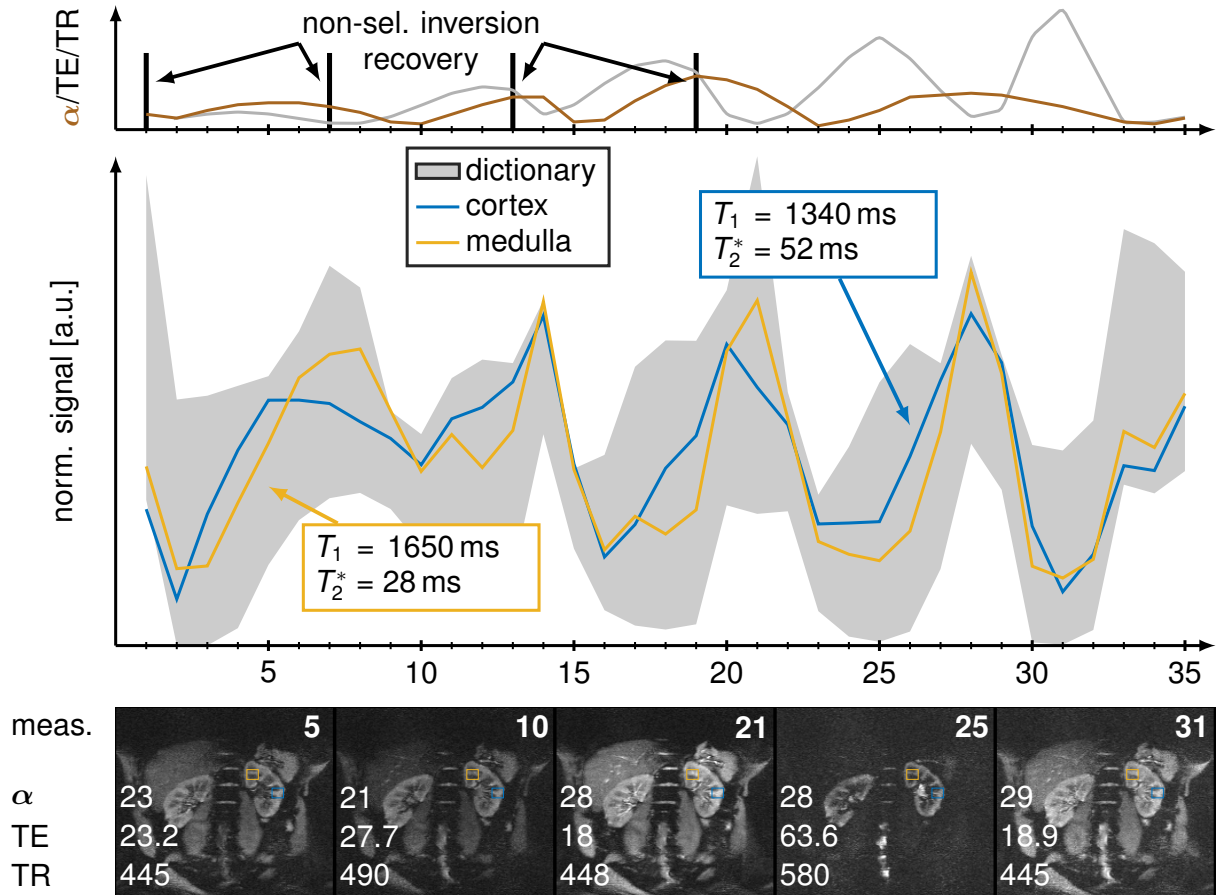


Figure 1: Evolution of the measured signal for all 35 measurements. On top the varying α ($17-43^\circ$), TE (16-76.5 ms), TR (383-625 ms) and the inversion pulses are depicted. TE and TR are depicted as the same line because their trend is proportional ($TR = 4 \cdot TE + const.$) and just minimal and maximal values differ. The evolution curve of the renal cortex (blue) and the renal medulla (yellow) is shown with its corresponding T_1 and T_2^* times for one exemplary measurement. All entries of the full dictionary are depicted as gray area. Baseline images on the bottom show different weightings for several α , TE and TR along the evolution curve.

based on the method by Cauley et al. [30] where the full dictionary is divided into multiple small dictionaries. The mean value of all small dictionaries is written in an additional look up table (LUT). The measured signal is matched with the LUT containing the mean values and the best matching groups are chosen to fully correlate with the measured signal. The best matching groups were precomputed by correlating the LUT containing the mean values with itself and sorted by the correlation values. For every group the sorted best matching groups were written in an additional LUT. The full dictionary was splitted into 4682 smaller dictionaries (groups) containing 15 entries each. 200 of these groups were used to match the pixelwise signal which were preselected by the LUT containing the mean of every group. The full dictionaries consisted of 70,236 entries with T_1 ranging from 100-3500 ms, T_2^* from 10-2000 ms with increasing step size and

flip angle efficiency (B_1^+) from 0.7-1.2 with a step size of 0.1. All entries with $T_1 < T_2^*$ were discarded. The calculation of the dictionary took less than 10 minutes. Parameter maps were reconstructed in-line on the scanner [9]. Inversion pulses were assumed to be ideal (180°) with no T_2^* decay during the pulse. Multi-threading was used to simultaneously match multiple slices at the same time for efficient post-processing.

Phantom experiments

Phantom measurements were performed to evaluate accuracy and precision of the MRF sequence compared to references measurements. Inversion-recovery turbo spin echo was performed for T_1 quantification with TI = 100, 200, 500, 1000, 2000, 3000, 5000, 10000 ms, TE/TR = 12/10000 ms, turbo factor = 16, FOV = 320×320 mm², matrix size (base resolution) = 256×256 (1.3×1.3 mm²), slice thickness = 5 mm, bandwidth = 1085 Hz/px. Multi GRE was performed for T_2^* quantification with 28 contrasts within TE = 2-50 ms, FOV = 320×320 mm², matrix size (base resolution) = 256×256 (1.3×1.3 mm), slice thickness = 5 mm, bandwidth = 390 Hz/px. MRF was performed with the common sequence parameters. 100 baseline images with different contrast weighting were acquired to calculate the parameter maps yielded by an increasing amount of measurements to study the convergence of the parametric maps. Hereby, the scheme of varying flip angles, TE and TR is repeated after every 35 measurements. The MRF maps were acquired 10 times for studying precision and reproducibility compared to MOLLI and multi GRE and reference IR and GRE. Precision was calculated by taking the standard deviation of the difference of every measurement to their mean. The phantom consisting of tubes was generated using 12 different mixtures of water, agarose and NiCl₂ as recommended by Captur et al. [31]. The whole phantom was submerged in water to reduce susceptibility artifacts.

In vivo experiments

In vivo measurements were performed in 8 healthy volunteers (6 male, 22-33 years old) to study the feasibility compared to commonly used methods as MOLLI for T_1 and multi GRE for T_2^* quantification. All breath-holds were performed in end-expiration. MRF, MOLLI and multi GRE were performed using the parameters as described in the previous section. Coronal slices were chosen as imaging planes.

Medulla and cortex were semi-automatically segmented using MATLAB (The MathWorks; Natick, MA). T_1 and T_2^* mean and standard deviations were calculated for all slices in the medulla and the cortex and all MRF measurements were registered using a 2D affine transformation using MATLAB (The MathWorks; Natick, MA). Ten MRF scans were performed to analyze precision of the measurements. Gaussian smoothing was performed on MRF baseline images to improve the matching process and therefore

the parameter map quality. The Gaussian filter was implemented in-line on the scanner before the group matching. For this, the magnitude images were convolved with a Gaussian filter $G(i, j)$ with kernel size $n = 5$ as follows:

$$G_{i,j} = \frac{1}{2\pi\sigma^2} \cdot \exp\left(-\frac{i^2 + j^2}{2\sigma^2}\right) \quad (1)$$

and the convolution in image space

$$I^*(x, y) = \sum_{i=1}^n \sum_{j=1}^n I\left(x - i + \frac{n-1}{2}, y - j + \frac{n-1}{2}\right) G(i, j) \quad (2)$$

with I^* the filtered pixel, I the image pixel, σ^2 the variance.

3 Results

3.1 Phantom

Figure 2 shows the evolution of the matched T_1 and T_2^* times for the match process with an increasing amount of measurements for 3 different tubes. More than 20 measurements were needed for convergence of T_1 and T_2^* . Thus, 35 measurements were used as a standard for the MRF acquisition. Deviations in T_1 and T_2^* times of less than 5% and 10% were achieved which are comparable to MOLLI and multi GRE. Standard deviations for T_2^* were lower than for multi GRE. Scan time was reduced by a factor of 8 for the 4 slices compared to MOLLI and multi GRE (8 measurements) considering 1 MRF acquisition providing both parameter maps with similar accuracy and precision in a phantom. Figure 3 depicts the T_1 and T_2^* map for MRF, MOLLI/multi GRE and the reference IR and GRE of one representative slice.

Figure 4 shows in the top panel (a,c) the measured T_1 plotted against the reference T_1 for MRF (blue) and MOLLI (yellow) in (a), and the measured T_2^* for MRF (blue) and multi GRE (orange) to the reference T_2^* in (c). Reference IR and GRE are depicted as a black line and the gray area illustrates 5% deviation to the reference. MRF T_1 times show less than 5% deviation compared to the reference. T_2^* deviations vary between 4% and 10%. The corresponding Bland-Altman plots are shown in the bottom panel (b,d). MRF yields higher standard deviations than MOLLI between 25 ms for small T_1 and up to 75 ms for higher T_1 times, whereas MOLLI has standard deviations less than 40 ms for all T_1 times. On the right panel (d), MRF T_2^* times show smaller deviations than multi GRE with maximum standard deviations of less than 10 ms, whereas multi GRE shows standard deviations up to 15 ms.

Reproducibility and precision was evaluated by measuring the MRF sequence 10 times. Interscan variability for T_1 was less than 10 ms and for T_2^* less than 1.5 ms for all slices.

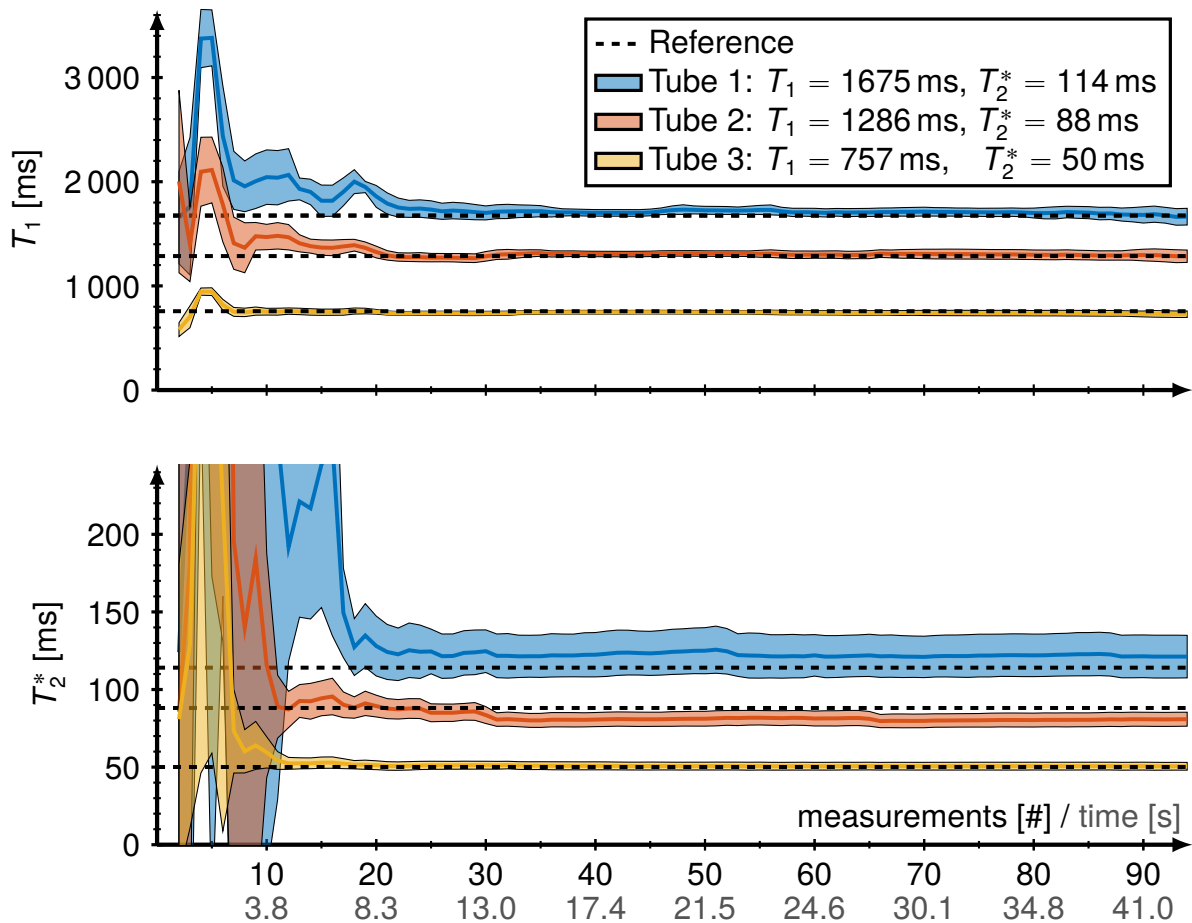


Figure 2: Convergence of the matched T_1 and T_2^* parameters for increasing measurements. 3 different tubes are depicted with high (blue), medium (orange) and small (yellow) T_1 and T_2^* values. For more than 20 measurements the matching converges to the reference value. The colored shaded areas show the standard deviations of the corresponding matched relaxation times.

3.2 In vivo

Figure 5 shows representative T_1 and T_2^* maps of 4 slices for one volunteer compared to the reference MOLLI and multi GRE in coronal slice. Standard deviations of the T_2^* maps were similar compared to multi GRE but MRF showed consistent higher T_2^* values. Mean MRF T_2^* times were $35.2 \text{ ms} \pm 5.6 \text{ ms}$ and multi GRE times were $30.3 \text{ ms} \pm 6.4 \text{ ms}$ in the medulla and $54.7 \text{ ms} \pm 7.8 \text{ ms}$ and $50.4 \text{ ms} \pm 7.2 \text{ ms}$ in the cortex. MRF T_1 times showed higher standard deviations and similar mean values compared to MOLLI. In the medulla mean MRF T_1 times were $1921 \text{ ms} \pm 182 \text{ ms}$ and for MOLLI $1950 \text{ ms} \pm 146 \text{ ms}$ and in the cortex mean MRF T_1 times were $1456 \text{ ms} \pm 126 \text{ ms}$ and for MOLLI $1432 \text{ ms} \pm 81 \text{ ms}$.

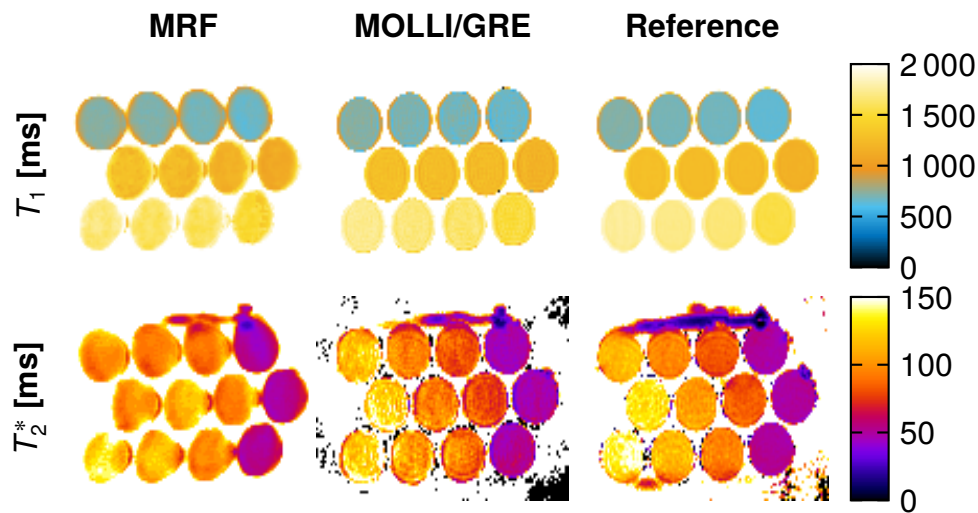


Figure 3: Representative quantitative T_1 (top) and T_2^* (bottom) maps in the phantom with 12 tubes. MRF on the left side, MOLLI/multi GRE in the middle and the reference IR and GRE on the right side.

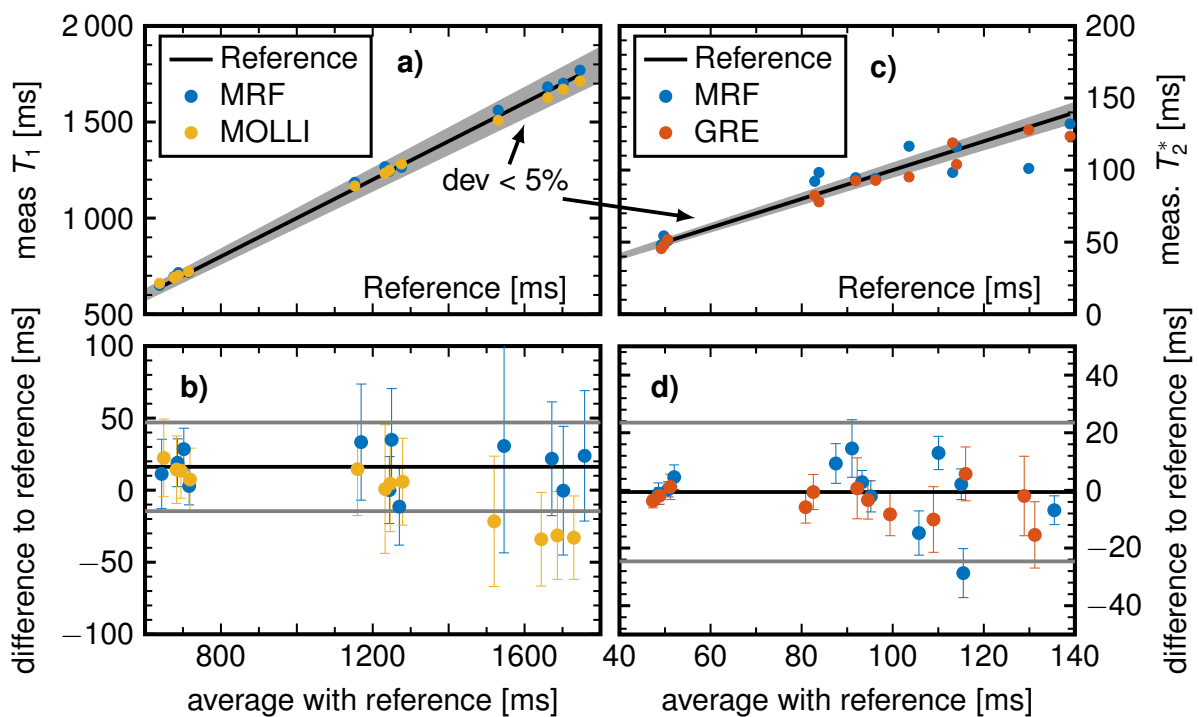


Figure 4: Comparison of T_1 on the left side (a) and T_2^* on the right side (c) between MRF (blue) compared to reference (black), MOLLI (yellow) and multi GRE (orange). The gray area limits 5% deviation to the reference. The bottom panel shows the Bland-Altman plot for T_1 (b) and T_2^* (d). The difference from MRF, MOLLI and multi GRE to the reference methods is shown with the corresponding standard deviations. The gray line limits the area of 2 standard deviations.

In vivo precision of T_1 acquired with MRF was 31 ms in the medulla and 65 ms in the cortex. Precision of T_2^* in the medulla was 1.4 ms and 1.8 ms in the cortex .

Ghosting artifact were alleviated using large FOV acquisitions and scan time was 15.4 seconds within one breath-hold. Online reconstruction on the scanner took less than 30 seconds.

Figure 6 shows the influence of Gaussian filtering on the correlation value, T_1 and T_2^* maps. As an example, a subject with noisy baseline images is shown. A fair compromise between sharp contours and edges and reduction of noise was obtained for $\sigma = 0.7$ which is shown in Fig. 7 where the correlation value, T_1 and T_2^* with respect to the variance of the smoothing filter are depicted. The correlation values in the cortex were greater than 0.99 for $\sigma = 0.7$ and greater than 0.97 for $\sigma = 0$. On the bottom panel the corresponding correlation value, T_1 and T_2^* is depicted over the variance for the cortex (blue) and the medulla (yellow). The standard deviation decreases for increasing variance of the Gaussian filter without changing the mean value of T_1 and T_2^* .

4 Discussion

This study demonstrates the feasibility of using an EPI-based MRF method to quantify the T_1 and T_2^* times in the kidneys covering 4 slices within one breath-hold. In phantom, good accuracy and precision was achieved with standard deviations comparable to MOLLI and multi GRE as shown in previous publications [8]. MRF yielded accurate results for all T_1 times, whereas MOLLI lacks accuracy for long T_1 times due to magnetization transfer [27]. Fast and stable convergence of the parameter maps were achieved for increasing number of measurements. MRF using 35 measurements was a good compromise between scan time and parameter map quality. The shapes of the tubes were distorted by the EPI echo train due to inhomogeneities in B_0 and eddy currents, which induce inaccuracies in gradient amplitudes [32, 33].

In vivo scans yielded reproducible and accurate parameter maps comparable with MOLLI and multi GRE with slightly overestimated T_1 and T_2^* times and higher standard deviations than MOLLI. T_2^* map quality was similar to multi GRE. T_1 times showed larger inter-subject variation and medulla T_1 MOLLI and MRF values were higher than in the literature [11, 15].

Quantitative diagnosis, requires a clear separation of diseased and healthy kidneys. Sensitivity is thus determined by the underlying pathological alteration and the precision of the measurement technique. Major variations are observed in diseased kidneys (CKD) by increased T_1 times of over 150 ms (10%) in the cortex, but just around 50 ms

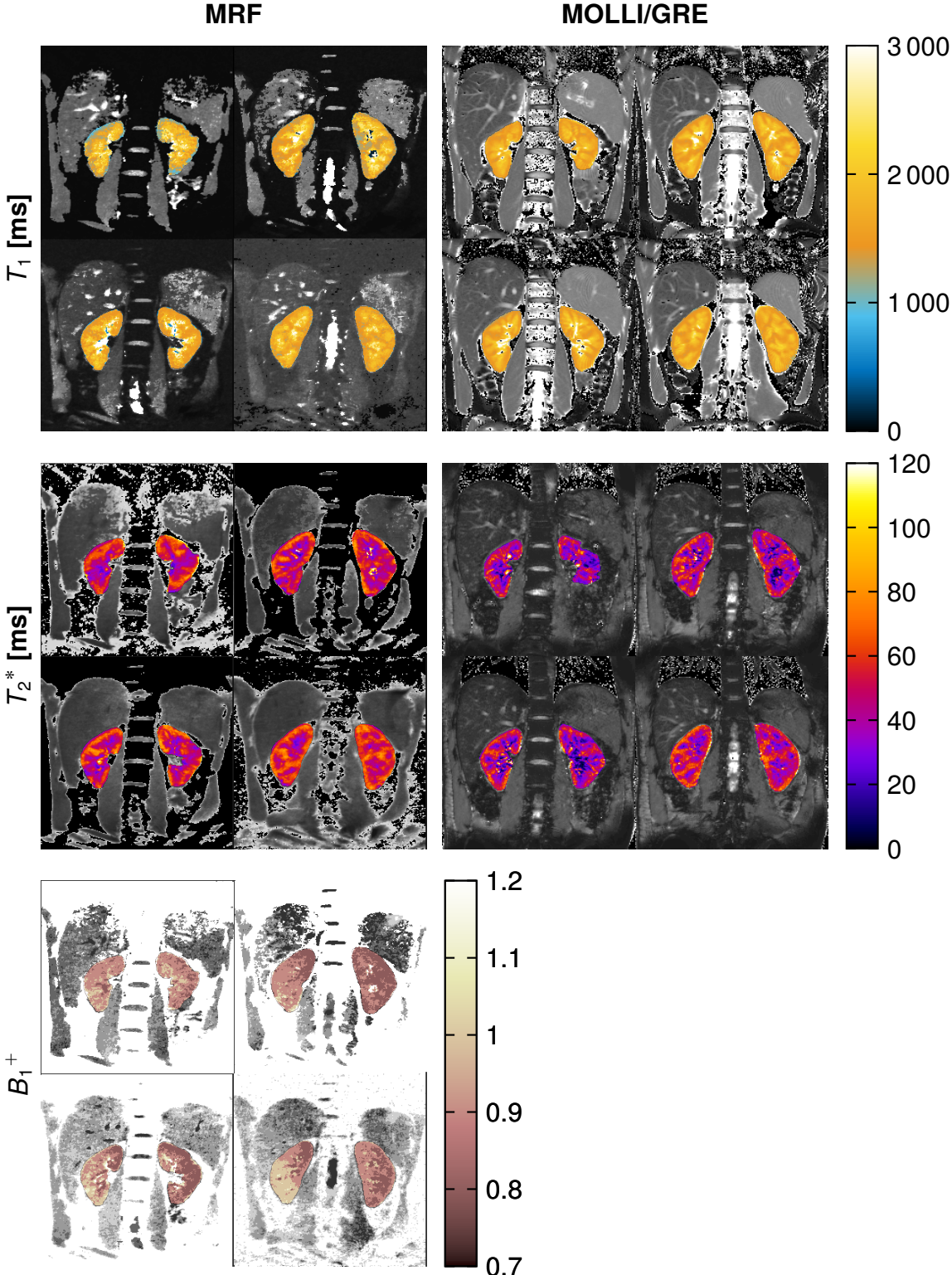


Figure 5: Exemplary baselines image, T_1 , T_2^* and B_1^+ maps for 4 slice of the MRF, MOLLI and multi GRE in the kidneys in coronal view.

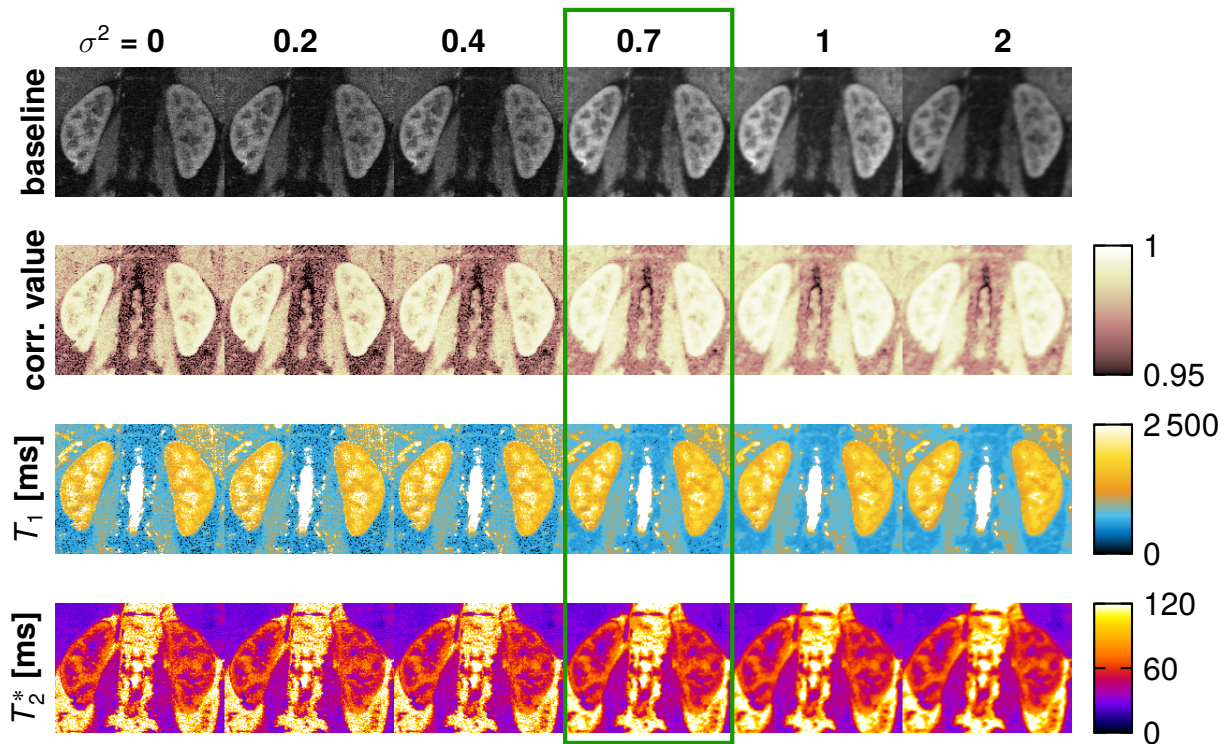


Figure 6: Top panel shows the baseline images with different variances of the Gaussian filter with a kernel size equal to 5. Correlation maps depict the matrix multiplication of the matching process which should be equal to 1 for a perfect match. T_1 and T_2^* maps are depicted to visualize the effect for different variances on the baseline images.

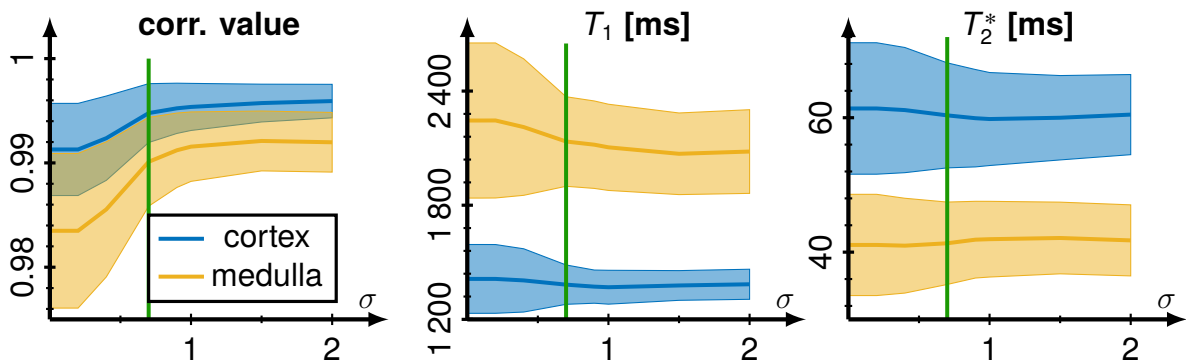


Figure 7: The correlation values, T_1 and T_2^* times are illustrated for the cortex (blue) and the medulla (yellow) for increasing variance. The shaded area depicts the corresponding standard deviation. The green lines mark the chosen noise setting.

(5%) in the medulla and increased T_2^* times of around 3-5 ms (10%) in the medulla and cortex [15]. Therefore, with the precision of the MRF parametric maps of around 30 ms for T_1 and less than 2 ms of T_2^* we assume that it is possible to identify pathological changes induced by CKD with our proposed method.

We based our sequence of the EPI-MRF as fully sampled baseline images which is ben-

eficial in clinical routines. This and the fast group match reconstruction in-line on the scanner enables the possibility to change imaging parameters such as the FOV during the clinical workflow based on patient size and position to overcome ghosting artifacts. Compared to conventional MRF methods using unbalanced SSFP sequences, our MRF method was resilient to banding artifacts and incomplete gradient refocusing [34, 35]. However, rapid acquisitions require a trade-off against noise-resilience. Therefore, we analysed the impact of Gaussian filtering on the baseline images. This improved the image quality of the T_1 and T_2^* maps and reduced the standard deviation without changing the mean value. The correlation value of every pixel was increased meaning that the matching process is more accurate.

MRF EPI has the draw back of potential motion during the readout, therefore complete baseline images can be used easily for motion correction in post-processing. Slice-tracking based on navigators can be used to port the method to free-breathing and is subject of future research.

The image quality of the MRF parameter maps is highly dependent on the image quality of the baseline images. Therefore, improving the EPI baseline image quality was shown to improve the MRF map quality. Reduction of ghosting artifacts [36, 37], Nyquist artifact [38, 39] and motion correction [40] were recently published, which all have the potential to improve the image quality of the proposed MRF method. Despite advanced shimming, field inhomogeneities disturb the k-space echo train and therefore lead to geometric distortions [41, 42]. Gain in SNR could be achieved by using a 3D EPI readout when imaging with high resolution at the cost of increasing minimal TE [43, 44].

Novel MRF reconstruction methods including deep learning can be used for accelerating the reconstruction and obtain more stable matching progress [45, 46, 47, 48, 49]. Optimizing the pulse sequence by a better choice of the flip angle, TE and TR may further decrease the noise as published recently [50].

This study has some limitations. Despite the nominally high spatial resolution, the effective resolution is lower due to the use of Gaussian filtering. The Siemens scanner treats the missing k-space lines by zero filling. Additionally, without using 5/8 partial Fourier, the maps are worse due to the longer TE. For this kidney MRF sequence, it was essential to push the TE as short as possible to overcome blurring. However, 5/8 partial Fourier reduces the lines in k-space and therefore further widens the point spread function. Susceptibility artifacts due to the air in the lung disturb the parametric MRF maps compared to the reference methods, which is widely known as EPI distortion. Therefore, distortion correction may improve the image quality [51, 52].

A small number of volunteers were measured with relatively low fat content and all young in age. Higher fat content and incorrect breath-hold will significantly reduce the SNR.

Larger cohorts in different age groups and patients with CKD or kidney transplants are needed to further evaluate the proposed sequence and to implement the kidney MRF in the clinical routine.

5 Conclusions

In this study we have shown the feasibility of an EPI-MRF sequence for simultaneous quantification of T_1 and T_2^* in the kidneys during a single breath-hold using 4 slices. Using single shot imaging and in-line reconstruction on the scanner system enables to monitor the baseline images while scanning to correct for patient specific artifacts in clinical work flow.

6 Acknowledgments

This article is based upon work from COST Action Magnetic Resonance Imaging Biomarkers for Chronic Kidney Disease (PARENCHIMA), funded by COST (European Cooperation in Science and Technology). www.cost.eu. For additional information please visit PARENCHIMA project website: www.renal.mri.org. This research project is partly supported of the Research Campus M2OLIE funded by the German Federal Ministry of Education and Research (BMBF) within the Framework “Forschungscampus: public-private partnership for Innovations” under the funding code 13GW0388A.

References

- [1] Ma Dan, Gulani Vikas, Seiberlich Nicole, et al. Magnetic resonance fingerprinting *Nature* 2013; **495**:187–192.
- [2] Rieger Benedikt, Zimmer Fabian, Zapp Jascha, Weingärtner Sebastian, Schad Lothar R.. Magnetic resonance fingerprinting using echo-planar imaging: Joint quantification of T1 and relaxation times *Magn Reson Med* 2016; **78**(5):1724-1733.
- [3] Khajehim Mahdi, Christen Thomas, Chen J. Jean. Magnetic Resonance Fingerprinting with Combined Gradient- and Spin-echo Echo-planar Imaging: Simultaneous Estimation of T1, T2 and T2* with integrated-B1 Correction *bioRxiv* 2019; **in process, doi = 10.1101/604546**.
- [4] Wang Charlie Yi, Coppo Simone, Mehta Bhairav Bipin, Seiberlich Nicole, Yu Xin, Griswold Mark Alan. Magnetic resonance fingerprinting with quadratic RF phase for measurement of T2* simultaneously with δf , T1, and T2 *Magn Reson Med* 2019; **81**(3):1849-1862.
- [5] Wyatt Cory R., Smith Travis B., Sammi Manoj K., Rooney William D., Guimaraes Alexander R.. Multi-parametric T2* magnetic resonance fingerprinting using variable echo times *NMR in Biomedicine* 2018; **31**(9):e3951.
- [6] Hamilton Jesse I., Jiang Yun, Chen Yong, et al. MR fingerprinting for rapid quantification of myocardial T1, T2, and proton spin density *Magn Reson Med* 2017; **77**(4):1446-1458.
- [7] Panda Ananya, Mehta Bhairav B., Coppo Simone, et al. Magnetic resonance fingerprinting – An overview *Curr Opin Biomed Eng* 2017; **3**:56 - 66.
- [8] Rieger Benedikt, Akçakaya Mehmet, Pariente José C., et al. Time efficient whole-brain coverage with MR Fingerprinting using slice-interleaved echo-planar-imaging *Sci Rep* 2018; **8**(1):2045-2322.
- [9] Hermann Ingo, Rieger Benedikt, Zapp Jascha, Weingärtner Sebastian, Schad Lothar R.. Optimized fast dictionary matching for magnetic resonance fingerprinting based on echo-planar imaging for enhanced clinical workflow *Proceedings from the 27th Annual Meeting ISMRM, Montreal, QC, Canada* 2019; :4529.
- [10] Chen Yong, Jiang Yun, Pahwa Shivani, et al. MR Fingerprinting for Rapid Quantitative Abdominal Imaging *Radiology* 2016; **279**(1):278-286.

- [11] Wolf Marcos, Boer Anneloes, Sharma Kanishka, et al. Magnetic resonance imaging T1- and T2-mapping to assess renal structure and function: a systematic review and statement paper *Nephrol Dial Transplant* 2018; **33**(2):ii41-ii50.
- [12] Schley Gunnar, Jordan Jutta, Ellmann Stephan, et al. Multiparametric magnetic resonance imaging of experimental chronic kidney disease: A quantitative correlation study with histology *PLOS ONE* 2018; **13**(7):1-18.
- [13] Thurman Joshua, Gueler Faikah. Recent advances in renal imaging *F1000 Research* 2018; **7**(F1000):278-286.
- [14] Villa Giulia, Ringgaard Steffen, Hermann Ingo, et al. Phase-contrast magnetic resonance imaging to assess renal perfusion: a systematic review and statement paper *MAGMA* 2019; **in process**, doi = [10.1007/s10334-019-00772-0](https://doi.org/10.1007/s10334-019-00772-0).
- [15] Cox Eleanor F., Buchanan Charlotte E., Bradley Christopher R., et al. Multiparametric Renal Magnetic Resonance Imaging: Validation, Interventions, and Alterations in Chronic Kidney Disease *Front Physiol* 2017; **8**:696.
- [16] Milani Bastien, Ansaloni Annalisa, Sousa-Guimaraes Sofia, et al. Reduction of cortical oxygenation in chronic kidney disease: evidence obtained with a new analysis method of blood oxygenation level-dependent magnetic resonance imaging *Nephrol Dial Transplant* 2016; **32**(12):2097-2105.
- [17] Burnier Michel, Pruijm Menno, Mendichovszky Iosif A, et al. Renal blood oxygenation level-dependent magnetic resonance imaging to measure renal tissue oxygenation: a statement paper and systematic review *Nephrol Dial Transplant* 2018; **33**(suppl 2):ii22-ii28.
- [18] Hedgire Sandeep S, McDermott Shaunagh, Wojtkiewicz Gregory R, Abtahi Seyed Mahdi, Harisinghani Mukesh, Gaglia Jason L. Evaluation of renal quantitative T2* changes on MRI following administration of ferumoxytol as a T2* contrast agent. *Int. J. Nanomed* 2014; **9**:2101-2207.
- [19] Nissen Johanna C., Mie Moritz B., Zöllner Frank G., Haneder Stefan, Schoenberg Stefan O., Michaely Henrik J.. Blood oxygenation level dependent (BOLD) – Bildgebung der Nieren: Konzepte und Anwendungen *Z Med Phys* 2010; **20**(2):88 - 100.
- [20] Look David C, Locker D R. Time Saving in Measurement of NMR and EPR Relaxation Times *Rev Sci Instrum* 1970; **41**(2):250-251.

PUBLICATION III

- [21] Messroghli Daniel R., Radjenovic Aleksandra, Kozerke Sebastian, Higgins David M., Sivananthan Mohan U., Ridgway John P.. Modified Look-Locker inversion recovery (MOLLI) for high-resolution T1 mapping of the heart *Magn Reson Med* 2004; **52**(1):141–146.
- [22] Radenkovic Dina, Weingärtner Sebastian, Ricketts Lewis, Moon James C., Captur Gabriella. T1 mapping in cardiac MRI *Heart Failure Reviews* 2017; **22**(4):415-430.
- [23] Pedersen Michael, Dissing Thomas H., Merkenborg J.A.N., et al. Validation of quantitative BOLD MRI measurements in kidney: Application to unilateral ureteral obstruction *Kidney Int* 2005; **67**(6):2305 - 2312.
- [24] Thacker Jon M., Li Lu-Ping, Li Wei, Zhou Ying, Sprague Stuart M., Prasad Potumarthi V.. Reduction of cortical oxygenation in chronic kidney disease: evidence obtained with a new analysis method of blood oxygenation level-dependent magnetic resonance imaging *Nephrol Dial Transplant* 2015; **50**(12):821-827.
- [25] Pruijm Menno, Mendichovszky Iosif A, Liss Per, et al. Renal blood oxygenation level-dependent magnetic resonance imaging to measure renal tissue oxygenation: a statement paper and systematic review *Nephrol Dial Transplant* 2018; **33**(suppl2):ii22-ii28.
- [26] Ding Yao, Mason Ralph P., McColl Roderick W., et al. Simultaneous measurement of tissue oxygen level-dependent (TOLD) and blood oxygenation level-dependent (BOLD) effects in abdominal tissue oxygenation level studies *J Magn Reson* 2013; **38**(5):1230-1236.
- [27] Kellman Peter, Hansen Michael S.. T1-mapping in the heart: accuracy and precision *Magn Reson Med* 2014; **16**(2).
- [28] Panek Rafal, Welsh Liam, Dunlop Alex, et al. Repeatability and sensitivity of measurements in patients with head and neck squamous cell carcinoma at 3T *J Magn Reson* 2016; **44**(1):72-80.
- [29] Kellman Peter, Wilson Joel R., Xue Hui, Ugander Martin, Arai Andrew E.. Extracellular volume fraction mapping in the myocardium, part 1: evaluation of an automated method *J Cardiovasc Magn Reson* 2012; **14**(1):63.
- [30] Cauley Stephen F., Setsompop Kawin, Ma Dan, et al. Fast group matching for MR fingerprinting reconstruction *Magn Reson Med* 2015; **74**(2):523-528.

- [31] Captur Gabriella, Gatehouse Peter, Keenan Kathryn E., et al. A medical device-grade T1 and ECV phantom for global T1 mapping quality assurance - the T1 Mapping and ECV Standardization in cardiovascular magnetic resonance (T1MES) program *J Cardiovasc Magn Reson* 2016; **18**(1):58.
- [32] Chen Nan-kuei, Wyrwicz Alice M.. Correction for EPI distortions using multi-echo gradient-echo imaging *Magn Reson Med* 1999; **41**(6):1206-1213.
- [33] Tsao Jeffrey. Ultrafast imaging: Principles, pitfalls, solutions, and applications *J Magn Reson* 2010; **32**(2):252-266.
- [34] Jiang Yun, Ma Dan, Seiberlich Nicole, Gulani Vikas, Griswold Mark A.. MR fingerprinting using fast imaging with steady state precession (FISP) with spiral readout *Magn Reson Med* 2015; **74**(6):1621-1631.
- [35] Barnet Christoph, Zanche Nicola De, Pruessmann Klaas P.. Spatiotemporal magnetic field monitoring for MR *Magn Reson Med* 2008; **60**(1):187-197.
- [36] Ianni Julianna D., Welch E. Brian, Grissom William A.. Ghost reduction in echo-planar imaging by joint reconstruction of images and line-to-line delays and phase errors *Magn Reson Med* 2018; **79**(6):3114-3121.
- [37] Kim Yoon-Chul, Nielsen Jon-Fredrik, Nayak Krishna S.. Automatic correction of echo-planar imaging (EPI) ghosting artifacts in real-time interactive cardiac MRI using sensitivity encoding *J Magn Reson* 2008; **27**(1):239-245.
- [38] Chang Hing-Chiu, Chen Nan-Kuei. Joint correction of Nyquist artifact and minuscule motion-induced aliasing artifact in interleaved diffusion weighted EPI data using a composite two-dimensional phase correction procedure *Magn Reson Imaging* 2016; **34**(7):974 - 979.
- [39] Xie Victor B., Lyu Mengye, Liu Yilong, Feng Yanqiu, Wu Ed X.. Robust EPI Nyquist ghost removal by incorporating phase error correction with sensitivity encoding (PEC-SENSE) *Magn Reson Med* 2018; **79**(2):943-951.
- [40] Dong Zijing, Wang Fuyixue, Ma Xiaodong, Dai Erpeng, Zhang Zhe, Guo Hua. Motion-corrected k-space reconstruction for interleaved EPI diffusion imaging *Magn Reson Med* 2018; **79**(4):1992-2002.
- [41] Finsterbusch Jürgen. Chapter 2.2 - B0 Inhomogeneity and Shimming in *Quantitative MRI of the Spinal Cord* (Cohen-Adad Julien, Wheeler-Kingshott Claudia A.M., eds.):68 - 90 San Diego: Academic Press 2014.

PUBLICATION IV

- [42] Saritas Emine U., Holdsworth Samantha J., Bammer Roland. Chapter 2.3 - Susceptibility Artifacts in *Quantitative MRI of the Spinal Cord* (Cohen-Adad Julien, Wheeler-Kingshott Claudia A.M., eds.):91 - 105 San Diego: Academic Press 2014.
- [43] Hu Yanle, Glover Gary H.. Three-dimensional spiral technique for high-resolution functional MRI *Magn Reson Med* 2007; **58**(5):947-951.
- [44] Todd Nick, Josephs Oliver, Callaghan Martina F., Lutti Antoine, Weiskopf Nikolaus. Prospective motion correction of 3D echo-planar imaging data for functional MRI using optical tracking *NeuroImage* 2015; **113**:1 - 12.
- [45] Hoppe E, Körzdörfer G, Würfl T, et al. Deep Learning for Magnetic Resonance Fingerprinting: A New Approach for Predicting Quantitative Parameter Values from Time Series *Stud Health Technol Inform* 2017; **243**:202-206.
- [46] Cohen Ouri, Zhu Bo, Rosen Matthew S.. Deep Learning for Rapid Sparse MR Fingerprinting Reconstruction *CoRR* 2017; **abs/1710.05267**.
- [47] Lundervold Alexander Selvikvag, Lundervold Arvid. An overview of deep learning in medical imaging focusing on MRI *Z Med Phys* 2019; **29**(2):102-127.
- [48] Maier Andreas, Syben Christopher, Lasser Tobias, Riess Christian. A gentle introduction to deep learning in medical image processing *Z Med Phys* 2019; **29**(2):96-101.
- [49] Schnurr Alena, Chung Khan, Russ Tom, Schad Lothar R, Zöllner Frank G. Simulation-Based Deep Artifact Correction with Convolutional Neural Networks for Limited Angle Artifacts *Z Med Phys* 2019; **29**(2):150-161.
- [50] Lee Philip K., Watkins Lauren E., Anderson Timothy I., Buonincontri Guido, Hargreaves Brian A.. Flexible and efficient optimization of quantitative sequences using automatic differentiation of Bloch simulations *Magn Reson Med* 2019; **82**(4):1438-1451.
- [51] In Myung-Ho, Speck Oliver. Highly accelerated PSF-mapping for EPI distortion correction with improved fidelity *MAGMA* 2012; **25**(3):183-192.
- [52] Hong Xin, To Xuan V., Teh Irvin, Soh Jian R., Chuang Kai-Hsiang. Evaluation of EPI distortion correction methods for quantitative MRI of the brain at high magnetic field *Magn Reson Imaging* 2015; **33**(9):1098 - 1105.

Accelerated white matter lesion analysis based on simultaneous T_1 and T_2^* quantification using Magnetic Resonance Fingerprinting and Deep Learning

Ingo Hermann, Eloy Martínez-Heras, Benedikt Rieger, Ralf Schmidt, Alena-Kathrin Golla, Jia-Sheng Hong, Wei-Kai Lee, Wu Yu-Te, Martijn Nagtegaal, Elisabeth Solana, Sara Llufríu, Achim Gass, Lothar R. Schad, Sebastian Weingärtner and Frank G. Zöllner

MAGN RESON MED. 2021; DOI.ORG/10.1002/MRM.28688

Abstract

Purpose: To develop an accelerated post-processing pipeline for reproducible and efficient assessment of white matter lesions using quantitative Magnetic Resonance Fingerprinting (MRF) and deep learning.

Methods: MRF using echo-planar imaging (EPI) scans with varying repetition and echo times were acquired for whole brain quantification of T_1 and T_2^* in 50 subjects with multiple sclerosis (MS) and 10 healthy volunteers along 2 centers. MRF T_1 and T_2^* parametric maps were distortion corrected and denoised. A CNN was trained to reconstruct the T_1 , T_2^* parametric maps, and the WM and GM probability maps.

Results: Deep learning based post-processing reduced reconstruction and image processing times from hours to a few seconds while maintaining high accuracy, reliability, and precision. Mean absolute error performed the best for T_1 (deviations 5.6%) and the logarithmic hyperbolic cosine loss the best for T_2^* (deviations 6.0%).

Conclusion: MRF is a fast and robust tool for quantitative T_1 and T_2^* mapping. Its long reconstruction and several post-processing steps can be facilitated and accelerated using deep learning.

1 Introduction

White matter (WM) lesions are a common brain imaging finding in multiple sclerosis (MS) affecting the central nervous system. WM lesions are commonly characterized by increased T_1 and T_2^* relaxation times [1]. T_2 -weighted imaging or fluid attenuated inversion recovery (FLAIR) is most commonly used in clinical MRI [2]. However, conventional magnetic resonance imaging (MRI) only provides limited insights into the pathological substrate of tissue changes (e.g. axonal loss, inflammation, demyelination). Specifically, qualitative imaging inherently hampers standardization and reproducibility. Therefore, quantification of relaxation times such as T_1 , T_2 and T_2^* is increasingly receiving interest for providing additional information beyond qualitative imaging [3, 4, 5]. However, most quantitative methods suffer from long acquisition times as the acquisition of multiple qualitative images is required. This renders quantitative MRI susceptible to intra-scan motion. Furthermore, due to inter-scan motion and image distortion, multiple successive scans commonly need to be co-registered in order to allow for joint analysis. Magnetic resonance fingerprinting (MRF) is a promising, time efficient approach for quantification of multiple tissue parameters in a single acquisition [6]. In MRF characteristic magnetization evolutions are generated for tissues by varying sequence parameters including flip angle, echo time (TE), and repetition time (TR) throughout the acquisition. Thus, MRF has shown the potential to differentiate between healthy and pathological tissue and may, therefore, be useful for clinical MRI [7]. Rieger et al. proposed an MRF sequence based on an echo-planar imaging (EPI) readout for simultaneous quantification of T_1 and T_2^* times covering the whole brain in less than 5 minutes [8, 9]. Lower undersampling factors are applied compared with spiral MRF, reducing the noise per magnitude image but also the total number of magnitude images. This method was recently shown to provide clinically robust T_1 and T_2^* in neuro and renal applications [8, 9, 10]. However, compared with other EPI scans high acceleration factors lead to a lower signal-to-noise ratio (SNR) than common for many clinical applications. Multiple denoising strategies have been proposed to improve the image quality and accuracy [11, 12, 13]. Recently, Marchenko-Pastur principal component analysis (MPPCA) was proposed to denoise EPI-diffusion MRI images [14]. This is of particular interest, as a recent study demonstrated the value of denoising the acquired MRF magnitude images to improve the quality of the quantitative maps [10]. The large number of magnitude images in an MRF acquisition leads to long reconstruction times, which has been acknowledged as one of the drawbacks of the MRF methodology [7, 15]. Additionally, several post-processing steps hinder the practicability in clinical usage. In wake of recent developments, deep learning has superseded other approaches in many ar-

eas of data processing. Numerous publications have shown the benefits of using deep learning for medical imaging [16, 17, 18, 19, 20, 21]. Specifically, deep learning accelerates processing steps and is capable of reconstructing MRI data [22, 23, 24]. Denoising plays an important role in MRI and several networks were evaluated to improve the visual image quality using generative adversarial networks and deep neuronal networks [25, 26, 27, 28, 29]. Furthermore, image synthesis has gained attention, which transforms a set of input images to a new set of image contrasts [30, 31]. These image transformations can also contain deformable registration and artifact correction which showed good accuracy using CNN's [32, 33, 34].

Especially for MRF, several models using fully-connected neuronal network [35, 36], recurrent and convolutional neuronal network (CNN) [18, 37, 38, 39] were analyzed showing promising results regarding the speed and accuracy of the reconstruction [40]. A deep learning reconstruction on MRF data using the spatio-temporal relationship between neighboring signal evolutions was proposed [41, 42], which showed an improvement in the reconstruction especially for undersampled complex MRF data. The U-Net has frequently been used to process medical data for segmentation and regression tasks [43, 44, 45, 46]. Since most of the MRF acquisition techniques acquire a large number of highly undersampled images, the reconstruction problem is high dimensional. Therefore, a two-step deep learning approach was proposed in [19] to, firstly, reduce the dimensionality by using feature extraction with a fully connected network [47] and secondly, a U-Net for spatially constrained quantification. The advantage of this learning-based model is that it contains tissue properties of the neighboring pixels which is more resilient to noise [48].

In this study we performed MRF-EPI for simultaneous quantification of T_1 and T_2^* in the whole brain on 50 patients with white matter lesions and 10 healthy volunteers and analyzed the T_1 and T_2^* times in WM and GM. Compared to conventional MRF methods, our MRF-EPI only slightly undersamples the k-space allowing for conventional parallel imaging reconstruction and yielding magnitude data that contains all relevant structural information. We developed a CNN for the MRF-EPI reconstruction of denoised and distortion corrected T_1 , T_2^* maps, and WM, GM probability maps. Furthermore, we compare different outputs, loss functions, and patches of the CNN for optimizing the entire reconstruction using deep learning.

2 Methods

This bi-center study was approved by the local institutional review board at both sites (2019-711N, BCB2012/7965), and written, informed consent was obtained prior to scanning. We performed MRF-EPI in 10 healthy volunteers (75% male, 22-30 (mean: 26) years, mean) and 18 patients (39% male, 23-73 (mean: 39) years) with MS on a 3T scanner (Magnetom Skyra, Siemens Healthineers, Erlangen, Germany) at site 1 and in 32 patients (37% male, 1-63 (mean:41) years) with MS at a 3T scanner (Magnetom Prisma, Siemens Healthineers, Erlangen, Germany) at site 2. Figure 1 depicts an overview of the MRF pipeline. The conventional steps (1-6) acquisition, denoising, dictionary generation, reconstruction, distortion correction, and masking are depicted in the first part. The approach for standardization and acceleration using deep learning is shown in the second part, combining steps 2 to 6 to a single CNN.

2.1 Magnetic Resonance Fingerprinting

The acquisition was based on the previously proposed MRF-EPI technique for which accuracy and precision to gold standard methods were already evaluated [8]. Dictionaries were generated per slice using MATLAB (The MathWorks; Natick, MA, USA) consisting of 131,580 entries with T_1 (30-4000 ms) in 5% steps, T_2^* (5-3000 ms) in 5% steps and flip angle efficiency B1+ (0.65-1.35) in steps of 0.05.

Sequence parameters for the MRF sequence were in-plane spatial resolution = 1x1 mm², slice thickness = 2 mm, bandwidth = 998 Hz/px, GRAPPA factor = 3, partial fourier = 5/8, variable flip angle (34-86°), TE (21-81.5 ms), TR (3530 - 6570 ms) and fat suppression. At site 2, additionally, simultaneous multi-slice (SMS) imaging was used with an acceleration factor of 3. The acquisition time for site 1 was 4 minutes and 23 seconds and 1 minute and 52 seconds at site 2 covering all 60 slices. Additionally, T_1 -FLAIR and T_2 -weighted images were acquired for lesions segmentation and distortion correction, respectively, using the same spatial resolution.

2.2 Principal-component-analysis denoising

We used Marchenko-Pastur principle component analysis (MPPCA) [14] to denoise the magnitude data of the MRF acquisition before reconstruction. Originally, the denoising strategy was proposed to estimate a non-Gaussian distribution on diffusion MRI data. The noise is estimated in a local neighborhood by the eigenvalues of principal component analysis using the Marchenko-Pastur distribution [14].

Quantitative T_1 and T_2^* maps were compared with and without denoising. Denoising was performed on a per slice basis using a 2-dimensional kernel. As we are not interested in the actual image contrast but in the absolute T_1 and T_2^* times, we use standard deviation to describe the noise in these values.

2.3 Distortion Correction

Distortion correction was performed to correct for susceptibility artifacts, especially around the nasal cavities [49]. Rigid registration was computed from the T_2 -weighted data to the MRF-magnitude data followed by a restricted non-linear registration along phase-encode direction from the magnitude to the T_2 -weighted data using ANTs [50]. Distorted maps were then visually compared to the FLAIR and T_2 -weighted images to ensure that all modalities are properly registered.

2.4 Data Processing

WM lesions were segmented manually by an expert radiologist on the FLAIR images. WM and gray matter (GM) were automatically segmented using SPM12 (Statistical Parametric Mapping version 12) [51] using the T_1 Maps acquired with MRF after denoising and distortion correction. The probability maps generated by SPM12 were transformed into binary masks by using a threshold (80%). Masks were visually analyzed and manually segmented WM lesions were extracted from the WM and GM mask to improve accuracy.

2.5 Deep Convolutional Neural Network for MRF Reconstruction

Our network was a modified U-Net [43] implemented in Matlab 2020a (The MathWorks; Natick, MA) using the Deep Learning Toolbox. The network architecture is displayed in Figure 1. The training was performed on a GPU (Tesla K40m, Nvidia, Santa Clara, CA) for approximately 1 day per network. As inputs, the 35 differently weighted MRF-EPI magnitude images were used. The generated output were the T_1 and T_2^* maps and WM- and GM-probability maps. A brain mask was applied to exclude background noise. Data of five patients was randomly selected for testing, while the remaining data was chosen for training (49 data sets) and validation (5 data sets). Data of six healthy volunteers were acquired without T_2 -weighted images and therefore, they are excluded from training. Two patients from site 1 and three patients from site two were chosen for the testing set. The 2D network was trained on individual slices.

Table 1: The different parameters for all the networks compared in this work are listed here.

Network parameters			
networks	input	outputs	loss function
1	patches	single T_1	MAE
2	patches	single T_2^*	MAE
3	patches	T_1, T_2^*	MAE
4	patches	T_1, T_2^*, WM, GM	MAE
5	patches	T_1, T_2^*, WM, GM	MSE
6	patches	T_1, T_2^*, WM, GM	LCL
7	patches	T_1, T_2^*, WM, GM	HL
8	full	single T_1	MAE
9	full	single T_2^*	MAE
10	full	T_1, T_2^*	MAE
11	full	T_1, T_2^*, WM, GM	MAE
12	full	T_1, T_2^*, WM, GM	MSE
13	full	T_1, T_2^*, WM, GM	LCL
14	full	T_1, T_2^*, WM, GM	HL

We trained half the networks with the full input resolution (240x240 voxels) and the other half using 32 random patches (64x64 voxels) per slice (Table 1). We evaluated the following four different loss functions (the reference value y_i , predicted value y_i^p and the number of values n):

the mean square error (MSE)

$$\text{MSE} = \frac{\sum_{i=1}^n (y_i - y_i^p)^2}{n}, \quad (1)$$

the mean absolute error (MAE)

$$\text{MAE} = \frac{\sum_{i=1}^n |y_i - y_i^p|}{n}, \quad (2)$$

the Huber loss (HL), which is a combination of MAE and MSE

$$\text{HL} = \begin{cases} \frac{1}{2}(y_i - y_i^p)^2, & \text{for } |y_i - y_i^p| \leq \delta \\ \delta|y_i - y_i^p| - \frac{1}{2}\delta^2, & \text{otherwise} \end{cases} \quad (3)$$

and the logarithm of the hyperbolic cosine (LCL)

$$\text{LCL} = \frac{\sum_{i=1}^n \log(\cosh(y_i - y_i^p))}{n}, \quad (4)$$

We used Adam for optimization with a learning rate of 0.0001, L2-Regularization of 0.0001, 50 training epochs, and batch size = 64 for all networks, which was empirically determined to be optimal. Additionally, we trained the networks using patches and the full input resolution and MAE with three different types of outputs. 1. The network was trained with a single output once for T_1 and another for T_2^* (single). 2. The network was trained with both T_1 and T_2^* in a single network (dual) and 3. the network was trained with four output maps T_1 , T_2^* , WM- and GM probability maps (four output). Relative differences between dictionary matched and predicted maps were calculated and correlation coefficient of mean T_1 and T_2^* times between prediction and reference in WM, GM, lesions, and the whole brain was calculated. Reconstructions were executed on the CPU (Intel(R) Core(TM) i5-6500 @ 3.20GHz).

2.6 Statistics

Mean T_1 and T_2^* times with standard deviations were calculated and pair-wise comparison was performed using Student's t-tests and correlation R-values. p-values less than 0.05 were considered significant. The mean Dice similarity coefficient was used as a statistical validation metric for the predicted WM and GM probability maps after binarizing them into logical masks.

Computational time was measured using a standard desktop PC.

3 Results

Image denoising was successfully performed using MPPCA and resulted in up to 50% decreased variability in the magnitude data and 15% reduced standard deviations of T_1 and T_2^* (Supporting Information Figure S1). Overall, denoising the MRF magnitude data took about 10 minutes per subject on a standard CPU.

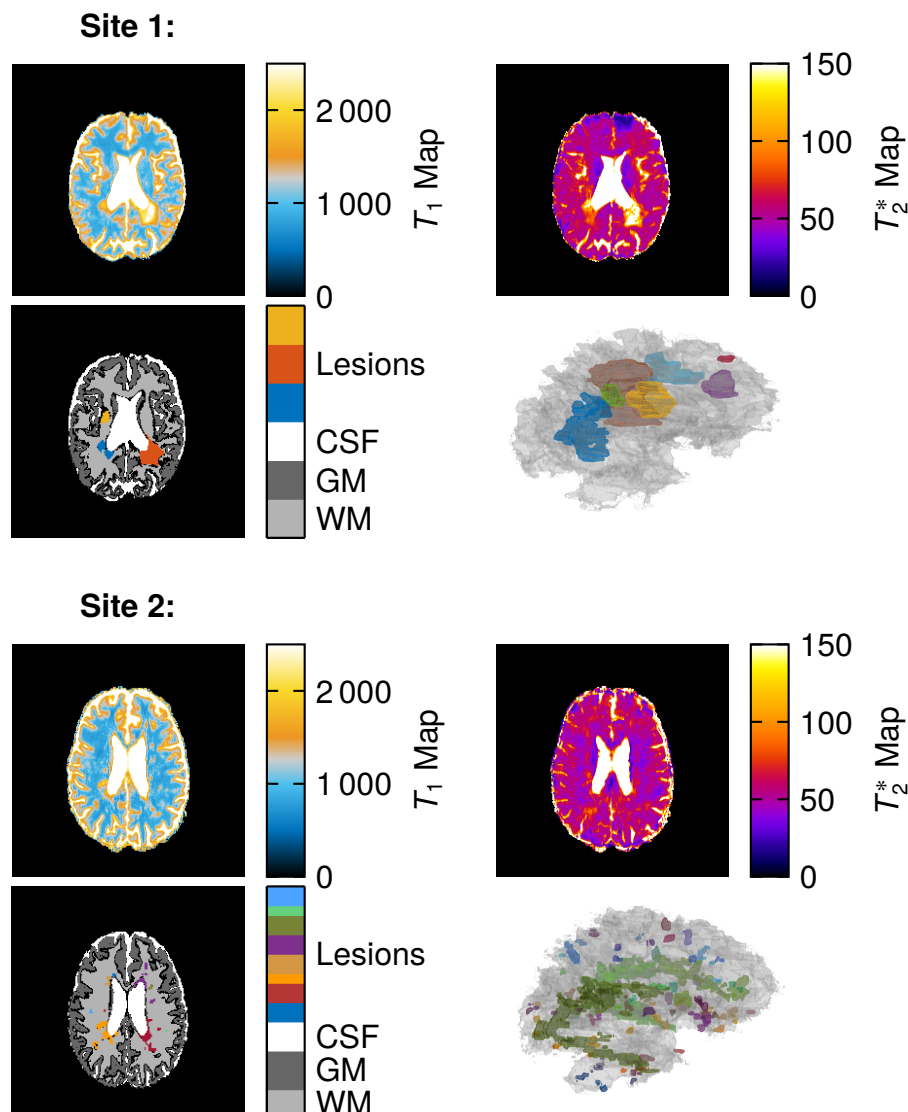


Figure 2: Representative T_1 and T_2^* map for one patient of site 1 (top) and one patient of site 2 (bottom). The segmented WM, GM, and CSF is shown combined with the manually segmented WM lesions. WM is shown semitransparent in 3D with the segmented lesions of representative different subjects from both sites. Different colors depict different lesions as they were automatically separated.

After the denoising and reconstruction of the parametric T_1 and T_2^* maps, EPI distortion correction was performed as exemplarily shown in Supporting Information Figure S2. Deviations in the relaxation times of up to 10% were observed in caudal slices next to the nasal cavities after applying the distortion correction. Distortion corrected mean T_1 and T_2^* times show only minor variations (<2%) in WM, GM and WM lesions compared with T_1 and T_2^* times without distortion correction. The distortion correction of the MRF data takes around one hour for one whole brain on a standard CPU.

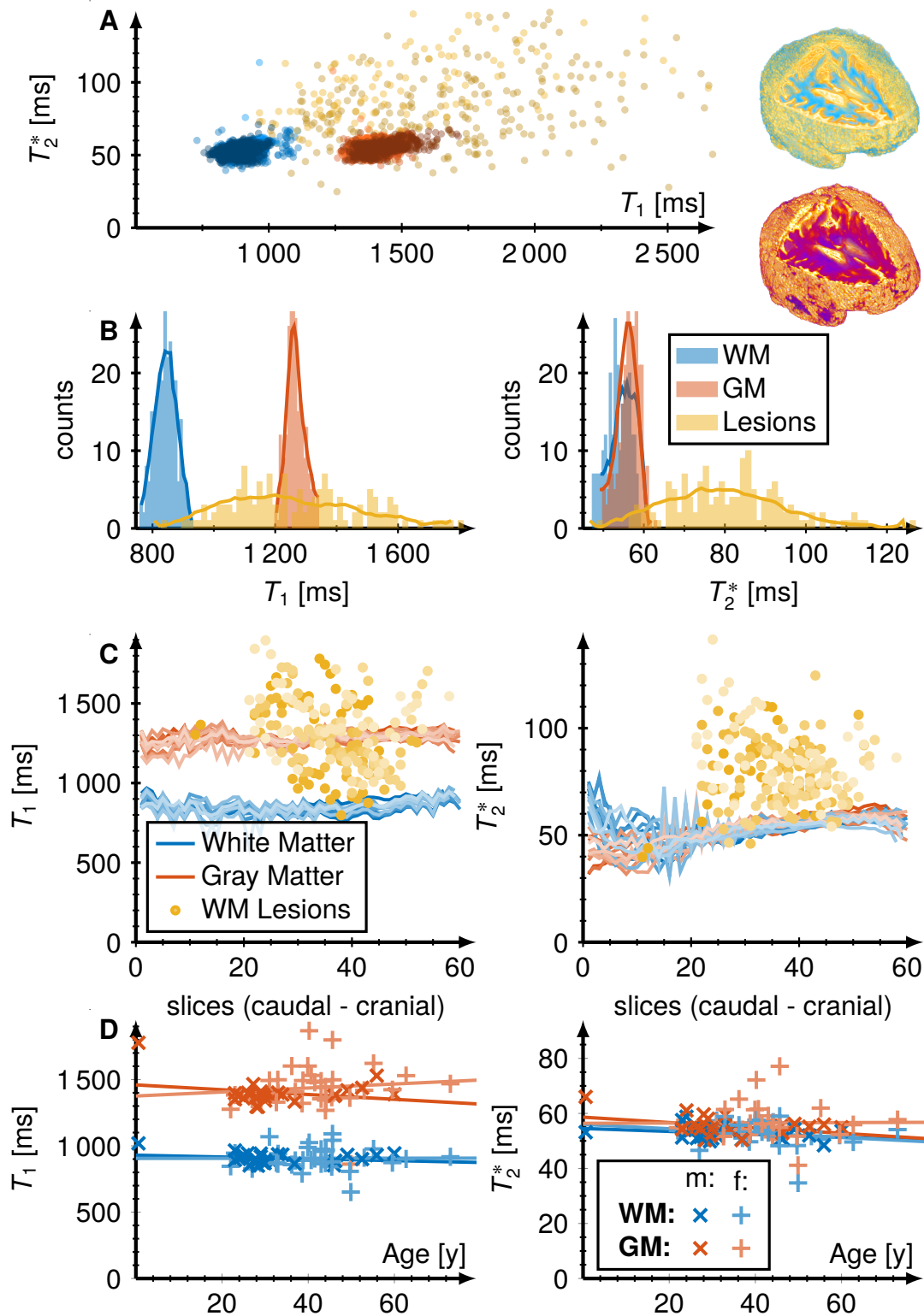


Figure 3: **A:** Mean T_2^* times over mean T_1 times for white matter (blue), gray matter (orange), and WM lesions (yellow) of all patients and subjects from both sites. Representative 3D T_1 and T_2^* maps were depicted on the right. **B:** Representative distributions of the T_1 and T_2^* times from A, which shows a much wider spread for the WM lesions considering T_1 and T_2^* times compared with WM and GM. In **C** the mean T_1 (left) and T_2^* (right) over the slice position for white matter (blue) and gray matter (orange) are depicted. Color brightness encode different subjects. In **D** the WM and GM T_1 and T_2^* times over the age and gender are shown.

Representative T_1 and T_2^* maps including annotations are shown in Figure 2 for both sites. Reconstruction of the parametric maps using a pattern matching algorithm took around 20 minutes per subject. Mean T_1 and T_2^* relaxation times for WM, GM, and WM lesions are depicted in Figure 3 and provided in the Supporting Information Tables S1-3. Differences between healthy and diseased subjects from both sites were less than 4% for T_1 and less than 2% for T_2^* in WM and less than 7% for T_1 and less than 3% for T_2^* in GM. MRF acquired in site 2 had 15% higher standard deviations in T_1 and T_2^* due to increased scan time acceleration. Mean T_1 relaxation times in WM lesions are widespread ranging from 800 ms, comparable to WM, up to 2500 ms. Mean T_2^* times in white matter lesions were consistently higher (70%) than WM and GM with mean T_2^* times up to 200 ms.

Clear separation between WM and GM was found in T_1 (Figure 3). We found a slight trend of increasing T_2^* (up to 10%) in WM and GM for increasing slice position ($R = 0.974$, $p < 0.0001$; Figure 3 C). T_2^* was shorter and had higher standard deviations in caudal slices in the vicinity to the nasal cavities. No significant increase in T_1 and T_2^* with either age or gender was observed (Figure 3 D). T_1 and T_2^* times in WM lesions were highly heterogeneous and independent of their localization and size ($p > 0.2$).

3.1 Deep Convolutional Network for MRF Reconstruction

The computation time of the proposed CNN for 60 slices was about five seconds on a standard CPU workstation.

The performance of the reconstruction during the training process is depicted in Figure 4. Already after 5 epochs, the reconstructed maps have a visual good agreement with the dictionary matched maps. Figure 5 shows the 2D histogram of a representative slice in one subject for the CNN predicted T_1 and T_2^* times over the dictionary matching. The relative difference showed major noise with few anatomical structures and mean deviations of less than 6% for T_1 and T_2^* . Variations in the CSF are increased as seen around the ventricle and at the skull. T_1 and T_2^* times, which exceed 3000 ms are cut and, therefore, the ventricle has variations of 0%. The average correlation coefficient R and the relative difference for T_1 and T_2^* were calculated for different loss function and outputs (Figure 6). The p-value for all correlations was $p < 0.001$. For the four output models, the smallest relative difference for T_1 was observed when using the MAE with deviations of 5.8% in the whole brain and for T_2^* using the LCL with 6.0% deviations in the whole brain.

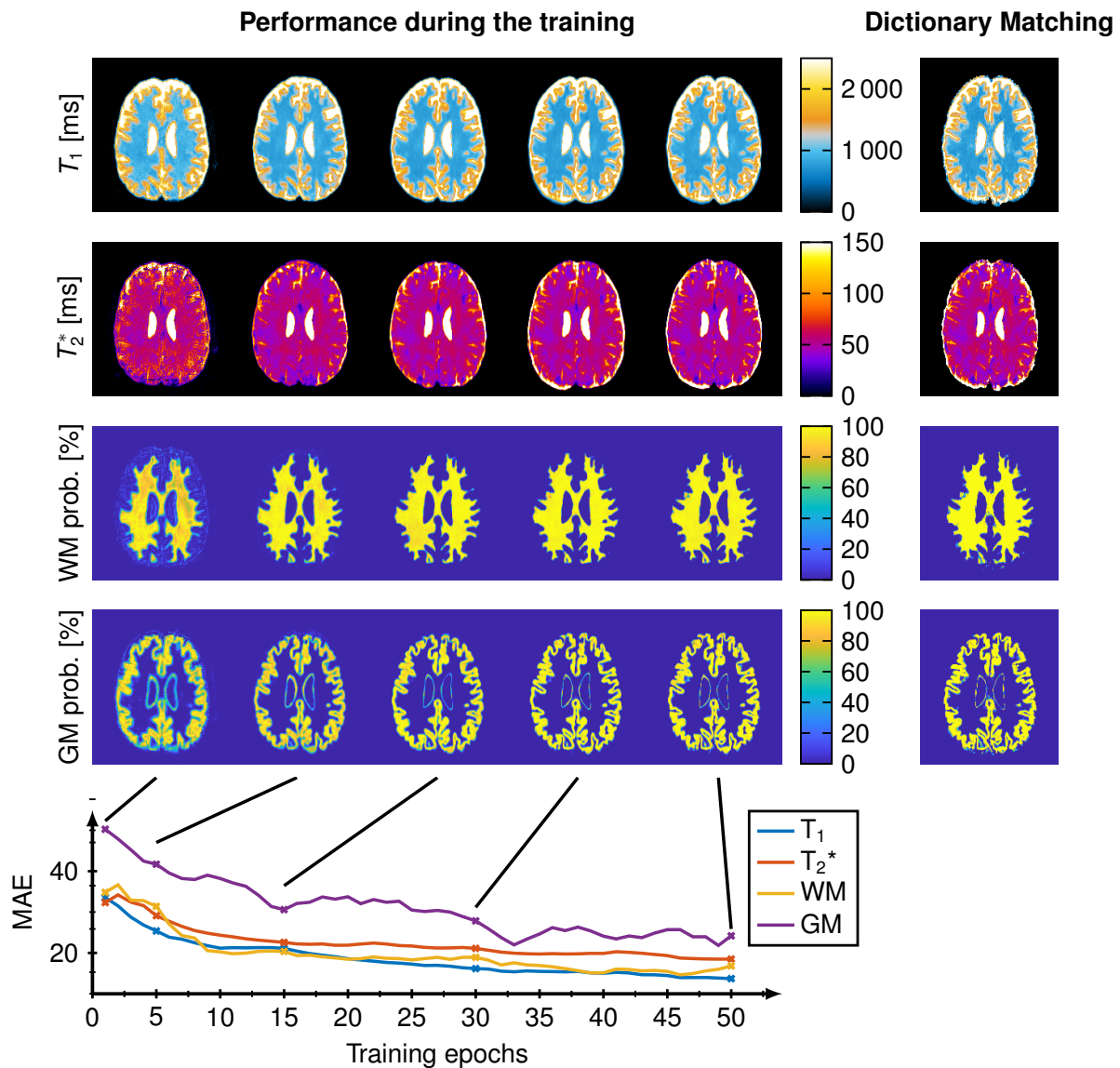


Figure 4: Visualization of the reconstruction during the training for one subject of the test data. The reconstructed T_1 , T_2^* , WM- and GM probability maps are depicted for 1, 5, 15, 30, and 50 training epochs, and the dictionary matching reference maps are shown on the right side. On the bottom, the MAE is depicted over the 50 training epochs.

Correlation coefficients in the whole brain were more than 0.99 except for the MSE (0.989) for T_1 and higher than 0.985 for T_2^* in the whole brain. The relative difference in T_1 and T_2^* was observed to be the highest in GM. All the relative differences and correlation coefficient are given in Supporting Information Table S4 for T_1 and Supporting Information Table S5 for T_2^* . The difference of the different loss functions is visually depicted in Figure 7, where the MSE smooths the predicted maps the most as clearly seen in the WM and GM-probability maps. The HL has increased T_2^* in WM and the MSE decreased T_1 in WM. In the WM probability maps, the LCL visually performed the

best as seen in the prediction around the lesion.

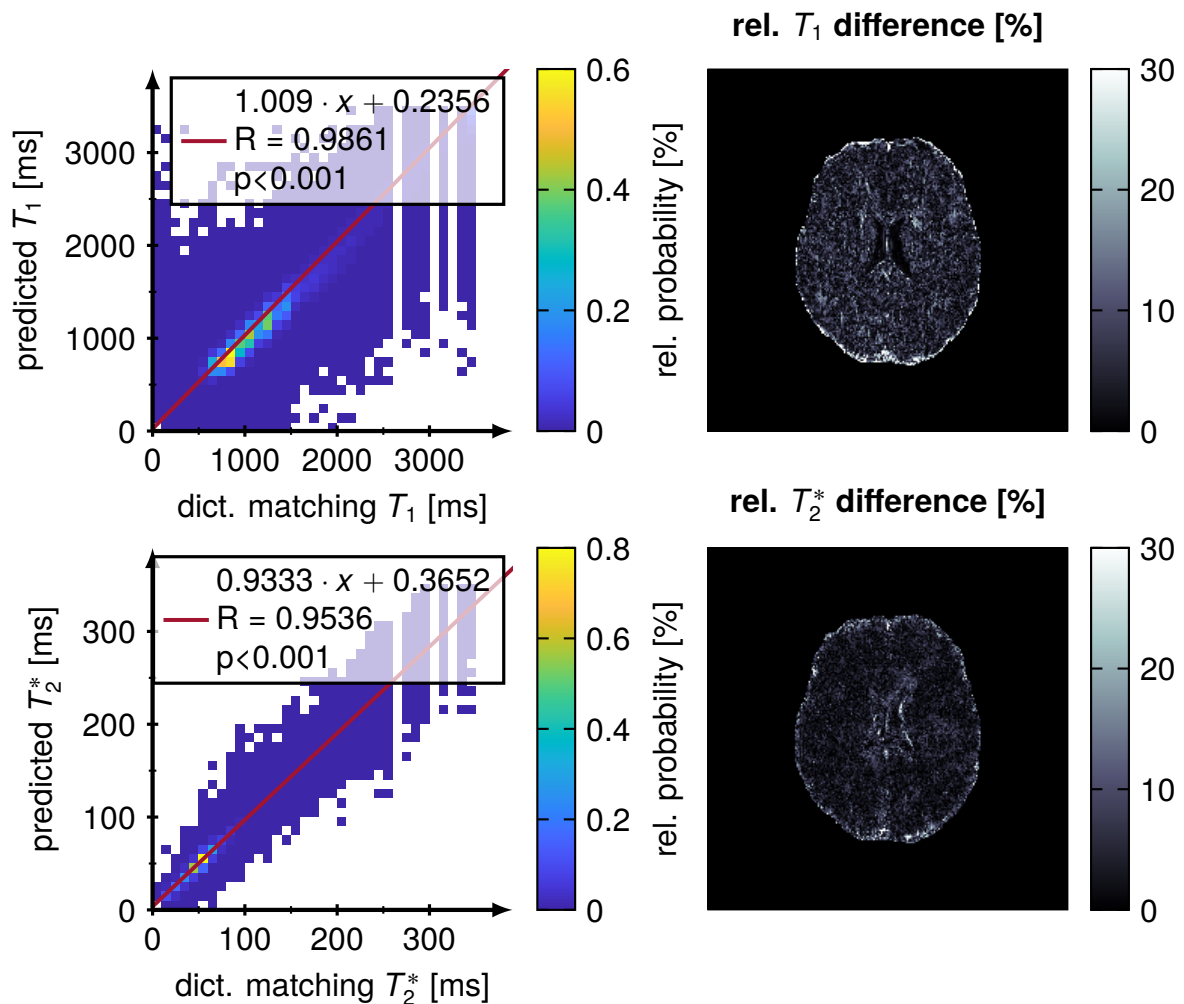


Figure 5: Prediction of the CNN-network for one slice of a representative subject. The histograms (left panel) depict the predicted T_1/T_2^* (top/bottom) of one slice over the T_1/T_2^* generated by dictionary matching. The linear fit (red) with corresponding fit parameters and R and p-values is shown. On the right side, the relative difference of T_1 and T_2^* is shown between the predicted and dictionary matched parametric maps. Voxel-wise differences range up to 30% around the ventricles, because of the very high T_1 and T_2^* times for the CSF rendering the prediction difficult for the network.

The difference of the different loss functions is visually depicted in Figure 7, where the reconstructed T_1 , T_2^* maps and WM-, GM probability maps are compared with the training input for one slice of a patient. The MSE smooths the predicted maps the most as clearly seen in the WM and GM-probability maps. The HL has increased T_2^* in WM and the MSE decreased T_1 in WM. In the WM probability maps, the LCL visually performed the best as seen in the prediction around the lesion. The training with full image input showed significant increases in the relative error (25.8% for T_1 and 21.6%

for T_2^*) and correlation coefficients of less than 0.90 for T_2^* in WM. Prediction in the WM performed better than in GM with around 4% higher correlation coefficient and correlation coefficients in WM lesions were observed to be higher than 0.98.

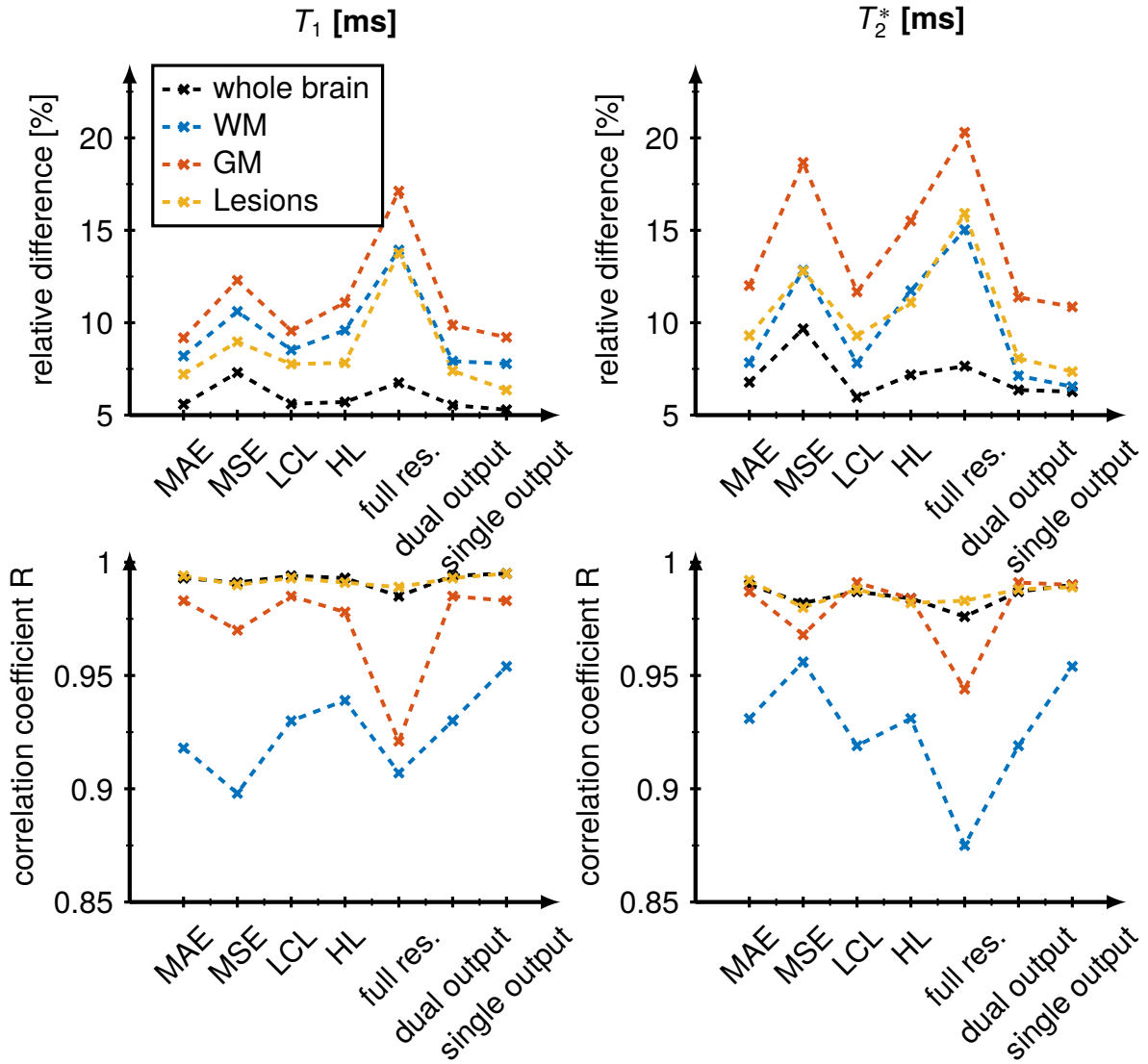


Figure 6: The Relative difference is shown between the predicted and dictionary matched T_1 (left) and T_2^* (right) for the whole brain (black), WM (blue), GM (orange), and lesions (yellow) compared to the different loss functions and network outputs. The first four data points (MAE, MSE, LCL, HL; Table 1, networks 4-7) are the networks trained with patches and four outputs. The fifth one (Table 1, networks 11) is trained with the full input resolution (full res.) and the MAE. The last two (dual output and single output; Table 1, networks 3 and 1+2) are trained using patches and the MAE loss function with one and two output maps respectively. On the bottom correlation coefficients for the linear fit between predicted and dictionary matched T_1 (left) and T_2^* (right) is shown for the different network outputs using the MAE (mean absolute error), MSE (mean squared error), LCL (logarithmic cosine loss) and the HL (Huber loss).

The mean Dice Coefficient across the test data for WM was 0.9 and for GM 0.91 after conversion into logical masks with a threshold of 80% for both SPM and DL probability maps (Table 1, network 4). Dice Coefficients decreased up to 15% when training was performed on the full input size without patches (mean WM: 0.81, mean GM: 0.79). When training on T_1 and T_2^* as a dual output, prediction showed a slightly increased correlation coefficient (around 1%) and decreased relative difference compared with the four output models. Single T_1 and single T_2^* as outputs reached the highest correlation coefficients and smallest relative error among all other networks.

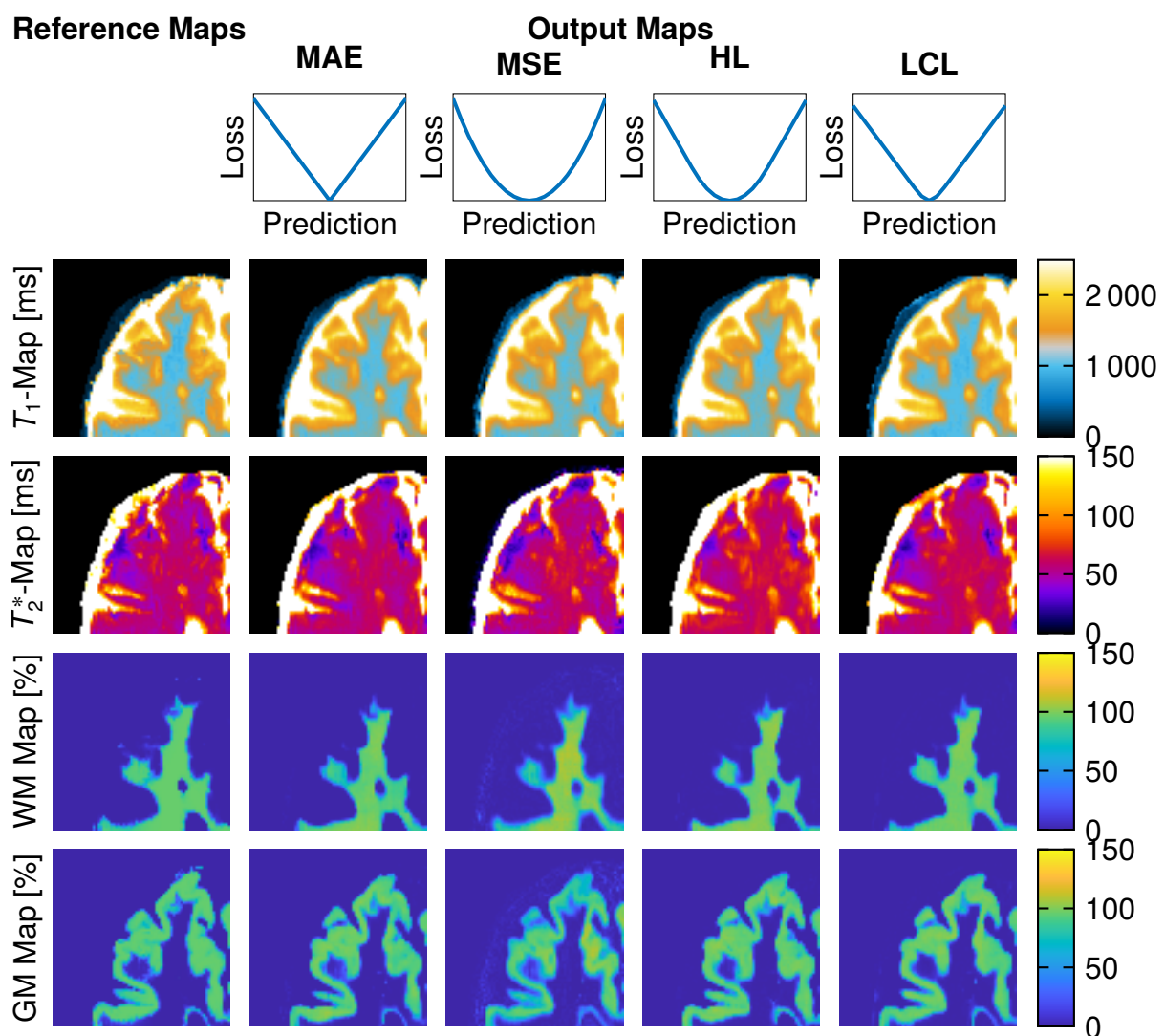


Figure 7: Comparison of the different loss functions to the dictionary matched input of one representative subject of the test data using the network 4 from Table 1. T_1 , T_2^* , WM- and GM probability maps are shown for the MAE (mean absolute error), MSE (mean squared error), LCL (logarithmic cosinus loss), and the HL (Huber loss). A small patch (40x40) of one slice of a representative subject is shown. It is seen that the mean squared loss is smoothing the WM and GM probability maps the most.

Figure 8 shows the mean T_1 and T_2^* times per subject between the DL and conventional reconstruction. A linear fit shows the correlation which was above 0.99 with $p < 0.0001$ for both T_1 and T_2^* . The bright colored markers depict the test data, which are aligned to the linear fit. We observe a small offset in T_1 (55 ms) and in T_2^* (2.2 ms) which is within the standard deviations (100 – 200 ms \sim 10%, 3 – 5 ms \sim 10%).

Figure 9 depicts the dice coefficient between the WM and GM masks generated from the probability maps using SPM and our DL approach for different thresholds. The black line depicts the highest dice coefficients with close correlation to a straight line with a correlation coefficient of 0.9965 for WM and 0.9974 for GM with both $p < 0.0001$. For a commonly used threshold of 80% for SPM the dice coefficient is shown for different thresholds of the DL WM and GM maps. For a threshold of 80% of the DL reconstruction, the mean dice coefficient yields for both, WM and GM values of higher than 0.9.

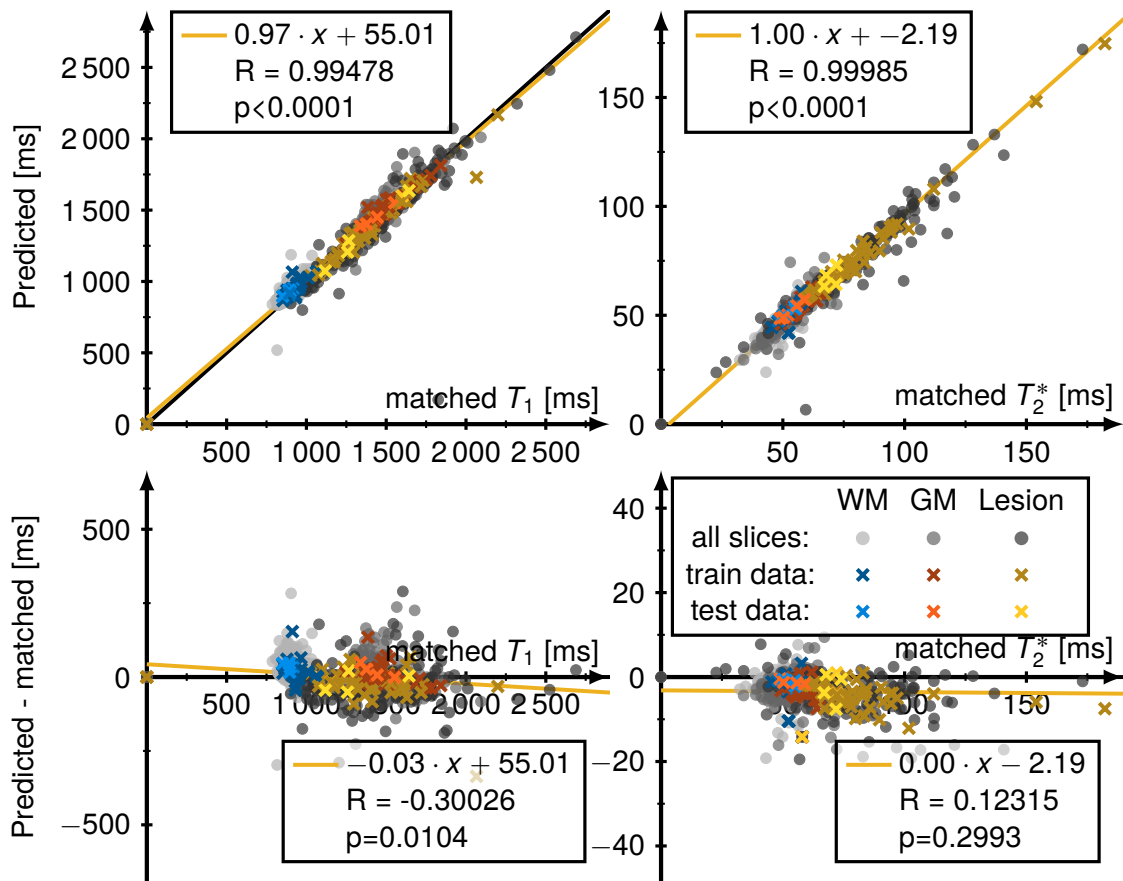


Figure 8: Predicted T_1 (left) and T_2^* (right) times over the dictionary matched T_1 and T_2^* times for the 4 output network using patches for training and the mean absolute loss. Mean values per subject of WM are shown in blue, of GM are shown in orange and for the lesion are shown in yellow. The increased brightness of the representative colors depicts the test data and the reduced brightness depicts the training and validation data. In three different gray shades, the single T_1 and T_2^* times per slice are shown. A linear fit is used to correlate the predicted and the dictionary matched quantitative maps with corresponding R- and p-values.

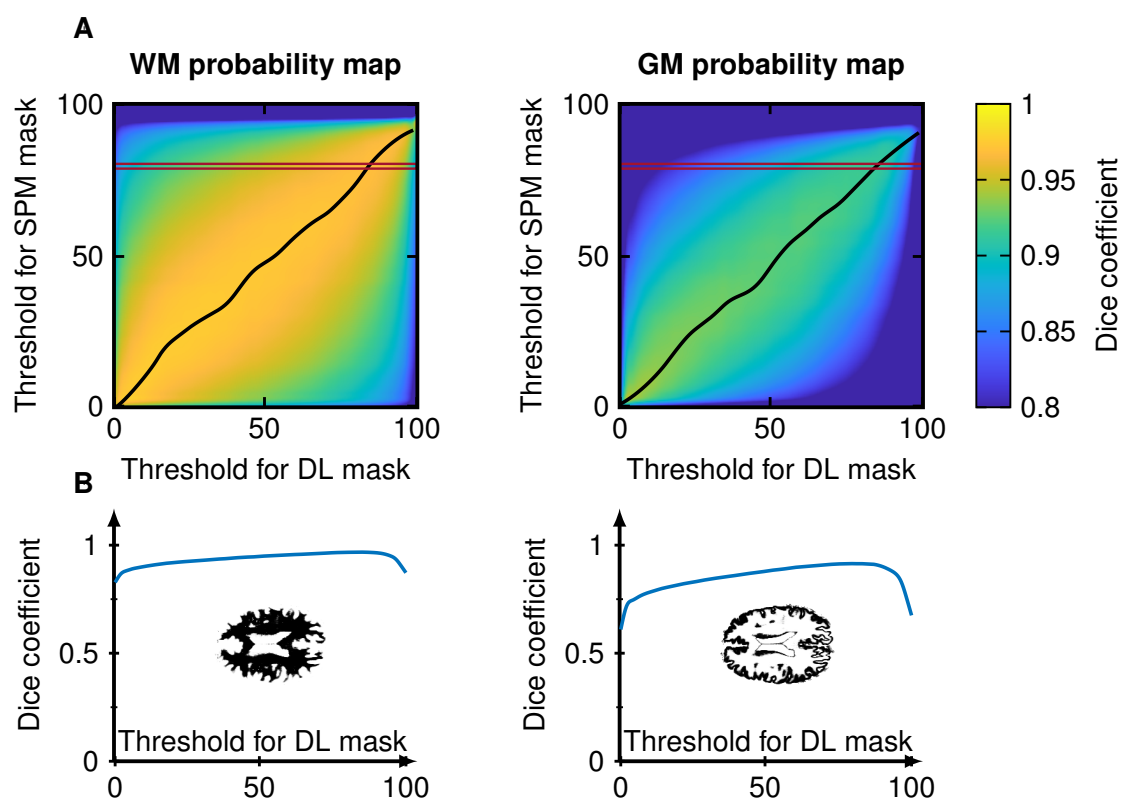


Figure 9: **A)** Dice coefficient for different thresholds of the SPM and DL (Deep Learning) WM (left) and GM (right) probability maps of a representative subject when using the MAE loss with four outputs and patches-wise training (Table 1, network 4). The black lines depict the maximum dice coefficient along with the different thresholds. The dice coefficient between both binary masks is shown in color encoding. **B)** The dice coefficient is shown for a fixed threshold of 80% of the SPM WM and GM masks dependent on the threshold of the DL mask, as marked in the red area **A)**, which both show a maximum dice coefficient at around 80%. Exemplary WM and GM probability maps are depicted.

4 Discussion

We acquired MRF-EPI for simultaneous quantification of T_1 and T_2^* times in the whole brain. With a single convolutional neural network, we accelerated and combined several post-processing steps as reconstruction, denoising, distortion correction, and masking.

MRF-EPI is a promising technique for quantification of T_1 and T_2^* of the whole brain in less than 5 minutes. T_1 and T_2^* times showed overall good agreement with literature [1, 3, 5, 52, 53, 54, 55, 56]. However, as previously noted MR relaxation times for WM and GM show wide variability among studies due to different sequences, fitting procedures and natural variability among subjects [52]. Accuracy and precision measurements for the proposed MRF-EPI sequences were performed in previous work and

therefore not analyzed in this study [8, 10]. WM lesions exhibit a wide range of T_1 and T_2^* relaxation times. The relaxation times were independent of their localization and size in the brain. WM lesions were successfully delineated from WM, GM, and CSF based only on quantitative MRF T_1 and T_2^* maps. Lesions which are difficult to separate from CSF on conventional images show a clear difference in the T_1 and T_2^* maps acquired with MRF due to long T_1 times in CSF of around 3000-4000 ms compared with T_1 times in lesions of around 1000-2000 ms. These high and widespread ranges of T_1 times in lesions might be due to altered interstitial fluid mobility and water content from edematous brain tissue [57]. Thus, the use of quantitative relaxometry obtained by MRF might potentially enhance the segmentation around the CSF. A fraction of WM lesions exhibit only a slight elevation of the T_1 times compared with WM and, therefore, yield similar or even smaller values compared with GM. This hampers the separation of WM lesions and GM. However, the additional assessment of T_2^* proved to be beneficial for the assessment of those lesions and showed improved separation against GM. The increased sensitivity in T_2^* might be explained by the fact that T_2^* times in WM and GM yield similar values and, hence, deviations in T_2^* in lesions benefit delineation against both WM and GM. This is a gain compared to conventional methods such as FLAIR or T_2 -weighted images. We found no significant increase in T_1 and T_2^* with either age or gender, although a number of studies demonstrated that T_1 does change with age [58, 59]. This might be due to the smaller number of subjects since we split between the healthy and diseased subjects and the narrow age range, especially for the healthy subjects. Further analysis of this might be performed when more subjects are measured. Only minor differences between data from site 1 and site 2 were observed (<7%), with no significant trends ($p > 0.2$). This demonstrates the potential of MRF as a quantitative method that is suitable for reproducible multi-center studies and a pathway to standardization. A slight trend of increasing T_2^* was identified in the cranial direction. This is unlikely to be a result of the acquisition scheme, as due to the slice interleaving any inaccuracies would be expected to appear interleaved as well. Instead, this effect might be explained by increasing B0 inhomogeneities in the axial direction. In site 2 additional scan time acceleration was achieved with SMS factor 3, reducing the effective scan time by a factor of two to three. However, the use of SMS acceleration inflicts an additional drop in SNR depending on the G-factor due to the coil geometry. Accordingly, the quantitative data was found to have increased standard deviations of up to 15% compared with data from site 1. This might be improved by extending the acquisition scheme when using SMS or by using regularized SMS reconstructions [60].

Our deep learning-based reconstruction yielded only minor differences between the T_1 and T_2^* times of WM, GM, and WM lesions compared with conventional dictionary

matching. These mean deviations of 5.8% for T_1 and 6.0% for T_2^* are small and in the range of different approaches (2-8%) [19, 37]. Of note is that there is no ground truth data and, therefore, the dictionary matched data is the reference with a precision of 5%. Our deep learning approach is in the area of this precision and might be more precise since the output is continuous for all parameters. However, the deep learning reconstruction time was around five seconds for all slices as compared to 20 minutes dictionary matching, 10 minutes denoising, and one hour distortion correction (90 minutes in total).

We trained our networks with different loss functions and found that the MAE and LCL performed better regarding our regression task compared to the commonly used MSE function [18, 36]. This might be due to the fact, that in the MSE the CSF is weighted higher as it has longer T_1 and T_2^* times and, therefore, it is more difficult for the network to learn the relatively small differences in WM and GM. Since the T_1 and T_2^* times in the CSF are not of great clinical interest we accept the loss in accuracy for the CSF. The Dice coefficient for WM and GM was in the range of reported literature (0.82-0.93) [46, 61, 62] and in the range of SPM (0.76-0.83) [63, 64] and above 0.87 for all loss functions if the training was performed with patches. This might be explained by the fact that data augmentation (random patch extraction) prevents overfitting and enriches the dataset. Overall improved performance was observed for the training using patches independent of the loss function and the output. We found an overall 25.8% decreased relative error for T_1 and 21.6% for T_2^* respectively. This might be due to the fact, that training with the full input resolution takes longer to converge. Compared with conventional highly undersampled MRF acquisition in our MRF-EPI approach, we do not need to extract first the features and reduce the dimensionality of the network input as proposed in other MRF deep learning reconstruction approaches [19, 47, 48]. Since the anatomical structure is retained, the network has to solve an image to images regression task, which might have smaller computational requirements. Fang et al. [19] used a U-Net after the dimensionality was reduced: for their dataset, 2304 time points were used compared to 35 time points for our MRF-EPI (66 times smaller). We also used the U-Net since it captures information of the input locally and globally. This is important since we also include denoising and distortion correction with the same and single network.

Our reconstruction task included denoising and distortion correction within the MRF reconstruction and therefore, training with patches (64x64 voxels) achieved better results since the observed distortion from the EPI readout is only local at the nasal cavities and the frontal lobe of the brain. We showed that it is possible to perform denoising, distortion correction, and MRF reconstruction with one network architecture with relative difference within the standard deviation of the quantitative parameters.

We were able to additionally generate the WM and GM probability maps as outputs with only slightly decreased accuracy of the test data considering T_1 and T_2^* in WM and GM. We have shown that the dice coefficient for the binarized WM and GM masks are in good correlation between our CNN and the reference SPM method. However, the network trained only on the T_1 and T_2^* maps (dual output) as an output performed better than the four output model. Using single T_1 and single T_2^* maps as an output performed the best with only minor improvement ($<1\%$) compared to the dual output model. We compared the relative differences for different tissue types instead of using the RMSE as commonly used [18, 36], because outliers and variations of quantitative measures within single tissue types result in an overestimated error for a voxel-by-voxel comparisons, especially in the CSF.

We showed that the predicted values correlate very well with the reference dictionary matched values for T_1 and T_2^* ($R>0.95$, $p<0.0001$) with only a slight offset, which is within the standard deviation. The correlation coefficient was the lowest for only WM since the range of single WM T_1 and T_2^* times is denser compared with GM and especially compared with lesions as provided in Figure 3.

We achieved standardized results as we trained on data from both sites without significant differences between both ($p<0.01$), even though the magnitude data from both sites varies due to different accelerations. However, changing the sequence parameters changes the magnitude evolutions. Therefore, new dictionaries have to be calculated and different or retrained networks are required. Transfer learning may facilitate the possibility, to update the network when imaging parameters are changed [24, 65].

Our study has some limitations. As GM suffers from partial volume effects, calculating the mean T_1 and T_2^* times strongly depends on the segmentation and the used threshold on the probability maps. Lesion segmentation could be an extra output from a CNN similar to the one such as investigated here. However, to obtain reliable results from this, more WM lesions data would be required, due to the large variation in lesion tissue parameters and the small fraction of lesions compared to WM and GM. In our experiments, the training datasets did not provide enough lesion examples for the training to converge without significantly affecting other outputs. The strength of deep learning approaches commonly stems from the abundance of training data [66, 67]. Therefore, the proposed reconstruction will likely benefit from larger data sets. Fractioning the full input into small patches is a first step to artificially generate more data, but data augmentation could be applied additionally. In this study, both sites operated on the platform of a single MRI vendor. A multi-vendor study is required for more universal comparisons.

5 Conclusions

MRF demonstrates to be an auspicious approach for quantifying T_1 and T_2^* in subjects with MS to obtain information in a standardized fashion along two clinical centers. This technique saves time by simultaneous acquisition of T_1 and T_2^* and might improve the segmentation pipeline of lesions as their quantitative measures are clearly separated from normal appearing brain tissue types. We showed that deep learning enables a drastic speed up in the post-processing pipeline without a loss in accuracy and precision by combining denoising, distortion correction, reconstruction, and masking.

References

- [1] Bonnier Guillaume, Roche Alexis, Romascano David, et al. Advanced MRI unravels the nature of tissue alterations in early multiple sclerosis *Annals of Clinical and Translational Neurology* 2014; **1**(6):423-432.
- [2] Trip S.A., Miller D.H.. Imaging in multiple sclerosis *J Neurol Neurosurg Psychiatry* 2005; **76**(Suppl 3):iii11-iii18.
- [3] Blystad I., Håkansson I., Tisell A., et al. Quantitative MRI for Analysis of Active Multiple Sclerosis Lesions without Gadolinium-Based Contrast Agent *American Journal of Neuroradiology* 2016; **37**(1):94–100.
- [4] Bauer Sonja, Wagner Marlies, Seiler Alexander, et al. Quantitative T2'-mapping in acute ischemic stroke *Stroke* 2014; **45**(11):3280-3286.
- [5] Hernández-Torres Enedino, Wiggermann Vanessa, Machan Lindsay, et al. Increased mean R2* in the deep gray matter of multiple sclerosis patients: Have we been measuring atrophy? *Journal of Magnetic Resonance Imaging* 2019; **50**(1):201-208.
- [6] Ma Dan, Gulani Vikas, Seiberlich Nicole, et al. Magnetic resonance fingerprinting *Nature* 2013; **495**:187–192.
- [7] Panda Ananya, Mehta Bhairav B., Coppo Simone, et al. Magnetic Resonance Fingerprinting-An Overview *Curr Opin Biomed Eng* 2017; **3**(1).
- [8] Rieger Benedikt, Akçakaya Mehmet, Pariente José C., et al. Time efficient whole-brain coverage with MR Fingerprinting using slice-interleaved echo-planar-imaging *Sci Rep* 2018; **8**(1):2045-2322.
- [9] Rieger Benedikt, Zimmer Fabian, Zapp Jascha, Weingartner Sebastian, Schad Lothar R.. Magnetic Resonance Fingerprinting using echo planar imaging Joint quantification of T1 and relaxation times *Magnetic Resonance in Medicine* 2017; **78**(5):1724-1733.
- [10] Hermann Ingo, Chacon-Caldera Jorge, Brumer Irène, et al. Magnetic resonance fingerprinting for simultaneous renal T1 and mapping in a single breath-hold *Magnetic Resonance in Medicine* 2020; **83**(6):1940-1948.
- [11] Mohan J., Krishnaveni V., Guo Yanhui. A survey on the magnetic resonance image denoising methods *Biomedical Signal Processing and Control* 2014; **9**(Complete):56-69.

- [12] Nowak R.N.. Wavelet-based Rician noise removal for magnetic resonance imaging *IEEE Transactions on Image Processing* 1999; **8**(10):1408-1419.
- [13] Saladi Saritha, Amutha Prabha N.. Analysis of denoising filters on MRI brain images *International Journal of Imaging Systems and Technology* 2017; **27**(3):201-208.
- [14] Veraart Jelle, Novikov Dmitry S., Christiaens Daan, Ades-aron Benjamin, Sijbers Jan, Fieremans Els. Denoising of diffusion MRI using random matrix theory *Neuroimage* 2016; **15**(142):394-406.
- [15] Bipin Mehta Bhairav, Coppo Simone, Frances McGivney Debra, et al. Magnetic resonance fingerprinting: a technical review *Magnetic Resonance in Medicine* 2019; **81**(1):25-46.
- [16] Lundervold Alexander Selvikvåg, Lundervold Arvid. An overview of deep learning in medical imaging focusing on MRI *Zeitschrift für Medizinische Physik* 2019; **29**(2):102 - 127. Special Issue: Deep Learning in Medical Physics.
- [17] Maier Andreas, Syben Christopher, Lasser Tobias, Riess Christian. A gentle introduction to deep learning in medical image processing *Zeitschrift für Medizinische Physik* 2019; **29**(2):86 - 101. Special Issue: Deep Learning in Medical Physics.
- [18] Hoppe Elisabeth, Thamm Florian, Körzdörfer Gregor, et al. Magnetic Resonance Fingerprinting Reconstruction Using Recurrent Neural Networks *Stud Health Technol Inform* 2019; **267**:126-133.
- [19] Fang Z., Chen Y., Liu M., et al. Deep Learning for Fast and Spatially Constrained Tissue Quantification From Highly Accelerated Data in Magnetic Resonance Fingerprinting *IEEE Transactions on Medical Imaging* 2019; **38**(10):2364-2374.
- [20] Akcakaya Mehmet, Moeller Steen, Weingärtner Sebastian, Ugurbil Kamil. Scan-specific robust artificial-neural-networks for k-space interpolation (RAKI) reconstruction: Database-free deep learning for fast imaging *Magnetic Resonance in Medicine* 2019; **81**(1):439-453.
- [21] Zhang Chi, Hosseini Seyed Amir Hossein, Weingärtner Sebastian, Ugurbil Kamil, Moeller Steen, Akçakaya Mehmet. Optimized fast GPU implementation of robust artificial-neural-networks for k-space interpolation (RAKI) reconstruction *PLOS ONE* 2019; **14**(10):1-14.

PUBLICATION IV

- [22] Hammernik Kerstin, Klatzer Teresa, Kobler Erich, et al. Learning a variational network for reconstruction of accelerated MRI data *Magnetic Resonance in Medicine* 2018; **79**(6):3055-3071.
- [23] Schlemper J., Caballero J., Hajnal J. V., Price A. N., Rueckert D.. A Deep Cascade of Convolutional Neural Networks for Dynamic MR Image Reconstruction *IEEE Transactions on Medical Imaging* 2018; **37**(2):491-503.
- [24] Knoll Florian, Hammernik Kerstin, Kobler Erich, Pock Thomas, Recht Michael P, Sodickson Daniel K. Assessment of the generalization of learned image reconstruction and the potential for transfer learning *Magnetic Resonance in Medicine* 2019; **81**(1):116-128.
- [25] Benou A., Veksler R., Friedman A., Riklin Raviv T.. Ensemble of expert deep neural networks for spatio-temporal denoising of contrast-enhanced MRI sequences *Medical Image Analysis* 2017; **42**:145 - 159.
- [26] Bermudez Camilo, Plassard Andrew J., Davis Larry T., Newton Allen T., Resnick Susan M., Landman Bennett A.. Learning Implicit Brain MRI Manifolds with Deep Learning *CoRR* 2018; **abs/1801.01847**.
- [27] Manjon Jose V., Coupe Pierrick. MRI denoising using Deep Learning and Non-local averaging *CoRR* 2019; **abs/1911.04798**.
- [28] You Xuexiao, Cao Ning, Lu Hao, Mao Minghe, Wang Wei. Denoising of MR images with Rician noise using a wider neural network and noise range division *Magnetic Resonance Imaging* 2019; **64**:154 - 159. Artificial Intelligence in MRI.
- [29] Manjón José Vicente, Coupé Pierrick. MRI denoising using Deep Learning and Non-local averaging *ArXiv* 2019; **abs/1911.04798**.
- [30] Jog A., Roy S., Carass A., Prince J. L.. Magnetic resonance image synthesis through patch regression in *2013 IEEE 10th International Symposium on Biomedical Imaging*:350-353 2013.
- [31] Jog Amod, Carass Aaron, Roy Snehashis, Pham Dzung L., Prince Jerry L.. Random forest regression for magnetic resonance image synthesis *Neuroimaging* 2017; **35**:475 - 488.
- [32] Cao X., Yang J., Zhang J., Wang Q., Yap P., Shen D.. Deformable Image Registration Using a Cue-Aware Deep Regression Network *IEEE Transactions on Biomedical Engineering* 2018; **65**(9):1900-1911.

- [33] Vos Bob D., Berendsen Floris F., Viergever Max A., Sokooti Hessem, Staring Marius, Isgum Ivana. A Deep Learning Framework for Unsupervised Affine and Deformable Image Registration 2018.
- [34] Ghosal Sayan, Ray Nilanjan. Deep deformable registration: Enhancing accuracy by fully convolutional neural net *Pattern Recognition Letters* 2017; **94**:81 - 86.
- [35] Golbabaee Mohammad, Chen Dongdong, Gómez Pedro A., Menzel Marion I., Davies Mike E.. A deep learning approach for Magnetic Resonance Fingerprinting *ArXiv* 2018; **abs/1809.01749**.
- [36] Cohen Ouri, Zhu Bo, Rosen Matthew S.. MR fingerprinting Deep RecOnstruction NEtwork (DRONE) *Magnetic Resonance in Medicine* 2018; **80**(3):885-894.
- [37] Hoppe Elisabeth, Körzdörfer Gregor, Würfl Tobias, et al. Deep Learning for Magnetic Resonance Fingerprinting: A New Approach for Predicting Quantitative Parameter Values from Time Series *Stud Health Technol Inform* 2017; **243**:202-206.
- [38] Oksuz Ilkay, Cruz Gastao, Clough James, et al. *Magnetic resonance fingerprinting using recurrent neural networks*;2019-April:1537–1540. IEEE Computer Society 2019.
- [39] Chen Yong, Fang Zhengnan, Hung Sheng-Che, Chang Wei-Tang, Shen Dinggang, Lin Weili. High-resolution 3D MR Fingerprinting using parallel imaging and deep learning *NeuroImage* 2020; **206**:116329.
- [40] Hamilton J. I., Seiberlich N.. Machine Learning for Rapid Magnetic Resonance Fingerprinting Tissue Property Quantification *Proceedings of the IEEE* 2020; **108**(1):69-85.
- [41] Balsiger Fabian, Shridhar Konar Amaresha, Chikop Shivaprasad, et al. Magnetic Resonance Fingerprinting Reconstruction via Spatiotemporal Convolutional Neural Networks in *Machine Learning for Medical Image Reconstruction* (Knoll Florian, Maier Andreas, Rueckert Daniel. , eds.)(Cham):39–46Springer International Publishing 2018.
- [42] Balsiger Fabian, Scheidegger Olivier, Carlier Pierre G., Marty Benjamin, Reyes Mauricio. On the Spatial and Temporal Influence for the Reconstruction of Magnetic Resonance Fingerprinting ;102 of *Proceedings of Machine Learning Research*(London, United Kingdom):27–38PMLR 2019.
- [43] Ronneberger O., P.Fischer , Brox T.. U-Net: Convolutional Networks for Biomedical Image Segmentation in *Medical Image Computing and Computer-Assisted*

PUBLICATION IV

Intervention (MICCAI);9351 of *LNCS*:234–241 Springer 2015. (available on arXiv:1505.04597 [cs.CV]).

- [44] Ding Pak Lun Kevin, Li Zhiqiang, Zhou Yuxiang, Li Baoxin. Deep residual dense U-Net for resolution enhancement in accelerated MRI acquisition in *Medical Imaging 2019* (Angelini Elsa D., Angelini Elsa D., Angelini Elsa D., Landman Bennett A., eds.) *Progress in Biomedical Optics and Imaging - Proceedings of SPIESPIE* 2019.
- [45] Han Changhee, Gesser Florian, Milacski Zoltán. CNN-based MRI Regression Using U-Net 2018.
- [46] Moeskops Pim, de Bresser Jeroen, Kuijf Hugo J., et al. Evaluation of a deep learning approach for the segmentation of brain tissues and white matter hyperintensities of presumed vascular origin in MRI *NeuroImage: Clinical* 2018; **17**:251 - 262.
- [47] Golbabaee Mohammad, Chen Dongdong, Gómez P. A., Menzel M., Davies M.. Geometry of Deep Learning for Magnetic Resonance Fingerprinting *ICASSP 2019 - 2019 IEEE International Conference on Acoustics, Speech and Signal Processing (ICASSP)* 2019; :7825-7829.
- [48] Fang Zhenghan, Chen Yong, Hung Sheng-Che, Zhang Xiaoxia, Lin Weili, Shen Dinggang. Submillimeter MR fingerprinting using deep learning–based tissue quantification *Magnetic Resonance in Medicine* 2020; **84**(2):579-591.
- [49] Wang Sijia, Peterson Daniel J., Gatenby J. C., Li Wenbin, Grabowski Thomas J., Madhyastha Tara M.. Evaluation of Field Map and Nonlinear Registration Methods for Correction of Susceptibility Artifacts in Diffusion MRI *Frontiers in Neuroinformatics* 2017; **11**:17.
- [50] Klein Arno, Andersson Jesper, Ardekani Babak A., et al. Evaluation of 14 nonlinear deformation algorithms applied to human brain MRI registration *NeuroImage* 2009; **46**(3):786 - 802.
- [51] Ashburner J, Balbastre Y, Barnes G, Brudfors M.. SPM12 *Wellcome Trust Centre for Neuroimaging. UCL* 2014; .
- [52] Bojorquez Jorge Zavala, Bricq Stéphanie, Acquitter Clement, Brunotte François, Walker Paul M., Lalande Alain. What are normal relaxation times of tissues at 3 T? *Magnetic Resonance Imaging* 2017; **35**:69 - 80.

- [53] Feng Xiang, Deistung Andreas, Reichenbach Jürgen R.. Quantitative susceptibility mapping (QSM) and $R2^*$ in the human brain at 3T: Evaluation of intra-scanner repeatability *Zeitschrift für Medizinische Physik* 2018; **28**(1):36 - 48.
- [54] Gracien René-Maxime, Maiworm Michelle, Brüche Nadine, et al. How stable is quantitative MRI? – Assessment of intra- and inter-scanner-model reproducibility using identical acquisition sequences and data analysis programs *NeuroImage* 2020; **207**:116364.
- [55] Abbas Zaheer, Gras Vincent, Möllenhoff Klaus, Keil Fabian, Oros-Peusquens Ana-Maria, Shah Nadim J.. Analysis of proton-density bias corrections based on T1 measurement for robust quantification of water content in the brain at 3 Tesla *Magnetic Resonance in Medicine* 2014; **72**(6):1735-1745.
- [56] Baudrexel Simon, Volz Steffen, Preibisch Christine, et al. Rapid single-scan T-mapping using exponential excitation pulses and image-based correction for linear background gradients *Magnetic Resonance in Medicine* 2009; **62**(1):263-268.
- [57] Wardlaw Joanna M., Valdés Hernández Maria C., Muñoz-Maniega Susana. What are White Matter Hyperintensities Made of? *Journal of the American Heart Association* 2015; **4**(6):e001140.
- [58] Cho Seong, Jones Dana, Reddick Wilburn E., Ogg Robert J., Steen R.Grant. Establishing norms for age-related changes in proton T1 of human brain tissue in vivo *Magnetic Resonance Imaging* 1997; **15**(10):1133 - 1143.
- [59] Kupeli Ali, Kocak Mehmet, Goktepel Mehmet, Karavas Erdal, Danisan Gurkan. Role of T1 mapping to evaluate brain aging in a healthy population *Clinical Imaging* 2020; **59**(1):56 - 60.
- [60] Demirel O. B., Weingärtner S., Moeller S., Akçakaya M.. Improved Regularized Reconstruction for Simultaneous Multi-Slice Cardiac MRI T1 Mapping in *2019 27th European Signal Processing Conference (EUSIPCO)*:1-5 2019.
- [61] Yogananda C. G. B., Wagner B. C., Murugesan G. K., Madhuranthakam A., Maldjian J. A.. A Deep Learning Pipeline for Automatic Skull Stripping and Brain Segmentation in *2019 IEEE 16th International Symposium on Biomedical Imaging (ISBI 2019)*:727-731 2019.
- [62] Mahbod Amirreza, Chowdhury Manish, Smedby , Wang Chunliang. Automatic brain segmentation using artificial neural networks with shape context *Pattern Recognition Letters* 2018; **101**:74 - 79.

PUBLICATION V

- [63] Palumbo L., Bosco P., Fantacci M.E., et al. Evaluation of the intra- and inter-method agreement of brain MRI segmentation software packages: A comparison between SPM12 and FreeSurfer v6.0 *Physica Medica* 2019; **64**:261 - 272.
- [64] Choi Uk-Su, Kawaguchi Hirokazu, Matsuoka Yuichiro, Kober Tobias, Kida Ikuhiro. Brain tissue segmentation based on MP2RAGE multi-contrast images in 7 T MRI *PLOS ONE* 2019; **14**(2):1-13.
- [65] Dar Salman Ul Hassan, Özbey Muzaffer, Çatl Ahmet Burak, Çukur Tolga. A Transfer-Learning Approach for Accelerated MRI Using Deep Neural Networks *Magnetic Resonance in Medicine* 2020; **84**(2):663-685.
- [66] Narayana Ponnada A., Coronado Ivan, Sujit Sheeba J., Wolinsky Jerry S., Lublin Fred D., Gabr Refaat E.. Deep-Learning-Based Neural Tissue Segmentation of MRI in Multiple Sclerosis: Effect of Training Set Size *Journal of Magnetic Resonance Imaging* 2020; **51**(5):1487-1496.
- [67] Cho Junghwan, Lee Kyewook, Shin Ellie, Choy Garry, Do Synho. How much data is needed to train a medical image deep learning system to achieve necessary high accuracy? *arXiv.org* 2015; .

Lesion probability mapping in MS patients using a regression network on MR Fingerprinting

Ingo Hermann, Eloy Martínez-Heras, Alena-Kathrin Golla, Ralf Schmidt, Elisabeth Solana, Sara Llufríu, Achim Gass, Lothar R. Schad and Frank G. Zöllner

SUBMITTED TO MAGN RESON MED. ON JANUARY 21ST, 2021

Abstract

Purpose: To develop a regression neural network for the reconstruction of lesion probability maps on Magnetic Resonance Fingerprinting using echo-planar imaging (MRF-EPI) in addition to T_1 , T_2^* , NAWM, and GM- probability maps.

Methods: We performed MRF-EPI measurements in 42 patients with multiple sclerosis and 6 healthy volunteers along two sites. A U-net was trained to reconstruct the denoised and distortion corrected T_1 and T_2^* maps, and to additionally generate NAWM-, GM-, and WM lesion probability maps.

Results: WM lesions were predicted with a dice coefficient of 0.61 ± 0.09 and a lesion detection rate of 0.85 ± 0.25 for a threshold of 33%. The network jointly enabled accurate T_1 and T_2^* times with relative deviations of 5.2% and 5.1% and average dice coefficients of 0.92 ± 0.04 and 0.91 ± 0.03 for NAWM and GM after binarizing with a threshold of 80%.

Conclusion: DL is a promising tool for the prediction of lesion probability maps in a fraction of time. These might be of clinical interest for the WM lesion analysis in MS patients.

1 Introduction

Assessment and segmentation of white matter (WM) lesions is an important step for the analysis and tracking of diseases such as multiple sclerosis (MS). WM lesions can be graded based on MRI images which showed a good correlation with symptom development in MS and clinical subtypes of MS [1, 2]. Lesion probability mapping is a method to differentiate between WM lesion groups as this corresponds to different ischemic components and neurodegeneration during disease progression [3, 4, 5, 6]. Additionally, WM lesions exhibit an increased T_1 , T_2 , and T_2^* relaxation time, and therefore, multiple quantitative approaches showed advantages in the detection, grading, and classification [7, 8, 9]. In particular, Magnetic Resonance Fingerprinting (MRF) has demonstrated a variety of applications for simultaneously quantifying multiple relaxation times at clinically acceptable scan times. In conventional MRF, thousands of highly undersampled images are acquired to produce a unique fingerprint, and these fingerprints are compared voxel-wise with a pre-calculated dictionary [10, 11]. Rieger et al. proposed an MRF method to quantify T_1 and T_2^* with an echo-planar imaging (EPI) readout [12], which showed promising results in renal and neural applications [13, 14, 15, 16]. The fact that only conventional undersampling factors lead to only slightly corrupted magnitude data reduces the time for reconstruction and increases its robustness. However, a major drawback of MRF is the tradeoff between reconstruction time and accuracy.

Deep learning (DL) has emerged into the field of MRI and achieved excellent results in data processing considering accuracy, precision, and speed. Hence, DL is increasingly outperforming conventional algorithms. Previous studies and reports suggest that convolutional neural networks (CNN) can solve high dimensional problems with excellent accuracy and in a short time for denoising, distortion correction, segmentation, classification, and reconstruction [17, 18, 19, 20, 21, 22, 23]. A promising architecture is the U-net, which has great diversity for applications such as segmentation and regression tasks [24, 25, 26]. Especially in MRF, the reconstruction of the enormous amount of acquired data can be improved and accelerated by using different network architectures such as CNN's and fully convolutional networks (FCN) [27, 28, 29, 30, 31, 32]. In previous work, a CNN was used for the denoising, distortion correction, reconstruction, and generation of NAWM and gray matter (GM) probability maps yielding results comparable to conventional methods in a fraction of time [16]. The proposed architecture combined several post-processing tasks, making the application fast and easy. However, the WM lesions have to be segmented for further analysis, which is always time-consuming and suffers from high intra and inter-observer variabilities [33]. To overcome these limitations of manual segmentation, different DL architectures and networks

have been used, yielding dice coefficients ranging from 0.48 to 0.95 for WM lesion segmentation [33, 34, 35, 36]. Therefore, in a recent publication, it was shown that this processing step can be improved by regression by also generating distance maps of the lesions [37]. This could provide more information about lesion geometry, structure, and changes similar to lesion probability mapping [2, 3].

In this work, we use the U-net as previously reported [16] to predict WM lesion probability maps by training the CNN with the manual annotated binary lesion masks.

2 Methods

2.1 Data

As previously reported [16], an MRF sequence based on echo-planar imaging was acquired across 6 healthy subjects and 18 patient with WM lesions at a 3T scanner (Magnetom Skyra, Siemens Healthineers; site 1) and 24 patient with WM lesions at a 3T scanner (Magnetom Prisma, Siemens Healthineers; site 2). The sequence parameters for both scanners were FOV = 240 x 240 mm, in-plane resolution = $1 \times 1 \text{ mm}^2$, slice thickness = 2 mm, GRAPPA factor = 3, partial fourier = 5/8, varying flip angle α (34-86°), TE (16-76.5 ms), TR (3530 - 6370 ms). At site 2, simultaneous multi-slice imaging was additionally used with an acceleration factor of 3.

2.2 CNN

A U-net was used for the denoising, distortion correction, and reconstruction of T_1 , T_2^* maps, and the NAWM-, GM-, and additionally lesion probability maps. The T_1 and T_2^* maps for training the network were reconstructed after denoising using Marchenko-Pastur Principle Component Analysis (MPPCA) [38]. The dictionary entries are in steps of 5%. Rigid registration was performed using B-spline interpolation from the undistorted T_1 map to the T_2 -weighted image using the Advanced Normalization Tools (ANT) [39]. The NAWM and GM maps were generated based on the distortion corrected T_1 maps using SPM (Statistical Parametric Mapping) [40] with a probability between 0 and 100%. Additionally, WM lesions were segmented manually by an expert radiologist, and to assess the inter-observer variability, lesions from ten patients were segmented two times (at least one week time gap), and the mean dice coefficient was calculated. The manually annotated binary lesion masks were used as a fifth training output of the CNN. The training input was always the 35 magnitude MRF-EPI data. We used two patients from site 1 and three patients from site 2 as test data and the same amount as validation data. We trained our network patch-wise using 64 random patches per slice with a patch size of 64x64 voxels, a mini batch-size of 64, 100 training epochs, and a

learning rate of 10^{-4} . Slices containing white matter lesions with a minimum volume of 100ml were augmented by a factor of five to overcome the small overall volume of the lesions compared to the whole brain. We trained four networks with all five output maps (T_1 , T_2^* , NAWM-, GM-probability maps, and WM lesion masks) and additionally the other networks with only the lesion masks as output. The following loss functions were used for one and five outputs: mean squared error (MSE), mean absolute error (MAE), logarithmic cosinus hyperbolic loss (LCL), and dice loss (DICE) as listed in Supporting Information Table S1. The naming MSE-1 and MSE-5 correspond to the loss function with the number of outputs. For all loss functions, the network was trained with both the five output maps and also only the lesion as output to validate the loss in accuracy when using multiple outputs. In previous work, it was observed that for multiple outputs the accuracy decreases of the network [16]. The accuracy compared with the conventional methods was validated with MSE-5 and MAE-5 since the MAE loss was previously shown to be the best architecture for the reconstruction of T_1 , T_2^* , NAWM-, and GM-probability maps.

2.3 Statistics

The Dice coefficient and the lesion detection rate were used as the similarity metric for the lesion segmentation. Therefore, the threshold for binarizing the reconstructed lesion probability maps was analyzed. NAWM and GM masks were binarized with a commonly used threshold of 80% [41] and mean dice coefficients along all subjects and slices were calculated. For the two other outputs (T_1 , T_2^*) the mean relative difference was calculated.

3 Results

The reconstruction with DL showed good agreement with conventional pattern matching reconstruction and a mean relative deviation of 5.2% for T_1 and 5.1% for T_2^* in the whole brain using MSE-5. The Dice coefficients for NAWM and GM after binarization with a threshold of 80% were 0.92 ± 0.04 for NAWM and 0.91 ± 0.03 for GM using MSE-5. The reconstruction of all five outputs took around one minute for the whole brain per subject, which is several orders of magnitude faster compared to the conventional processing (denoising, MRF reconstruction, distortion correction, masking, and lesion segmentation) of about three hours.

Figure 1 shows the T_1 , T_2^* , NAWM-, GM-, and lesion probability maps generated by the CNN (MSE-5) for different training epochs (1, 5, 15, 30, 70, 100) compared to the conventionally reconstructed maps and the segmented masks. Visual good image

quality was obtained for T_1 , T_2^* , NAWM-, and GM probability maps after already 5 epochs. After around 15 epochs, the network starts to predict the lesion probability maps and slowly converges towards 100 epochs.

The dice coefficient was strongly dependent on the threshold for binarizing the probability maps which was shown in Figure 2. A maximum dice coefficient of 0.75 is observed for a threshold of 41% for the training data (depicted in blue) and a maximum dice coefficient of 0.62 for a threshold of 23% for the test data (depicted in orange) respectively. For further analysis, a threshold of 33% was used to binarize the lesion probability maps into masks. At lower thresholds, the lesion detection rate increases. The dice coefficient

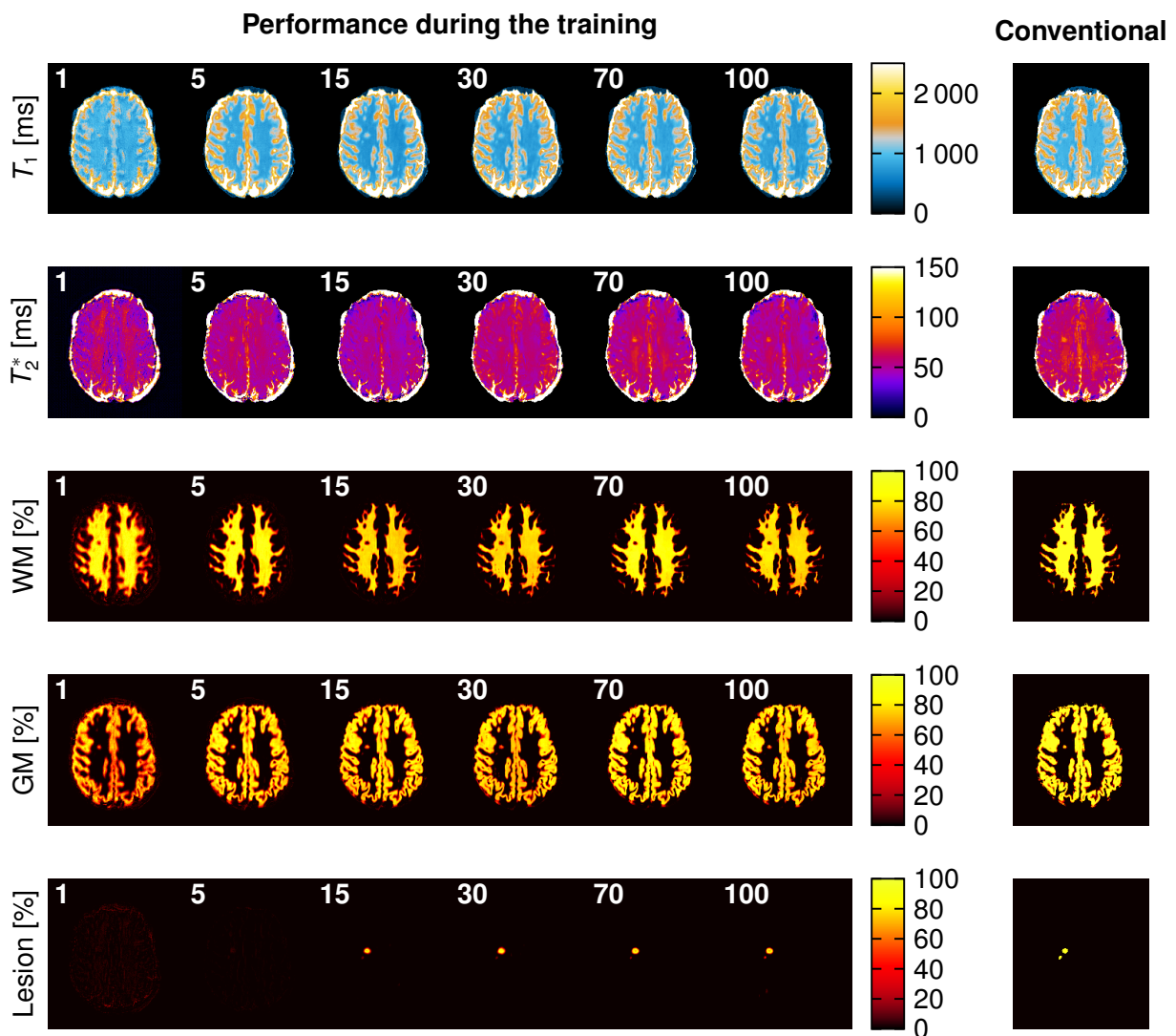


Figure 1: Visualization of the reconstruction during the training. The reconstructed T_1 , T_2^* , NAWM-, GM, and Lesion-probability maps are depicted for 1, 5, 15, 30, 70, and 100 training epochs (white number) and the dictionary matching reference maps are shown on the right side for MSE-5.

and the lesion detection rate were 0.61 ± 0.09 and 0.85 ± 0.25 for the test data using the threshold of 33%. The average dice coefficient with its inter-observer variability across different annotations was 0.68 ± 0.23 .

In Figure 3, the lesion probability is plotted versus the number of training epochs for different networks. It can be seen that training only with 1 output instead of 5 results in faster convergence of the dice coefficient, however, the dice coefficient for all three methods converges to 0.61 after about 60 epochs. The mean lesion detection rate over the entire test data was higher than 0.82 for all networks. The training with MAE-5 takes longer to start predicting lesions. The networks MAE-1, LCL-5, LCL-1, and DICE-1 converge to a local minimum while training, resulting in all lesion probabilities equal to zero. The representative lesion masks for different epochs of the MAE-5 is shown color-encoded as a 2D representation and as a cross-section of the lesion (Figure 3). An increased probability was observed at the edges of the lesion and a flat plateau in the center of the lesion.

For every test patient, one representative slice is shown in Figure 4 with the lesion probability color-encoded, and the manual annotation highlighted in blue. For patients number 1, 2, and 5 the depicted lesions of the slice correlate very well with the annotation. For patient number 3, the CNN predicted three lesions with a small probability, which were then excluded from the mask after thresholding. Only in patient number 4,

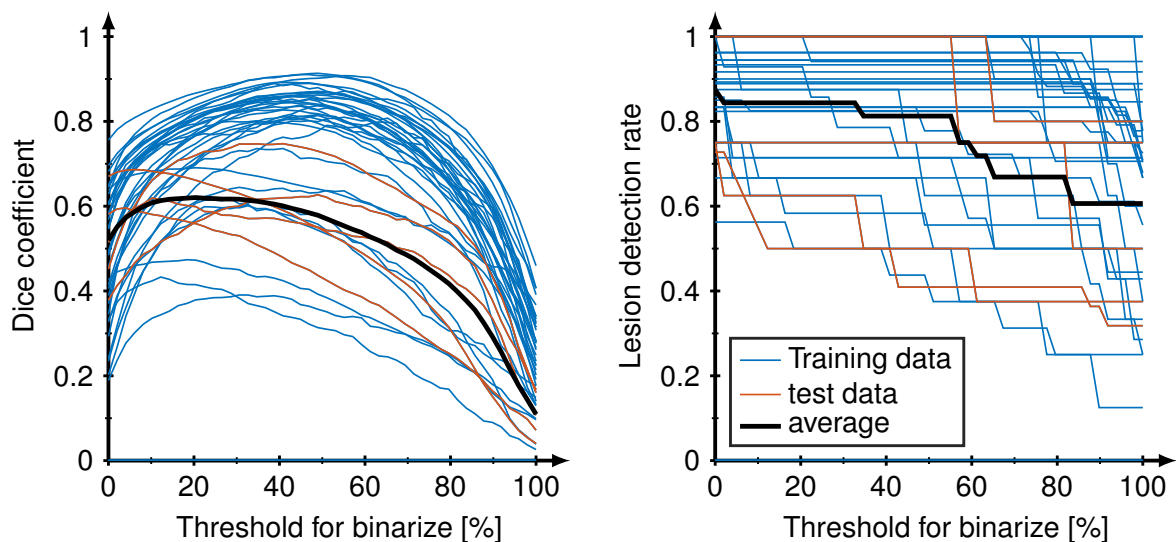


Figure 2: The dice coefficient (left) and the lesion detection rate (right) for all training data (blue) and test data (orange) are shown over the threshold to binarize the lesion probability maps. The black lines depict the average across the test data. A maximum dice coefficient is observed at a threshold of around 50%. The lesion detection rate decreases for an increasing threshold because the background of the lesion probability map is non-zero.

the network did not predict the annotated lesion near the GM. The dice coefficient and lesion detection rate are shown for all subjects in Figure 4. The test data are shown in larger marks with lighter blue and yellow colors. The CNN predicted no lesions in healthy subjects.

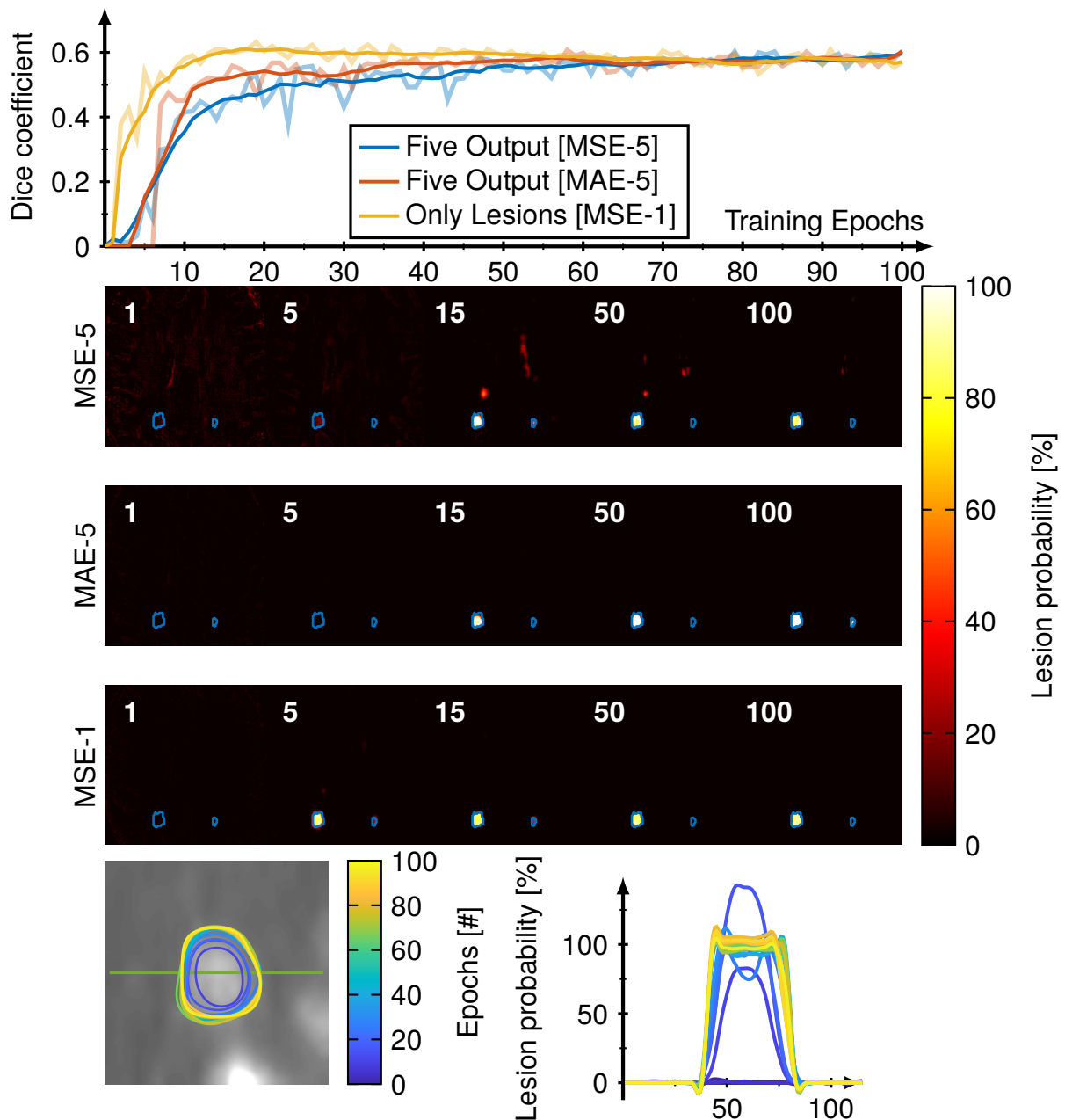


Figure 3: The dice coefficient for three different networks is depicted (five outputs with MSE [MSE-5], five outputs with MAE [MAE-5], and only lesions with MSE [MSE-1]). The dice coefficient is plotted for all three networks over the training epochs and the smoothed data is shown in the foreground colors. The corresponding lesion probability maps are shown for 1, 5, 15, 50, and 100 epochs below.

Figure 5 shows the percentage increase of a WM lesion compared to the mean NAWM times for T_1 , T_2^* , and the lesion probability generated by the CNN. The manually annotated lesion is marked in blue. A good visual correlation between the lesion probability and the increase in T_1 and T_2^* is observed, as depicted below for the two cross-sections (green and red). It was also observed that the lesion probability is increased and steeper for lesions that have increased relaxation times.

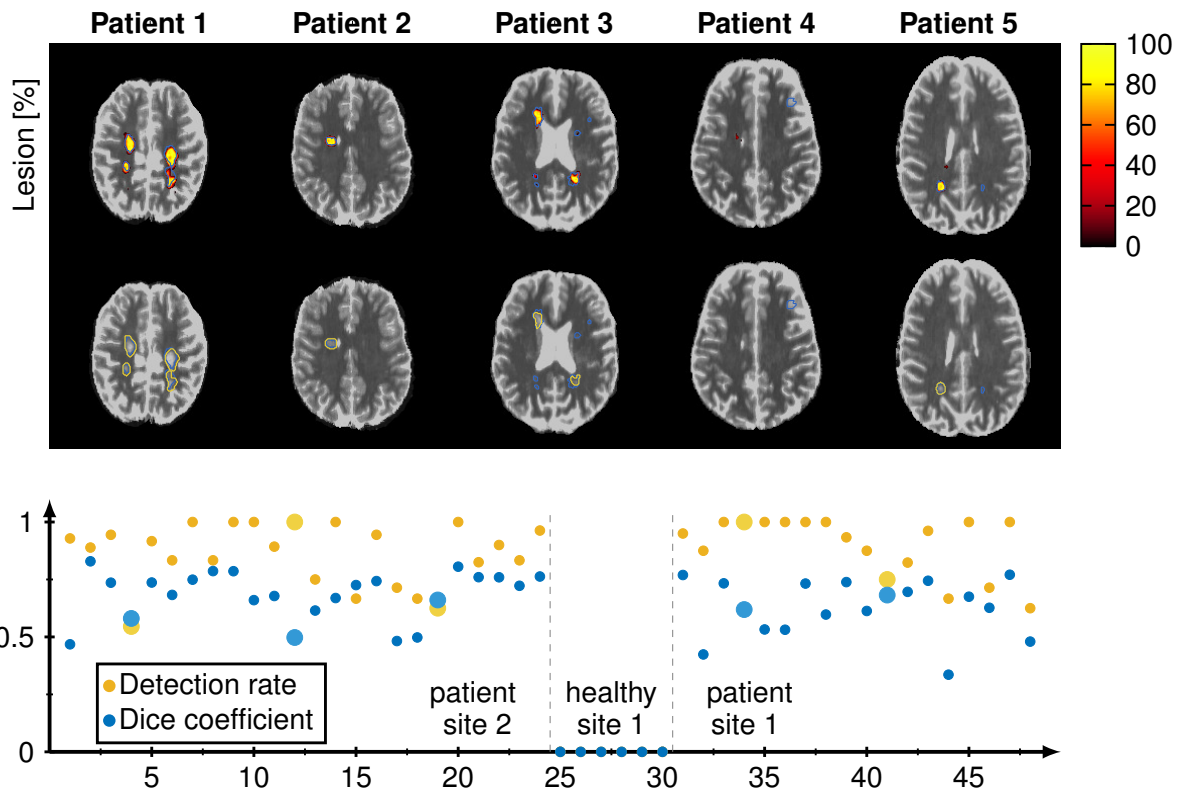


Figure 4: The reconstructed lesions probability maps are overlaid on the magnitude data in color encoding for all five different patients from the test set. Manual annotation is depicted in blue. Below the probability map is binarized and depicted in yellow in addition. The dice coefficient and white matter lesion detection rate is depicted for every patient and healthy subject for both sites. The average lesions detection rate is 0.88 and the average dice coefficient is 0.67 for all patients. The test data is shown in larger marks and brighter color and yields an average lesion detection rate of 0.85 and an average dice coefficient of 0.61 using the MSE-5.

4 Discussion

In this study, we have shown that the CNN is capable of predicting lesion probability maps, which correlate with an increase in T_1 and T_2^* times in NAWM. After binarizing the probability maps, the dice coefficient was 0.61 ± 0.09 for the test data, which is comparable to the inter-observer variability of the manual drawer (0.68 ± 0.23) and is

comparable to literature (0.47-0.95) [33, 36]. However, the CNN is more robust compared with manual annotations. We have shown that the network only predicts lesion probability maps for the loss functions MAE and MSE. This could be due to the fact that outliers, such as the small spherical lesions, are weighted more heavily with MSE and MAE compared with LCL or the dice loss. This was also observed for MAE-1, despite MAE-5 was able to predict lesions. In each case, training with one or all five output masks converged to the same dice coefficient regardless of the network, demonstrating the ability to reconstruct all maps within a single architecture (Figure 3).

Additionally, the network was able to perform the tasks of reconstruction, denoising, distortion correction, and segmentation within a single architecture with promising accuracy. T_1 and T_2^* maps as well as the NAWM- and GM-probability maps showed good agreement as also previously reported [16] with a mean relative error of 5.2% for T_1 and T_2^* and mean dice coefficients of higher than 0.9 for NAWM and GM. It was observed, that the network first learns to reconstruct the T_1 , T_2^* , NAWM, and GM probability maps,

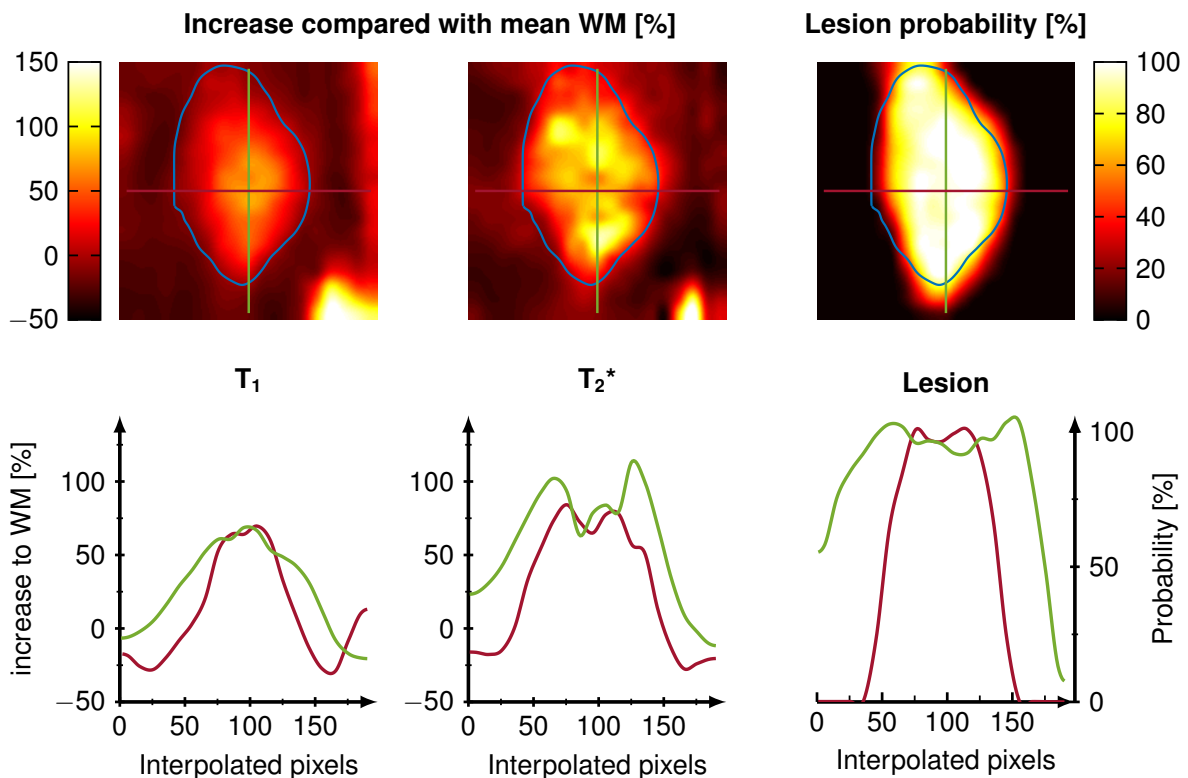


Figure 5: One lesion is depicted in a zoomed-in version with a bilinear interpolation of factor 10. The increase in T_1 and T_2^* compared with the mean NAWM is color encoded in percentage and the lesion probability generated by the CNN is shown on the right side. The manual annotation is drawn as a blue line. Below the voxel-wise values are depicted for one horizontal (red) and one vertical (green) cut through the lesion.

as evidenced by the good visual image quality after only 5 epochs. This could be explained by the several orders increase in the number of non-zero voxels in these maps compared to the low number of lesion voxels per slice.

The lesion probability maps visually correlate well with the increase in T_1 and T_2^* compared to the mean NAWM times. This could indicate that larger or more intense lesions are also predicted as such by the CNN. Therefore, these lesion probability maps could be used to automatically rate and differentiate different lesions based on the MRF input data. This is similar to the results of other lesion probability mapping methods. However, these methods rely either on manual grading, voxel-wise, or local spatial dependent models, which are time-consuming and susceptible to patient-specific covariances [1, 2, 3, 5]. In addition, our approach could include the underlying information of the evolution of the MRF scan. It has been shown that principal component analysis (PCA), which also uses the input magnitude MRF data, allows separation of the brain into multiple components such as myelin and WM lesions [42]. The CNN might be able to learn and distinguish these underlying components, improving lesion segmentation and prediction. This is an information gain compared to manual annotators and compared to lesion segmentation methods based solely on the quantitative parametric maps [36, 37].

This study has some limitations. Because the lesions were manually segmented, there is a large amount of variation in the annotation, which was also evident in the relatively high inter-observer variability (0.68). This could be improved by performing more annotations from multiple annotators to reduce this variability, but this is very time-consuming. The reduced variability in the lesion masks could also lead to better and faster training performance of the network, yielding higher dice coefficients. WM lesions are often difficult to differentiate from NAWM in the T_1 and T_2^* maps without knowledge of surrounding layer information because NAWM lesions appear similar to lobes of the GM inside the NAWM. The reconstruction could be improved by using a 3D CNN with 3D patches. However, we have tried to train a 3D architecture, but the 3D CNN was not able to predict any lesions and the accuracy for the other outputs was compromised. This could be because 3D architectures require more data and longer training compared with 2D CNNs. Therefore, more data needs to be acquired for comparable 3D results, which will be the content of further work. This could also be the reason why some loss functions could not generate lesion probability maps.

5 Conclusion

In this work we showed, that training with lesion masks can be used to generate lesion probability maps, which might improve diagnostics. Additionally, the single CNN is a promising tool for the reconstruction, denoising, distortion correction of T_1 and T_2^* maps and additionally to generate NAWM, GM probability maps. The reconstruction for a whole brain took less than one minute, which is more than a 100 fold acceleration compared with conventional processing.

References

- [1] Kincses ZT, Ropele S, Jenkinson M, et al. Lesion probability mapping to explain clinical deficits and cognitive performance in multiple sclerosis *Mult. Scler.* 2011; **17**(6):681-689.
- [2] Ge T, Müller-Lenke N, Bendfeldt K, Nichols TE, Johnson TD. Analysis of multiple sclerosis lesions via spatially varying coefficients *Ann Appl Stat* 2014; **8**(2):1095-1118.
- [3] Enzinger Christian, Smith Stephen, Fazekas Franz, et al. Lesion probability maps of white matter hyperintensities in elderly individuals - Results of the Austrian stroke prevention study *J. Neurol.* 2006; **253**:1064-70.
- [4] DeCarli C, Fletcher E, Ramey V, Harvey D, Jagust J.. Anatomical mapping of white matter hyperintensities (WMH): exploring the relationships between periventricular WMH, deep WMH, and total WMH burden *Stroke* 2005; **36**(1):50-55.
- [5] Filli Lukas, Hofstetter Louis, Kuster Pascal, et al. Spatiotemporal distribution of white matter lesions in relapsing–remitting and secondary progressive multiple sclerosis *Mult. Scler.* 2012; **18**(11):1577-1584.
- [6] Holland Christopher M., Charil Arnaud, Csapo Istvan, et al. The Relationship between Normal Cerebral Perfusion Patterns and White Matter Lesion Distribution in 1,249 Patients with Multiple Sclerosis *J Neuroimaging* 2012; **22**(2):129-136.
- [7] Bonnier Guillaume, Roche Alexis, Romascano David, et al. Advanced MRI unravels the nature of tissue alterations in early multiple sclerosis *Ann Clin Transl Neurol* 2014; **1**(6):423-432.
- [8] Blystad I., Håkansson I., Tisell A., et al. Quantitative MRI for Analysis of Active Multiple Sclerosis Lesions without Gadolinium-Based Contrast Agent *Am J Neuroradiol* 2016; **37**(1):94–100.
- [9] Hernández-Torres Enedino, Wiggermann Vanessa, Machan Lindsay, et al. Increased mean R2* in the deep gray matter of multiple sclerosis patients: Have we been measuring atrophy? *J Magn Reson Imaging* 2019; **50**(1):201-208.
- [10] Ma Dan, Gulani Vikas, Seiberlich Nicole, et al. Magnetic resonance fingerprinting *Nature* 2013; **495**:187–192.
- [11] Panda Ananya, Mehta Bhairav B., Coppo Simone, et al. Magnetic Resonance Fingerprinting-An Overview *Curr Opin Biomed Eng* 2017; **3**(1).

- [12] Rieger Benedikt, Zimmer Fabian, Zapp Jascha, Weingartner Sebastian, Schad Lothar R.. Magnetic Resonance Fingerprinting using echo planar imaging Joint quantification of T1 and relaxation times *Magn Reson Med* 2017; **78**(5):1724-1733.
- [13] Rieger Benedikt, Akçakaya Mehmet, Pariente José C., et al. Time efficient whole-brain coverage with MR Fingerprinting using slice-interleaved echo-planar-imaging *Sci Rep* 2018; **8**(1):2045-2322.
- [14] Hermann Ingo, Chacon-Caldera Jorge, Brumer Irène, et al. Magnetic resonance fingerprinting for simultaneous renal T1 and T2* mapping in a single breath-hold *Magn Reson Med* 2020; **83**(6):1940-1948.
- [15] Khajehim Mahdi, Christen Thomas, Chen J. Jean. Magnetic Resonance Fingerprinting with Combined Gradient- and Spin-echo Echo-planar Imaging: Simultaneous Estimation of T1, T2 and T2* with integrated-B1 Correction *bioRxiv* 2019; (10.1101/604546).
- [16] Hermann Ingo, Martínez-Heras Eloy, Rieger Benedikt, et al. Accelerated white matter lesion analysis based on simultaneous T1 and T2* quantification using Magnetic Resonance Fingerprinting and Deep Learning *Magn Reson Med* 2021; (10.1002/mrm.28688).
- [17] Lundervold Alexander Selvikvåg, Lundervold Arvid. An overview of deep learning in medical imaging focusing on MRI *Z Med Phys* 2019; **29**(2):102 - 127.
- [18] Benou A., Veksler R., Friedman A., Riklin Raviv T.. Ensemble of expert deep neural networks for spatio-temporal denoising of contrast-enhanced MRI sequences *Med Image Anal* 2017; **42**:145 - 159.
- [19] Cao X., Yang J., Zhang J., Wang Q., Yap P., Shen D.. Deformable Image Registration Using a Cue-Aware Deep Regression Network *IEEE Trans Bio-Med Eng* 2018; **65**(9):1900-1911.
- [20] Maier Andreas, Syben Christopher, Lasser Tobias, Riess Christian. A gentle introduction to deep learning in medical image processing *Z Med Phys* 2019; **29**(2):86 - 101.
- [21] Akcakaya Mehmet, Moeller Steen, Weingärtner Sebastian, Ugurbil Kamil. Scan-specific robust artificial-neural-networks for k-space interpolation (RAKI) reconstruction: Database-free deep learning for fast imaging *Magn Reson Med* 2019; **81**(1):439-453.

- [22] Hammernik Kerstin, Klatzer Teresa, Kobler Erich, et al. Learning a variational network for reconstruction of accelerated MRI data *Magn Reson Med* 2018; **79**(6):3055-3071.
- [23] Schlemper J., Caballero J., Hajnal J. V., Price A. N., Rueckert D.. A Deep Cascade of Convolutional Neural Networks for Dynamic MR Image Reconstruction *IEEE Trans Med Imaging* 2018; **37**(2):491-503.
- [24] Ronneberger O., P.Fischer , Brox T.. U-Net: Convolutional Networks for Biomedical Image Segmentation in *Medical Image Computing and Computer-Assisted Intervention (MICCAI)*;9351 of *LNCS*:234–241Springer 2015.
- [25] Yao Wei, Zeng Zhigang, Lian Cheng, Tang Huiming. Pixel-wise regression using U-Net and its application on pansharpening *Neurocomputing* 2018; **312**:364 - 371.
- [26] Moeskops Pim, de Bresser Jeroen, Kuijf Hugo J., et al. Evaluation of a deep learning approach for the segmentation of brain tissues and white matter hyperintensities of presumed vascular origin in MRI *Neuroimage Clin.* 2018; **17**:251 - 262.
- [27] Hoppe Elisabeth, Körzdörfer Gregor, Würfl Tobias, et al. Deep Learning for Magnetic Resonance Fingerprinting: A New Approach for Predicting Quantitative Parameter Values from Time Series *Stud Health Technol Inform* 2017; **243**:202-206.
- [28] Fang Z., Chen Y., Liu M., et al. Deep Learning for Fast and Spatially Constrained Tissue Quantification From Highly Accelerated Data in Magnetic Resonance Fingerprinting *IEEE Trans Med Imaging* 2019; **38**(10):2364-2374.
- [29] Balsiger Fabian, Scheidegger Olivier, Carlier Pierre G., Marty Benjamin, Reyes Mauricio. On the Spatial and Temporal Influence for the Reconstruction of Magnetic Resonance Fingerprinting ;102 of *Proceedings of Machine Learning Research*(London, United Kingdom):27–38PMLR 2019.
- [30] Hoppe Elisabeth, Thamm Florian, Körzdörfer Gregor, et al. Magnetic Resonance Fingerprinting Reconstruction Using Recurrent Neural Networks *Stud Health Technol Inform* 2019; **267**:126-133.
- [31] Fang Zhengnan, Chen Yong, Hung Sheng-Che, Zhang Xiaoxia, Lin Weili, Shen Dinggang. Submillimeter MR fingerprinting using deep learning–based tissue quantification *Magn Reson Med* 2020; **84**(2):579-591.
- [32] Chen Yong, Fang Zhengnan, Hung Sheng-Che, Chang Wei-Tang, Shen Dinggang, Lin Weili. High-resolution 3D MR Fingerprinting using parallel imaging and deep learning *NeuroImage* 2020; **206**:116329.

- [33] Lladó Xavier, Oliver Arnau, Cabezas Mariano, et al. Segmentation of multiple sclerosis lesions in brain MRI: A review of automated approaches *Inf. Sci.* 2012; **186**(1):164 - 185.
- [34] La Rosa Francesco, Abdulkadir Ahmed, Fartaria Mário João, et al. Multiple sclerosis cortical and WM lesion segmentation at 3T MRI: a deep learning method based on FLAIR and MP2RAGE *Neuroimage Clin.* 2020; **27**:102335.
- [35] McKinley Richard, Wepfer Rik, Grunder Lorenz, et al. Automatic detection of lesion load change in Multiple Sclerosis using convolutional neural networks with segmentation confidence *Neuroimage Clin.* 2020; **25**:102104.
- [36] Zeng Chenyi, Gu Lin, Liu Zhenzhong, Zhao Shen. Review of Deep Learning Approaches for the Segmentation of Multiple Sclerosis Lesions on Brain MRI *Front. Neuroinform.* 2020; **14**:55.
- [37] Wijnen Kimberlin M. H., Dubost Florian, Yilmaz Pinar, et al. Automated Lesion Detection by Regressing Intensity-Based Distance with a Neural Network in *Medical Image Computing and Computer Assisted Intervention – MICCAI 2019* (Shen Dinggang, Liu Tianming, Peters Terry M., et al. , eds.)(Cham):234–242Springer International Publishing 2019.
- [38] Veraart Jelle, Novikov Dmitry S., Christiaens Daan, Ades-aron Benjamin, Sijbers Jan, Fieremans Els. Denoising of diffusion MRI using random matrix theory *NeuroImage* 2016; **15**(142):394-406.
- [39] Klein Arno, Andersson Jesper, Ardekani Babak A., et al. Evaluation of 14 nonlinear deformation algorithms applied to human brain MRI registration *NeuroImage* 2009; **46**(3):786 - 802.
- [40] Ashburner J, Balbastre Y, Barnes G, Brudfors M.. SPM12 2014.
- [41] Tudorascu Dana L., Karim Helmet T., Maronge Jacob M., et al. Reproducibility and Bias in Healthy Brain Segmentation: Comparison of Two Popular Neuroimaging Platforms *Front. Neurosci.* 2016; **10**:503.
- [42] Nagtegaal Martijn, Koken Peter, Amthor Thomas, et al. Myelin water imaging from multi-echo T2 MR relaxometry data using a joint sparsity constraint *NeuroImage* 2020; **219**:117014.

3

DISCUSSION

Quantitative magnetic resonance imaging is a promising tool for non-invasive assessment of tissue condition, which has been shown to correlate with a variety of diseases and provide clinically relevant information [28, 76, 77, 78]. However, conventional quantification methods suffer from several dependencies and susceptibilities. First, relaxation times were found to be susceptible to various patient-specific dependencies such as age, gender, and biological constituent [79], scanner-dependent parameters such as field strength [80], excitation pulse shape, sequence-dependent settings such as the use of inversion or saturation recovery [81], k-space reordering such as linear or centric [82], or sequence parameters such as flip angle, echo time, and repetition time [83]. Second, the acquisition of multiple relaxation times is time-consuming and this is especially troublesome to patients who cannot hold still, have respiratory distress, or claustrophobia. Third, the separately acquired parametric maps need to be registered and undergo multiple post-processing steps for further analysis.

The aim of this work was to develop and evaluate new simultaneous quantification methods that are resistant to larger variations and in clinically applicable measurement time.

3.1 The effect of flow on cardiac T_1 measurements

In general, flowing blood has several effects on the quantification of T_1 . It has been shown that the most important and dominant effect is the in-flow of non-prepared spin. Conventionally, a non-selective preparation pulse is acquired, to excite every spin of the entire body equally. In practice, a non-selective preparation pulse excites only parts of the body. This results in in-flowing spins which are partially unaffected from the non-selective pulse. We showed in simulations, phantom experiments, and in vivo experiments for the first time, that this effect might lead to a decrease in T_1 of up to 50%. In this work, a constant factor of the in-flowing unprepared spins was used to simplify the

complex dependence. However, several other factors such as body shape, size, position, bore radius, and bore shape are confounding factors. More complex simulations covering these effects may be necessary to accurately analyze the additional factors, which is part of further research. In addition, phantom experiments with pulsatile flow [84] and anatomy similar to the human heart [85] might be needed to account for additional perturbing factors. However, knowledge of the reduced T_1 relaxation times due to non-prepared in-flowing spins is important because variations in the estimated T_1 relaxation time lead to variations in the estimated ECV. ECV is an important biomarker of the extracellular (interstitial) volume for several pathologies such as in amyloidosis and myocardial fibrosis [86]. It has been shown that deviations of up to 17% can occur on the synthetic Hct which propagates towards the ECV value linearly, which might lead to an incorrect or unspecific diagnosis [87]. The other flow-dependent effects are the in-flow and out-flow of spins during image acquisition and the exchange of spins during a heartbeat, which results in only small changes in the T_1 time. In particular, the exchange of spins during a heartbeat compensates for the effect of spins flowing in and out. However, this is only fulfilled at an ejection fraction of 100%. Patients with heart failure may have an ejection fraction of only 50% and therefore have a mixture of stationary spins and flowing spins. On our experiments, blood T_1 -times were determined in vivo in the descending aorta, where a complete exchange of spins from heartbeat to heartbeat is warranted. Deviations in T_1 quantification of up to 20% were observed in vivo due to increased flow velocity by measuring at peak velocities (late systole) and in the absence of flow (late diastole). For further analysis, the effects of flow in the short-axis view (most commonly used slice orientation for quantitative cardiac MR) in the myocardium should be investigated, including the effect of ejection fraction and turbulent flow. From our measurements, we conclude that these effects are small compared with the in-flow of non-prepared spins and are within the range of quantification variances and therefore negligible. As a first approach, our simplified analysis helps to better understand the effects of flow on the T_1 relaxation time. The strong effect of flow on the T_1 times can partially be suppressed by the use of saturation recovery sequences. On the one hand, saturation pulses are conventionally performed in every heartbeat which decreases the time for non-prepared spins to flow inside the imaging plane. On the other hand, in-plane saturation is reduced because the magnetization history is reset every heartbeat. In this work, we measured and analyzed for the first time the effect of flow on the blood T_1 quantification in vivo. We demonstrated that saturation recovery methods for cardiac T_1 mapping are more resistant to flow-dependent effects such as the in-flow of non-prepared spins and blood flow velocity, especially when using the three-parameter fit model.

3.2 Simultaneous quantification of T_1 , T_2 , and T_2^*

A saturation-based method for simultaneous quantification of T_1 , T_2 , and T_2^* in the myocardium has been proposed. As mentioned before, ECV mapping is often used for the assessment of pathologies [87]. However, ECV mapping is based on measurements with contrast agents, which has been discredited in the last year by convincing evidence of deposition in the brain [88]. Nowadays, quantitative imaging strives for methods without contrast agents such as quantification of the relaxation times T_1 , T_2 , and T_2^* [89]. It has been shown that these relaxation times are important biomarkers for detection and discrimination of different pathologies and a variety of diseases [26, 90]. We have proposed a sequence called SATURN for the assessment of all three relaxation times, which provides comparable accuracy and precision compared to conventional methods. The proposed sequence is seven heartbeats long with two four-second pauses before the T_2 preparation pulses to warrant complete recovery before the preparation pulses. Since the saturation recovery pulses reset the magnetization history, it might be natural to use them in addition to the T_2 preparation pulses, overcoming the need for a several-second rest period. However, the recovery between the saturation recovery and the T_2 -preparation pulse is too short to achieve sufficient SNR for accurate T_2 quantification. The use of free-breathing recordings often overcomes the additional time required, as a typical breathing cycle is within the range of the acquired rest period. As a further improvement, the sequence could acquire multiple slices interleaved to fill these rest periods with acquisitions in other slices. To do this, slice-selective T_2 preparations must be acquired to avoid repetitive excitation with the preparation pulses. However, these slice-selective preparation pulses are sensitive to the profiles of the slice selection pulses, resulting in a signal loss at the edges [91]. Another way to acquire multiple slices to further save time is by an acquisition using simultaneous multi-slice acquisition [92]. The preparation pulses remain non-selective and image acquisition is performed in three slices simultaneously. Thus, the choice of rest periods is a good compromise between accuracy and measurement time. Good accuracy was observed for the quantification of T_1 . Compared to the gold standard saturation recovery method SASHA, fewer T_1 contrasts are acquired with SATURN, which might reduce the quantification precision. Since the sequence is acquired under free-breathing, the acquisition can be prolonged, and multiple averages can be acquired without bothering the patient. For each additional saturation preparation, the acquisition time is increased by only around two heartbeats (for a gating efficiency of 50%). However, the use of multi gradient-echo readout leads to an overall larger number of acquired contrasts and, thus improves quantification and compensates for the smaller amount of saturation prepa-

rations. Compared to inversion recovery methods such as MOLLI, SATURN, like conventional saturation-based methods, suffers from the fact that higher heart rates result in a shorter dynamic range. This reduces the precision and robustness of the fit [32]. The saturation recovery pulse could be placed in the preceding heartbeat to achieve a longer T_1 regrowth and, therefore, an improved sampling of the T_1 relaxation curve [93]. However, this leads to more complicated reconstructions and acquisitions. Another approach to increase the dynamic range would be to use a combination of saturation and inversion recovery pulses [81]. This was tested in experiments, hence, due to the more complex fitting model, no gain in the T_1 quantification was achieved. In patients with high heart rates, the image acquisition may be too long and thus suffer from cardiac motion. Therefore, higher acceleration factors are needed. It has been shown that for acceleration factors of $R=4$, T_1 fit quality decreases significantly. Therefore, advanced reconstruction methods such as low-rank composition and regularization can improve T_1 reconstruction. It should be noted that these methods increase the complexity of post-processing and may over-regularize small anatomical structures or pathologies. In addition, regularization could be used to increase the number of echoes per readout to achieve a more accurate sampling of the T_2^* decay. Compared to conventional T_2^* quantification methods that use TEs in the range of up to 18 ms [94], we compromise the relatively small maximum TE of 10 ms by using a truncation model [53]. This truncation model assumes that the T_2^* -decay converges to the noise floor and therefore a two-parameter exponential fit leads to a more accurate T_2^* quantification. Therefore, only measurements with sufficient SNR are considered for the five parameter fit. These effects discussed in the previous section such as reduced SNR and rest periods were simulated and agree well with both phantom and in vivo measurements. Since SNR is small for SATURN, the k-space is sampled using centric reordering. This means that the k-space center is sampled first, which exhibits increased signal but also increased change in signal over time. These higher slopes for the exponential decay at early time points, lead to blurring of the parametric maps due to the wider point spread function [82]. An improved sampling pattern could be investigated in further work with radial, spiral, or even more complex k-space sampling such as in compressed sensing. In particular, the analysis of the point spread function for different k-space reordering can be of interest. An optimum between signal intensity and image quality can be found in simulations and subsequently validated in measurements. This could shorten the overall acquisition time, increase SNR, and reduce the blurring effect.

Among other methods for simultaneous quantification of the relaxation times [54, 55, 57, 59, 65, 95, 96], SATURN is the first for the quantification of all three relaxation time. Many methods only focussed on T_1 and T_2 mapping [55, 65, 97]. However, T_2^* mapping

3.3. SIMULTANEOUS QUANTIFICATION USING MAGNETIC RESONANCE FINGERPRINTING

is increasingly gaining interest because of its strength to visualize changes in magnetic susceptibilities. On the one side, iron with high susceptibilities can be assessed as a predictive factor for heart injury [98]. On the other side, susceptibility differs in oxygenated and de-oxygenated blood, hence, it is useful for the detection of myocardial ischemia [99, 100]. SATURN enables a fast, robust, and resilient quantification of T_1 , T_2 , and T_2^* in clinically acceptable time. Additionally, it was shown in patients, that SATURN can depict pathological changes of the myocardium such as increased T_1 and T_2 times in a patient with hypertrophic cardiomyopathy. The possibility to image the whole heart without further bothering the patient with long breath-hold commands and the fact of intrinsically co-registered parametric maps marks SATURN as an excellent method, especially when multi-modality is necessary to ensure unambiguous diagnoses.

3.3 Simultaneous quantification using Magnetic Resonance Fingerprinting

Magnetic resonance fingerprinting has been one of the most significant innovations in MRI within this decade. The potential to quantify multiple relaxation times and physiological parameters simultaneously and the short acquisition time have led MRF to a plethora of applications [57, 63, 101, 102]. Compared to neurological and cardiac applications, abdominal and especially renal imaging have been lacking. MRF sequences proposed for the brain were too slow to quantify multiple slices within a single breath-hold, and cardiac MRF sequences were insufficient because of the additional ECG triggering. In this work, a renal MRF-EPI sequence was developed that allows simultaneous quantification of T_1 and T_2^* covering four slices within a single breath-hold. Compared with conventional methods, this results in a 10-fold speedup and an improvement in image resolution [103]. This MRF approach differs from the originally proposed method [61, 62]. Interpretable magnitude images are acquired, which preserve all anatomical information. This increases the measurement time per acquisition and thus decreases the maximum images acquired. However, the single magnitude images do not suffer from superior artifacts. Compared to thousands of images required, the MRF-EPI needs only 35 acquired images for robust quantification of T_1 and T_2^* . This was validated by a convergence analysis for an increased amount of acquired images showing that already 20 acquired images are sufficient. Because the amount of data is enormously reduced compared with conventional methods [73], this allows implementing the reconstruction directly at the scanner. Therefore, a fast group matching algorithm was implemented [104]. The possibility to correct for ghosting artifacts immediately after acquisition by enlarging the imaging volume allows an advantageous

and easy application in the clinic. An important dependency with MRF-EPI is that image quality is directly dependent on the quality of the underlying magnitude data. Therefore, it has been shown that improving the magnitude data by increasing SNR using denoising strategies improves the quality of the reconstructed parametric maps [63]. However, MRF-EPI requires a trade-off between fast acquisitions and sufficient SNR. In this approach, the k-space is corrupted by using Partial Fourier 5/8 and Grappa with acceleration factor 3. Reducing these acceleration factors results in increased minimum echo time, which significantly degrades the reconstructed parametric maps. Several factors could achieve a gain in SNR such as 3D imaging [105], improved k-space sampling such as in EPTI [106], the use of compressed sensing [107], or stronger and faster gradient systems. Therefore, this renal MRF technique is promising for future applications because the image quality benefits from factors that have evolved drastically in the last decade. It was observed that the standard deviation of the proposed MRF sequence was small compared with the variations which are commonly seen in diseased kidneys such as chronic kidney disease or kidney transplants [108, 109, 110]. MRF-EPI yielded robust results in the kidneys. Hence, it could also be applied in other abdominal regions such as the liver or prostate, as some clinical studies are already beginning to show. The liver might be more challenging due to susceptibility artifacts occurring near the lungs. Moreover, the information of MRF acquisition can be increased by adding additional parametric maps such as T_2 [111], $T_1\rho$ [112], RAFF [113], oxygenation [114], or diffusion [115]. Here, the corresponding preparations have to be implemented before the image readout generating these additional contrasts and has to be added in the dictionary simulations. However, the measurement time is extended, and the complexity of the dictionary increases exponentially. This shows that MRF-EPI has a great potential for further improvement and optimization and could become established into clinical routines.

Originally, the MRF-EPI sequence has been developed for neural applications. The advantage of EPI readout in the brain is that artifacts due to motion and susceptibility are rare. Patients with multiple sclerosis were studied in a clinical trial at the University Hospital of Mannheim and the University Hospital of Barcelona. MRF-EPI was acquired in 60 slices in less than five minutes and achieved excellent image quality of the T_1 and T_2^* maps. These relaxation times are promising biomarkers for inflammatory processes and might improve the WM lesion segmentation. Increased T_1 and T_2^* times were observed in these lesions, with T_2^* leading to clear separation to both WM and GM. However, the major drawback of MRF is the long processing due to denoising, reconstruction, distortion correction, and masking.

3.4 Deep Learning accelerated reconstruction

In publication IV, it has been shown that neural networks in the form of a u-net are excellent at solving multidimensional tasks and overcoming the conventionally existing trade-off between acquisition time and reconstruction accuracy. The u-net was able to perform the following tasks such as denoising, reconstruction, distortion correction, and WM/GM masking in less than one minute, resulting in a speedup factor of more than 100 compared to conventional processing. Because the network has been trained on data from two sites with different magnetization evolutions, the network demonstrated robustness in dealing with different sequence parameters. When MRF-EPI is applied with different sequence parameters, new dictionaries must be computed. Thus, the neural network needs to be retrained, which could be performed using transfer learning [116]. This enables the possibility to retrain parts of the network without significantly changing the already learned processing. The proposed deep learning reconstruction solves a voxel-to-voxel image regression task, including denoising and geometric operations to correct for distortions. This allows training with a relatively small amount of data, as conventionally required [71, 73]. To simplify the training process, each layer was divided into small patches, which was shown to improve local geometric transformation such as in distortion correction. It has been shown that the network improved greatly (up to 25%) when training the network with patches compared to the full input resolution. Besides, the choice of loss functions is important to achieve the best results. Compared to MSE, which is the most commonly used in other MRF reconstruction approaches [71, 72, 117], the publication IV showed improved results for MAE and LCL. This could be due to the relatively large error in CSF when using the MSE. However, quantification of the CSF is less clinically relevant. Further work could include new designs of loss functions to optimize for this loss in accuracy such as a relative loss. In addition to the reconstruction of T_1 and T_2^* maps, the DL reconstruction generated WM and GM probability maps. As mentioned before, these are of great interest because relaxation times vary dependent on patient-specific parameters [79]. Therefore, a quantitative statement must be related to patient-specific mean relaxation times in WM and GM. This results in improved comparability between patients, between sequences, and between MRI scanners as the entire processing is performed from the same network. Additional masks such as the CSF or other specific areas of the brain could easily be included in the training process. It has been shown that training with multiple output maps only slightly affects the precision and accuracy and can be compensated by an increased amount of epochs. The proposed DL approach demonstrated the wide variety of methods that could be combined within a single network architecture.

3.5 Deep Learning lesion probability mapping

Additionally, the network was improved by incorporating the lesion masks into the training process. Thus, we have shown that a regression neural network can predict WM lesions and additionally generate probability maps that can provide deeper insights into the underlying biological processes within the lesions. The predicted lesion probability correlated very well with the increase in T_1 and T_2^* relaxation times. Similar to principal component analysis [118], the neural network might separate the biological components such as myelin. Lesion probability mapping is a method to differentiate between WM lesion groups as this corresponds to different ischemic components and neurodegeneration during disease progression [119, 120, 121, 122]. This could be advantageous over conventional lesion segmentations which are commonly based on the FLAIR images or the parametric maps but not on the underlying contrast weightings. The reconstructed WM lesion masks depend strongly on the threshold for binarization of the lesion probability maps. A maximum dice coefficient has been found for 41% of the training data but only 25% of the test data. This difference could indicate that the network has not yet converged and therefore requires longer training with additional augmentation. More data is always an advantage for training neural networks. This is especially significant when reconstruction is performed in 3 dimensions. 3D reconstructions benefit from volumetric information, which makes it easier to distinguish WM lesions and GM lobes, which are indistinguishable when looking at a single slice. WM lesions typically appear as 3D spheres, hence, the slice-by-slice analysis used in this thesis suffers from the lack of information from adjacent slices. Hence experiments with 3D networks resulted in a strongly degraded reconstruction. Additionally, only the networks with MAE and MSE could reconstruct the lesion probability maps, which also indicates the lack of data. The lesion probability maps might improve diagnostic decision-making, which has to be evaluated in more detail, especially considering the clinical impact. Therefore, different WM lesions could manually be rated and compared with the determined probability. With this, we showed that masking and segmentation processes can be included in a single regression neural network which opens up a wide field for novel methods and applications. It has been shown that the neural network is capable of solving complex and extensive reconstruction problems. WM lesion segmentation yielded high precision and dice coefficients similar to manual annotations with the potential of outperforming conventional segmentation and classification processes.

4

CONCLUSION

The aim of this work was to develop novel quantification methods, particularly for the heart, the kidneys, and the brain, to allow rapid non-invasive imaging of the most relevant relaxation times in vivo. Two fundamentally different approaches were developed. For cardiac imaging, quantification was performed with preparation pulses, whereas for brain and kidney measurements, MRF based on variable flip angles, TE, and TR was implemented. Both approaches were evaluated in simulations, phantom measurement, healthy subjects, and patients. In addition, the entire MRF post-processing was replaced using a single neural network for easy clinical use.

In the first step, the influence of blood flow on the conventional T_1 mapping sequences was analyzed. Only the in-flow of non-prepared spins leads to a significant shortening of the blood T_1 time. The other two factors induced by blood flow were within the tolerance of the quantification variance and partially compensated each other. For the first time, the effect of blood flow was assessed in phantom measurements and in vivo measurements and was confirmed by the simulations. Saturation recovery sequences were found to be resistant to flow effects, especially when a three-parameter fit model was used.

Based on these results and the trend toward non-invasive imaging without contrast agents, a novel method for simultaneous quantification of all three relevant relaxation times T_1 , T_2 , and T_2^* was proposed. Good visual image quality and accurate estimation of relaxation times were obtained in both phantom and in vivo measurements. This technique is of importance regarding several aspects. All parametric maps are intrinsically registered, which minimizes post-processing steps. The parametric maps are reconstructed inline on the scanner, which allows straightforward clinical use. The

CHAPTER 4. CONCLUSION

sequence is acquired during free-breathing, which is essential for patients who have difficulty in holding their breath. Additionally, this facilitates the assessment of the entire myocardium in a clinically acceptable measurement time. SATURN demonstrated good sensitivity in pathologies such as hypertrophic cardiomyopathy and hypertensive heart disease, and is therefore a promising approach for further clinical applications.

In the second part of this thesis, simultaneous quantification of the renal T_1 and T_2^* times using an MRF-EPI was achieved. Good quantification accuracy and precision were observed in the kidneys with a 10-fold speedup compared to conventional quantification methods. In addition, it was shown that denoising of the magnitude images before reconstruction resulted in improved image quality. The high accuracy and precision promised sensitivity to renal disease. This sequence is of great clinical interest and can be easily transferred to other abdominal regions.

In a two-site clinical study, T_1 and T_2^* times were analyzed in WM lesions in patients with MS. Increased T_1 and T_2^* times were observed in WM lesions compared with WM, and lesions were distinguishable from GM and CSF. Improved lesion detection and segmentation can be performed with these parametric maps. The need for a long processing time of several hours due to denoising, reconstruction, distortion correction, masking, and lesion segmentation was solved by the use of a single neural network. A good correlation compared with conventional processing was observed in a fraction of time. In addition, the neural network was capable of segmenting lesions and assigning probabilities to these WM lesions. These determined probabilities are in good correlation with the increased T_1 and T_2^* times observed in WM lesions. This is of great clinical interest, as the network learns from underlying structures captured in the MRF evolution, with the potential to outperform manual annotations.

In this work, novel non-invasive quantitative methods have been developed, analyzed, and clinically evaluated that showed great utility, especially considering measurement and processing time. The quantitative parametric maps generated by these new methods provide combined information about the underlying biological tissue for improved diagnosis and prediction of pathologies in a variety of diseases.

REFERENCES

- [1] *Cardiovascular Disability: Updating the Social Security Listings*;7. Institute of Medicine (US) Committee on Social Security Cardiovascular Disability Criteria 2010.
- [2] Gerlach Walther, Stern Otto. Der experimentelle Nachweis der Richtungsquantelung im Magnetfeld *Z. Phys.* 1922; **9**(1):349-352.
- [3] Rabi I. I., Zacharias J. R., Millman S., Kusch P.. A New Method of Measuring Nuclear Magnetic Moment *Phys. Rev.* 1938; **53**:318–318.
- [4] Bloch F.. Nuclear Induction *Phys. Rev.* 1946; **70**:460–474.
- [5] Purcell E. M., Torrey H. C., Pound R. V.. Resonance Absorption by Nuclear Magnetic Moments in a Solid *Phys. Rev.* 1946; **69**:37–38.
- [6] Mansfield P., Grannell P. K.. NMR 'diffraction' in solids? *J Phys C Solid State Phys* 1973; **6**(22):422–427.
- [7] Lauterbur P. C.. Image Formation by Induced Local Interactions: Examples Employing Nuclear Magnetic Resonance *Nature* 1973; **242**(190):422.
- [8] Brewer RG, Hahn EL.. Atomic memory *Sci. Amer.* 1984; **251**(6):50-57.
- [9] Elster AD. Gradient echo imaging: techniques and acronyms *Radiology* 1993; **186**(1):1-8.
- [10] Ernst R. R., Anderson W. A.. Application of Fourier Transform Spectroscopy to Magnetic Resonance *Review of Scientific Instruments* 1966; **37**(1):93-102.
- [11] Markl Michael, Leupold Jochen. Gradient echo imaging *J Magn Reson Imaging* 2012; **35**(6):1274-1289.
- [12] Ferreira P.F., Gatehouse , Mohiaddin R.H.. Cardiovascular magnetic resonance artefacts *J Cardiovasc Magn Reson* 2013; **15**(41).
- [13] Mansfield P, Maudsley A A, Bains T. Fast scan proton density imaging by NMR *J. Phys. E: Sci. Instrum.* 1976; **9**(4):271–278.
- [14] Haase A, Frahm J, Matthaei D, Hanicke W, Merboldt K.-D. FLASH imaging. Rapid NMR imaging using low flip-angle pulses *J. Magn. Reson.* 1986; **67**(2):258 - 266.
- [15] Baksi Arun John, Pennell Dudley John. Gradient echo imaging *Top Magn Reson Imaging* 2014; **23**(1):13-20.

REFERENCES

- [16] Carr HY. Steady-state free precession in nuclear magnetic resonance *Phys. Rev.* 1958; **112**:1693-1701.
- [17] Chavhan Govind B., Babyn Paul S., Jankharia Bhavin G., Cheng Hai-Ling M., Shroff Manohar M.. Steady-State MR Imaging Sequences: Physics, Classification, and Clinical Applications *RadioGraphics* 2008; **28**(4):1147-1160.
- [18] Xiang Qing-San, Hoff Michael N.. Banding artifact removal for bSSFP imaging with an elliptical signal model *Magn Reson Med* 2014; **71**(3):927-933.
- [19] Stehling MK, Turner R, Mansfield P. Echo-planar imaging: magnetic resonance imaging in a fraction of a second. *Science* 1991; **254**:43-50.
- [20] Mansfield, P . Snap-shot MRI 2013. Nobel Lecture, 8 Dec 2003.
- [21] Poustchi-Amin Mehdi, Mirowitz Scott A., Brown Jeffrey J., McKinstry Robert C., Li Tao. Principles and Applications of Echo-planar Imaging: A Review for the General Radiologist *RadioGraphics* 2001; **21**(3):767-779.
- [22] Damadian Raymond. Tumor detection by nuclear magnetic resonance *Science* 1971; **171**:1151-3.
- [23] Look D. C., Locker D. R.. Time Saving in Measurement of NMR and EPR Relaxation Times *Rev. Sci. Instrum* 1970; **41**(2):250-251.
- [24] Hawkes RC., Holland GN., Moore WS., Roebuck EJ., Worthington BS.. Nuclear magnetic resonance (NMR) tomography of the normal heart *J Comp Assist Tomogr* 1981; **5**:605–612.
- [25] Larsson H. B. W., Frederiksen J., Petersen J., et al. Assessment of demyelination, edema, and gliosis by in vivo determination of T1 and T2 in the brain of patients with acute attack of multiple sclerosis *Magn Reson Med* 1989; **11**(3):337-348.
- [26] Messroghli Daniel R., Moon James C., Ferreira Vanessa M., et al. Clinical recommendations for cardiovascular magnetic resonance mapping of T1, T2, T2* and extracellular volume: A consensus statement by the Society for Cardiovascular Magnetic Resonance (SCMR) endorsed by the European Association for Cardiovascular Imaging (EACVI) *J Cardiovasc Magn Reson* 2017; **19**(1):75.
- [27] Cardiovascular Disease [Online; accessed January 20, 2021].
- [28] Seraphim Andreas, Knott Kristopher D., Augusto Joao, Bhuva Anish N., Manisty Charlotte, Moon James C.. Quantitative cardiac MRI *J Magn Reson Imaging* 2020; **51**(3):693-711.

- [29] Messroghli Daniel R., Nordmeyer Sarah, Dietrich Thore, et al. Assessment of Diffuse Myocardial Fibrosis in Rats Using Small-Animal Look-Locker Inversion Recovery T1 Mapping *Circ Cardiovasc Imaging* 2011; **4**(6):636-640.
- [30] Nakamori Shiro, Dohi Kaoru, Ishida Masaki, et al. Native T1 Mapping and Extracellular Volume Mapping for the Assessment of Diffuse Myocardial Fibrosis in Dilated Cardiomyopathy *JACC Cardiovasc Imaging* 2018; **11**(1):48 - 59.
- [31] Messroghli Daniel, Niendorf Thoralf, Schulz-Menger Jeanette, Dietz Rainer, Friedrich Matthias. T1 Mapping in Patients with Acute Myocardial Infarction *J Cardiovasc Magn Reson* 2009; **5**(1):2.
- [32] Roujol Sebastien, Weingärtner Sebastian, Foppa Murilo, et al. Accuracy, Precision, and Reproducibility of Four T1 Mapping Sequences: A Head-to-Head Comparison of MOLLI, ShMOLLI, SASHA, and SAPPHERE *Radiology* 2014; **272**(3):683-689.
- [33] Goebel Juliane, Seifert Ingmar, Nensa Felix, et al. Can Native T1 Mapping Differentiate between Healthy and Diffuse Diseased Myocardium in Clinical Routine Cardiac MR Imaging? *PLoS ONE* 2016; **11**(5):1-12.
- [34] Weingärtner Sebastian, Meßner Nadja M., Budjan Johannes, et al. Myocardial T1-mapping at 3T using saturation-recovery: reference values, precision and comparison with MOLLI *J Cardiovasc Magn Reson* 2017; **18**(1):84.
- [35] Teixeira Tiago, Hafyane Tarik, Stikov Nikola, Akdeniz Cansu, Greiser Andreas, Friedrich Matthias G.. Comparison of different cardiovascular magnetic resonance sequences for native myocardial T1 mapping at 3T *J Cardiovasc Magn Reson* 2016; **18**(1):65.
- [36] Messroghli Daniel R., Radjenovic Aleksandra, Kozerke Sebastian, Higgins David M., Sivananthan Mohan U., Ridgway John P.. Modified Look-Locker inversion recovery (MOLLI) for high-resolution T1 mapping of the heart *Magn Reson Med* 2004; **52**(1):141–146.
- [37] Deichmann R, Haase A. Quantification of T1 values by SNAPSHOT-FLASH NMR imaging *J. Magn. Reson.* 1992; **96**(3):608 - 612.
- [38] Scheffler Klaus, Lehnhardt Stefan. Principles and applications of balanced SSFP techniques *Eur. Radiol* 2003; **13**(11):2409–2418.
- [39] Kelvin Chow, A. Flewitt Jacqueline, D. Green Jordin, J. Pagano Joseph, G. Friedrich Matthias, B. Thompson Richard. Saturation recovery single-shot

REFERENCES

- acquisition (SASHA) for myocardial T1 mapping *Magn Reson Med* 2014; **71**(6):2082-2095.
- [40] Hermann Ingo, Uhrig Tanja, Chacon-Caldera Jorge, Akcakaya Mehmet, Schad Lothar R, Weingärtner Sebastian. Towards measuring the effect of flow in blood T_1 assessed in a flow phantom and in vivo *Phys. Med. Biol.* 2020; **65**.
- [41] Verhaert David, Thavendiranathan Paaladinesh, Giri Shivraman, et al. Direct T2 Quantification of Myocardial Edema in Acute Ischemic Injury *JACC Cardiovasc Imaging* 2011; **4**(3):269 - 278.
- [42] Kellman Peter, Aletras Anthony H., Mancini Christine, McVeigh Elliot R., Arai Andrew E.. T2-prepared SSFP improves diagnostic confidence in edema imaging in acute myocardial infarction compared to turbo spin echo *Magn Reson Med* 2007; **57**(5):891-897.
- [43] Ridouani Fourat, Tacher Vania, Derbel Haytham, et al. Myocardial native T2 measurement to differentiate light-chain and transthyretin cardiac amyloidosis and assess prognosis *J Cardiovasc Magn Reson* 2018; **20**(1):58.
- [44] Kotecha Tushar, Martinez-Naharro Ana, Treibel Thomas A., et al. Myocardial Edema and Prognosis in Amyloidosis *J. Am. Coll. Cardiol.* 2018; **71**(25):2919 - 2931.
- [45] Giri Shivraman, Chung Yiu-Cho, Mancini Ali, Rajagopalan Sanjay, Raman Subha V., Simonetti Orlando P.. T2 quantification for improved detection of myocardial edema *J Cardiovasc Magn Reson* 2009; **11**(1):56.
- [46] Akçakaya Mehmet, Weingärtner Sebastian, Roujol Sébastien, Nezafat Reza. On the selection of sampling points for myocardial T1 mapping *Magn Reson Med* 2015; **73**(5):1741-1753.
- [47] Wiesmueller Marco, Wuest Wolfgang, Heiss Rafael, Treutlein Christoph, Uder Michael, May Matthias Stefan. Cardiac T2 mapping: robustness and homogeneity of standardized in-line analysis *J Cardiovasc Magn Reson* 2020; **22**(1):38.
- [48] Giri Shivraman, Shah Saurabh, Xue Hui, et al. Myocardial T2 mapping with respiratory navigator and automatic nonrigid motion correction *Magn Reson Med* 2012; **68**(5):1570-1578.
- [49] Baeßler Bettina, Schaarschmidt Frank, Stehning Christian, et al. Reproducibility of three different cardiac T2-mapping sequences at 1.5T *J Magn Reson Imaging* 2016; **44**(5):1168-1178.

- [50] Triadyaksa Pandji, Oudkerk Matthijs, Sijens Paul E.. Cardiac T2* mapping: Techniques and clinical applications *Journal of Magnetic Resonance Imaging* 2020; **52**(5):1340-1351.
- [51] Ghugre Nilesh R, Enriquez Cathleen M, Gonzalez Ignacio, Nelson Marvin D, Coates Thomas D, Wood John C.. MRI detects myocardial iron in the human heart. *Magn Reson Med* 2006; **56**(3):681-6.
- [52] Chavhan Govind B., Babyn Paul S., Thomas Bejoy, Shroff Manohar M., Haacke E. Mark. Principles, Techniques, and Applications of T2*-based MR Imaging and Its Special Applications *RadioGraphics* 2009; **29**(5):1433-1449.
- [53] Sandino Christopher M, Kellman Peter, Arai Andrew E, Hansen Michael S, Xue Hui. Myocardial T2* mapping: influence of noise on accuracy and precision *J Cardiovasc Magn Reson* 2015; **17**:7.
- [54] Akçakaya Mehmet, Weingärtner Sebastian, Basha Tamer A., Roujol Sébastien, Bellm Steven, Nezafat Reza. Joint myocardial T1 and T2 mapping using a combination of saturation recovery and T2-preparation *Magn Reson Med* 2016; **76**(3):888-896.
- [55] Christodoulou Anthony G., Shaw Jaime L., Nguyen Christopher, et al. Magnetic resonance multitasking for motion-resolved quantitative cardiovascular imaging *Nat. Biomed. Eng* 2018; **2**(4):215-226.
- [56] Hamilton Jesse I., Jiang Yun, Ma Dan, et al. Cardiac MR fingerprinting for T1 and T2 mapping in four heartbeats *J Cardiovasc Magn Reson* 2016; **18**(1):W1.
- [57] Cruz G., Jaubert O., Botnar R.M., Prieto C.. Cardiac Magnetic Resonance Fingerprinting: Technical Developments and Initial Clinical Validation *Curr Cardiol Rep* 2019; **21**(9):91.
- [58] Qi Haikun, Bustin Aurelien, Cruz Gastao, et al. Free-running simultaneous myocardial T1/T2 mapping and cine imaging with 3D whole-heart coverage and isotropic spatial resolution *Magn Reson Imaging* 2019; **63**:159 - 169.
- [59] Blume Ulrike, Lockie Timothy, Stehning Christian, et al. Interleaved T1 and T2 relaxation time mapping for cardiac applications *J Magn Reson Imaging* 2009; **29**(2):480-487.
- [60] Weingärtner Sebastian, Roujol Sébastien, Akçakaya Mehmet, Basha Tamer A., Nezafat Reza. Free-breathing multislice native myocardial T1 mapping using the slice-interleaved T1 (STONE) sequence *Magn Reson Med* 2015; **74**(1):115–124.

REFERENCES

- [61] Ma Dan, Gulani Vikas, Seiberlich Nicole, et al. Magnetic resonance fingerprinting *Nature* 2013; **495**:187–192.
- [62] Rieger Benedikt, Zimmer Fabian, Zapp Jascha, Weingärtner Sebastian, Schad Lothar R.. Magnetic resonance fingerprinting using echo-planar imaging: Joint quantification of T1 and relaxation times *Magn Reson Med* 2016; **78**(5):1724-1733.
- [63] Hermann Ingo, Chacon-Caldera Jorge, Brumer Irène, et al. Magnetic resonance fingerprinting for simultaneous renal T1 and T2* mapping in a single breath-hold *Magn Reson Med* 2020; **83**(6):1940-1948.
- [64] Buonincontri Guido, Sawiak Stephen J.. MR fingerprinting with simultaneous B1 estimation *Magn Reson Med* 2016; **76**(4):1127-1135.
- [65] Hamilton Jesse I., Jiang Yun, Chen Yong, et al. MR fingerprinting for rapid quantification of myocardial T1, T2, and proton spin density *Magn Reson Med* 2017; **77**(4):1446-1458.
- [66] Su Pan, Mao Deng, Liu Peiying, et al. Multiparametric estimation of brain hemodynamics with MR fingerprinting ASL *Magn Reson Med* 2017; **78**(5):1812-1823.
- [67] Jiang Yun, Ma Dan, Seiberlich Nicole, Gulani Vikas, Griswold Mark A.. MR fingerprinting using fast imaging with steady state precession (FISP) with spiral readout *Magn Reson Med* 2015; **74**(6):1621-1631.
- [68] Assländer Jakob, Glaser Steffen J., Hennig Jürgen. Pseudo Steady-State Free Precession for MR-Fingerprinting *Magn Reson Med* 2017; **77**(3):1151-1161.
- [69] McGivney D. F., Pierre E., Ma D., et al. SVD Compression for Magnetic Resonance Fingerprinting in the Time Domain *IEEE Trans Med Imaging* 2014; **33**(12):2311-2322.
- [70] Davies Mike E., Puy Gilles, Vandergheynst Pierre, Wiaux Yves. A Compressed Sensing Framework for Magnetic Resonance Fingerprinting *CoRR* 2013; **abs/1312.2465**.
- [71] Hoppe Elisabeth, Körzdörfer Gregor, Würfl Tobias, et al. Deep Learning for Magnetic Resonance Fingerprinting: A New Approach for Predicting Quantitative Parameter Values from Time Series *Stud Health Technol Inform* 2017; **243**:202-206.
- [72] Cohen Ouri, Zhu Bo, Rosen Matthew S.. MR fingerprinting Deep RecOnstruction NEtwork (DRONE) *Magn Reson Med* 2018; **80**(3):885-894.

- [73] Fang Z., Chen Y., Liu M., et al. Deep Learning for Fast and Spatially Constrained Tissue Quantification From Highly Accelerated Data in Magnetic Resonance Fingerprinting *IEEE Trans Med Imaging* 2019; **38**(10):2364-2374.
- [74] Zhang Chi, Hosseini Seyed Amir Hossein, Weingärtner Sebastian, Ugurbil Kamil, Moeller Steen, Akçakaya Mehmet. Optimized fast GPU implementation of robust artificial-neural-networks for k-space interpolation (RAKI) reconstruction *PLoS ONE* 2019; **14**(10):1-14.
- [75] Wang Z., Zhang Q., Yuan J., Wang X.. MRF denoising with compressed sensing and adaptive filtering in *2014 IEEE 11th International Symposium on Biomedical Imaging (ISBI)*:870-873 2014.
- [76] Chen Yong, Jiang Yun, Pahwa Shivani, et al. MR Fingerprinting for Rapid Quantitative Abdominal Imaging *Radiology* 2016; **279**(1):278-286.
- [77] Bonnier Guillaume, Roche Alexis, Romascano David, et al. Multicontrast MRI Quantification of Focal Inflammation and Degeneration in Multiple Sclerosis *BioMed Res. Int.* 2015; .
- [78] Kim PK, Hong YJ, Im DJ, et al. Myocardial T1 and T2 Mapping: Techniques and Clinical Applications *Korean J Radiol* 2017; **18**(1):113-131.
- [79] Morrow Jasper M., Sinclair Christopher D. J., Fischmann Arne, et al. Reproducibility, and age, body-weight and gender dependency of candidate skeletal muscle MRI outcome measures in healthy volunteers *Radiology* 2014; **24**:1610-1620.
- [80] West Janne, Blystad Ida, Engström Maria, Warntjes Jan B. M., Lundberg Peter. Application of Quantitative MRI for Brain Tissue Segmentation at 1.5 T and 3.0 T Field Strengths *PLoS ONE* 2013; **8**(9).
- [81] Weingärtner Sebastian, Meßner Nadja M., Budjan Johannes, et al. Myocardial T1-mapping at 3T using saturation-recovery: reference values, precision and comparison with MOLLI *J Cardiovasc Magn Reson* 2016; **18**(1):84.
- [82] Qin Qin. Point spread functions of the T2 decay in k-space trajectories with long echo train *Magn Reson Imaging* 2012; **30**(8):1134 - 1142.
- [83] McDiarmid Adam K., Broadbent David A., Higgins David M., et al. The effect of changes to MOLLI scheme on T1 mapping and extra cellular volume calculation in healthy volunteers with 3 tesla cardiovascular magnetic resonance imaging *Quant. Imaging. Med. Surg.* 2015; **5**(4).

REFERENCES

- [84] Hein I. A., O'Brien W. D.. A flexible blood flow phantom capable of independently producing constant and pulsatile flow with a predictable spatial flow profile for ultrasound flow measurement validations *IEEE Trans Bio-Med Eng* 1992; **39**(11):1111-1122.
- [85] David A., Le Touze D., Warin-Fresse K., et al. In-vitro validation of 4D flow MRI measurements with an experimental pulsatile flow model *Diagn. Interv. Imaging* 2019; **100**(1):17 - 23.
- [86] Scully PR, Bastarrika G, Moon JC, Treibel TA.. Myocardial Extracellular Volume Quantification by Cardiovascular Magnetic Resonance and Computed Tomography *Curr Cardiol Rep.* 2018; **20**:15.
- [87] Haaf Philip, Garg Pankaj, Messroghli Daniel R., Broadbent David A., Greenwood John P., Plein Sven. Cardiac T1 Mapping and Extracellular Volume (ECV) in clinical practice: a comprehensive review *J Cardiovasc Magn Reson* 2016; **18**(1):89.
- [88] El-Khatib Ahmed H., Radbruch Helena, Trog Sabrina, et al. Gadolinium in human brain sections and colocalization with other elements *Neurology - Neuroimmunology Neuroinflammation* 2019; **6**(1).
- [89] Delgado Anna Falk, Van Westen Danielle, Nilsson Markus, et al. Diagnostic value of alternative techniques to gadolinium-based contrast agents in MR neuroimaging—a comprehensive overview *Insights into Imaging* 2019; **10**(84).
- [90] Kanzaki Yumiko, Watanebe Tomohiko, Maeda Daichi, Ito Takahide, Sohmiya Koichi, Hoshiga Masaaki. Abstract 10791: Non-contrast T1, T2 and T2 Star Mapping in Patients With Dilated Cardiomyopathy: Comparison With Late Gadolinium Enhancement *Circulation* 2019; **140**(Suppl_1):A10791-A10791.
- [91] Dyvorne Hadrien, Balchandani Priti. Slice-selective adiabatic magnetization T2-preparation (SAMPA) for efficient T2-weighted imaging at ultrahigh field strengths *Magn Reson Med* 2016; **76**(6):1741-1749.
- [92] Weingärtner Sebastian, Moeller Steen, Schmitter Sebastian, et al. Simultaneous multislice imaging for native myocardial T1 mapping: Improved spatial coverage in a single breath-hold *Magn Reson Med* 2017; **78**(2):462-471.
- [93] Meßner N. M., Budjan J., Loßnitzer D., et al. Saturation-Recovery Myocardial T1-Mapping during Systole: Accurate and Robust Quantification in the Presence of Arrhythmia *Sci. Rep.* 2018; **8**(1):5251.

- [94] Kellman Peter, Xue Hui, Spottiswoode Bruce S., et al. Free-breathing T2* mapping using respiratory motion corrected averaging *J Cardiovasc Magn Reson* 2015; **3**(17):1741-1753.
- [95] Shao Jiabin, Zhou Ziwu, Nguyen Kim-Lien, Finn J. Paul, Hu Peng. Accurate, precise, simultaneous myocardial T1 and T2 mapping using a radial sequence with inversion recovery and T2 preparation *NMR BioMed* 2019; **32**(11):e4165.
- [96] Weingärtner Sebastian, Roujol Sébastien, Akçakaya Mehmet, Basha Tamer A., Nezafat Reza. Free-breathing multislice native myocardial T1 mapping using the slice-interleaved T1 (STONE) sequence *Magn Reson Med* 2015; **74**(1):115-124.
- [97] Akçakaya Mehmet, Basha Tamer A., Weingärtner Sebastian, Roujol Sébastien, Berg Sophie, Nezafat Reza. Improved quantitative myocardial T2 mapping: Impact of the fitting model *Magn Reson Med* 2015; **74**(1):93-105.
- [98] Kahnouji Masoumeh, Rashidinejad Hamid Reza, Yazdanpanah Mohammad Shahram, Azdaki Nahid, Naghibzadeh-Tahami title=.
- [99] Friedrich Matthias G., Niendorf Thoralf, Schulz-Menger Jeanette, Gross C. Michael, Dietz Rainer. Blood Oxygen Level-Dependent Magnetic Resonance Imaging in Patients with Stress-Induced Angina *Circulation* 2003; **108**(18):2219-2223.
- [100] Friedrich Matthias G., Karamitsos Theodoros D. Oxygenation-sensitive cardiovascular magnetic resonance *J Cardiovasc Magn Reson* 2013; **15**(43).
- [101] Panda Ananya, Mehta Bhairav B., Coppo Simone, et al. Magnetic Resonance Fingerprinting-An Overview *Curr. Opin. Biomed. Eng.* 2017; **3**(1).
- [102] Hermann Ingo, Martínez-Heras Eloy, Rieger Benedikt, et al. Accelerated white matter lesion analysis based on simultaneous T1 and T2* quantification using Magnetic Resonance Fingerprinting and Deep Learning *Magn Reson Med* 2021; (10.1002/mrm.28688).
- [103] Ding Yao, Mason Ralph P., McColl Roderick W., et al. Simultaneous measurement of tissue oxygen level-dependent (TOLD) and blood oxygenation level-dependent (BOLD) effects in abdominal tissue oxygenation level studies *J Magn Reson Imaging* 2013; **38**(5):1230-1236.
- [104] Cauley Stephen F., Setsompop Kawin, Ma Dan, et al. Fast group matching for MR fingerprinting reconstruction *Magn Reson Med* 2015; **74**(2):523-528.

REFERENCES

- [105] Hu Yanle, Glover Gary H.. Three-dimensional spiral technique for high-resolution functional MRI *Magn Reson Med* 2007; **58**(5):947-951.
- [106] Wang Fuyixue, Dong Zijing, Reese Timothy G., et al. Echo Planar Time-resolved Imaging (EPTI) *Magn Reson Med* 2019; **81**(6):3599-3615.
- [107] Lustig Michael, Pauly John M.. SPIRiT: Iterative self-consistent parallel imaging reconstruction from arbitrary k-space *Magn Reson Med* 2010; **64**(2):457-471.
- [108] Cox Eleanor F., Buchanan Charlotte E., Bradley Christopher R., et al. Multiparametric Renal Magnetic Resonance Imaging: Validation, Interventions, and Alterations in Chronic Kidney Disease *Front Physiol* 2017; **8**:696.
- [109] Burnier Michel, Pruijm Menno, Mendichovszky Iosif A, et al. Renal blood oxygenation level-dependent magnetic resonance imaging to measure renal tissue oxygenation: a statement paper and systematic review *Nephrol Dial Transplant* 2018; **33**(suppl 2):ii22-ii28.
- [110] Wolf Marcos, Boer Anneloes, Sharma Kanishka, et al. Magnetic resonance imaging T1- and T2-mapping to assess renal structure and function: a systematic review and statement paper *Nephrol Dial Transplant* 2018; **33**(2):ii41-ii50.
- [111] Khajehim Mahdi, Christen Thomas, Chen J. Jean. Magnetic Resonance Fingerprinting with Combined Gradient- and Spin-echo Echo-planar Imaging: Simultaneous Estimation of T1, T2 and T2* with integrated-B1 Correction *bioRxiv* 2019; (604546).
- [112] Wyatt Cory R., Barbara Thomas M., Guimaraes Alexander R.. T1 ρ magnetic resonance fingerprinting *NMR Biomed* 2020; **33**(5):e4284.
- [113] Liimatainen Timo, Sorce Dennis J., O'Connell Robert, Garwood Michael, Michaeli Shalom. MRI contrast from relaxation along a fictitious field (RAFF) *Magn Reson Med* 2010; **64**(4):983-994.
- [114] Christen T., Pannetier N.A., Ni W.W., et al. MR vascular fingerprinting: A new approach to compute cerebral blood volume, mean vessel radius, and oxygenation maps in the human brain *NeuroImage* 2014; **89**:262 - 270.
- [115] Bammer Roland, Holdsworth Samantha J., Veldhuis Wouter B., Skare Stefan T.. New Methods in Diffusion-Weighted and Diffusion Tensor Imaging *Magn Reson Imaging Clin N Am* 2009; **17**(2):175 - 204.

- [116] Dar Salman Ul Hassan, Ozbey Muzaffer, Catli Ahmet Burak, Cukur Tolga. A Transfer-Learning Approach for Accelerated MRI Using Deep Neural Networks *Magn Reson Med* 2020; **84**(2):663-685.
- [117] Hoppe Elisabeth, Thamm Florian, Körzdörfer Gregor, et al. Magnetic Resonance Fingerprinting Reconstruction Using Recurrent Neural Networks *Stud Health Technol Inform* 2019; **267**:126-133.
- [118] Nagtegaal Martijn, Koken Peter, Amthor Thomas, et al. Myelin water imaging from multi-echo T2 MR relaxometry data using a joint sparsity constraint *NeuroImage* 2020; **219**:117014.
- [119] Enzinger Christian, Smith Stephen, Fazekas Franz, et al. Lesion probability maps of white matter hyperintensities in elderly individuals - Results of the Austrian stroke prevention study *J. Neurol.* 2006; **253**:1064-70.
- [120] DeCarli C, Fletcher E, Ramey V, Harvey D, Jagust J.. Anatomical mapping of white matter hyperintensities (WMH): exploring the relationships between periventricular WMH, deep WMH, and total WMH burden *Stroke* 2005; **36**(1):50-55.
- [121] Filli Lukas, Hofstetter Louis, Kuster Pascal, et al. Spatiotemporal distribution of white matter lesions in relapsing–remitting and secondary progressive multiple sclerosis *Mult. Scler.* 2012; **18**(11):1577-1584.
- [122] Holland Christopher M., Charil Arnaud, Csapo Istvan, et al. The Relationship between Normal Cerebral Perfusion Patterns and White Matter Lesion Distribution in 1,249 Patients with Multiple Sclerosis *J Neuroimaging* 2012; **22**(2):129-136.

LIST OF PUBLICATIONS

4.1 Journal Articles related to this thesis

- **I. Hermann**, T. Uhrig, J. Chacón-Caldera, M. Akçakaya, L. Schad and S. Weingärtner.
Towards measuring the effect of flow in blood T_1 assessed in a flow phantom and in vivo.
Phys Med Biol. 2020; 65: 095001. <https://doi.org/10.1088/1361-6560/ab7ef1>
- **I. Hermann**, J. Chacón-Caldera, I. Brumer, B. Rieger, S. Weingärtner, L. Schad and F. Zöllner.
Magnetic resonance fingerprinting for simultaneous renal T_1 and T_2^* mapping in a single breath-hold.
Magn Reson Med. 2020; 83: 1940-1948. <https://doi.org/10.1002/mrm.28160>
- **I. Hermann**, E. Martínez-Heras, B. Rieger, R. Schmidt, A. Golla, J. Hong, W. Lee, W. Yu-Te, M. Nagtegaal, E. Solana, S. Llufríu, A. Gass, L. R. Schad, S. Weingärtner, F. G. Zöllner.
Accelerated white matter lesion analysis based on simultaneous T_1 and T_2^* quantification using Magnetic Resonance Fingerprinting and Deep Learning
Magn Reson Med. 2021; n/a: n/a. <https://doi.org/10.1002/mrm.28688>
- **I. Hermann**, P. Kellman, O. Demirel, M. Akçakaya, L. Schad and S. Weingärtner.
Free-breathing simultaneous T_1 , T_2 , and T_2^* quantification in the myocardium
Magn Reson Med. 2021; n/a: n/a. <https://doi.org/10.1002/MRM.28753>

Under Review:

- **I. Hermann**, A. Golla, E. Martínez-Heras, R. Schmidt, E. Solana, S. Llufríu, A. Gass, L. R. Schad, F. G. Zöllner.
Lesion probability mapping in MS patients using a regression network on MR Fingerprinting
Magn Reson Med. 2021; submitted as a technical note

4.2 Further Journal Articles

- G. Villa, S. Ringgaard, **I. Hermann**, R. Noble, P. Brambilla, D. Khatir, F. Zöllner, S. Francis, N. Selby, A. Remuzzi and A. Caroli.
Phase Contrast Magnetic Resonance Imaging to assess renal perfusion: a systematic review and statement paper.
Magn Reson Mater Phy, 2020; 33, 3–21. <https://doi.org/10.1007/s10334-019-00772-0>
- A. de Boer, G. Villa, O. Bane, M. Bock, E.F. Cox, I.A. Dekkers, P. Eckerbom, M.A. Fernández-Seara, S.T. Francis, B. Haddock, M.E. Hall, P. Hall Barrientos, **I. Hermann**, P.D. Hockings, H.J. Lamb, C. Laustsen, R.P. Lim, D.M. Morris, S. Ringgaard, S.D. Serai, K. Sharma, S. Sourbron, Y. Takehara, A.L. Wentland, M. Wolf, F.G. Zöllner, F. Nery and A. Caroli, Consensus-Based Technical Recommendations for Clinical Translation of Renal Phase Contrast MRI. J Magn Reson Imaging (2020). <https://doi.org/10.1002/jmri.27419>

4.3 Conference Contribution

- **I. Hermann**, D. Tamada, J. Tourais, S. Reeder, L. Schad and S. Weingärtner. Toward phase-based T_2 quantification during transient state for rapid myocardial parameter mapping. Proc. SCMR, San Diego, USA, (2021), p.
- **I. Hermann**, P. Kellman, O. Demirel, M. Akçakaya, L. Schad and S. Weingärtner. Joint quantification of T_1 , T_2 and T_2^* during free breathing in the myocardium. Proc. SCMR, San Diego, USA, (2021), p.
- J. Tourais, **I. Hermann**, O. Demirel, S. Weingärtner and M. Akçakaya. Reproducibility and Accuracy of 2D High Resolution Myocardial TRAFF2. Proc. SCMR, San Diego, USA, (2021), p.
- **I. Hermann**, P. Kellman, L. Schad and S. Weingärtner Free breathing simultaneous T_1 , T_2 and T_2^* quantification using gradient echo readouts in the myocardium. Proc. ESMRMB Congress, Barcelona, (2020) 37, p.1-12
- A. Schnurr, M. Schöben, **I. Hermann**, R. Schmidt, G. Chlebus, L. Schad and F. Zöllner. Relevance Analysis of MRI Sequences for MS Lesion Detection. Proc. ESMRMB Congress, Barcelona, (2020) 37, p.77-78

- **I. Hermann**, R. Schmidt, B. Rieger, E. Martínez-Heraz, E. Solona, S. Llufríu, A. Gass, L. Schad and F. Zöllner. Detection of multiple sclerosis lesion with T_1 and T_2^* MR Fingerprinting. Proc. Intl. Soc. Mag. Reson. Med., Sydney, Australia, (2020) 28, p. 400
- **I. Hermann**, J. Chacón-Caldera, I. Brumer, S. Weingärtner, L. Schad and F. Zöllner. Renal magnetic resonance fingerprinting for simultaneous T_1 and T_2^* quantification. Proc. Intl. Soc. Mag. Reson. Med., Montreal, Canada, (2020) 28, p. 397
- **I. Hermann**, M. Sigl, S. Schönberg, L. Schad and F. Zöllner. 4D Flow for estimation of global and local pulse wave velocity in stenotic femoral arteries. Proc. Intl. Soc. Mag. Reson. Med., Montreal, Canada, (2020) 28, p. 4176
- M. Nagtegaal, **I. Hermann**, J. de Bresser and F. Vos. Detection of small cerebral lesions using multi-component MR Fingerprinting with local joint sparsity. Proc. Intl. Soc. Mag. Reson. Med., Montreal, Canada, (2020) 28, p. 1828
- **I. Hermann**, I. Brumer, B. Rieger, J. Chacón-Caldera, S. Weingärtner, L. Schad and F. Zöllner. Abdominal magnetic resonance fingerprinting for T_1 and T_2^* quantification of the kidneys. Proc. ESMRMB Congress, Rotterdam, NL, (2019) 36, p.261
- A. Schnurr, **I. Hermann**, R. Schmidt, A. Gass, F. Zöllner and L. Schad. Fully Convolutional Neural Network Segmentation of Multiple Sclerosis Lesions using T_1 and T_2^* Maps. Proc. ESMRMB Congress, Rotterdam, NL, (2019) 36, p.312
- **I. Hermann**, T. Uhrig, J. Chacón-Caldera, M. Akçakaya, L. Schad and S. Weingärtner. Effect of inflow and in-plane saturation in SASHA and MOLLI T_1 and T_1^* maps in a perfusion phantom and in-vivo. Proc. Intl. Soc. Mag. Reson. Med., Montreal, Canada, (2019) 27, p.1964
- **I. Hermann**, B. Rieger, J. Zapp, S. Weingärtner, and L. Schad. Optimized fast dictionary matching for magnetic resonance fingerprinting based on echo-planar imaging for enhanced clinical workflow, Proc. Intl. Soc. Mag. Reson. Med., Montreal, Canada, (2019) 27, p. 4529
- J. Chacón-Caldera, L. Hatz, A. Kruse, T. Uhrig, F. Zimmer, S. Hubertus, **I. Hermann**, L. Schad and F. Zöllner. Investigating Variability Sources in Kidney Perfusion Measurements with Pulsed ASL: A Phantom and In Vivo Pilot Study. Proc. Intl. Soc. Mag. Reson. Med., Montreal, Canada, (2019) 27, p.5020

LIST OF PUBLICATIONS

- G. Kabelitz, D. Bauer, A. Schnurr, **I. Hermann**, F. Zöllner, L. Schad and K. Chung. Evaluation phantom for multimodal imaging and image-guided needle interventions. 4th Conference on Image-Guided Interventions, (2019)
- **I. Hermann**, T. Uhrig, C. J, M. Akçakaya, L. Schad and S. Weingärtner. Flow dependency of blood T_1 measurements assessed in a perfusion phantom and in vivo. Proc. SCMR, Bellevue, USA, (2019), p.QF3-005

ABBREVIATIONS

AHA	...	American Heart Association
bSSFP	...	balanced Steady State Free Precession
CKD	...	Chronic Kidney Disease
CNN	...	Convolutional Neural Network
CSF	...	CerebroSpinal Fluid
DL	...	Deep Learning
ECG	...	ElectroCardioGram
ECV	...	ExtraCellulare Volume
EPI	...	Echo Planar Imaging
FLAIR	...	FLuid-Attenuated Inversion Recovery
FLASH	...	Fast Low-Angle SHot
FOV	...	Field Of View
GM	...	Gray Matter
GRAPPA	...	GeneRalized Autocalibrating Partial Parallel Acquisition
GRE	...	GRadient Echo
HCM	...	Hypertrophic CardioMyopathy
HCT	...	HematoCriT
HHD	...	Hypertensive Heart Disease
IR	...	Inversion Recovery
LCL	...	Log Hyperbolic Cosine Loss
LL	...	Look-Locker
LLR	...	Locally Low Rank
LUT	...	Look-Up Table
MAE	...	Mean Absolute Error
MSE	...	Mean Squared Error

MOLLI	...	MO dified L ook- L ocker I nversion recovery
MPPCA	...	M archenko- P astur P rincipal C omponent A nalysis
MR	...	M agnetic R esonance
MRF	...	M agnetic R esonance F ingerprinting
MRI	...	M agnetic R esonance I maging
MRM	...	M agnetic R esonance in M edicine
MRT	...	M agnet R esonanz T omographie
MS	...	M ultiple S clerosis
NAWM	...	N ormal- A ppearing W hite M atter
NMR	...	N uclear M agnetic R esonance
RF	...	R adio- F requency
SASHA	...	S aturation S ingle- s Hot A cquisition
SATURN	...	S turation A nd T_2 -prepared R elaxometry with N avigator-gating
SD	...	S tandard D eviation
SE	...	S pin E cho
SMS	...	S imultaneous M ulti- S lice
SNR	...	S ignal to N oise R atio
SPIRiT	...	i Terative S elf-consistent P arallel I maging R econstruction
SPM12	...	S tatistical P arametric M apping version 12
SR	...	S aturation R ecovery
TE	...	E cho T ime
TI	...	I nversion T ime
TR	...	R epetition T ime
TS	...	S aturation T ime
TSE	...	T urbo S pin E cho
WM	...	W hite M atter

DECLARATION

This thesis is the result of my independent investigation under supervision. Where my work is indebted to the work or ideas of others, for example from the literature or the internet, I have acknowledged this within the thesis.

I declare that this study has not already been accepted for any other degree, nor is it currently being submitted in candidature for any other degree. I am aware that a false declaration could have legal implications.

Erklärung:

Hiermit erkläre ich, die vorliegende Arbeit selbständig verfasst zu haben und keine anderen als die in der Arbeit angegebenen Quellen und Hilfsmittel benutzt zu haben.

Mannheim, February 10, 2021

.....
Ingo Hermann